Multi-qubit gates in a trapped-ion quantum computer

DISSERTATION
zur Erlangung des Grades eines Doktors der Naturwissenschaften

vorgelegt von
M.Sc. Patrick H. Huber

eingereicht bei der
Naturwissenschaftlich-Technischen Fakultät der
Universität Siegen

Siegen 2024

Betreuer und erster Gutachter
Prof. Dr. Christof Wunderlich
Universität Siegen

Zweiter Gutachter
Prof. Dr. Christian Ospelkaus
Universität Hannover

Tag der mündlichen Prüfung
30.09.2024

"If I have seen further, it is by standing on the shoulders of Giants." [1]

[1] Turnbull, H. W. ed., 1959. The Correspondence of Isaac Newton: 1661-1675, Volume 1, London, UK: Published for the Royal Society at the University Press. p. 416

Zusammenfassung

Quantencomputer versprechen Rechenprobleme effizienter zu lösen, als dies mit klassischen Computern je möglich wäre. Gefangene $^{171}Yb^{+}$ -Ionen in einer linearen Paul-Falle, die einem Magnetfeldgradienten ausgesetzt sind, wurden bereits verwendet um Quantencomputing zu demonstrieren. Dabei werden die Qubits in Hyperfeinzuständen des elektronischen Grundzustands von $^{171}Yb^{+}$ kodiert. Die Suszeptibilität der Qubit-Niveaus gegenüber Magnetfeldern durch einen linearen Zeeman-Effekt erzeugt die Kopplung der Qubits und ermöglicht außerdem eine individuelle Adressierung im Frequenzraum. In einem Register von Ionen-Qubits, die in einer linearen Paul-Falle gespeichert sind, ist die durch den Magnetfeldgradienten erzeugte Kopplung eine inhärente "Alle-zu-Alle"-Kopplung. Die Implementierung eines bestimmten Quantenschaltkreises in einem Register von Ionen-Qubits erfordert die Abstimmung der Kopplungsstärke. In dieser Arbeit wird dies mit bis zu vier Qubits unter Verwendung einer gepulsten dynamischen Entkopplungssequenz erreicht, die die Qubits vor Dephasierung schützt, während die Kopplung gewählt werden kann. Die direkte Implementierung von Quantengattern mit drei oder mehr Qubits ist vorteilhaft, um das Potential eines Quantencomputers mit gefangenen Ionen voll auszuschöpfen. Ein Beispiel ist das hier implementierte Toffoli-Gatter. Ein treibendes Feld, das auf das Ziel-Qubit angewendet wird, wird verwendet, um eine Qubit-Rotation auf dem Ziel-Qubit in Abhängigkeit vom Zustand der Kontroll-Qubits durchzuführen. Um die Qubits während dieser Zeit vor Dephasierung zu schützen und die dauerhafte Wechselwirkung der Qubits zu ermöglichen, wird eine dynamische Entkopplungssequenz angewendet und mit dem treibenden Feld auf dem Ziel-Qubit verschachtelt. Das Toffoli-Gatter wird dann eingesetzt, um einen Drei-Qubit- "Greenberger Horne Zeilinger"-Zustand und einen Halbaddierer zu realisieren. Halbaddierer, die als elementare Einheiten in der klassischen Informatik verwendet werden, bilden die Grundlage klassischer Rechenwerke. In einem Quantencomputer können sie mit Hilfe des hier vorgestellten Toffoli-Gatters und eines CNOT-Gatters realisiert werden. Perzeptren sind als Teil künstlicher neuronaler Netze ein anderer Baustein der modernen Informatik. Im Rahmen dieser Arbeit wird ein Perzeptron-Gatter an einem Register aus drei Qubits demonstriert, wobei zwei Qubits als Steuerqubits und eines als Perzeptron dienen. Eine abstimmbare sigmoidale Anregung des Perzeptrons wird mittels eines adiabatischen Antriebsfeldes erzeugt, das mit einer dynamischen Entkopplungssequenz verschachtelt ist, um die Kohärenzzeiten zu verlängern und die Wechselwirkungsstärke zwischen den Qubits abzustimmen. Das Perzeptron wird dann in einem zweischichtigen neuronalen Netz eingesetzt, um eine XNOR-Operation zu implementieren. Zusätzlich zur Anwendung als Qubit erlaubt die Abhängigkeit der Qubit-Resonanz vom Magnetfeld, ein Ionen-Qubit als Quantensensor für Magnetfelder und damit unter Nutzung eines Magnetfeldgradienten zur Messung von Kräften im 10^{-23} N-Bereich zu verwenden.

Abstract

Quantum computers promise to solve computational problems more efficiently than classical computers ever could. Trapped $^{171}Yb^{+}$ ions in a linear Paul trap exposed to a magnetic field gradient have already been used to demonstrate quantum computing. The qubits are encoded in hyperfine states of the electronic ground state of $^{171}Yb^{+}$ ions. The susceptibility of the qubit levels to magnetic fields by a linear Zeeman effect generates the coupling of the qubits and allows for individual addressing in frequency space. In a register of qubits stored in a linear Paul trap, the coupling generated by the magnetic field gradient is an inherent all-to-all coupling. Implementing a given quantum circuit on a register of qubits requires tuning the coupling strength. Here tuning the coupling with up to four qubits is demonstrated using a pulsed dynamical decoupling sequence, which protects the qubits from dephasing while the coupling can be chosen. Direct implementation of quantum gates with three or more qubits is necessary to exploit the full capabilities of a trapped-ion quantum computer. An example is the Toffoli gate implemented here. A driving field, applied to the target qubit, is used to perform a conditional rotation based on the control qubits state, while a dynamical decoupling sequence protects the coherence of the qubits. The Toffoli gate is then applied in a half-adder and is used to generate a three-qubit Greenberger Horne Zeilinger state. Half-adders, which are used as elementary units in classical computer science, form the basis of classical arithmetic units. In a quantum computer, they can be realized using the Toffoli gate and a CNOT gate. Perceptrons are a part of neural networks, a fundamental building block in modern computer science. Here a Perceptron gate is demonstrated on a register of three qubits where two qubits serve as control qubits and one as a perceptron. The characteristic tunable sigmoid excitation of the perceptron is shown using an adiabatic driving field interleaved with a dynamical decoupling sequence to prolong coherence times and tune the interaction strength between the qubits. The perceptron is then applied in a two-layer neural network to implement an XNOR operation. In addition to its use as a qubit, the dependence of the qubit resonance on the magnetic field allows an ion qubit to be used as a quantum sensor for magnetic fields and thus, using a magnetic field gradient, to measure forces in the 10^{-23} N range.

Contents

1

Introduction

Information technology has revolutionized the way we live. Whether it is the constant availability of information, the automation of production, or the ability to conduct research that was impossible a century ago. The development of computers has changed the world we live in. Fundamental research is the foundation of today's information technology. Mechanical calculating machines in the 19th century [1] paved the way for their electrical counterparts using relays or tubes in the 20th century. The invention of the first transistor in 1947 [2], its miniaturization and the massive increase in the number of transistors available led to modern semiconductor-based computers [3]. As a result of fundamental research at CERN, the next revolution in computer science was launched [4]. The need to connect researchers across the campus, and later across the globe, led to the development of the Internet as we know it today. Computers have become increasingly powerful, interconnected, and capable of calculations and numerical simulations unimaginable a century ago. Currently, computer science is being revolutionized again, as neurons have been implemented into mathematical models [5]. Despite three centuries of development and amazing results, classical computers are limited. All information in a computer is encoded in a logic that can distinguish between two states, namely 0 and 1. Numbers are therefore represented in a binary system such that a binary number containing n digits can represent a number between 0 and 2^n. Complex calculations are performed using basic arithmetic operations, which can be broken down into more basic operations. For example, the multiplication of two numbers is implemented using adding operations, which are implemented as an operation that bit-wise adds two numbers. These adders consist of half-adders, and these half-adders are based on logical gates such as AND, OR, or NOT operations. The gates are then implemented using digital circuits of transistors, which are the basic element of all computers. Although the number of arithmetic operations performed by modern processors is on the order of billions to trillions per second, there are computational problems

in science that are so complex that even the impressive performance of semiconductor processors is insufficient to solve them. Quantum mechanical problems, for example, are of interest in chemistry and can lead to important discoveries. Because the mathematical dimensionality of quantum mechanical problems increases rapidly and the Hilbert space describing possible configurations is huge, even small chemical systems cannot be solved accurately on today's computers. To solve quantum mechanical problems, Richard Feynman proposed a computer based on a quantum system [6]. Such a computer, called a quantum computer, could cover the vast configuration space of chemical systems because it would be based on quantum mechanics itself.

In addition to chemical systems, it is believed that a quantum computer will be able to solve other problems that are currently intractable by classical computers. Some examples are the factorization of numbers into prime factors or the traveling salesman problem. This class of problems is inherently interesting to solve, and possible solutions could have a significant impact on our daily lives. Therefore, the development of a quantum computer capable of solving previously unsolvable problems is of great interest to society.

A quantum computer will not make classical computers obsolete, but rather will become an additional computing platform to solve specific problems that are primarily relevant in professional use cases such as research and development.

One promising platform for a quantum computer is a trapped-ion quantum computer. In such systems, each qubit is represented by the state of an atom. The system used in this thesis is particularly promising because it has several advantages over other quantum computing platforms. The qubits are reproducible and controllable and can be stored for long periods of time.

Similar to the development of classical computer science, the development of quantum computers has reached the point where the first devices have started to leave the laboratory environment. Typical systems still occupy entire rooms, just as classical computers did in the beginning. In addition, modern classical computers used for scientific research or large-scale data analysis still occupy entire facilities. However, the commercialization of quantum computers is just beginning.

So far, quantum computers (QCs) require special environments and trained personnel to operate and maintain, and they are not easily scalable. The need for constant maintenance

by trained personnel needs to be overcome in a commercial environment. Therefore, the first part of this thesis is dedicated to automation, allowing the user to focus on his research. Furthermore, chapter 2 will give an overview of the basic physical effects used. Since each ion can also be used as a sensor of magnetic fields, advances in the automatic calibration of the quantum computer allow the study of fundamental physics, such as the measurement of the ion's position. Using this technique, the diagnosis of the ion chain forming a register in a QC can be applied to select an appropriate error mitigation strategy in case a qubit ends up in a dark state.

A key advantage of trapped-ion QC over other systems is the inherent all-to-all coupling between all qubits in a register. This all-to-all coupling allows conditional operations to be performed directly on the entire register. Efficient control of the qubit interactions is essential for the implementation of advanced quantum algorithms. Therefore, in chapter 4 a method to tune the coupling between qubits in a register using radio frequency control pulses is outlined and demonstrated. The parallelization of computational tasks is crucial. Using the qubit coupling control scheme presented here will allow parallelized quantum circuits to run on quantum computers with always-present interactions between qubits.

The inherent all-to-all coupling within the quantum register is a valuable tool for implementing quantum logic gates consisting of three or more qubits. This reduces the complexity and runtime of quantum circuits by avoiding the decomposition of a circuit into two qubit gates. An essential operation in a classical computer is the addition of two numbers. In chapter 5, a half-adder is implemented using a Toffoli gate in which two control qubits control a target qubit, similar to classical computation. The classical computing infrastructure consumes a significant part of the world's electrical energy, and quantum computers will contribute to this energy demand in the future, so it is of interest to study the fundamental energy consumption of quantum computers. For this purpose, the implemented half-adder circuit can serve as a toy model to estimate the power consumption of current quantum computers and to outline possible ways to estimate the power consumption of future quantum computing platforms.

The latest revolution in classical computer science is the neural network implemented in a mathematical model. They can be seen as a mathematical graph with vertices representing neurons and edges representing their respective connections. The inherent all-to-all coupling in a trapped-ion quantum computer makes these systems promising candidates

for implementing neural networks, where each qubit is a neuron and their interconnections are realized by the coupling. Using techniques introduced in chapters 4 and 5, chapter 6 presents the implementation of a perceptron gate controlled by two control qubits.

After classical computing, quantum computing is evolving along a similar path, possibly opening the door to unforeseen applications.

2

Basic principles

This chapter briefly describes the basics necessary to understand the work presented here. This is not the first thesis describing the hardware and principles of a trapped-ion quantum computer. Each of the previous dissertations on the experimental setup used focuses on different aspects of the experiment. The Ph.D. thesis of Anastasia Khomorova [7] focuses on the setup of the ion trap, the microwave and the laser system required for the basic operation. The next thesis to be mentioned is the PhD thesis of Christian Piltz [8], which focuses on the dynamical decoupling of qubits from their environment, the selective coupling in a three-ion crystal, the addressing of single qubits in a quantum byte, and the implementation of a quantum Fourier transform on three qubits. The most recent Ph.D. thesis was written by Theeraphot Sriarunothai [9] and is dedicated to multi-qubit gates and quantum-enhanced deliberation learning. All of them describe the experiment in detail.

The experiment was first set up in 2012 [10], and the majority of the experiment's hardware has remained the same. Therefore, the description of the experimental setup in this chapter will be relatively brief. Nevertheless, it will provide an overview of the experiment for the reader to understand the work presented in this thesis. While working on this experiment, I was accompanied by Patrick Barthel, who was simultaneously working on his Ph.D. thesis. His thesis will show the implementation of robust two-qubit gates and two-qubit entangling dressed state gates. In particular, the description of the microwave system required for coherent control of the qubit is discussed in detail. It is recommended to read this thesis to get a better insight into the current state of the art experiment. If, at some point, more details are needed, a look at the other dissertations should be enlightening.

The chapter is organized as follows: First, the ion trap is described, followed by the hyperfine qubit levels of the ytterbium ion and its interaction with a microwave field. Later, the structure of a typical experiment is presented, and the current detection scheme

and data analysis methods are explained.

With these information as a basis, it is possible to understand the experimental procedures described, such as automated ion loading, stabilization of cooling fluorescence, and fast addressing frequency correction. At the end of this chapter, the effective Hamiltonian coupling the motional state and the spin state of the ions is described. This allows to understand the principle of sideband cooling and the induced qubit-qubit interaction needed to implement conditional quantum dynamics.

2.1 Trapped ions in a magnetic field gradient

An essential requirement to realize a quantum computer based on a system of ions is to trap these ions and isolate them from the environment. This trap has been realized in a linear Paul trap introduced by Wolfgang Paul over half a century ago [11]. The basic principle of trapping a charged particle in free space in a vacuum using electrodynamic forces allowed the development of a trapped-ion quantum computer. The experimental apparatus used in this work was built in 2011 and described in detail in the PhD thesis of Anastasia Khomorova [7]. Here a short introduction is given to understand the principles of all following chapters of this thesis.

To confine charged particles in three dimensions, an effective three-dimensional potential well must be realized. Because electrostatics is described by the Laplace equation $\Delta\phi = 0$, where ϕ is the electrostatic potential, it follows that an electrostatic force cannot have a stable minimum. Since $\partial_x^2\phi + \partial_y^2\phi + \partial_z^2\phi = 0$, at least one part of the sum must be negative. This implies a repulsive force when the stored particle is slightly displaced. W. Paul realized that this could be circumvented by using a time-dependent electric field [11]. A set of six electrodes can produce the necessary fields. Four electrodes generate a confining radially symmetric potential in the xy plane, while the other two electrodes generate a confining potential in the axial z direction. To satisfy the above conditions, two opposing electrodes in the xy plane, shown in the simplified version of the trap in fig. 2.1.1, are set to an AC voltage, and two opposing electrodes in the xy plane are set to a DC potential. This creates the radial confinement potential. The axial confinement potential in the z direction is provided by two electrodes facing each other in this direction. In summary, the electrodes

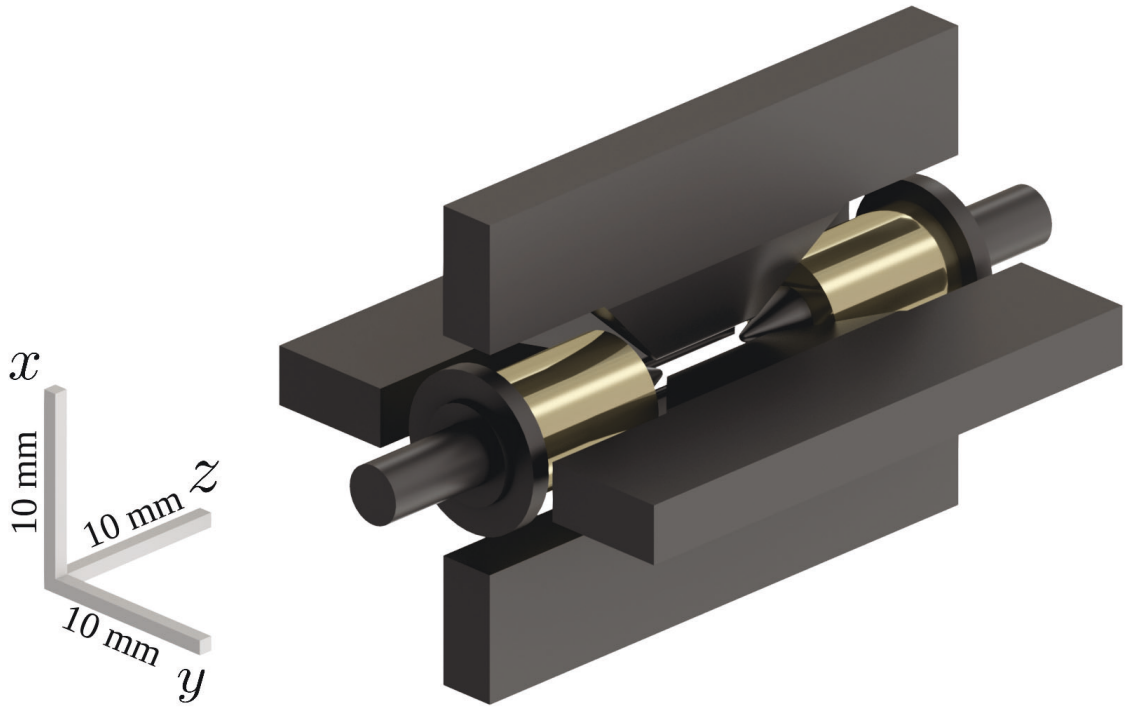

Figure 2.1.1: Simplified view of the linear Paul trap setup by A. Khomorova [7]. The four electrodes generate a trapping potential in the radial xy-plane, which, combined with the DC potential of the axial electrodes, allows stable trapping in three dimensions. The round electrodes generate a trapping DC potential along the z axis. The weaker confinement along the z direction compared to the radial confinement in the xy plane allows a set of ions to crystallize along the z axis, forming the linear Coulomb crystal that will serve as the quantum processor. The silver cylinders are sintered SmCo permanent magnets oriented in a way that the same magnetic pole faces the center of the trap, creating a magnetic gradient of 19 T/m [7, 12].

generate an effective quadratic potential in 3D that trap charged particles. The quadratic shape of the effective trapping potential quantizes the motion of the trapped particles:

$$\Phi = \frac{1}{2}m\omega_r^2 r^2 + \frac{1}{2}m\omega_z^2 z^2, \tag{2.1.1}$$

where m is the mass of the $^{171}Yb^+$ -ion, ω_r is the radial trapping frequency, and ω_z is the axial trapping frequency. A trapped particle in a harmonic (quadratic) potential is a well-known example in quantum mechanics for which its describing equation, the Schrödinger equation, can be solved. The solution of the Schrödinger equation yields a quantized harmonic oscillator with equidistant energies for all possible solutions. Its energies are

$E_n = (1/2 + n)\hbar\omega$, and its energy splitting is $\Delta E = \hbar\omega$, where $\hbar$ is the reduced Planck constant and ω is the resonant frequency of the quantized motion. ω_z depends on the quadratic potential and is called the trapping frequency. Due to the symmetry of the effective potential, there are two trapping frequencies. ω_r is the trapping frequency in the radial direction and ω_z is the trapping frequency in the axial direction. By choosing the voltages at the electrodes, the trap frequencies ω_r and ω_z can be chosen. Since the trapped ions are charged particles, each ion repels the other ions present due to the Coulomb force. A choosing the axial confinement potential along the z-axis shallow enough, allows the trapped ions to align in a linear ion chain. A linear ion crystal is formed when the ratio of the radial trapping frequencies to the axial trapping frequencies obeys [13]

$$\frac{\omega_r}{\omega_z} > 0.73N^{0.86}, \tag{2.1.2}$$

where N is the number of ions stored in the trap. If a linear ion chain forms, the length scale l for the distance between the ions in the chain is given by [14]

$$l = \sqrt[3]{\frac{q_e^2}{4\pi\epsilon_0 m_{\mathrm{Yb}}\omega_z^2}} \propto \omega_z^{-2/3} \tag{2.1.3}$$

where q_e is the electron charge, ϵ_0 is the vacuum permittivity, m_{Yb} is the mass of the $^{171}\mathrm{Yb}^+$ ion, and ω_z is the angular trap frequency along the trapping axis z. In the case of our experiment, the length scale is $l \approx 10\,\mu\mathrm{m}$. Each linear ion chain consisting of N ions is a set of N coupled oscillators, where each ion participates in different vibrational modes of the crystal.

These vibrational modes are part of the coupling scheme used in this setup, which couples the motion of the ions to their internal degrees of freedom. With the MAgnetic Gradient Induced Coupling(MAGIC) direct qubit-qubit coupling can be realized. It requires a magnetic field gradient in this case generated by a set of permanent magnets. The permanent magnets are installed so that the same pole of each magnet faces the center of the trap. This configuration produces a zero magnetic field at the center of the trap with a magnetic field gradient oriented along the trap axis of $19\,\mathrm{T/m}$. The linear ion chain is slightly displaced from the trap center to produce an offset magnetic field, allowing the ions to align their spin with the field and define the quantization axis in the laboratory frame. Overall, a linear chain of ions in the axial direction z allows a one-dimensional approximation of the

dynamics of the system. The quantized axial secular motion, together with the magnetic field gradient, gives rise to the induced spin-spin coupling in the system, which is exploited in the MAgnetic Gradient Induced Coupling (MAGIC) scheme [15].

2.2 The $^{171}Yb^{+}$ ion qubit

A qubit is a system with two different energy eigenstates, which can be labeled $|0\rangle$ and $|1\rangle$. A useful qubit must have some crucial properties. First, one should be able to distinguish the two levels to read the qubit [16–18]. Another requirement is the ability to initialize the qubit to a desired state [19–21]. The next ingredient for a useful qubit is the ability to coherently control its state [22, 23]. Furthermore, the qubit should hold its quantum information for some time and therefore must have a coherence time long enough to perform the desired quantum operation [24]. Since computation requires the existence of conditional operations, it should also be possible to realize conditional dynamics with the qubit [25]. In addition, qubits used in a future quantum computer should be reproducible to allow a clear scale-up concept. [15]

Using atoms as qubits is a reasonable choice because atoms of the same isotope are identical in their physical properties of nucleus and electron configuration. Using atoms therefore eliminates variations in production of the qubits.

A good candidate for a qubit is an atom that has a non-zero nuclear spin in its ground state, which limits possible candidates to isotopes with an odd number of nucleons. To make it as easy as possible to work with this isotope, it is advantageous that the level scheme is simple. The element of choice is the Yb atom, or more precisely the $^{171}Yb^{+}$ ion, which has a hyperfine structure due to its nuclear spin of $I = 1/2$. The Yb atom, once ionized, forms a hydrogen-like ion with a $^{2}S_{1/2}$ orbit as its ground state. The free electron spin couples with the free nuclear spin and produces a hyperfine splitting of the electronic $^{2}S_{1/2}$ ground state [26,27]. The energy splitting of the hyperfine level in the GHz regime is small compared to the electronic transitions in the optical THz regime. This is advantageous because it allows manipulation of the quantum state by radiation in the radiofrequency (RF) regime and increases the lifetime of the excited hyperfine state. The qubit state $|0\rangle$ is encoded in the hyperfine ground state $|^{2}S_{1/2}, F = 0\rangle$, while $|1\rangle$ is encoded in the state

$|^2S_{1/2}, F = 1, m_F = +1\rangle$. The state $|^2S_{1/2}, F = 1, m_F = -1\rangle$ is also a valid choice for the state $|1\rangle$, which also depends linearly on the magnetic field but with the opposite sign, but in this thesis the state is not used. The state $|^2S_{1/2}, F = 1, m_F = 0\rangle$ does not show a linear magnetic Zeeman shift and could therefore serve as a memory. These states are represented in fig. 2.2.1. They form the physical qubit and can be prepared and read out optically as described in section 2.5.

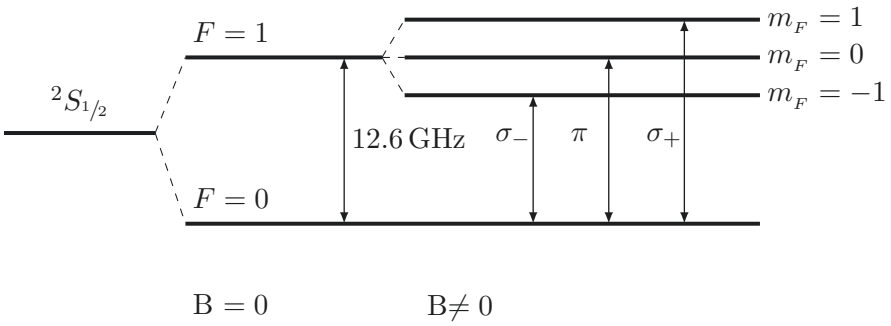

Figure 2.2.1: Level scheme of the hyperfine $^{171}Yb^+$ ground state $^2S_{1/2}$. The nuclear and electronic spin 1/2 couple to the total angular momentum F. An external magnetic field B lifts the degeneracy of the state $|^2S_{1/2}, F = 1\rangle$, making the states $|^2S_{1/2}, F = 1, m_F = -1, 0, +1\rangle$ distinguishable in their energy. This allows addressing the different transitions in frequency space. [28]

Using the hyperfine levels in $^{171}Yb^+$ provides a naturally long lifetime of the population of the state $|1\rangle$ [27], whereas the relatively small frequency of 12.6 GHz allows for a reasonably easy coherent control of the qubit, based on well-established RF technology and commercially available hardware. The generation of RF fields in this regime with reasonable frequency, amplitude, and phase control is possible without demanding field generation.

The transitions $|^2S_{1/2}, F = 1, m_F = \pm 1\rangle \leftrightarrow |^2S_{1/2}, F = 0\rangle$ are called magnetic $\sigma_\pm$ transitions, while the transition $|^2S_{1/2}, F = 1, m_F = 0\rangle \leftrightarrow |^2S_{1/2}, F = 0\rangle$, which does not change the magnetic quantum number m_f, is called the π transition. The nuclear spin I and the angular momentum J of the electronic orbital couples to the total angular momentum $F = I + J$ with $|I - J| \leq F \leq |I + J|$. Since the relevant orbital is an S orbital, the orbital angular momentum L is zero, and $J = L + S$ is generated by the electronic spin angular momentum.

This coupling of angular momenta leads to the hyperfine splitting(HFS) where the energy

gap between two levels is given by

$$\Delta E_{HFS} = \frac{A}{2}\left[F(F+1) - I(I+1) - J(J+1)\right], \text{with} \tag{2.2.1}$$

$$A = \frac{g_I \mu_k B_0}{\sqrt{J(J+1)}}. \tag{2.2.2}$$

Here g_I denotes the nuclear g factor, μ_K is the nuclear magnetic moment, and B_0 corresponds to the magnetic field generated by the electronic shell at the position of the nucleus. In the case of $^{171}\mathrm{Yb}^{+}$, the hyperfine constant A is determined precisely for the ground state $^2S_{1/2}$ [26, 27] as

$$\frac{A}{\hbar} = 2\pi \cdot 12\ 642\ 812\ 118.471(9)\,\mathrm{Hz}. \tag{2.2.3}$$

Here $\hbar$ is the reduced Plancks constant.

Exposing the $^{171}\mathrm{Yb}^{+}$ ion to a magnetic field defines the quantization axis relative to the magnetic field and orients the ion in the lab frame. This lifts the degeneracy corresponding to the magnetic quantum number m_F. In our case of $F = I \pm 1/2$, the energy dependence of the transition can be described analytically by using the Breit-Rabi equation [29]:

$$\Delta E(B, F, m_F) = -\frac{\Delta E_0}{4I+2} + m_F g_I \mu_K B + (-1)^{F+1}\frac{\Delta E_0}{2}\sqrt{1 + \frac{4m_F}{2I+1}XB + X^2B^2}, \tag{2.2.4}$$

$$\text{with } \Delta E_0 = A(I + 1/2), \tag{2.2.5}$$

$$\text{and } X = \frac{g_J \mu_B - g_I \mu_K}{A(I+1/2)}. \tag{2.2.6}$$

Here g_J is the g factor of the electronic shell, and μ_B is the Bohr magneton. The nuclear g factor is given as $g_I = 0.9837$ [30]. In the case of a nuclear spin of $I = 1/2$ this leads to $\Delta E_0 = A$. For $^{171}\mathrm{Yb}^{+}$ we have $I = 1/2$ and therefore, this simplifies to

$$\Delta E(B, F, m_F) = -\frac{A}{4} + m_F g_I \mu_K B + (-1)^{F+1}\frac{A}{2}\sqrt{1 + 2m_F XB + X^2B^2}. \tag{2.2.7}$$

The transition energy is given by the energy difference between the two levels. For the σ_+ transition, the energy is calculated as follows:

$$h\nu_{\sigma_+}(B) = E_{|^2S_{1/2},F=1,m_F=+1\rangle} - E_{|^2S_{1/2},F=0,m_F=0\rangle} \tag{2.2.8}$$

$$= g_I\mu_K B + \frac{A}{2}\sqrt{1+2XB+X^2B^2} + \frac{A}{2}\sqrt{1+X^2B^2}. \tag{2.2.9}$$

As described in section 2.1, the ions trapped in this Paul trap form a linear ion crystal. This crystal defines the position of the ion within the trap. Together with the magnetic field gradient generated by the permanent magnets installed in the setup, the dependence of the transition frequencies $\nu_{\sigma_\pm}$ on the magnetic field allows the individual addressing of the ions by RF radiation [31]. In our experimental setup, the distance between the addressing frequencies is about $\nu_2 - \nu_1 \approx 2\pi \cdot 3.2\,\mathrm{MHz}$ for a two-ion crystal and a trap frequency of $\omega \approx 2\pi \cdot 120\,\mathrm{kHz}$. This allows us to address each ion by selectively selecting its resonance. It has been shown that this splitting of the ion resonances allows RF qubit manipulation with a low crosstalk of about 10^{-5} [32] for an 8-ion Coulomb crystal.

2.3 Quantum dynamics

The quantum dynamics exploited in a trapped-ion quantum computer can be formulated as a Hamiltonian, which represents the energy operator of the system. In the case of an ion string of length N, the total energy of the system is given by the Hamiltonian given by the equation (2.3.1). This Hamiltonian contains all relevant energy contributions to the system. In addition to the energy contributions already mentioned, there is a direct effective spin-spin coupling: the MAgnetic Gradient Induced Coupling (MAGIC) [33]. It is mediated by the magnetic field gradient, the motion of the ions in the trap and the Zeeman splitting. The effective Hamiltonian is:

$$H = \underbrace{\frac{\hbar}{2}\sum_{n=1}^{N}\nu(z^{(n)})\sigma_z^{(n)}}_{I} + \underbrace{\sum_{n=1}^{N}\hbar\omega_n(a_n^\dagger a_n)}_{II} - \underbrace{\frac{\hbar}{2}\sum_{n<l}^{N}J_{nl}\sigma_z^{(n)}\sigma_z^{(l)}}_{III}. \tag{2.3.1}$$

Here (I) is the energy contribution of the Zeeman split hyperfine levels, containing the transition frequency ν of ion n at the position $z^{(n)}$, (II) the energy of the Harmonic oscillator potential of all N vibrational modes with frequencies ω_n, where $a_n^\dagger$ and a_n is

the creation and annihilation operator of a vibrational excitation respectively, (III) is the energy contribution of the MAGIC spin-spin interaction. Additionally $\sigma_{x,y,z}^{(n)}$ are the Pauli operators acting on the n-th qubit:

$$\sigma_x = \begin{pmatrix} 0 & 1 \\ 1 & 0 \end{pmatrix}, \quad \sigma_y = \begin{pmatrix} 0 & -i \\ i & 0 \end{pmatrix}, \quad \sigma_z = \begin{pmatrix} 1 & 0 \\ 0 & -1 \end{pmatrix}.$$

The coupling of all ions in the crystal is given by:

$$H_{zz} = -\frac{\hbar}{2} \sum_{n<l}^{N} J_{nl} \sigma_z^{(n)} \sigma_z^{(l)}. \tag{2.3.2}$$

Since the eigenvalues of σ_z are ± 1, the element of the sum $\pm J_{nl}\sigma_z^{(n)}$ changes the sign of the contribution of ion n depending on the state of ion l. The effective J coupling is mediated by the coupling of two ions to the same vibrational mode ϵ_{nl} [33]. Its magnitude is given as

$$J_{ij} = \sum_{l=1}^{N} \omega_l \epsilon_{il} \epsilon_{jl}, \tag{2.3.3}$$

with

$$\epsilon_{nl} = \eta_{eff} S_{nl}, \tag{2.3.4}$$

$$\eta_{eff} = \partial_z \nu_n(B(z)) \frac{\Delta z_l}{\omega_l}, \tag{2.3.5}$$

where $\Delta z_l = \sqrt{\hbar / 2m\omega_l}$ is the extension of the ions wave function in the l-th excited vibrational state of the ion with mass m and S_{nl} is the dimensionless amplitude of the n-th ions vibrational mode l. In total, it follows that assuming a linear dependence of $\nu(B)$, the effective J coupling scales as

$$J_{ij} \propto \left(\frac{\partial_z B(z)}{\omega} \right)^2, \tag{2.3.6}$$

where ω is the energy split of the harmonic oscillator formed by the quadratic trapping potential. Note that this spin-spin coupling is always present in the given experimental setup and directly connects all qubits in an ion string.

For the scope of this work, these dynamics generated by the Hamiltonian are fixed so that

the coupling and the energy of the harmonic motion from equation (2.3.1) are constant. The only external control available is the driving RF field Ω. By performing a rotating wave approximation (RWA) with respect to the ion resonance frequency and neglecting the contribution of the harmonic trapping potential, the effective Hamiltonian becomes

$$H^{eff} = \frac{\hbar}{2}\sum_{n=1}^{N}\left(\Omega_n\cos(\phi_n)\sigma_x^{(n)} + \Omega_n\sin(\phi_n)\sigma_y^{(n)} + \delta_n\sigma_z^{(n)}\right) - \frac{\hbar}{2}\sum_{n<l}^{N} J_{nl}\sigma_z^{(n)}\sigma_z^{(l)}, \qquad (2.3.7)$$

where δ_n is the relative detuning between the atomic resonance and the applied RF field, Ω_n is the Rabi frequency of the RF driving field resonant with ion n, and ϕ_n is the phase of the applied RF field to the reference frame co-rotating with the spin.

In the setup typically the coupling strength is of the order $J_{ij} \approx 2\pi \cdot 40\,\mathrm{Hz}$, whereas the possible Rabi frequencies are of the order of $\Omega \approx 2\pi \cdot 40\,\mathrm{kHz}$. The relative difference is about three orders of magnitude and thus justifies dropping the J coupling term in this Hamiltonian in the presence of a strong Ω driving field. In addition, if Ω is constant in time, the time evolution of a single qubit can be written as the exponential of a time-independent Hamiltonian

$$U(t, t_0) = e^{-\frac{i}{\hbar}H(t-t_0)}. \qquad (2.3.8)$$

In the case of a driving field present, it follows that

$$U(t_1, t_0, \phi, \Omega, \delta) = e^{-i\frac{(t_1-t_0)\Omega}{2}\vec{n}\cdot\vec{\sigma}}, \qquad \vec{n} = \frac{1}{\Omega}\begin{pmatrix}\Omega_0\cos(\phi)\\ \Omega_0\sin(\phi),\\ \delta\end{pmatrix} \qquad \vec{\sigma} = \begin{pmatrix}\sigma_x\\ \sigma_y\\ \sigma_z\end{pmatrix}. \qquad (2.3.9)$$

Here $\vec{n}$ defines the rotation axis with phase ϕ and detuning δ between the driving field and atomic resonance. The time t_0 and t_1 correspond to the pulse start and stop time and $\Omega = \sqrt{\Omega_0^2 + \delta^2}$ is the generalized Rabi frequency. Having $\theta = (t_1 - t_0)\Omega$, the unitary time evolution operator can be written in terms of the rotation angle θ and the phase ϕ. These angles correspond to the angles of the Bloch sphere representation of the quantum state.

Typical single qubit rotations are rotating the qubits state by $\theta = \pi$ or $\theta = \pi/2$. They are called π or $\pi/2$-pulses respectively. The short notation for these specific pulses is

$$R(\theta = \pi, \phi) = \pi_\phi \quad \text{or} \quad R(\theta = \pi/2, \phi) = \frac{\pi}{2}_\phi. \qquad (2.3.10)$$

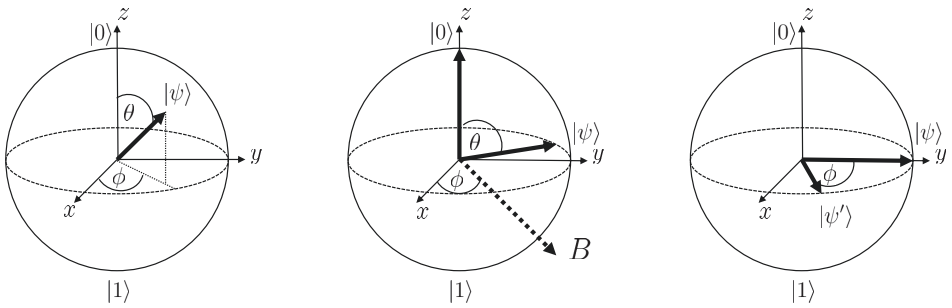

(a) (b) (c)

Figure 2.3.1: (a) Bloch sphere representation of a state $|\psi\rangle$ by the angles θ and ϕ (b) Induced rotation of a state from $|0\rangle$ to $|\psi\rangle$ by a rotation $R(\theta, \phi)$. The rotation is generated by a resonant magnetic field B, resonant with the qubit transition, for B which is stationary during the pulse evolution. The phase ϕ defines the direction of the magnetic field in the equatorial plane that drives the transition. (c) Shows the phase acquired over time from state $|\psi\rangle$ to state $|\psi'\rangle$.

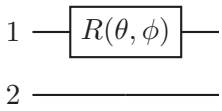

Figure 2.3.2: In terms of a circuit model, single qubit rotations are depicted as boxes, indicating the angle and phase of rotation. Here the single qubit rotation $R(\theta, \phi)$ is executed on qubit one, while nothing happens with qubit two. The operator discribing this scenario is $U = R(\theta, \phi) \otimes \mathbb{1}$

At times when no driving field Ω is present, the effective Hamiltonian reduces to

$$H_{zz} = -\frac{\hbar}{2} \sum_{n<l}^{N} J_{nl} \sigma_z^{(n)} \sigma_z^{(l)}, \tag{2.3.11}$$

coupling all qubits present simultaneously.

Note that in the linear approximation only qubits in the states $|^2S_{1/2}, F = 1, m_F = -1\rangle$ or $|^2S_{1/2}, F = 1, m_F = +1\rangle$ couple.
In contrast to these two states, an ion in the $|^2S_{1/2}, F = 1, m_F = 0\rangle$ state will not participate in a qubit-qubit interaction in the linear approximation.

Since the magnetic field gradient is continuous, the Hamiltonian is time-independent. Therefore, the unitary time evolution can be expressed as in the equation (2.3.8). However, the effective Hamiltonian does not have to be dominated by either a driving field or a coupling. The intermediate regime is also possible and is used to generate a unitary evolution of a multi-qubit system, which can produce interesting quantum dynamics. For example, in chapter 6 the implementation of a quantum mechanical perceptron is demonstrated using an intermediate regime. In general, the unitary evolution of the quantum system can include anything that the effective Hamiltonian can realize. Note that in the case of a quantum register containing more than one qubit, this evolution may include pulses or free evolution times in parallel. A schematic illustrating a local rotation on one qubit while a second qubit is idle is shown in fig. 2.3.2.

2.4 Quantum circuits

In a working quantum computer, the algorithms executed can be represented as quantum circuits and can be decomposed into building blocks. Ultimately, these building blocks of a quantum circuit represent the elementary operations provided by the quantum processor executing the quantum algorithm. Thus, the available elementary building blocks define the structure of a quantum circuit for a given hardware.

In our case, any quantum circuit that we can execute with the system shown above must follow a certain structure. Section 2.5 will show that the valuable feature of requiring only global laser beams leads to the restriction that re-initialization is not possible during the execution of a circuit once it is initialized to $|0\rangle^{\otimes N}$. The same holds for a readout, since the global laser beam would project all qubits to $|0\rangle$ or $|1\rangle$, respectively.

A general quantum circuit that can be executed is shown in fig. 2.4.1.

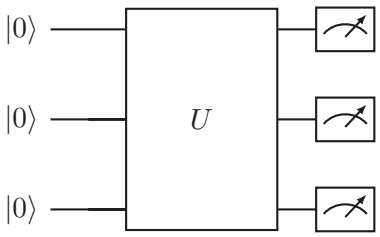

Figure 2.4.1: Circuit diagram for the possible experiment settings in the current setup. In the beginning, all qubits are initialized to state $|0\rangle$. The unitary time evolution acting on all qubits is generated by the system Hamiltonian presented in equation (2.3.7) and may consist of arbitrary RF fields and spin-spin interactions. In the end all qubits are projected and measured.

2.5 Experimental methods

This thesis deals with the implementation of multi-qubit quantum gates, the tuning of the qubit-qubit interaction, and the measurement of the center-of-mass position of an ion in the trap. All these implementations need to be quantified in order to estimate their potential. A similar experimental procedure is always used to quantify the properties of the gates or to measure the properties of the $^{171}Yb^{+}$ ion.

One of the advantages of the applied magnetic field gradient for single qubit addressing and spin-spin coupling is the experimental simplicity of the laser setup and RF control. A global light field is sufficient for all operations requiring the manipulation of qubits in the optical frequency range. Due to the individual addressability in the RF frequency domain, a global RF field is also sufficient. The reduction to global fields limits the possible structure of the experiments. The global light field for the preparation and measurement of the ion state limits the experiments to a specific sequence of actions as shown in figs. 2.4.1 and 2.5.1. Reading the state of the qubit using a global light field will project each qubit into either $|0\rangle$ or $|1\rangle$ state, destroying any superposition of states in the quantum register, which stops the execution of a quantum algorithm. The preparation with this light field initializes all qubit states to $|0\rangle$. Between the preparation of the qubits in the initial state $|0\rangle$ and the readout, the absence of a light field allows the quantum system to evolve unobserved. This darkness is the key to the existence of superpositions and the generation of entangled states. To measure a property of a quantum system, the experiment must be repeated in order to reconstruct the quantum state. In addition to the preparation,

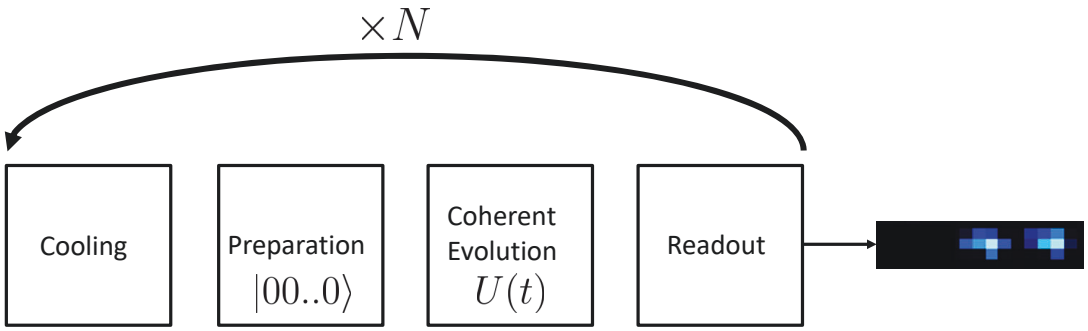

Figure 2.5.1: Schematic of one experimental cycle showing the individual steps performed in most experiments. Each cycle defines the experiment for a given unitary evolution $U(t)$ and delivers the measurement result as one bit string during the readout step. Depending on the experiment, the cooling step might contain a Doppler cooling and a sideband cooling step as shown in section 2.5.2 and section 2.5.3. Figure 2.4.1 shows the corresponding circuit diagram.

evolution, and readout steps, it is necessary to cool the motion of the ion in the trap to allow precise manipulation of the qubit. A set of experimental steps is called a cycle, as shown in fig. 2.5.1. Each cycle has a defined set of measurement parameters of the unitary evolution $U(t)$. Due to the probabilistic nature of quantum mechanics, it is necessary to repeat the experiment to find the output probability.

2.5.1 Loading $^{171}Yb^{+}$

Before a quantum computation can begin, the desired number of qubits must be loaded into the trap. If there is no chemical reaction of the $^{171}Yb^{+}$ ions with the background gas present in the vacuum recipient, a single loading of the trap is sufficient. Due to the geometry of the trap, the trapping potential is deep enough to keep the ions in the trap as long as the trap drive voltage is present.

Loading is accomplished using a source of enriched ^{171}Yb, which is thermally evaporated and ionized in a two-step laser ionization process. The origin of the name of this method is the heating process for the source, which is called the oven. Once the oven is heated,

thermally a neutral atomic beam is emitted through the center of the trap. A laser beam near 398 nm excites an electron of the neutral atom. A second laser field then transfers enough energy to the electron that it is no longer bound to the atom. The laser beam for the second step of ionization must have a wavelength < 394 nm [34]. This is necessary to excite the electron into the continuum. A laser with a wavelength of 369 nm is already available in the setup for Doppler cooling, preparation and readout. It is used for the second ionization step. The electron leaves the trap due to its different mass-to-charge ratio, but the confining RF potential traps the ionized $^{171}Yb^{+}$. Since the source of neutral atoms is a heated sample of ^{171}Yb, the loading procedure is not deterministic. However, reducing the atomic flux by lowering the oven temperature reduces the trapping rate enough to allow individual $^{171}Yb^{+}$ ions to be trapped.

2.5.2 Doppler cooling

Immediately after loading, the hot ions are trapped, but their kinetic energy causes them to oscillate around the trap. Cooling of these ions is required for the ions to form the Coulomb crystal, which serves as the quantum register. An ion crystal defines the position of the ions in the trap. Doppler cooling is based on the directed transfer of momentum during the absorption of a photon from a laser beam and the periodic motion of the ion. The Doppler effect shifts the frequency of a light field as a function of the speed of the observer. This allows the scattering rate to be changed based on the direction of the ion's motion. From the absorber's point of view, the Doppler-shifted frequency is linearly approximated by $\nu' = \nu(1 - v/c)$. Where ν is the frequency of the emitted laser photon and v is the velocity of the ion/observer relative to the emitter.

The optical dipole transition $|^2S_{1/2}, F = 1, m_F = 0\rangle \leftrightarrow |^2P_{1/2}, F = 0\rangle$ with a wavelength of about 369 nm is used for Doppler-cooling. The lifetime of the state $|^2P_{1/2}, F = 0\rangle$ is 8.12 ns [35, 36] and allows for frequent relaxation of the exited state by emission of a photon. The non vanishing probability of off-resonant excitation of the state $|^2P_{1/2}, F = 1\rangle$ requires a RF field to close the cooling cycle since the state $|^2P_{1/2}, F = 1\rangle$ decays to the state $|^2S_{1/2}, F = 0\rangle$. This would interrupt the cooling process. Application of a RF field resonant with the transition $|^2S_{1/2}, F = 1, m_F = 0\rangle \leftrightarrow |^2S_{1/2}, F = 0\rangle$ transfers the population back to state $|^2S_{1/2}, F = 1, m_F = 0\rangle$ which again is nearly resonant with the laser light field.

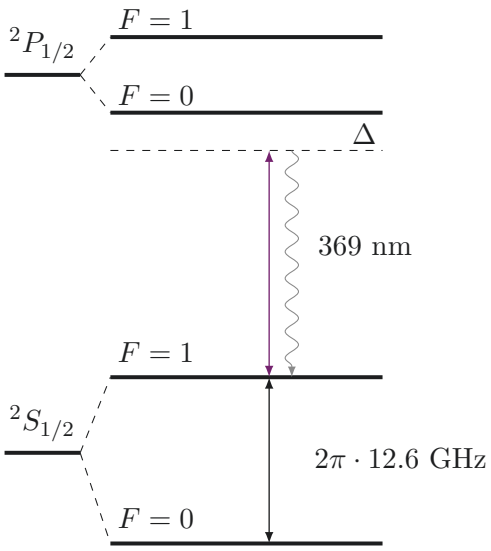

Figure 2.5.2: Partial term scheme of $^{171}Yb^+$ (not to scale) in the rest frame of the ions, showing the optical transition relevant for Doppler cooling. Here Doppler cooling is performed on the optical dipole transition $|^2S_{1/2}, F = 1\rangle \leftrightarrow |^2P_{1/2}, F = 0\rangle$. The light field is detuned by $\Delta \approx -2\pi \cdot 19\,\mathrm{MHz}$ to lower frequencies compared to the center of optical resonance. This is comparable to the width of the optical transition and therefore shows the largest slope of the scattering rate as a function of velocity. This implements the most effective Doppler cooling by absorption of momentum along the beam axis. The ion is decelerated as it moves towards the laser source and this, in combination with the harmonic trapping potential forcing the ion to have a periodic velocity component in the laser direction, generates an effective cooling [28].

The absorption of a photon transfers the momentum $\hbar\nu/c$ to the ion. Since this absorption occurs more frequently as the ion moves toward the laser source, the ion slows down. The spontaneous decay emits a photon so that the average momentum of the spontaneous emission cancels out. As the ion moves away from the laser source, the frequency of the light is shifted away from the atomic resonance, reducing the absorption rate. The detuning is chosen so that the laser is about half a FWHM red detuned from the optical resonance of a resting ion. This choice of detuning $\Delta = -2\pi \cdot 19\,\mathrm{MHz}$ uses the strongest slope of the spectrum to achieve efficient Doppler cooling. See section D for details on the $^{171}Yb^+$ term scheme. The periodic motion of the ion in the trapping potential then leads to effective cooling of the ion. However, the achievable temperature T_D is limited by the momentum of the emitted photons. It is [37]:

$$k_B T_D = \frac{\hbar\Gamma}{2} = \langle n \rangle \hbar\omega_T. \tag{2.5.1}$$

Where $\Gamma = 2\pi \cdot 19.6\,\mathrm{MHz}$ is the line width of the transition and T_D is the Doppler temperature, while k_B is the Boltzmann constant and $\omega_T = 2\pi \cdot 128\,\mathrm{KHz}$ is the trap frequency. This results in a minimal thermal excitation of about 80 phonons or $47\,\mu\mathrm{K}$. Cooling further requires a sub Doppler cooling technique which is sideband cooling in this thesis.

2.5.3 Sideband cooling

When the Doppler cooling is finished, some residual thermal excitation remains. The sideband cooling technique briefly described here allows the cooling of an ion close to the motional ground state of the quantum mechanical harmonic oscillator. Equal energy splitting $\Delta E = \hbar\omega_m$ of the harmonic oscillator formed by the trapping potential and using the coupling between the spin and the vibrational state allows the ion to be cooled. The coupling between the motion and the spin state generates two motion sidebands at the frequency $\nu = \nu_{\sigma_+} \pm \omega_m$ of the magnetically sensitive σ_+ transition. These transitions occur at a frequency offset equal to the energy splitting of the harmonic oscillator ω_m. Detuning the RF field $|^2S_{1/2}, F = 0\rangle \leftrightarrow |^2S_{1/2}, F = 1, m_F = 1\rangle$ by a frequency $-\omega_m$ will drive a motional sideband transition. Choosing the red sideband transition at the frequency $\nu_{\sigma_+} - \omega_m$ absorbs a motion excitation. Excitation of the optical transition $|^2S_{1/2}, F = 1, m_F = 1\rangle \leftrightarrow |^2P_{1/2}, F = 1\rangle$ allows the following spontaneous decay of $|^2P_{1/2}, F = 1\rangle \rightarrow |^2S_{1/2}, F = 0\rangle$ to close the cooling cycle. The decay can be used as a suitable dissipative process. The principle scheme is shown in fig. 2.5.3.

By repeating this cycle, a motion excitation, called a phonon, is absorbed each time. The cooling rate is given by the duration of the entire cooling cycle and limits the minimum thermal excitation of the system, since a heating process also takes place during the cooling process. This limits the minimum motion excitation to more than zero quanta. While the Rabi frequency for driving the sideband transition is given by:

$$\Omega_{n,n-1} = \Omega\eta_{eff}\sqrt{n}, \tag{2.5.2}$$

where $\Omega_{n,n-1}$ denotes the Rabi frequency for the transition from n to $n-1$ phonons, Ω

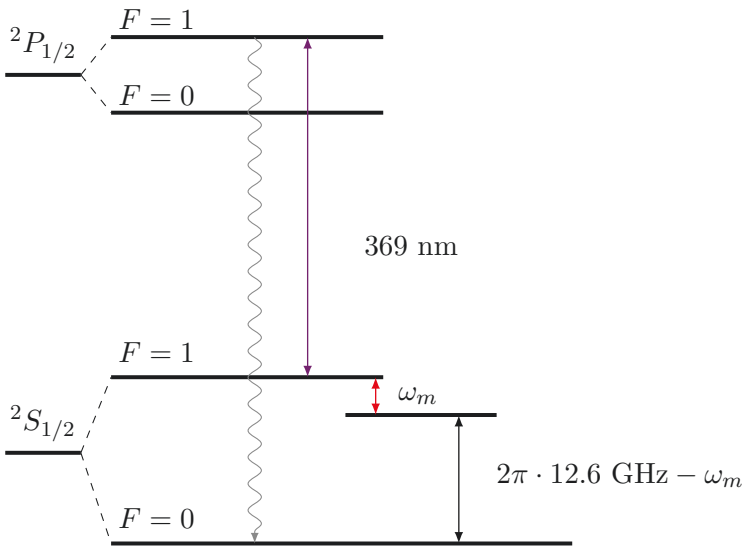

Figure 2.5.3: Sideband cooling scheme (not to scale). Here the optical transition $|^2S_{1/2}, F = 1, m_F = 1\rangle \leftrightarrow |^2P_{1/2}, F = 1\rangle$ is driven, while a red detuned RF field drives the transition between $|^2S_{1/2}, F = 0\rangle \leftrightarrow |^2S_{1/2}, F = 1, m_F = 1\rangle - \hbar\omega_m$ implementing sideband cooling. The RF field is detuned by $\hbar\omega_m$, which is the energy of the vibrational mode to be cooled. Each cycle reduces the excitation of the vibrational mode m by one, eventually ending in the motional ground state for mode m. $O(\omega_m) = 2\pi \cdot 100\,\text{kHz}$.

is the resonant Rabi frequency of the carrier, η_{eff} is the effective Lamb Dicke parameter and n is the phonon number. If more than one ion is loaded in the trap, and if they form a crystal, they behave as a system of coupled harmonic oscillators. As such several vibrational modes in the crystal are present. Each with different energy and different ions participating in this motion [14].

The ion crystal's Center Of Mass(COM) mode frequency is associated with the energy splitting of the harmonic oscillator generated by the trapping potential and is independent of the number of ions in the crystal. Since each ion contributes the same mass as well as the same charge, the COM frequency is constant. The other vibrational modes of the crystal have a higher frequency than the COM mode. Due to this, selecting the frequency of the RF driving field allows selecting which mode to cool accordingly [9]. In principle, it is desired to cool all vibrational modes as well as possible. A cooling scheme allowing to cool of different crystal vibrational modes simultaneously is presented in section 2.7.

2.5.4 Preparation of the logical ground state

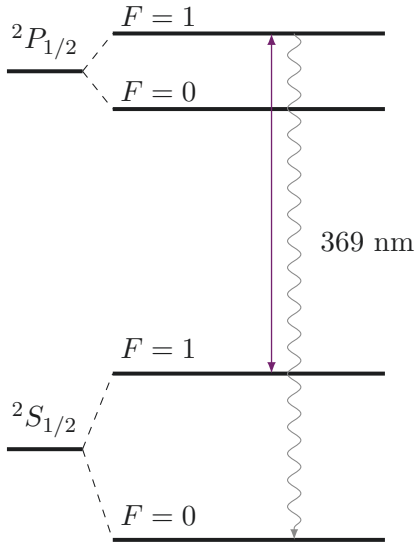

Figure 2.5.4: Preparation of the ground state $|0\rangle$. The population in state $|^2S_{1/2}, F = 1\rangle$ is excited to state $|^2P_{1/2}, F = 1\rangle$ using laser light near 369 nm. It decays to the state $|^2S_{1/2}, F = 1\rangle$ or $|^2S_{1/2}, F = 0\rangle$. The branching ratio of decays in the $^{171}Yb^+$ ion can be found in the appendix section D. Is the qubit in state $|^2S_{1/2}, F = 0\rangle$=$|0\rangle$, no resonant laser light is present and the state $|0\rangle$ is prepared [28, 38].

Every quantum computation requires a defined qubit state at the beginning. To prepare a $^{171}Yb^+$ qubit in the $|0\rangle$ state, the $|1\rangle$ state must be depleted. Tuning the frequency of the laser light close to 369 nm allows selective depletion of the $|1\rangle$ state. If the laser light is resonant with the transition $|^2S_{1/2}, F = 1\rangle = |1\rangle \leftrightarrow |^2P_{1/2}, F = 1\rangle$ the state $|^2P_{1/2}, F = 1\rangle$ is populated. By spontaneous emission $|^2P_{1/2}, F = 1\rangle$ preferentially decays to the state $|^2S_{1/2}, F = 0\rangle = |0\rangle$. When the excited state decays to $|1\rangle$, the laser field excites the electron back to $|^2P_{1/2}, F = 1\rangle$. This is repeated until the qubit is finally prepared in the state $|0\rangle$. The principle is shown in fig. 2.5.4. The transition at 369 nm has a Full-Width Half Maximum (FWHM) of $2\pi \cdot 36(2)$ MHz [37] and is therefore broad enough in frequency space to cover all three transitions of $|^2S_{1/2}, F = 1, m_F = +1, 0, -1\rangle$. This allows all $|^2S_{1/2}, F = 1, m_F = +1, 0, -1\rangle$ states to be depleted and drives the system to the $|0\rangle$ state.

2.5.5 Detection of the qubits state

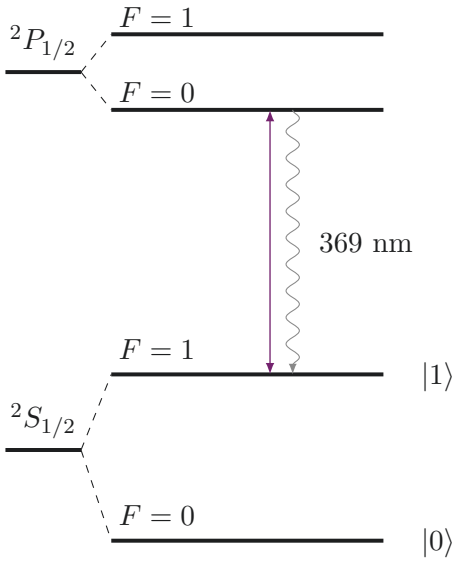

Figure 2.5.5: Partial term scheme of $^{171}Yb^+$ (not to scale) showing the relevant optical transition for detection. To detect the qubit state, laser light close to 369 nm is used to drive the transition $|1\rangle \leftrightarrow |^2P_{1/2}, F = 0\rangle$ generating fluorescence if the ion was in state $|1\rangle$. A possible off-resonant excitation of state $|^2P_{1/2}, F = 1\rangle$ allows the ion to decay to the state $|0\rangle$, limiting the number of photons during the readout process. The frequency difference between $|^2P_{1/2}, F = 1\rangle$ and $|^2P_{1/2}, F = 0\rangle$ is $\nu = 2\pi \cdot 2.1\,\text{GHz}$ [28]

To read the result at the end of the unitary evolution, each qubit is assigned one of the binary logical values. This is realized by a projective measurement of the qubit state. Shining laser light on the ions resonant with the transition $|^2S_{1/2}, F = 1\rangle \leftrightarrow |^2P_{1/2}, F = 0\rangle$ will excite the ion if and only if the state $|1\rangle = |^2S_{1/2}, F = 1\rangle$ is occupied. Once the ion is excited, a photon is emitted by spontaneous decay $|^2P_{1/2}, F = 0\rangle \rightarrow |^2S_{1/2}, F = 1\rangle$. Since the laser light is present, the ion will be excited again so that in each excitation, de-excitation cycle a photon is emitted near 369 nm. This excitation cycle is shown in fig. 2.5.5. The emitted photons are eventually collected by the objective lens and projected onto the Electron Multiplying Carge Coupled Device (EMCCD) camera chip. The camera, which is used to observe the emitted fluorescence of the ions, allows to spatially resolve the ion on an image. This image is digitized and then analyzed to assign a logical 1 if and only if fluorescence is detected at the position of the ion in the image. Otherwise a logical 0 is assigned to the readout. Since the state $|^2P_{1/2}, F = 1\rangle$ might be excited of resonantly a

spontaneous decay to $|^2S_{1/2}, F = 0\rangle = |0\rangle$ might occur [21]. This effect limits the number of photons emitted by an initially bright $|1\rangle$ qubit. Due to a limited solid angle imaged by the camera, absorption or reflection processes in the imaging optics, the number of photons detected during a readout when the ion is bright is limited. How to distinguish a signal of a few photons from the background signal is shown in section 2.5.6. It is therefore advantageous to collect as much fluorescence light as possible during a readout.

It should be noted that during the readout the three states $|^2S_{1/2}, F = 1, m_F = \pm 1, 0\rangle$ are all read out as a logical $|1\rangle$. These three states undergo a Zeeman splitting of about $2\pi \cdot 10 - 2\pi \cdot 20\,\mathrm{MHz}$ and are covered by the same laser light field. Increasing the magnetic field will increase this splitting correspondingly, resulting in a decrease in fluorescence [37].

2.5.6 Calculation of excitation probabilities

At the end of each experiment, a projective measurement is performed, where the readout is an image of the ion string. In the following, it is described how the image taken during the readout process is interpreted to finally calculate an excitation probability P of a quantum state in z basis. Due to the limited number of photons collected by the camera, the distinction between the logical readout 0 and 1 is performed using a double-threshold method.

Discriminating the logical state of a qubit between $|0\rangle$ and $|1\rangle$ using the double-threshold method requires finding the area on the CCD chip exposed to fluorescence light for each individual ion and finding the threshold values to ensure optimal detection fidelity. This subsection describes the principle of calibration of the detection system as implemented in the current setup.

Calibration of a system always requires comparison with a known reference. In this case, the known reference is the ion itself. For this calibration, it is assumed that after shining in the 369 nm laser field for a sufficient time, the whole qubit register is initialized in state $|00..0\rangle$ with certainty. This initialization is described in section 2.5.4. Since the laser light fields for the initialization and readout process are laser fields covering the entire register, the register is prepared and read out globally.

In principle not much of the system is known at this point, for example the addressing

frequencies ν_{σ_+} of the σ_+ transition between $|^2S_{1/2}, F = 0\rangle \leftrightarrow |^2S_{1/2}, F = 1, m_F = 1\rangle$ of the qubit is unknown, as well as the exact Rabi frequency Ω_{σ_+} of this transition. Using the insensitivity of the π transition frequency ν_{σ_π} $|^2S_{1/2}, F = 0\rangle \leftrightarrow |^2S_{1/2}, F = 1, m_F = 0\rangle$ to the first order of magnetic fields, a specific reference pulse can be applied. The Rapid Adiabatic Passage (RAP) pulse, where $\Omega(t)$ is Gaussian shaped while the RF frequency ν is ramped across the atomic resonance [19]. This pulse has been shown to reliably excite the qubit state from $|0\rangle$ to $|1\rangle$ without precise knowledge of either the atomic resonance frequency or the exact Rabi frequency of the applied RF field.

To perform the calibration measurement, the following two steps are performed:

1. preparation of the register in the ground state $|00..0\rangle$ and a readout.

2. Preparation of the register in the ground state $|00..0\rangle$ application of a RAP-pulse on the $|^2S_{1/2}, F = 0\rangle \leftrightarrow |^2S_{1/2}, F = 1, m_F = 0\rangle$ transition exciting state $|11..1\rangle$ and a readout.

After image acquisition, a matrix containing a value for each pixel in the readout image is analyzed to calibrate the detection.

The acquired physical signal is amplified and digitized in the camera during the readout process. This process is not noise free and therefore affects the readout image by adding electronic noise to each pixel. In addition to the electronic noise, which produces a minimum base level of the signal, misalignment of the readout laser and imaging errors in the imaging setup will add additional signals in the readout area of the CCD chip. Once the detection is calibrated, the two thresholds found compensate for the extra base level in the readout signal.

The first step is to identify the ion signal region in the image. In a second step, the readout images must be post-selected and then the two thresholds must be found.

The first step is to identify the pixels that represent the light collected from a single ion. Three images are acquired during the measurement cycle. During the Doppler cooling step, the ions scatter light that is partially collected by the objective and imaged on the CCD camera. The Doppler cooling images contain the most fluorescence. The raw, unprocessed Doppler-cooling images are described by $d_{(i,j),n}$, where n is the experiment

cycle in which the image was acquired and i (j) indexes the column (row) of the image. First, the Doppler cooling images are summed $D_{ij} = \sum_n d_{(i,j),n}$. Due to the orientation of the imaging system, the light from a single ion may be spread over several pixels, which must be correctly assigned. The ions are arranged horizontally in a linear chain in the acquired images. Averaging the values of the first column of the image $d_{bas} = \sum_j D_{1j}/N_{row}$ gives an estimate of the base level of the signal. Here N_{row} is the number of rows in the acquired image and D_{1j} is the first column of the summed Doppler cooling image. This approximate base level and a relative threshold, r_{th}, allow finding a matrix that indicates the region of the ions as

$$A_{ij} = \begin{cases} 1 & D_{ij} > r_{th} d_{bas} \\ 0 & else \end{cases} . \tag{2.5.3}$$

In the next step, the ions need to be assigned individual regions.

To do this, the ion regions must be separated by at least one pixel that is not assigned as an ion region. In order to capture as much signal as possible from a single ion, it is advantageous to assign an ion area as large as possible, as long as the readout noise of the CCD chip does not degrade the measured signals. To do this, the relative threshold for ion identification r_{th} is chosen as small as possible, as long as the ions can be separated. Here the set $\{(i,j)\}_k$ denotes the set of pixel coordinates assigned to ion k. An example is shown in fig. 2.5.6.

After successful ion identification, the average background signal can be calculated by averaging over all pixels of the image that are at least one pixel away from the identified ion regions. The distance of one pixel to the ion area ensures that the pixels used to determine the background do not contain ion fluorescence. This average background fluorescence is subtracted from all images for subsequent analysis.

During the repeated execution of experimental cycles, various events may occur that could affect the measurement result if not handled properly. For example, the ion could decay from the state $|^2P_{1/2}, F = 0\rangle \rightarrow |^2D_{3/2}\rangle$. This state has a lifetime of $\tau_{|^2D_{3/2}\rangle} = 52.7\,\text{ms}$, which is considerably longer than the lifetime of the state $\tau_{|^2P_{1/2}\rangle} = 8.12\,\text{ns}$. More details about the $^{171}\text{Yb}^+$ therm scheme can be found in section D. As a result, the ion is in an undefined state, no longer participating in cooling and no longer being addressed by

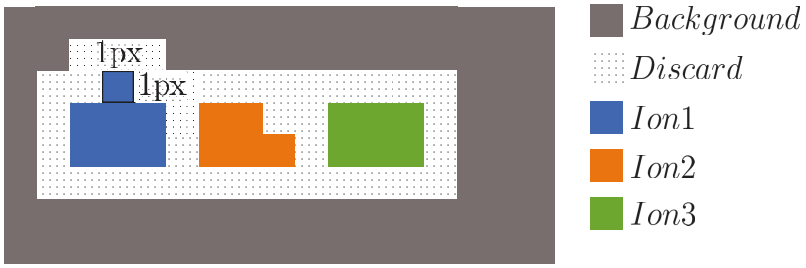

Figure 2.5.6: Instructive example of ion identification and background selection. The area indicated in blue corresponds to the ion area of ion 1, the area indicated in orange corresponds to ion 2, and the area indicated in green corresponds to ion 3. The gray area is used to calculate the mean background signal of the image. The dashed areas are not used by the analysis but ensure proper separation of the found ion areas.

microwave radiation. The measurement cycle in which such an event occurs corrupts the experimental data and must be removed from further analysis. This type of event and the formation of unwanted molecules in the ion string show a decrease in the measured Doppler cooling fluorescence and can therefore be removed from the data set to be analyzed.

After successful ion identification and background correction, the fluorescence during Doppler cooling is analyzed. The total ion Doppler cooling fluorescence of the cycle n and the kth ion is given by

$$D'_{k,n} = \sum_{\{(i,j)\}_k} \Big(d_{(i,j),n} - d_{gnd} \Big). \tag{2.5.4}$$

The average total Doppler cooling fluorescence for the kth ion is calculated by evaluating the acquired Doppler cooling image for each cycle n. Based on the average total ion fluorescence and assuming that the ion remains in the same state until the end of the cycle, a measurement is accepted if the measured Doppler fluorescence is higher than a threshold r_d relative to the average fluorescence

$$\text{Cycle } n-1, n, n+1 \text{ is rejected if } D'_{k,n} < r_d \cdot \langle D'_{k,n} \rangle_n. \tag{2.5.5}$$

When the Doppler cooling fluorescence is below this threshold, the readout of the quantum state $f'_{k,n}$ is rejected. Here $\langle D'_{k,n} \rangle_n$ is the averaged Doppler-cooling fluorescence of ion k averaged over all cycles n. The total ion fluorescence $f'_{k,n}$ for the image containing the

quantum logical information of cycle n and the kth ion is given by

$$f'_{k,n} = \sum_{\{(i,j)\}_k} f_{(i,j),n}, \tag{2.5.6}$$

where $f_{(i,j),n}$ is the readout image of cycle n containing the logical readout of the quantum state. The number of photons measured during the experiment is limited by off-resonant excitation to the state $|^2P_{1/2}, F = 1\rangle$ and spontaneous decay to $|^2S_{1/2}, F = 0\rangle$ [21], which destroys the state $|1\rangle$. This results in a Poissonian distribution of different expectation values for the measured signal of the EMCCD camera depending on the logical qubit state. These Poissonian distributions for the dark and bright states of the ion partially overlap. This leads to an ambiguity of the detected events in the overlapping region. To clearly distinguish a bright state $|1\rangle$ from a dark state $|0\rangle$, a double-threshold method is used. Details of this double-threshold are given in [39]. This method defines a lower and an upper threshold. Events with fluorescence below the lower threshold, $f' < Th_d$, are identified as dark state d, and events with fluorescence, $Th_b < f'$, above the upper threshold are identified as bright state b. All other events with fluorescence between the lower and upper thresholds, $Th_d < f' < Th_b$, are considered ambiguous and are discarded.

Applying the two threshold method flags each ion as either a logical 0, 1 or discarded. An example of the distribution is shown in fig. 2.5.7. Based on the experiment performed for a given setting in a cycle, there are two ways to interpret the flagged events. One possible interpretation is as a single ion excitation probability independent of the state of the other ions in the chain. Another interpretation is a product state representing a number between 0 and $2^n - 1$, where n is the number of qubits present. In the case of the single ion excitation interpretation, the procedure is as follows. For each repetition of the cycle, the useful result is bright or dark. By evaluating all repetitions of a cycle, N_b events are identified as bright and N_d events are identified as dark. This allows the calculation of a relative excitation probability

$$P_{\tilde{b}} = \frac{N_b}{N_b + N_d}. \tag{2.5.7}$$

There is a non-vanishing probability of misidentifying a bright state as a dark state γ_2 and a probability of misidentifying a dark state as a bright state γ_1. These probabilities, as well as the applied threshold, are the result of a calibration measurement to find the best possible thresholds. Details can be found in [39]. Knowing this quantity allows to correct

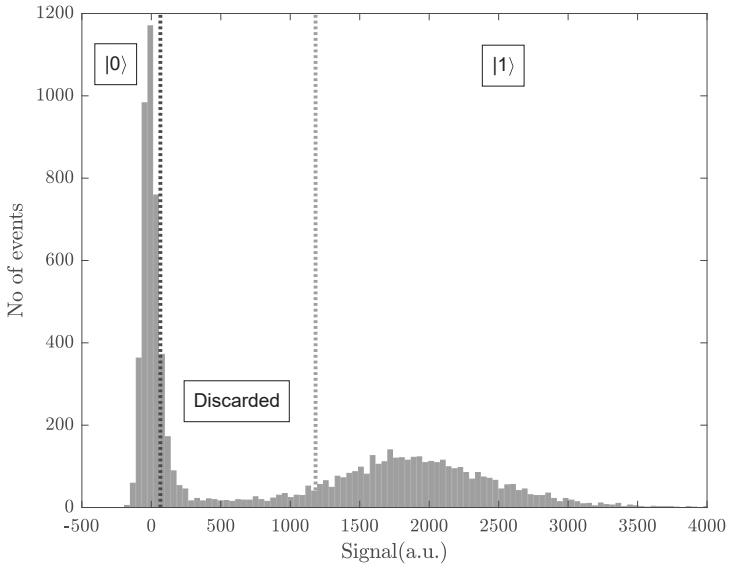

Figure 2.5.7: Background signal corrected histogram of detected ion fluorescence for ion 2 in a three-ion crystal. Using the two-threshold method, symmetrically discarding 20% of the events for the bright prepared state and the dark prepared state yields a detection fidelity for the state $P_{|1\rangle} = 0.991(15)$, $P_{|0\rangle} = 0.991(15)$. Events showing an ion fluorescence below the lower threshold are detected as $|0\rangle$, events showing a fluorescence above the higher threshold are detected as $|1\rangle$, and events in between are discarded.

this misidentification as

$$\begin{pmatrix} P_{\tilde{b}} \\ P_{\tilde{d}} \end{pmatrix} = \begin{pmatrix} 1-\gamma_2 & \gamma_1 \\ \gamma_2 & 1-\gamma_1 \end{pmatrix} \begin{pmatrix} P_b \\ P_d \end{pmatrix}. \tag{2.5.8}$$

Where P_b is the true probability of finding the ion in state $|1\rangle$, P_d is the true probability of finding the ion in state $|0\rangle$, γ_1 is the probability of identifying it as dark while it is bright, and γ_2 is the probability of identifying it as bright while it is dark. Taking this into account allows calculating the correct Probability of finding the system in state $|1\rangle$

$$P_b = \frac{(1-\gamma_1)P_{\tilde{b}} - \gamma_1(1-P_{\tilde{b}})}{(1-\gamma_1)(1-\gamma_2) - \gamma_1\gamma_2}. \tag{2.5.9}$$

The uncertainty in excitation probability P_b is given by the variance of the data sample of all cycle repetitions:

$$\mathrm{Var}(P_b) = \frac{N(N_b+1) - N_b^2 + 1}{(N+2)^2(N+3)}. \tag{2.5.10}$$

Here $N = N_b + N_d$. Each measured excitation probability is calculated using this method. Based on this variance, the statistical error bar on measured data points presented in this thesis is calculated as $\sigma_P = \sqrt{\mathrm{Var}(P_b)}$.

The following procedure is used when it is necessary to interpret the state as a product state. The method described so far can be used to calculate and correct the excitation probability of each ion at the end of an experiment. These probabilities reflect the frequencies of occurrence of bright events for a given experimental setting. On the other hand, suppose that the state of the ion string is interpreted as a logical state of a quantum register. In this case, the readout is a product state, i.e., the state of the register must be interpreted as one of the 2^n logical states it can represent. Thus, the readout of an experiment is no longer a single possibility, but a vector of length 2^n, where each entry represents a logical state.

So far, the method relies on discarding a certain fraction of the readout events. If the readout is analyzed separately for each ion, this discarded fraction adds to the measurement effort. This is acceptable since the additional measurement effort is about 20%. If the readout is to be interpreted as a bit string, each ion must be assigned either 0 or 1. This happens with the probability $P_{success} = (1 - P_{discard})$ per ion. Thus, assuming statistical independence, the probability of getting a valid readout of a register of size N is $P_{success} = (1 - P_{discard})^N$. For a typical setting in this thesis, $P_{discard} = 0.2$ and $N = 3$ ions, $P_{success} \approx 0.51$ follows. Even for a three-ion system, a significant fraction of the measurements will be discarded. In this case, this leads to a doubling of the measurement time needed to collect data with a desired statistical significance. Scaling the system to more qubits therefore requires more efficient state detection. This unfavorable scaling must be overcome in future data analysis.

The read out probability vector is

$$\vec{P} = \begin{pmatrix} P_{|000\rangle} \\ P_{|001\rangle} \\ P_{|010\rangle} \\ \vdots \\ P_{|111\rangle} \end{pmatrix} = \begin{pmatrix} P_0 \\ P_1 \\ P_2 \\ \vdots \\ P_7 \end{pmatrix}. \tag{2.5.11}$$

Here $P_{|000\rangle} = P_0$ is the probability to find the register in state 0. To calculate this probability vector of the register, the following steps are performed:

1. If the readout fluorescence of one or more ions is in the range between the two thresholds, the readout is rejected and no longer considered in further analysis.

2. For each experiment cycle, the logical readout string is constructed as $S = (l_1, l_2, l_3)$ where l_i is the logical state of the ion where the readout of each ion must be flagged valid.

3. For each logical readout string S, an integer value is assigned $v = \sum_{i=1}^{N} S_i 2^{i-1}$.

4. The probability P_v is then calculated as $P_v = N_v/N_{tot}$ where N_v is the number of occurred readouts of value v in all repetitions, where N_{tot} is the total number of valid readouts.

During this readout, there is a possibility of misinterpretation of the readout due to imperfect separation of the individual ion fluorescence on the camera and electronic noise. To quantify this error, a detection calibration must be performed.

Extending the scheme above, a linear map between the real excitation probability vector $\vec{P}$ and the measured probability vector $\tilde{\vec{P}}$ can be found:

$$\tilde{\vec{P}} = \begin{pmatrix} P_{\widetilde{0}} \\ P_{\widetilde{1}} \\ P_{\widetilde{2}} \\ \vdots \\ P_{\widetilde{2^N-1}} \end{pmatrix} = \begin{pmatrix} M_{00} & M_{01} & M_{02} & \cdots & M_{0(2^N-1)} \\ M_{10} & M_{11} & M_{12} & \cdots & M_{1(2^N-1)} \\ M_{20} & M_{21} & M_{22} & \cdots & M_{2(2^N-1)} \\ \vdots & & & \ddots & \\ M_{(2^N-1)0} & & \cdots & & M_{(2^N-1)(2^N-1)} \end{pmatrix} \cdot \begin{pmatrix} P_0 \\ P_1 \\ P_2 \\ \vdots \\ P_{2^N-1} \end{pmatrix} = M\vec{P}. \tag{2.5.12}$$

Here, the diagonal elements correspond to the probability of correctly reconstructing the excitation probability for each possible state such that, in the ideal case, $M = \mathbb{1}$. If the two thresholds for each ion are known, an additional calibration of the product state detection is required.

All possible product states must be prepared and detected to find the map M between the actual and reconstructed quantum states. The preparation of a defined state is realized by preparing the state $|00..0\rangle$ using laser light as described above and applying a RAP pulse

on the σ_+ transition of the ions to selectively excite the qubits to the desired product state. The register is then read out. The preparation of $\vec{P}$ in a defined state allows to find M, as the first column is the measured $\vec{\tilde{P}}(0)$ for a system prepared to state $0 = |00..0\rangle$. The second column corresponds to $\vec{\tilde{P}}(1)$ for the prepared state $1 = |00..1\rangle$ and so on.

Applying the inverse matrix

$$M^{-1}\vec{\tilde{P}} = \underbrace{M^{-1}M}_{\mathbb{1}}\vec{P} = \vec{P}, \tag{2.5.13}$$

allows extraction of the excitation probabilities for the system's state, compensating for detection errors.

An example of a measured 8-state detection matrix M is shown in fig. 2.5.8. The cells in dark colors show probability values close to 1, while the cells in light blue show probabilities close to 0. From this matrix, some properties of the detection setup and the detection method can be seen. For each state reported, there is a non-vanishing probability of detecting a completely dark state, e.g. $|000\rangle$. If only one ion is to be prepared in an excited state, in this case the states $|001\rangle, |010\rangle$ and $|100\rangle$, the probability of finding the state $|000\rangle$ is approximately $3 \cdot 10^{-2}$, whereas if the prepared state contains two excited ions, $|011\rangle, |101\rangle$ and $|110\rangle$, the probability of finding the state $|000\rangle$ is approximately equal to $5 \cdot 10^{-3}$. The probability of finding a readout containing two-bit flip errors is suppressed compared to errors containing one bit flip, as would be expected.

Using this calibration measurement allows reconstruction of the true state of the system without systematic detection errors by applying the inverse of the detection matrix M^{-1} to the readout state. The statistical errors of this correction must be taken into account, since the calibration measurement always contains statistical errors. For this calculation, the statistical error of the elements in the inverse matrix must be calculated. The error propagation using a matrix inversion operation is given by [40]:

$$\mathrm{Cov}(M^{-1}_{\alpha\beta}, M^{-1}_{ab}) = \sum_{i,j,k,l} M^{-1}_{\alpha i} M^{-1}_{j\beta} M^{-1}_{ak} M^{-1}_{lb} cov(M_{ij}, M_{kl}). \tag{2.5.14}$$

In case of known variances in the form of standard errors, the sum can be reduced to

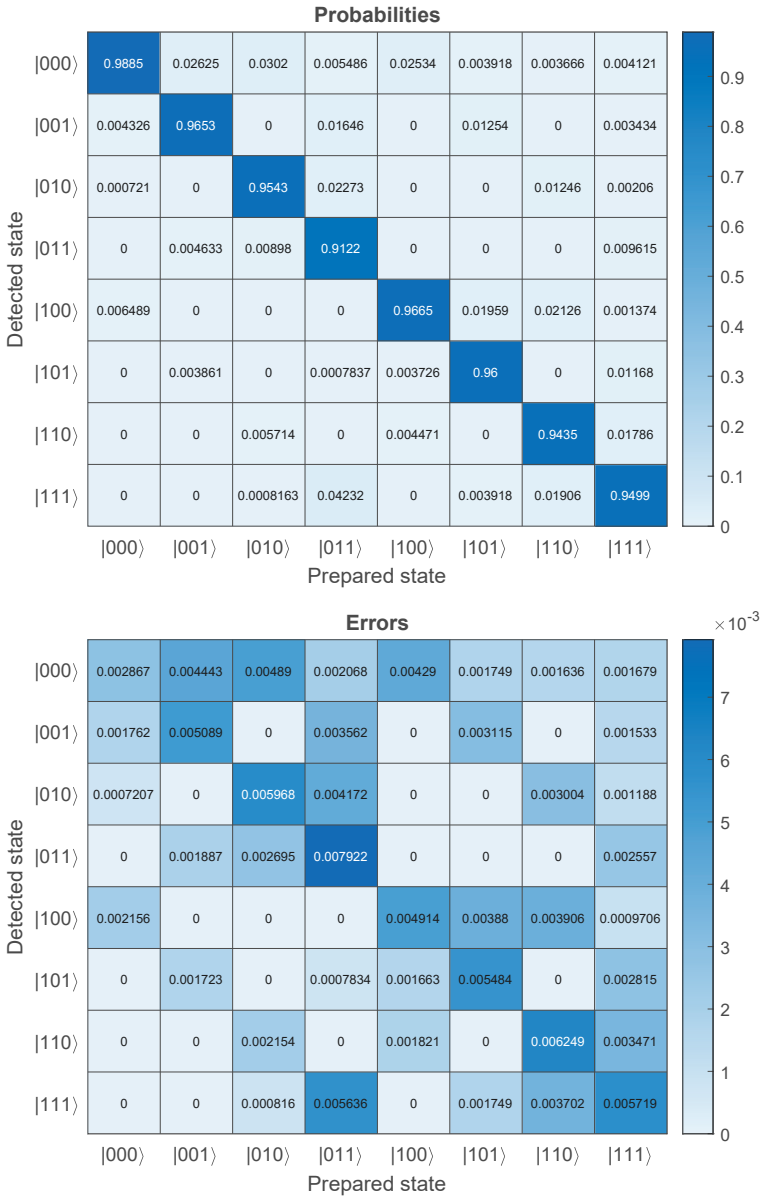

Figure 2.5.8: Measured detection matrix M of output states $|lmo\rangle$ for given input states $|ijk\rangle$. The upper matrix shows the detection matrix M, while the lower matrix shows the standard errors σ_M for each value in the upper matrix. This measurement consists of the preparation of the desired state $|ijk\rangle$ by a RAP pulse on the σ_+ transition of each ion to be prepared in the state $|1\rangle$ and a readout. The frequency of the occurring state is calculated to extract the excitation probabilities.

calculate the standard deviation of the elements of the inverse matrix as:

$$\sigma^2_{M^{-1}_{\alpha\beta}} = \sum_{i,j} \left(M^{-1}_{\alpha i} \sigma_{M_{ij}} M^{-1}_{j\beta} \right)^2. \tag{2.5.15}$$

Using the matrix multiplication

$$P_i = \sum_j M^{-1}_{ij} \widetilde{P}_j, \tag{2.5.16}$$

one can use Gaussian error propagation to calculate the errors of the reconstructed state assuming a Gaussian distribution as follows:

$$\sigma^2_{P_i} = \sum_j \left(M^{-1}_{ij} \sigma_{\widetilde{P}_j} \right)^2 + \sum_j \left(\widetilde{P}_j \sigma_{M^{-1}_{ij}} \right)^2. \tag{2.5.17}$$

Using eq. (2.5.16), a readout probability distribution $\vec{\widetilde{P}}$ can be mapped to the real probability distribution $\vec{P}$. The error for the calculated probabilities $\widetilde{P}_i$ can be calculated according to [9] as

$$\sigma_{\widetilde{P}_i} = \sqrt{\mathrm{Var}(\widetilde{P}_i)} = \sqrt{\frac{(k_i+1)(N+M-k_i-1)}{(N+M)^2(N+M+1)}}, \tag{2.5.18}$$

where k_i is the number of occurrences of the bit string i, N is the number of measurements, and $M = 2^{N_{ion}}$ is the number of possible readouts.

Measuring the full detection matrix is therefore only feasible for a small set of ions, since the number of prepared states and thus the measurement effort scales exponentially.

A possible extension to larger quantum systems would require a significant reduction of the measurement effort. Assuming that bit flip and next neighbor crosstalk are the dominant error sources, it would be sufficient to sample only a few bit patterns. A possible set of patterns for a qubyte could be as follows:
$|10010010\rangle, |01001001\rangle$, and $|00100100\rangle$. From these three examples, the possibilities of misidentifying a $|0\rangle$ state as $|1\rangle$ can be deduced, given that the next neighboring ion is in the $|1\rangle$ state. The states $|01010101\rangle$ and $|10101010\rangle$ would allow to study the rate of false identifications given that both neighboring qubits are in state $|1\rangle$. The states $|00000000\rangle$ and $|11111111\rangle$ allow to estimate the probability of a random bit flip. These bit patterns can be easily extended to larger quantum systems while keeping the measurement effort the same. This reduced measurement does not allow to reconstruct the full detection ma-

trix, but assuming only next-neighbor crosstalk, this reduced set of measurements may be sufficient to quantify next-neighbor detection crosstalk. Thus, the mitigation of detection crosstalk in large quantum registers remains to be investigated.

2.6 Fast addressing-frequency measurement

A critical capability for any quantum computer is to address its qubits to implement local rotations on desired qubits. Here, addressing of individual qubits is realized by applying a global RF field resonant with the desired qubit transitions. The use of Zeeman split hyperfine levels as qubits allows frequency addressing. Using a linear ion crystal with defined ion positions and a magnetic field gradient shifts the resonance frequency for each ion, making it unique. The exact addressing frequency must be known to minimize pulse errors. Compensating for a drifting addressing frequency requires a fast measurement within seconds that allows the known resonance frequency to be used in the experiment. To do this efficiently, a method developed during my master thesis [28] can be used. It is summarized here, since this method was used for the measurements presented in chapter 3.

After applying an RF pulse of duration τ to a qubit prepared in state $|0\rangle$, the excitation probability as a function of the phonon number n can be expressed as

$$P_n(\delta,\tau) = \frac{\Omega_n^2}{\Omega_n^2+\delta^2}\sin^2\left(\sqrt{\Omega_n^2+\delta^2}\frac{\tau}{2}\right). \tag{2.6.1}$$

Here, Ω_n is the Rabi frequency of the observed transition when n phonons are present, and δ is the detuning relative to the observed resonance. The Rabi frequency Ω_n can be calculated as [41]

$$\Omega_n = \Omega L_n^0(\eta^2), \tag{2.6.2}$$

where n is the phonon number, and L_n^0 are the associated Laguerre polynomials.

Since the cooling step only consists of Doppler cooling for fast measurement, the thermal excitations need to be considered:

$$P(\overline{n},\delta,\tau) = \sum_{n=0}^{2\overline{n}} \frac{P_n(\delta,\tau)}{(\overline{n}+1)\left(\frac{\overline{n}}{\overline{n}+1}\right)^n}. \tag{2.6.3}$$

This defines the expected shape of an atomic resonance for an ion stored in a harmonic trapping potential at a given mean thermal excitation of $\overline{n}$ phonons.

As shown in equation (2.6.1), applying a detuned tophat RF pulse excites the addressed ion. Since the shape of the resonance is known, the measurement to determine the ion's resonance can be efficient by minimizing the number of data points to acquire. Measuring the excitation probability of an ion after the application of an RF pulse intentionally detuned to the atomic resonance to lower (higher) frequency by $\kappa\Omega$ yields the excitation probability $P_{\pm} = P(\overline{n}, \Delta \pm \kappa\Omega, \tau)$. Precalculation of

$$g(\Delta) = \frac{P_+ - P_-}{P_+ + P_-} \tag{2.6.4}$$

allows to numerically invert the map g to find $\Delta = g^{-1}([P_+ - P_-]/[P_+ + P_-])$. The measured value of Δ then is the offset of the expected to the real resonance frequency.

The width of the transition scales with the Rabi frequency Ω, reduction of Ω, therefore, allows the measurement of the resonance frequency to be more precise. All relevant resonance frequencies can be measured simultaneously by applying an RF pulse to each ion before readout. This has been demonstrated up to a register of eight qubits in the current setup.

Since the addressing frequencies of the ions can vary during the course of an experiment, these fast addressing frequency measurements are interleaved between the cycles of the experiments. This allows to follow the slow changes of the atomic resonances and reduces the pulse errors and the dephasing of the qubit state, since the rotating frame of the qubits is better known.

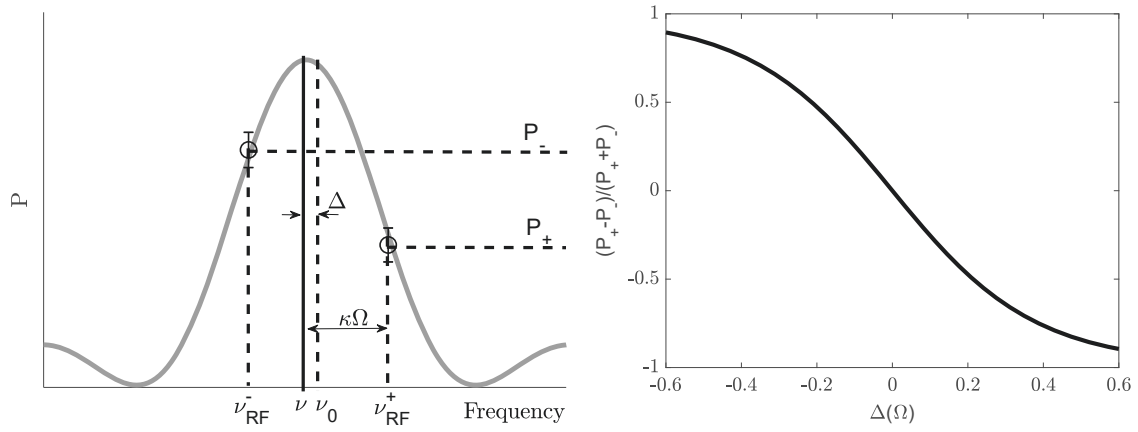

Figure 2.6.1: (a) Schematic of the resonance as a function of RF frequency for a fixed pulse duration. Here ν_0 is the assumed resonance frequency before this recalibration step. The frequencies $\nu_\pm$ are the frequencies at which the resonance is sampled. It is calculated as $\nu_\pm = \nu_0 \pm \kappa\Omega$. $P_\pm$ is the excitation probability after applying a top hat pulse with frequency $\nu_\pm$. (b) Map between the normalized excitation probability $(P_+ - P_-)/(P_+ + P_-)$ difference and the frequency correction to apply Δ. Measuring two excitation probabilities $P_\pm$ after applying two detuned RF pulses is sufficient to measure the resonant frequency of a $|^2S_{1/2}, F = 0\rangle \leftrightarrow |^2S_{1/2}, F = 0, m_F = \pm 1, 0\rangle$ [28].

Observation of the atomic σ_+ transition $|^2S_{1/2}, F = 0\rangle \leftrightarrow |^2S_{1/2}, F = 0, m_F = 1\rangle$ is sufficient to calculate the magnetic field at the position of the ions using the equation eq. (2.2.4) and thus allows to calculate the resonance frequencies of the π transition $|^2S_{1/2}, F = 0\rangle \leftrightarrow |^2S_{1/2}, F = 0, m_F = 0\rangle$ and the resonance frequency of the σ_- transition $|^2S_{1/2}, F = 0\rangle \leftrightarrow |^2S_{1/2}, F = 0, m_F = -1\rangle$.

In the current experimental setup, the statistical uncertainty of the addressing frequency measurement exceeds the coupling strength in the register $\sigma_\nu > J_{ij}$. In the upcoming setups with stronger coupling between the qubits, this is no longer true. The coupling can be seen as a state dependent detuning, making it necessary to increase the driving fields Rabi frequency or the use of broadband pulses to compensate for addressing errors due to the state of other qubits in the register. Nevertheless, the addressing error due to the coupling will be relevant and requires further investigation in the future.

2.7 Multi-tone sideband cooling

To perform experiments involving the coupling of qubit states with vibrational excitation of the ion crystal, it is often necessary to cool all the vibrational modes of the ion crystal close to its motional ground state. As shown in [9, 42], one ion in the crystal can be used to sympathetically cool the other ions. Using the cooling scheme presented in this work, individual serial cooling of vibrational modes was previously required, taking up to 120 ms to cool a single mode of the ion crystal [9]. In the current setup, three frequency generators, each capable of generating a single tone, allow an RF field containing three tones. This can be used to cool three vibrational modes of a three-ion crystal simultaneously, reducing the cooling time required per cycle.

In a three ion crystal, the vibrational mode frequencies are given in terms of the Center Of Mass (COM) mode as, $\nu_{COM}, \nu_2 = 1.732\ \nu_{COM}$ and $\nu_3 = 2.408\ \nu_{COM}$ which can be found numerically [14].

The absolute amplitudes are given by

$$S = \begin{pmatrix} 0.577 & 0.577 & 0.577 \\ 0.707 & 0 & -0.707 \\ -0.408 & 0.816 & -0.408 \end{pmatrix}, \tag{2.7.1}$$

where the rows of S denote the vibrational mode, columns of S denote the ion, and the entries of S are the relative amplitudes of the oscillation. This dynamical matrix allows the extraction of a recipe to cool three motional modes of a three-ion crystal:

- Cool mode 2 on ion 1,
- Cool mode 3 on ion 2,
- Cool the COM mode on ion 3.

This combination of ions and vibrational modes assigned the ion with the largest amplitude to the mode, resulting in the strongest coupling and cooling. As described in section 2.5.3, sideband cooling requires both a laser field and an RF field to be present simultaneously. It has been found that for a given RF Rabi frequency Ω, sideband cooling works best when the intensity of the laser field is matched. Due to the different Rabi frequencies of the sideband

transitions of the other modes on different ions, the Rabi frequencies of the RF transition must be matched. Experimentally, it is advantageous to choose the largest possible RF Rabi frequency. Optimizing the frequency of the RF fields of each sideband transition then maximizes the cooling rate. Because of the light field present to complete the cooling cycle, the optimal sideband cooling frequencies of the RF transition must be found. Since the number to be optimized is the residual excitation of the vibrational modes, it is sufficient to optimize the frequencies to address the modes. Full sideband spectroscopy is a time-consuming task to measure the phonon excitation as used in [9]. Instead, a method is used here in which the red sideband can no longer be driven, indicating that the ions are in their motional ground state. Thus, it is sufficient to optimize the experimental set to search for a vanishing red sideband transition. Since the sideband frequencies are known and the full microwave power is used to increase the cooling rate, the only free parameter left to vary is the intensity of the laser at 369 nm. The intensity of the light field must be adjusted to match the microwave Rabi frequency for optimal cooling. If they match, a global optimum for the laser field intensity used can be found, as shown in fig. 2.7.1. The optimum is indicated by a minimum of the observed excitation after application of a readout pulse resonant with the red sideband transition as a function of the applied cooling laser intensity I. Compared to full sideband spectroscopy, this method is about 30 times more time-efficient, since only one point is sampled for each cooling laser power level instead of a full spectrum.

By applying sideband cooling to three ions and three modes in parallel, the three vibrational modes are cooled simultaneously by irradiation with three RF fields. The heating rate of the system limits the minimum achievable vibrational excitation. The dominant heating is that of the COM mode. To effectively heat higher order modes, each ion must be subjected to a force of different amplitude or direction. This results in a two-stage parallel sideband cooling scheme. Similarly, COM mode cooling can be enhanced by simultaneously cooling the COM mode on three ions with three RF fields. This increases the cooling rate and further reduces the residual excitation.

In the first step, all three modes of a three-ion crystal are cooled simultaneously, followed by a step in which the COM mode is cooled on all three ions. This second step can be relatively short because the motion of the ions in the COM mode is pre-cooled. This

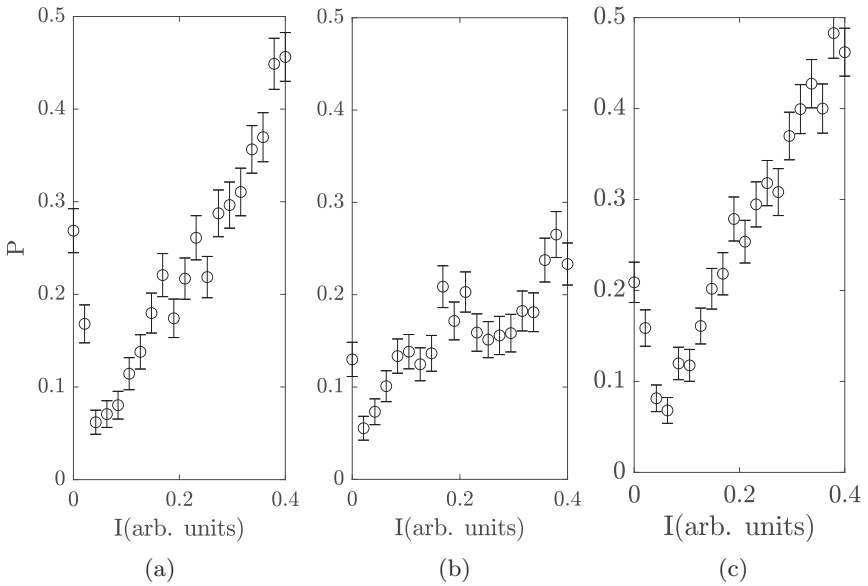

Figure 2.7.1: Experimental result of the search for the optimal optical cooling intensity I. Here the intensity I of the laser light near 369 nm is varied during the 50 ms sideband cooling step as described in section 2.7. The qubits are then prepared in the $|000\rangle$ state as described in section 2.5.4, and a microwave readout pulse resonant to the red sideband transition is applied to each qubit in the absence of a light field. (a) Ion 1 readout of mode 2 (b) Ion 2 readout of mode 3 (c) Ion 3 readout of COM mode. The resulting excitation probability P indicates the presence of a red sideband transition, where a vanishing sideband transition indicates ground state cooling. All three modes show a dip at about 0.1, indicating simultaneous cooling of the three modes. The scanned range of laser power is limited to efficiently implement the sideband cooling optimization, so that even at the highest laser power applied, the system is already cooled.

two-step scheme is implemented in the experiments performed here with 50 ms cooling on three different modes and 10 ms cooling on the COM mode on three ions. This reduces the cooling time from 300 ms using the classical method [9] to 60 ms using the technique introduced here. The duration of coherent evolution in the experiments performed for this work is less than 20 ms, making sideband cooling the most time-consuming task in an experiment. Therefore, the application of this fast sideband cooling scheme speeds up data acquisition by a factor of five in the case of a three-mode SBC.

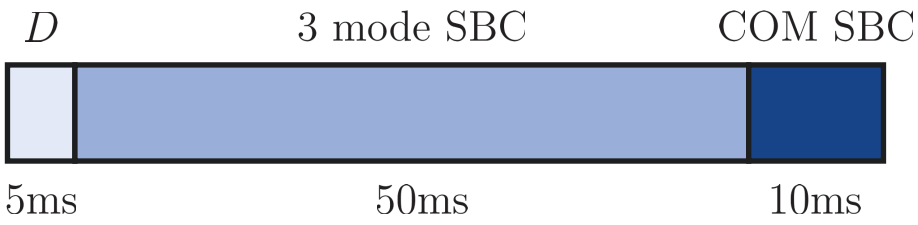

Figure 2.7.2: Timeline of a two-stage sideband cooling process. (D) is the fast Doppler cooling of 5 ms duration, followed by a 50 ms parallel three-mode sympathetic sideband cooling. Finally, a 10 ms parallel three-qubit COM cooling is applied to cool the COM mode at three times the cooling rate during the three-mode SBC to reduce the residual phonon level limited by the predominant COM mode heating.

2.8 Lab automation

One step in developing a quantum computer is to automate the system as much as possible to allow for automated operation. During the time in the lab, it became clear that it would be beneficial to reduce the human factor in the experiment to increase reproducibility and improve results. Automating routine tasks improves the reliability of the experiment and allows the operator to focus on other aspects of the experiment. Some common tasks are loading the trap or adjusting the laser frequencies. These two tasks have been automated and are described below.

The phenomenological description of the detection of unwanted molecules in the ion crystal allows to decide whether it is necessary to reload or not. This procedure is described in chapter 3.

2.8.1 Automatic loading

Loading the trap is a standard lab task. The trapping potential is deep enough that even uncooled ions remain in the trap overnight, so it is rare for an ion to be lost. Therefore, reloading the trap with $^{171}Yb^{+}$ is necessary if the trap has been turned off, a molecule has formed, or the number of $^{171}Yb^{+}$ in the trap is incorrect. Regardless of the reason for reloading the trap, the loading procedure is always the same. Here I will describe how to

automate the loading process. This procedure is based on experience in daily lab operation and may be improved in the future:

- Switching the trap drive:
  At the beginning of a loading procedure, the trap drive is switched off for a short moment. This allows us to get rid of ions in a dark state. The trapping potential is switched by switching the frequency generator's output amplitude, which generates the signal to the RF resonator.

- Heating the oven:
  To load $^{171}Yb^{+}$, atomic ^{171}Yb is thermally evaporated by heating an oven [43]. To heat, the oven current is switched and left on during the loading process.

- Setting the lasers:
  The 369 nm laser is set roughly to the Doppler cooling setting detuned by about $2\pi \cdot 100$ MHz to the atomic resonance of a resting ion, to allow it to cool down fast ions after ionization.

- The RF field is set to the π transition to close the Doppler cooling cycle.

- The 935 nm repump laser is switched on.

- The 399 nm laser for ionization is switched on and scanned across the atomic resonance line to allow for laser ionization.

- The camera image is observed using a long exposure time.

- If one pixel of the camera image exceeds a hard set threshold, indicating the presence of an ion, the ionizing laser is switched off.

- Waiting some seconds to let the ion or ions cool down and form a crystal.

- Scanning the laser frequency and observing the ion fluorescence as incoherent spectroscopy is used to determine the optical resonance.

- Counting the number of ions in the trap. If not enough ions are present, continue loading; otherwise, finish the loading procedure.

- Setting the 935 nm repump laser to resonance found by spectroscopy, and the 369 nm

laser about $2\pi \cdot 100\,\mathrm{MHz}$ detuned.

- Switching on the 399 nm ionizing laser.
- Waiting till sufficiently many ions are counted.

Depending on the parameters: 399 nm laser power, 369 nm laser power, sweep speed and range of the 399 nm laser frequency, overlap and beam size of both lasers, and heating power of the atomic oven, loading times for $^{171}\mathrm{Yb}^{+}$ are on the order of 5 min for the first ion to be loaded. If the oven remains on during loading, additional ions can be loaded in about three minutes. This procedure relies on proper ion counting and a quasi-deterministic appearance of freshly loaded ions in the crystal, which limits the loading rate so that one ion is cooled down before the next ion is ionized.

2.8.2 Laser spectroscopy

The optical transition of 369 nm from $|^2S_{1/2}, F = 1\rangle \leftrightarrow |^2P_{1/2}, F = 0, 1\rangle$ is used in the experiment each time the ions are initialized, cooled, or readout, so knowledge of the optical resonances is necessary to run the experiment. In addition to the UV transition at about 369 nm, the infrared transition at about 935 nm must be known. The 935 nm transition $|^2D_{3/2}\rangle \leftrightarrow |^3D[3/2]_{1/2}\rangle$ pumps the qubit back to the $|^2S_{1/2}\rangle$ state. More details about the ion resonances can be found in the appendix D. Both optical transitions have to be found spectroscopically. This is done using the resonance fluorescence detected by the camera. All fluorescence obtained is of wavelength 369 nm. The 935 nm transition is observed indirectly by observing the photons emitted by the 369 nm spontaneous emission, while the 369 nm transition is driven red detuned to maintain Doppler cooling during the process.

Each spectroscopy performed is structured as follows:

- An image containing Doppler cooling fluorescence is acquired.
- An ion area is estimated by selecting pixels exceeding a fixed threshold.
- In the case of the 935 nm laser scan, the laser power is reduced from $P_{935} = 1.1\,\mathrm{mW}$ to $P_{935} \approx 110\,\mu\mathrm{W}$ to reduce power broadening on the transition to FWHM $\approx 2\pi{\cdot}50\,\mathrm{MHz}$.

- The laser wavelength close to 369 nm is detuned to the red from the current frequency.
- Successive images are acquired while the laser frequency is scanned stepwise in $f_{step,935} = 2\pi \cdot 6.4\,\text{MHz}$ from the red towards the blue detuning.
- For each image, the fluorescence is found, summing up the values of each pixel in the ion area.
- In the case of the laser scan of the 935 nm laser, a Gaussian profile is fitted to the fluorescence curve to find the resonance.

In the case of a scan of the 369 nm laser wavelength, it is necessary to perform the wavelength sweep from the red to the blue detuning, since blue detuned to the resonance, the 369 nm laser will Doppler heat the system, causing the ion crystal to melt. The point at which the Doppler cooling stops working and the crystal melts can be found in the integrated fluorescence data over the ion regions as a rapid drop. An example of a laser spectrum observing the transition at about 369 nm is shown in fig. 2.8.1.

The laser frequency is shifted to about $2\pi \cdot 19\,\text{MHz}$ below the rapid drop of the measured fluorescence to achieve optimal Doppler cooling efficiency. In this part of the optical resonance, the largest slope of the scattering rate as a function of laser frequency occurs, resulting in optimal Doppler cooling.

2.8.3 Stabilization of cooling fluorescence

During all experiments, the 369 nm laser field frequency may drift slowly. This can be caused by ambient pressure, temperature, and humidity. This is due to the locking to the resonance of a reference cavity. The cavity is in air, so a change in the refractive index due to a change in the above parameters changes the resonant frequency of the cavity and therefore the frequency of the laser locked to it. Since the thresholds found during the detection calibration process are only valid as long as the number of photons captured when the qubit is projected onto $|1\rangle$ remains constant, the fluorescence obtained must be kept stable. Furthermore, the fluorescence must be the same for all experiments using the same detection calibration. To ensure this, a scan of the laser frequency is performed automatically before the experiment starts, as described in section 2.8.2.

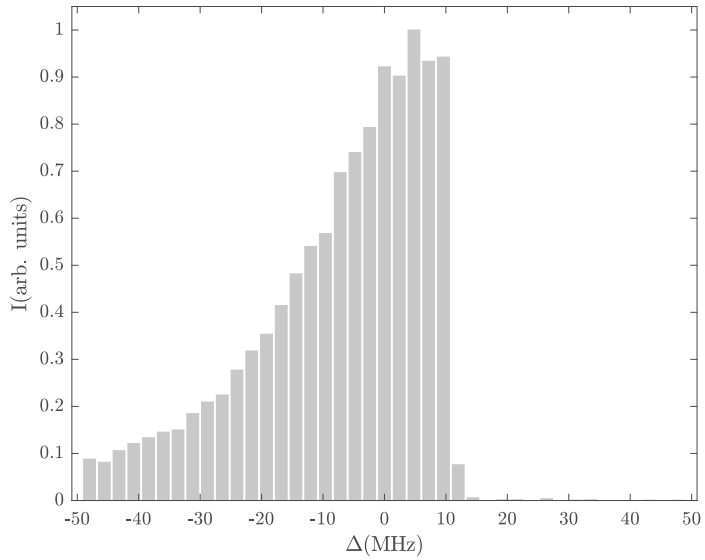

Figure 2.8.1: Example spectrum of the 369 nm cooling transition $|^2S_{1/2}, F = 1\rangle \leftrightarrow |^2P_{1/2}, F = 0\rangle$. The laser is tuned from lower frequencies to higher frequencies since, at the resonance, the Doppler-cooling does not work anymore, and the ion string melts, producing a rapid drop in measured fluorescence. Here $\Delta = 2\pi \cdot 0\,\mathrm{MHz}$ corresponds to no detuning of the laser frequency relative to the lasers frequency prior to the spectroscopy performed. Using a laser frequency detuned by approximately $-\Delta = 2\pi \cdot 19\,\mathrm{MHz}$ from the rapid drop in fluorescence is used for Doppler cooling the ion string during the experiments. This corresponds to the steepest slope of the resonance, indicating the best Doppler cooling configuration.

After the resonance is found, the frequency of the 369 nm laser field is detuned by $2\pi \cdot 19\,\mathrm{MHz}$ to the red. This is done automatically before starting an experiment, including the calibration measurement to find the detection thresholds. This ensures that the thresholds are valid at the beginning of the experiment. However, the laser frequency may drift during the experiment.

To compensate for this drift, live analysis of the Doppler cooled fluorescence can be used. Once the experiment is started, the Doppler cooling images should always contain the same fluorescence. After the experiment has started, a floating average over the last N_{avg} Doppler cooling images d_{in} is calculated based on the detection ion areas:

$$D_k = \sum_{n=k-N_{avg}}^{k} \sum_{i=1}^{N_{ion}} d_{in}. \tag{2.8.1}$$

At the start of the experiment, the reference fluorescence $D_{ref} = D_{N_{avg}}$ is evaluated after N_{avg} cycles. After a period of τ_{stab}, D_k is calculated and compared with D_{ref}, if the deviation is greater than D_{win}, a frequency step f_{step} is applied:

$$\Delta f_{appl} = \begin{cases} f_{step} & \text{when} \quad D_{ref} - D_k > D_{win} \\ -f_{step} & \text{when} \quad D_{ref} - D_k < -D_{win} \\ 0 & \text{else.} \end{cases} \tag{2.8.2}$$

Typical choices during the experiment are $N_{avg} = 100$, $f_{step} = 2\pi \cdot 0.48\,\text{MHz}$ and $\tau_{stab} = 2\,\text{s}$. With these parameters, the application of this technique allows to compensate sufficiently slow drifts of the laser frequency, less than $2\pi \cdot 240\,\text{kHz/s}$.

3

Quantum sensing

Microscopes have paved the way for advances in basic research. The development of optical microscopy has historically led to breakthroughs in science. Although limited by the wavelength of light used in optical microscopes, the resolution of optical microscopes was improved through the use of novel techniques. Scanning near-field optical microscopy [44] has been used extensively at wavelengths in the visible regime [45] and has been extended to the radiofrequency regime [46, 47]. The highest wavelength-relative resolution attained to date was reported by Keilmann et al. [46] as $\Delta x/\lambda < 5 \times 10^{-7}$ using wavelengths up to 20 cm. Using a spatially varying magnetic field and a probe sensitive to magnetic fields, the position of the probe can be measured. Electron spins in single nitrogen vacancy defect centers in diamond can be selectively addressed [48, 49], and were used for measuring magnetic fields, in the present gradient resulting in a wavelength-relative resolution of 2.8×10^{-6} using a wavelength of 10.4 cm. [50]. Combining scanning force microscopy and magnetic resonance imaging was proposed in 1991 [51] and demonstrated shortly after [52]. Trapped atomic ions have been succesfully employed probes for magnetic fields [53–55], electric fields, and forces in the yoctonewton regime [56–60].

In this chapter, a single $^{171}\mathrm{Yb}^{+}$ ion is used as a quantum sensor of magnetic fields to calculate the position of the ion and ultimately as a sensor of tiny DC electric forces.

At the end of this chapter, measurements of the resonance frequency of the qubits, routinely performed during lab operations, are used to indirectly diagnose whether or not an ion that is not visible and not addressed by laser light has formed a molecule. In addition, precise knowledge of the qubit resonance frequency allows us to observe the axial trap frequency and the J-coupling.

3.1 Measuring $\partial_z B$

A $^{171}Yb^{+}$ -ion trapped in a quadratic potential as described in chapter 2 can be Doppler-cooled, state-selectively prepared and read out with laser radiation close to 369 nm. An EMCCD camera observes it with a pixel size of 16 µm. The imaging optics used here provides a magnification of 12.5 and images the fluorescence light of ions on about $12 \cdot 8$ pixels. Given the setup used in its normal mode of operation, the observed ion fluorescence extends over ≈ 10 µm in the trap. This is sufficient to spatially identify and separate the qubits in the trap. The size of the image and the width of the ion wave function in the trap can easily be mistaken for a limit to the resolution of the ion position. In this chapter, the center of the ion wave function in the trap is referred to as the position of the ion. Although the ion wave function extends over $\Delta z = \sqrt{\frac{\hbar}{2m_{Yb}\omega_z}} \approx 16$ nm, the center of the wave function and therefore the position can be defined with higher accuracy.

To measure the position of the ions, a measurement of the magnetic field with a known magnetic field gradient can be used. To determine the magnetic field gradient in the setup, it is necessary to probe the magnetic field at different points along the trap axis. Assuming a harmonic potential and Coulomb repulsion between charged ions, the position of the ions in a Coulomb crystal can be calculated for a given trap frequency [14]. The distance between the ions is therefore defined by electrostatics and can be determined without using optical imaging or the magnetic field at the ion position. A linear Coulomb crystal can therefore be used as a reference for the ion position to determine the magnetic field gradient.

The following steps were performed to measure the gradient. These steps are explained in the following paragraphs.

1. Measurement of the axial trapping frequency ω_z by resonant excitation of the movement of the ions in the trap.

2. Calculating the ion's relative positions in the trap by minimizing the overall potential as shown in eq. (3.1.2).

3. Measurement of the addressing frequencies ν_i of a string of ions as shown in section 2.6.

4. Calculating the magnetic field from the measured resonance frequencies at the qubits position by inverting eq. (2.2.9).

5. Calculating the gradient from calculated ion positions and magnetic fields as shown in fig. 3.1.1.

To measure the axial trap frequency ω_z, an AC voltage is applied to an electrode while it frequency ν_{AC} is scanned over the resonance and the ion image is observed. When the applied AC signal is close to the resonance ($\nu_{AC} = \omega_z$), the motion of the ions in the trap is excited until it is visible by a distortion of the image on the camera. The frequency of the voltage applied to the electrode is then resonant with the ion motion. The lowest frequency that occurs while a distortion of the ion image along the trapping axis is observed is the Center Of Mass (COM) mode. Its frequency is independent of the number of ions in the linear Coulomb crystal and can therefore be clearly identified.

The different qubit resonance frequencies of all ions in the crystal allow for addressing the ions individually. In the case of a Coulomb crystal containing multiple ions, the qubit resonances can be measured simultaneously for all qubits using the method described in section 2.6. Periodic recalibration of qubit resonances is routinely applied to minimize addressing errors during the execution of quantum circuits. Therefore, long data sets of continuous frequency calibration are available.

Two properties can be extracted: The magnetic field gradient and the stability of the trap frequency, and hence the long-term stability of the J-coupling, can be estimated.

According to [14], the ions' position in a trap is determined by the minimum of the electric potentials assuming harmonic axial confinement and the Coulomb potentials generated by each ion. The positions are given as

$$z_i = u_i \left(\frac{q_e^2}{4\pi\epsilon_0 m_{\mathrm{Yb}} \omega_z^2} \right)^{1/3}, \tag{3.1.1}$$

where q_e is the elementary charge, m_{Yb} is the mass of an Ytterbium ion, $\omega_z = 2\pi \cdot 128.24(1)\,\mathrm{kHz}$ is the trap frequency and u_i is the solution to the equation:

$$0 = u_i - \sum_{j=1}^{i-1} \frac{1}{(u_i - u_j)^2} + \sum_{j=i+1}^{N} \frac{1}{(u_i - u_j)^2}. \tag{3.1.2}$$

Ion	Scaled positions u_i	Absolut positions z_i	magnetic field B
1	-1.43680	$-15.4853(8)\,\mu m$	$346.60(2)\,\mu T$
2	-0.45438	$-4.8971(3)\,\mu m$	$548.70(2)\,\mu T$
3	0.45438	$4.8971(3)\,\mu m$	$735.68(2)\,\mu T$
4	1.43680	$15.4853(8)\,\mu m$	$937.89(2)\,\mu T$

Table 3.1.1: Calculated ion position of 4 ions for a measured axial trapping frequency of $\omega_z = 2\pi \cdot 128.24(1)\,\text{kHz}$ measured by observing a blurring of the ion image while an alternating electric field excites the motion of the ions. The magnetic field B is calculated as an average of the ion resonance frequencies over a consecutive observation time of 6h using 357 measurements of the addressing frequency per qubit. The errors are calculated as standard errors of the samples of B, while the error on z is calculated from the error on ω_z.

The trap frequency was determined manually in this case with an estimated error of $2\pi \cdot 10\,\text{Hz}$, where the measured trapping frequency is $\omega_z = 2\pi \cdot 128.24\,\text{kHz}$. Based on this uncertainty according to eq. (3.1.1), the error of the relative length scale is

$$\frac{\sigma_z}{z} = \frac{2}{3}\frac{\sigma_{\omega_z}}{\omega_z} \approx 5 \cdot 10^{-5}. \tag{3.1.3}$$

The calculated ion positions' results are shown in table 3.1.1.

The magnetic field gradient corresponds to the linear slope of $B(z)$ and is derived by a fit to the measured data shown in fig. 3.1.1 and table 3.1.1 respectively. Since the errors in the calculated position are given by the frequency error of the measured trap frequency, they are correlated. The systematic error of this axis is $\sigma_z/z \approx 5 \cdot 10^{-5}$. The slope is linear in the scaling errors of the z-axis, so the relative errors add up to

$$\frac{\sigma_{\partial_z B}}{\partial_z B} = \left(\frac{\sigma_{\partial_z B}}{\partial_z B}\right)_{fit} + \left(\frac{\sigma_{z_i}}{z_i}\right)_{syst}, \tag{3.1.4}$$

where $\partial_z B$ is the magnetic field gradient. The magnetic field gradient is found to be

$$\partial_z B = 19.09(1)\,\text{T/m}. \tag{3.1.5}$$

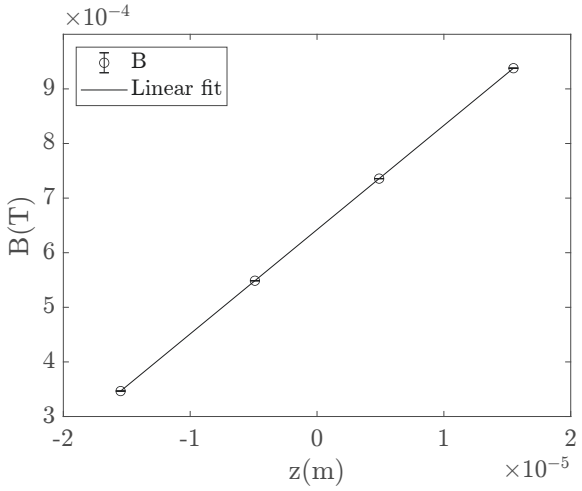

Figure 3.1.1: Linear fit of the magnetic field at the ion position for a measured trap frequency $\omega_z = 2\pi \cdot 128.24(1)\,\mathrm{kHz}$. The barely visible error bars correspond to standard errors. From the linear fit $\partial_z B_{fit} = 19.092(1)\,\mathrm{T/m}$ can be estimated. Incorporating the systematic error of $\sigma_z/z \approx 5 \cdot 10^{-5}$ derived in eq. (3.1.3), in total, the magnetic field gradient can be estimated to be $\partial_z B = 19.09(1)\,\mathrm{T/m}$. The calculated position and magnetic fields can be found in table 3.1.1.

3.2 Observing an $^{171}Yb^{+}$ ion

The minimal motional excitation as shown in section 2.5.2 is $\overline{n} = 80$ after a Doppler cooling step is applied. Two assumptions are made. The Rabi frequency Ω_n depends on the phonon number n. This is described by the equation (2.6.2). Second, the thermal occupation of the vibrational modes is described by (2.6.3). These equations can be used to synthesize the shape of an atomic resonance. In fig. 3.2.1 the calculated shape is given for two exemplary phonon numbers. From this shape, a numerical search for the point where the expected excitation probability is 0.5 yields the Full-Width Half Maximum (FWHM) of the resonance. In a range from $\overline{n} = 20$ to $\overline{n} = 100$ the FWHM of the resonance changes by $1.7 \cdot 10^{-2}\Omega$. This demonstrates the robustness of the method summarized in section 2.6 against thermal excitations of the ion motion, and therefore a fast Doppler cooling step is sufficient for the measurement.

Using this shape of the atomic resonance and equation (2.6.4), the measurement of two excitation probabilities is sufficient to determine a frequency offset Δ. Equation (2.5.10)

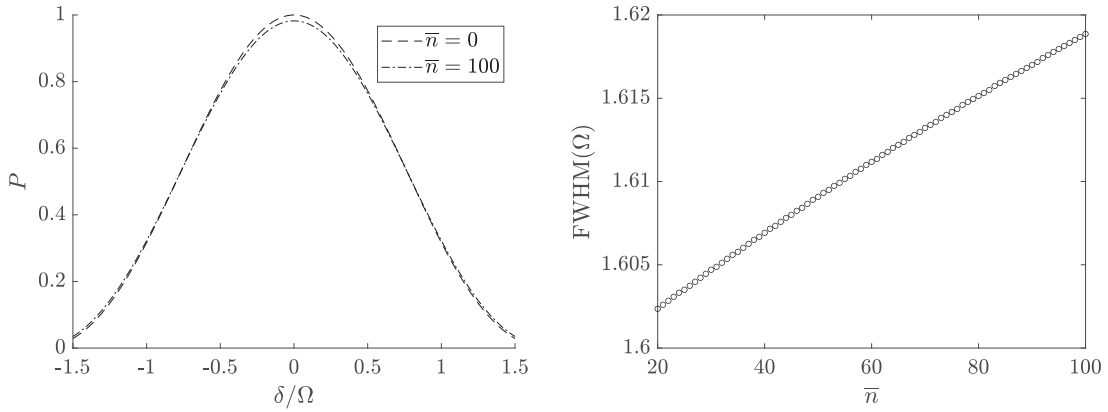

(a) (b)

Figure 3.2.1: (a) Exemplary calculated excitation probability P of the hyperfine resonance $|^2S_{1/2}, F = 0\rangle \leftrightarrow |^2S_{1/2}, F = 0, m_F = 1\rangle$ with different motional excitations $\overline{n} = 0; 100$ as a function of the detuning δ with respect to the atomic resonance in units of the Rabi frequency Ω. (b) Full-width half maximum (FWHM) of the synthesized atomic resonances in units of the Rabi frequency Ω. The relative change of the resonance width of about 0.02 justifies the validity of the resonance measurement if only a Doppler cooling step with $\overline{n} = 80$ phonons, in the end, is applied.

allows to calculate the error of a measured excitation probability $\sigma_{P_\pm}$ and using eq. (2.6.3) allows to calculate $P_\pm$ for a given Δ, as shown in [28]. The error in the frequency measurement can be calculated as

$$\sigma_\Delta = \left(\frac{\partial g}{\partial \Delta}\right)^{-1} \sqrt{\frac{2P_+^2\sigma_{P_-}^2 + 2P_-^2\sigma_{P_+}^2}{P_+ + P_-}}. \tag{3.2.1}$$

The updated frequency is $\nu = \nu_0 + \Delta$ and therefore the statistical error of the updated frequency is $\sigma_\nu = \sigma_\Delta$. The resulting statistical errors are shown in fig. 3.2.2 for a fixed measurement time and a fixed frequency offset Δ. For a given number of repetitions of $N_{rep} = 50$ corresponding to a measurement time of 2 s the minimal achievable statistical error is $\sigma_\Delta = 0.06 \cdot \Omega$. For a fixed measurement duration of two seconds, the expected statistical uncertainty for a given frequency offset Δ during this measurement is shown in fig. 3.2.2. Around $\Delta = 0.8 \cdot \Omega$, the error rapidly increases, limiting a beneficial window for corrections with $\Delta < 0.8 \cdot \Omega$. For a given offset Δ, also the scaling of the statistical error with the measurement time is shown, indicating a $\sigma_\nu/\Omega \propto 1/\sqrt{T}$ scaling.

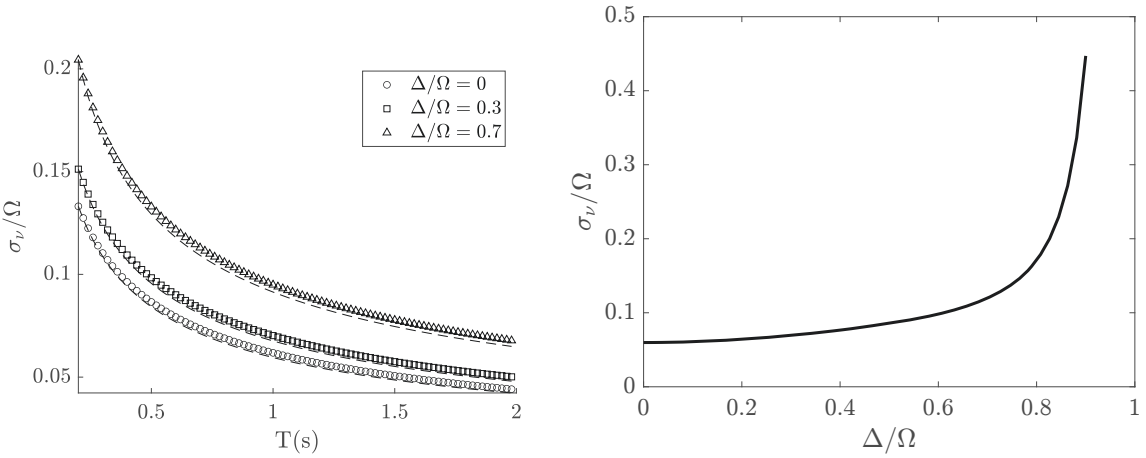

(a) (b)

Figure 3.2.2: (a) Relative statistical uncertainty of the addressing frequency σ_ν/Ω, given a frequency offset during the measurement of $\Delta/\Omega = [0, 0.3, 0.7]$. Indicated points correspond to calculated uncertainties based on the calculated measurement error, as shown above, dashed lines are showing an $\propto 1/\sqrt{T}$ scaling, where T is the measuring time. (b) Calculated uncertainty for an experiment of a fixed duration 2 s as a function of the frequency offset using equation (3.2.1).

First, the fast adaptive addressing frequency measurement was implemented to compensate for drifts in the addressing frequency. To demonstrate the ability to resolve the position of an ion along the z axis, a change in position is introduced by changing the minimum position of the trapping potential. This potential along the z direction is generated by the voltage applied to the end cap electrodes shown in fig. 2.1.1. Figure 3.2.3 shows a schematic of the end cap electrodes that generate the trapping potential. To calculate the trapping potential, the electrodes in the calculation are replaced by a dummy charge at the center of the electrode tips. This reduces the problem to one dimension.

The electrostatic potential can be calculated as

$$\phi = \frac{1}{4\pi\epsilon_0}\left(\frac{q_1}{z - z_1} + \frac{q_2}{z_2 - z}\right). \tag{3.2.2}$$

Solving $\partial_z \phi = 0$ results in:

$$z = \sqrt{\left(\frac{q_1 z_2 - q_2 z_1}{q_1 - q_2}\right)^2 - \frac{q_1 z_2^2 - q_2 z_1^2}{q_2 - q_1}} + \frac{q_1 z_2 - q_2 z_1}{q_1 - q_2}, \tag{3.2.3}$$

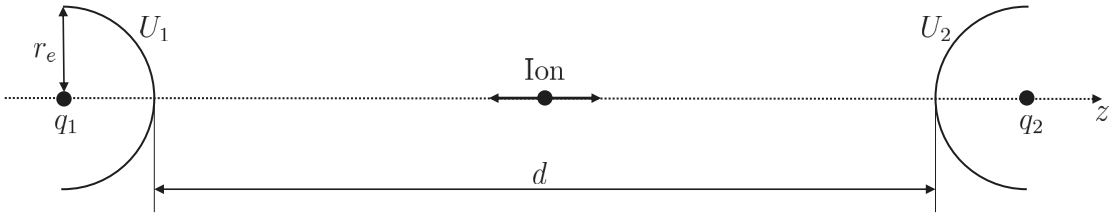

Figure 3.2.3: Schematic of the experimental setup to introduce a shift of the position of the ion by changing voltage U_2. The radius of the metallic end cap electrodes is $r_e = 0.15\,\text{mm}$, the distance between the electrode tips is $d = 3\,\text{mm}$. The charges q_1 and q_2 represent the replacement charge for the voltage applied to the end caps, generating the trapping potential at the location of the ion.

where z is the position of the ion, z_i are the positions of the replacement charges q_i and ϵ_0 is the vacuum permittivity. The replacement charges here are $q_i = 4\pi\epsilon_0 r_e U_i$ where r_e is the end cap tips' radius and U_i is the voltage applied.

An offset magnetic field is required to define the quantization axis and lift the degeneracy of $|^2S_{1/2}, F = 1, m_F = \pm 1, 0\rangle$. An imbalanced voltage is applied to the end cap electrodes, shifting the ions position in the trap out of the low magnetic field region. The voltages where $U_1 = 15.38\,\text{V}$ and $U_2 = 19\,\text{V}$ resulting in a displacement of the ion from the center of $r_{dis} = 87.3\,\mu\text{m}$. To modify the voltage U_2 in the mV range to obtain a shift on the nm scale, a second voltage U_{var} is added to U_2 using a voltage divider. $U_2' = U_2 + 9.8 \cdot 10^{-3} U_{var}$.

A quadratic fit of the calculated trapping potential at the ion's location yields a calculated trap frequency $\omega_{calc} = 2\pi \cdot 181.48\,\text{kHz}$. In contrast, the measured trap frequency is $\omega_{trap} = 2\pi \cdot 108.10\,\text{kHz}$. This discrepancy can be caused by the trap geometry, by imperfect assembly of the trap electrodes, or by possible offset voltages on the DC ground electrodes. The real trap differs from the ideal assumptions because the ions remain in the trap even when no voltage is applied to the trap electrodes. The deviation from the idealized model assumptions can be taken into account by introducing a factor $\kappa = \omega_{trap}/\omega_{calc}$. The resulting linear response to the changed voltage is $\Delta z = \kappa \Delta U_2' \widetilde{k}$ with $\widetilde{k} = 2.11 \cdot 10^{-7}\,\text{m/V}$ found by fitting the calculated potential with a parabola and extracting the minimum.

Since the ions resonance drifts during the experiment, a measurement with a biased voltage $\Delta U = U_2 - U_1 \neq 0$ is alternated with a measurement with $\Delta U = 0$. Figure 3.2.4 shows the measurements of the ions resonance. Using the Allan variance, a drift rate of the ions

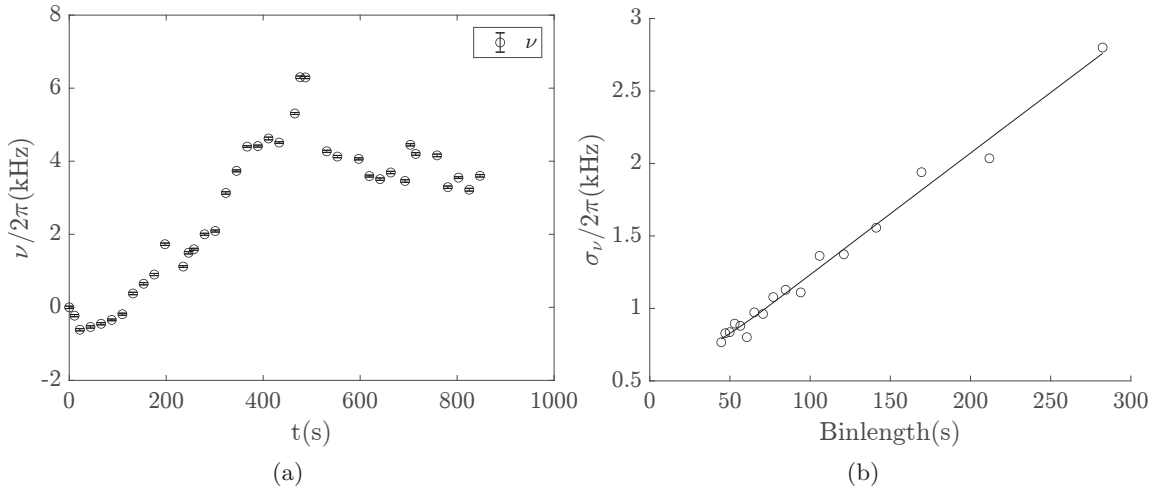

Figure 3.2.4: (a) Measurement of the ions resonance ν during the experiment when the additional voltage imbalance is switched off. Error bars are standard errors and are barely visible. (b) The fit of the Allan variance for different lengths of bins. A drift rate of $\sigma_A = 8.3\,\mathrm{Hz/s}$ can be extracted.

resonance of $\sigma_A = 2\pi \cdot 8.3\,\mathrm{Hz/s}$ is estimated. Details of the procedure used to estimate this can be found in [28]. From these measured frequencies, an amplitude of the magnetic field $B(\nu)$ can be calculated by inverting equation (2.2.4). Assuming a constant magnetic field gradient along the z direction of $\partial_z B = 19.09(1)\,\mathrm{T/m}$ the position of the ion can be inferred from

$$z = \frac{B(\nu)}{\partial_z B}. \tag{3.2.4}$$

The unbiased position during voltage biased measurements is not accessible. The ion position is given by linear interpolation between successive measurements without additional voltage bias. This is shown in fig. 3.2.5. Comparing these positions gives the position offset due to the applied voltage bias. Measurements with $\Delta U = 0$ are $z_{2k\pm1}$ and measurements with $\Delta U \neq 0$ are z_{2k}. The induced position change and its error can be calculated as:

$$\Delta z_{ind,k} = z_{2k} - \frac{z_{2k-1} + z_{2k+1}}{2}, \tag{3.2.5}$$

$$\sigma_{\Delta z_{ind,k}} = \sqrt{\sigma^2_{z_{2k}} + \frac{1}{2}\sigma^2_{z_{2k-1}} + \frac{1}{2}\sigma^2_{z_{2k+1}}}. \tag{3.2.6}$$

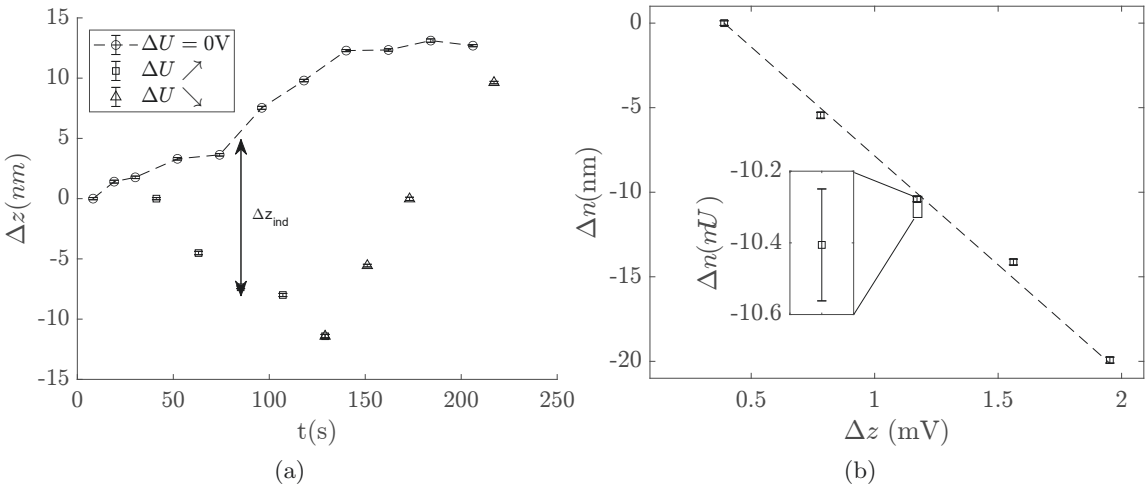

Figure 3.2.5: (a) Series of position measurements with and without additional voltage bias ΔU at the endcap electrodes to induce ion displacement. The positions with $\Delta U = 0$ are interpolated (dashed line) at times where a bias $\Delta U \neq 0$ is applied to extract the induced ion displacement Δz_{ind}. (b) Comparison of the expected ion displacement $\Delta z = \Delta U \cdot 1.25 \cdot 10^{-7}\,\mathrm{m/V}$, shown as a dashed line, and the measured displacements from (a), where no fit was performed. The error bars shown are standard errors and are barely visible. A drift of ν produces deviations from the expected displacements within the experiment, which did not exactly follow the linear assumption.

The measurement typically consists of 50 repetitions for two different RF pulses applied. Therefore, 100 cycles have to be measured, resulting in a measurement duration of 2 s, since the duration of a single cycle is 20 ms. A statistical error of the measured addressing frequencies of $\sigma_\nu = 2\pi \cdot 28\,\mathrm{Hz}$ could be achieved during these measurements. Converted to a position it is $\sigma_z = 0.12\,\mathrm{nm}$. The extension of the atomic wave packet in the trap is given by $\Delta z_l = \sqrt{\hbar/2m\omega_l} = 16.5\,\mathrm{nm}$, which is about two orders of magnitude larger than the achieved resolution of its position. It should be emphasized that the measured ion positions reported here correspond to the center of mass (COM) position. This does not contradict the extension of the ion wave packet. Another noteworthy feature is that this experiment was performed using RF radiation around $\omega_{rf} \approx 2\pi \cdot 12.6\,\mathrm{GHz}$, which corresponds to a wavelength of $\lambda_{rf} = 2.38\,\mathrm{cm}$. Thus, the wavelength used to detect a position is $5 \cdot 10^9$ times larger than the resolution, making it the best relative wavelength resolution reported today.

Another feature of the experiment is the weak confinement along the z axis. The effective potential is given by the equation (2.1.1). The axial component of the effective potential Φ_z is given by:

$$\Phi_z = \frac{1}{2} m_{\mathrm{Yb}} \omega_z^2 z^2 = q_e \phi_z, \tag{3.2.7}$$

where ϕ_z is the electric potential and q_e is the elementary charge. From this potential, the force is given by

$$F_z = \partial_z \Phi_z = \underbrace{m_{\mathrm{Yb}} \omega_z^2}_{k} z = 1.31 \cdot 10^{-13}\,\mathrm{N/m} \cdot z. \tag{3.2.8}$$

and therefore the error of the force can be calculated as:

$$\sigma_{F_z} = k\sigma_z = 1.57 \cdot 10^{-23} N. \tag{3.2.9}$$

A harmonic trapping potential is characterized by a linear dependence of the ion position on the applied force. Therefore, Hook's law can be applied. Hook's constant $k = 1.31 \cdot 10^{-13}\,\mathrm{N/m}$ for an ion mass of $m_{\mathrm{Yb}} = 170.94\,\mathrm{u} = 2.84 \cdot 10^{-25}\,\mathrm{kg}$ and an axial trapping frequency of $\omega_z = 2\pi \cdot 108.1\,\mathrm{kHz}$. Together with a position resolution of $O(10^{-10}\,\mathrm{m})$ a force resolution of $O(10^{-23}\,\mathrm{N})$ can be achieved.

The results of the measurements are summarized in table 3.2.1.

A typical physical property of a force measurement device is its sensitivity in units of

Parameter	value
Measurement time	2 s
Driving field Rabi frequency Ω	$2\pi \cdot 367$ Hz
Trap frequency ω_z	$2\pi \cdot 108.1$ kHz
Statistical uncertainty of frequency σ_ν	$2\pi \cdot 28$ Hz
Sensitivity for resonance frequency	$40\,\mathrm{Hz}/\sqrt{\mathrm{Hz}}$
Statistical uncertainty of DC magnetic field σ_B	2.3 nT
Sensitivity for DC magnetic field	$3.2\,\mathrm{nT}/\sqrt{\mathrm{Hz}}$
Statistical uncertainty of position σ_z	0.12 nm
Sensitivity of position	$0.17\,\mathrm{nm}/\sqrt{\mathrm{Hz}}$
Statistical uncertainty of force σ_F	$1.6 \cdot 10^{-23}$ N
Sensitivity of force	$2.2 \cdot 10^{-23}\,\mathrm{N}/\sqrt{\mathrm{Hz}}$
Natural drift rate σ_A	8.3 Hz/s

Table 3.2.1: Overview of measurements obtained with a single ion in a 19.09(1) T/m magnetic field gradient along the trapping axis.

$s = Ft^{-1/2}$ with units of $\mathrm{N}/\sqrt{\mathrm{Hz}}$, where F is a force and t is the measurement time. The sensitivity defined as such is an instructive measure to calculate the possible resolution $\sigma_F = s/\sqrt{t}$ directly from the sensitivity and the applied measurement time. The experimental procedure must be as fast as possible to obtain a good sensitivity.

The results obtained in this section are summarized in the table 3.2.1 and a publication is in preparation.

3.3 Measuring the stability of the trapping potential

When a coulomb crystal is used as a register of qubits, periodic recalibration of the addressing frequencies is performed. The calibration data can also be used to observe the trapping potential.

Assuming that the magnetic field gradient is constant, the measurement of the addressing frequencies of the qubits allows the calculation of changes in the dimensions of the crystal as shown in the previous section. Since the dimensions of the crystal l as shown in eq. (3.1.1) [14] scale as $l \propto \omega_z^{-2/3} \propto z_i - z_j$, a measure of the axial positions can be used to observe the axial trapping frequency.

During a day of continuous lab operation, the resonance frequencies of the qubits are routinely calibrated. Based on 6 h of continuous measurements, fig. 3.3.1 shows the calculated change of the inter-ion spacing $\Delta z_{ij} = z_i - z_j$. The example histogram of Δz_{23} over the day has a width of $\sigma_{\Delta z_{23}} = 0.82\,\text{nm}$. At an interion distance of $\overline{\Delta z_{23}} = 9.793(1)\,\mu\text{m}$ the relative error is $\sigma_{\Delta z_{23}}/\overline{\Delta z_{23}} = 8.4 \cdot 10^{-5}$. The relative error of the trapping frequency is therefore $\sigma_{\omega_z}/\omega_z = 3/2 \cdot \sigma_{\Delta z_{23}}/\overline{\Delta z_{23}} = 1.3 \cdot 10^{-4}$.

The axial trapping frequency is related to the coupling in an ion crystal as $J \propto \omega_z^{-2}$. Thus, the relative stability of the J-coupling is

$$\frac{\sigma_J}{J} = 2\frac{\sigma_{\omega_z}}{\omega_z} = 2.6 \cdot 10^{-4} \tag{3.3.1}$$

This relative stability during the day refers to the contributions due to fluctuations in the trap frequency. The trap frequency measurements are taken approximately every 20 s. This measurement does not resolve changes in trap frequency on a faster time scale. Therefore, this stability must be considered as long-term stability.

Parameter	Relative stability over a day
Relative inter ion distance $\sigma_{\Delta z_{23}}/\overline{\Delta z_{23}}$	$8.4 \cdot 10^{-5}$
Relative trap frequency $\sigma_{\omega_z}/\omega_z$	$1.3 \cdot 10^{-4}$
Relative J coupling σ_J/J	$2.6 \cdot 10^{-4}$

Table 3.3.1: Relative stability of the inter ion distance over a day and the accordingly derived quantities for trapping frequency and J-coupling.

3.4 Identification of an unrecoverable dark state

The trap is installed in an ultra-high vacuum recipient to protect the qubits from the environment. Nevertheless, there is some background gas in the setup. Occasionally, collisions of the ion crystal with the background gas occur. Such a collision can drive the system into a long-lived metastable state, or a chemical reaction can occur. If a chemical reaction occurs, a molecule consisting of a Ytterbium ion and a background gas atom is formed, changing the energy level structure. Either case is a problem. In both cases, the

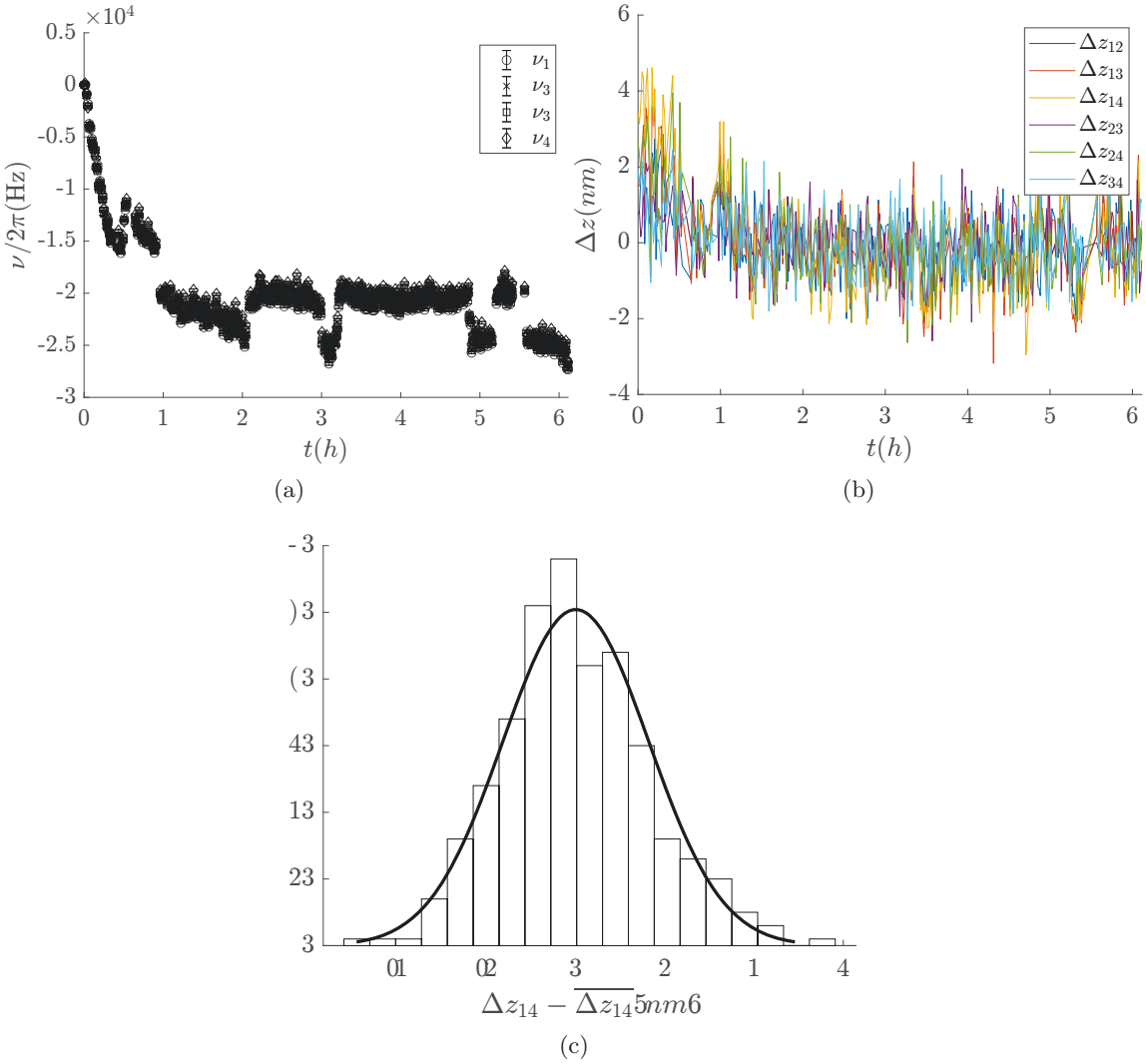

Figure 3.3.1: (a) Addressing frequency calibration data for four ions during one day of measurements. The initial frequencies $\nu_n(t = 0)$ have been subtracted to remove the frequency offset of about $2\pi \cdot 3.2\,\mathrm{MHz}$ for clarity. (b) Drift of the position of the ions relative to each other $\Delta z_{23} = z_3 - z_2$. Although the addressing frequency of all qubits jump as seen in (a), the distance between the ions is continuous. (c) Histogram of the ion spacing Δz_{23} during the day minus the mean spacing of $\overline{\Delta z_{23}} = 9.793\,\mu\mathrm{m}$. The width of the distribution is $\sigma_{\Delta z_{23}} = 0.82\,\mathrm{nm}$.

cooling, preparation, and readout laser is no longer resonant near 369 nm, so there are no emitted photons to detect. In this case, the ion is dark. Ions in the dark state are not cooled and are not addressed by the microwave fields. Due to the unknown state of dark ions, they would interfere with the calculation being performed. A molecule would change the vibrational mode structure that produces the all-to-all coupling, thereby changing the coupling between the bright ions. It would couple to the bright ions in an uncontrolled way and cannot be used for a calculation itself. If $^{171}Yb^{+}$ is in a unknown metastable state $|^2F_{7/2}, F = 3, 4\rangle$, the dark ion would also couple to the bright ions in an uncontrolled way and thus spoil the computation. Therefore, the trapped-ion qubits cannot be used as long as the dark state exists in the register. The long-lived metastable state can be resolved by applying an appropriate re-pumping scheme to pump the ion back to the desired state. This is done using a laser light field near 638 nm. Using this technique, the population trapped in the $|^2F_{7/2}\rangle$ state is transferred to the $|^1D[5/2]_{[5/2]}\rangle$ state. From this excited state, the ion undergoes spontaneous emission back to the $|^2D_{3/2}\rangle$ state. In the primary re-pumping scheme, the population in $|^2D_{3/2}\rangle$ is efficiently transferred back to the ground state and can therefore be recovered. The ionic level scheme can be found in the appendix as fig. D.1. Therefore, these long-lived metastable states are resolvable. In contrast, when a molecule is formed, the exact dissociation energy is unknown and therefore cannot be resolved. When such an event occurs, it is necessary to reload the trap to get rid of the molecular ion. Reloading the trap is time-consuming, and then the system needs time to thermally stabilize before reliable operation is possible. Therefore, it is advantageous to keep the ions in the trap as long as possible. Distinguishing between these two states would allow a decision to be made whether or not to reload the trap. Looking at the camera image, it is not possible to distinguish the resolvable state $|^2F_{7/2}, F = 3, 4\rangle$ from a permanently dark molecule. If the ion has formed a molecule, the addressing frequency of the other bright ions in the trap may change. Fig. 3.4.1 and fig. 3.4.2 show the addressing frequency and Doppler cooling florescence during an experiment when an ion in a crystal consisting of three $^{171}Yb^{+}$ ions went dark. What can be seen in the Doppler cooling fluorescence plots is that at different times the Doppler cooling fluorescence disappears for one ion and reappears for another. This indicates a jump of the dark ion between trapping sites. These jumps can occur on a time scale long enough to perform a resonance frequency calibration of the qubit addressing frequency as described in section 2.6. In fig. 3.4.2 the measured addressing frequency of the bright qubits jumps, indicating that a molecule has

formed. In fig. 3.4.1 no such jump is visible. In this case the state has recovered.

In the example of the permanent dark state shown in fig. 3.4.2, the trapping frequency ω_z was measured and was found to change. In the permanently dark state, $\omega_z' = 2\pi \cdot 102.81(1)\,\mathrm{kHz}$, while the trapping frequency with 3 bright ions present was $\omega_z = 2\pi \cdot 104.55(1)\,\mathrm{kHz}$. As discussed earlier in this chapter, the trapping potential forms a harmonic oscillator. For a classical harmonic oscillator, the resonant frequency is given by $\omega = \sqrt{k/m}$. This allows us to calculate the relative change in mass based on the trapping frequency as:

$$\sqrt{\frac{m_2}{m_1}} = \frac{\omega_1}{\omega_2}. \tag{3.4.1}$$

The mass in the case where all three ions are bright is $m_1 = 3m_{\mathrm{Yb}} \approx 3 \cdot 171\,\mathrm{u}$, while for the case where one molecule is present it is $m_2 = 3m_{\mathrm{Yb}} + M$. The additional mass was therefore $M = 17.5(3)\,\mathrm{u}$, where u is the unit of atomic mass. The atomic mass of oxygen is 16 u, and the atomic mass of hydrogen is 1 u. A candidate for a molecule therefore would be one oxygen and one hydrogen atom. Water contributes to the residual gas pressure and could be a candidate for a chemical reaction. It is known that reactions with water molecules can occur [61]. The additional molecule would therefore have a weight of 17 u. During lab operation, dark states occurred several times in an ion crystal. The trap frequency was not measured at each event, but when it was measured the change in trap frequency was found. Measuring the trap frequency by applying an AC electric field requires the removal of filters in the trapping setup and therefore takes some time. Thus, states recovered within a few minutes are difficult to identify using the method of resonant excitation of the ion motion in the trap.

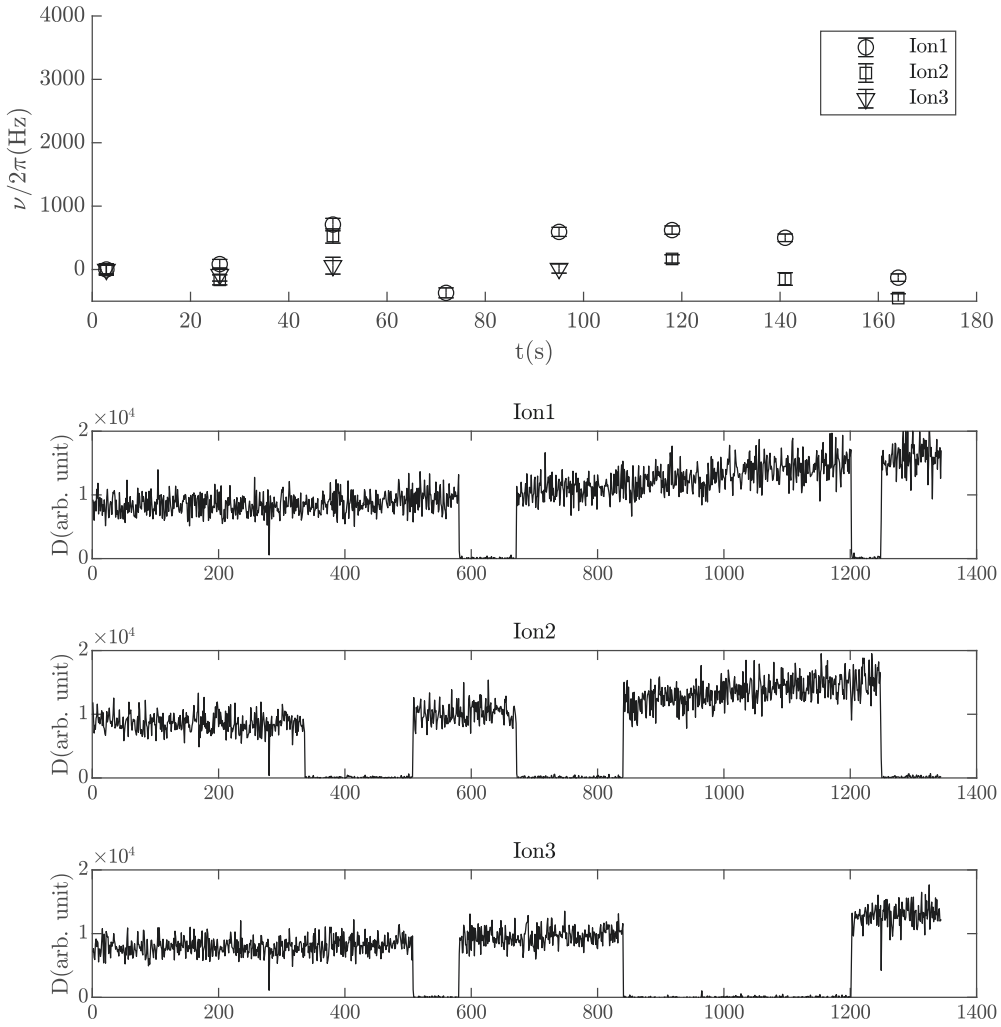

Figure 3.4.1: (Top) Addressing frequencies ν of three ions during a J-coupling measurement that was discarded due to an ion going dark. An ion has gone dark but reappears later, the frequency offsets are removed here for clarity. (Bottom three) Doppler cooling fluorescence D. The scale on the horizontal axis corresponds to measurement cycles. The horizontal axis can be associated with a time due to the fixed cycle duration. At time $t \approx 45\,\mathrm{s}$ ion 2 went dark, indicated by the first drop of Doppler cooling fluorescence. At this time, the Doppler cooling fluorescence stabilization described in section 2.8.3 tries to stabilize the overall Doppler cooling fluorescence, so the Doppler cooling fluorescence of the bright ions increases until the end of the experiment. At time $t \approx 65\,\mathrm{s}$ the dark ion jumps from site 2 to site 3, indicated by the drop of the fluorescence at site 3 while the fluorescence at site 2 recovers. At time $t \approx 75\,\mathrm{s}$ the dark ion jumps from site 3 to site 1. A total of seven jumps occur during 100 s. Jumps from location 3 to 1 indicate a random resorting of the ion crystal.

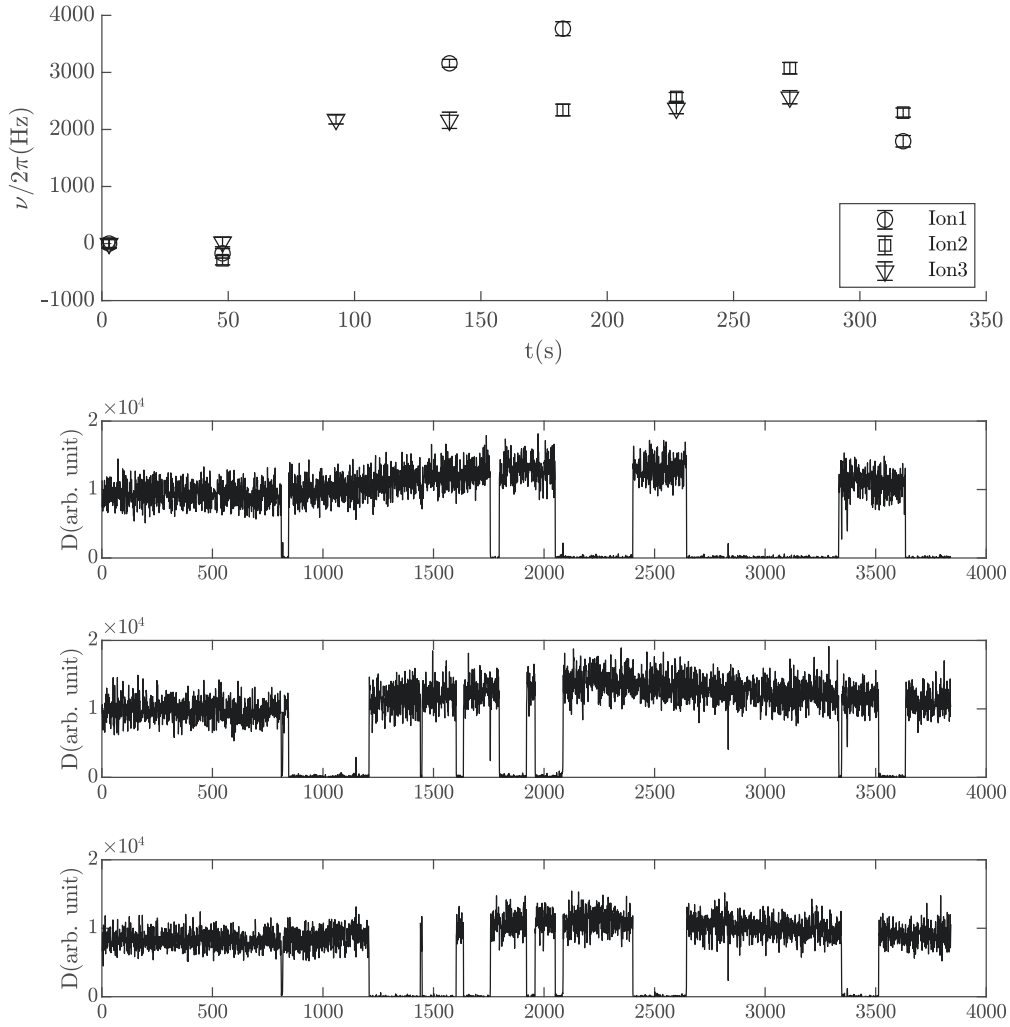

Figure 3.4.2: (Top) Addressing frequencies ν of three ions during a Rabi frequency calibration that was discarded due to an ion going dark. An ion has gone dark at this time, the measured addressing frequencies change. The dark ion remained dark after this experiment was completed. The frequency offsets of the addressing frequencies ν are removed for clarity at $t = 0$. (Bottom three) Doppler cooling fluorescence D. The scale on the horizontal axis corresponds to measurement cycles. The horizontal axis can be associated with a time due to the fixed cycle duration. At time $t \approx 70\,\mathrm{s}$ ion 1 went dark, indicated by the first drop of Doppler cooling fluorescence. At this time, the fluorescence stabilization described in section 2.8.3 attempts to stabilize the overall Doppler cooling fluorescence, so that the Doppler cooling fluorescence of the bright ions increases. At time $t \approx 72\,\mathrm{s}$ the dark ion jumps from site 1 to site 2, indicated by the drop in fluorescence at site 2 while the fluorescence at site 1 recovers. At time $t \approx 100\,\mathrm{s}$ the dark ion jumps from site 2 to site 3. A total of 16 jumps occur during 270 s. Jumps from site 1 to 3, as they occur at $t \approx 210\,\mathrm{s}$, indicate a random repositioning of the ion crystal. The trap frequency in this case changed from $\omega_z = 2\pi \cdot 104.55(2)\,\mathrm{kHz}$ to $\omega_z' = 2\pi \cdot 102.82(2)\,\mathrm{kHz}$, measured by resonant excitation of the ions motion in the trap. The change in ω_z indicates an additional mass of 16.5 u. A jump in the resonance frequency indicates the presence of an additional mass.

From this observation, a strategy can be derived for when it is necessary to reload the ion crystal. If at an instance where an ion enters a dark state, the addressing frequencies of the other ions change significantly, a heavy molecule was formed, and it is necessary to reload the trap.

The trapping potential along the trapping axis is generated by electrostatic fields. Therefore, the electrostatic potential that defines the quadratic trapping potential does not depend on the mass of the trapped particles, but only on their charge.

The effective radial potential depends on the mass of the trapped charged particle. Adding mass to the trapped ions will therefore weaken the radial confinement. An electric field present in the presence of imperfect micromotion compensation will consequently shift the position of the center of mass of the ion string, resulting in an observable change in the resonance frequency of the visible ions.

3.5 Background gas collisions

Background gas collisions create dark states within an ion crystal. A collision, even if there is no chemical reaction and no transition to a dark state, corrupts the result of the quantum computation. In this subsection, the collision rate with background gas is estimated and an error rate is derived.

Once a dark ion is trapped in a string of bright ions, different configurations of the ion crystal become distinguishable from the camera image and can therefore be used to calculate the rate of background gas collisions. A collision with a background gas is necessary to change the crystal configuration, as shown in fig. 3.4.2 and fig. 3.4.1. The rate of rearrangement of the ion crystal can be used to infer the rate at which collisions occur [62]. After a collision with a background gas at room temperature of 300 K, it is very likely that the new configuration of the ion crystal is random. In the publication by Hankin [62], background gas temperatures of $O(10\,\mathrm{K})$ are sufficient to induce a change in the ion string configuration. For this example with $n = 3$ ions, there are $3! = 6$ possibilities for the crystal to rearrange. Two of them, the exchange of the two bright ion positions, would not be visible when observing the Doppler cooling fluorescence. Both ions would still appear bright. If the configuration does not change during the collision, no event will be detected.

Given an ion crystal of size n with one dark ion, $n-1$ different reconfigurations of the ion string can be detected using the Doppler cooling fluorescence. The configuration of the bright ions cannot be detected in such a way that there are $(n-1)!$ cases that look the same. The total number of possible configurations is $n!$, and therefore the real collision rate can be calculated as

$$\frac{\Gamma_O}{\Gamma} = \frac{(n-1)[(n-1)!]}{n!} = \frac{n-1}{n}, \tag{3.5.1}$$

where Γ is the rate of collisions that change the ion-string configuration, while Γ_O is the rate of observed reconfigurations. For the current setup it follows that the real collision rate is about 3/2 times larger than the observed reconfiguration rate Γ_O. From the measurements presented here, an observed collision rate of $\Gamma_O \approx 7 \cdot 10^{-2}\,\mathrm{s}^{-1}$ can be estimated. The real collision rate is therefore about $\Gamma \approx 1.05 \cdot 10^{-1}\,\mathrm{s}^{-1}$.

Each collision with background gas destroys the quantum information stored in the register and reorders the qubits. If a collision occurs during the execution of a quantum algorithm, an unrecoverable error will occur. In the current setup, for a three ion gate such as the Toffoli gate described in chapter 5 with a run time of $T \approx 17\,\mathrm{ms}$ with the possibility $P_{col} = \Gamma T \approx 1.7 \cdot 10^{-3}$ an irrecoverable error might occur. The probability of a background gas collision scales with the number of qubits in the register. The collision rate per qubit for the current setup is therefore $\Gamma_n = \Gamma/n \approx 0.3 \cdot 10^{-1}\,\mathrm{s}^{-1}$. In a larger qubit register, it does not matter which qubit is hit by a background gas particle, and the current computation will be spoiled.

3.6 Summary

A Paul trap, as used in this work, allows the study of single atoms in isolation from their environment. The confinement of the $^{171}Yb^{+}$ ion by electrostatic fields, the applied magnetic field gradient and the susceptibility of the confined atom to the magnetic field, allow the remarkable results presented in this chapter.

All of these properties are necessary to operate as a MAGIC quantum computer reliably. What is a challenge for quantum computing is an opportunity for demonstrating the sensing of tiny electric forces.

In this chapter it is demonstrated how to detect DC magnetic fields on the scale of nT and to measure the COM position of an ion on the order of 0.1 nm.

These results were obtained using a single $^{171}Yb^{+}$ ion stored in a linear Paul trap and subjected to a magnetic field gradient while the wavelength of the RF control field exceeded the error in the ion position by a factor of $5 \cdot 10^{-9}$, making it the best relative wavelength resolution reported. Combined with the confinement of the $^{171}Yb^{+}$ ion in the trapping potential, a force on the order of 10^{-23} N can be resolved. This technique may pave the way for future scanning probe microscopy using the most miniature probe imaginable, a single ion.

Applied to the MAGIC quantum computer, observing the resonance frequency of the ion also allows diagnosis of the axial trapping potential. In the current setup, the axial trap frequency ω_z is stable on the order of 10^{-4} during a day of lab operation. Assuming a perfectly stable magnetic field gradient, the stability of the J coupling is estimated to be on the order of 10^{-4}.

Furthermore, it was shown how the resonance frequency of the qubits in a register allows an indirect observation of the mass of an ion in the dark state. In future trapped-ion quantum computers, this technique will allow the diagnosis of a quantum register. It allows us to decide if a heavy molecule has formed or if a re-pumping scheme can be applied. This may be important in future multi-species trapped ion quantum computers for diagnosing qubits that are never exposed to laser light.

In addition, a collision rate of ions and background gas in the vacuum recipient was measured by observing the Doppler cooling fluorescence. The collision rate per qubit for the current setup is found to be $\Gamma_n = \Gamma/n \approx 0.3 \cdot 10^{-1}\,\mathrm{s}^{-1}$.

4

Tuning the qubit-qubit interaction

The inherent always-on all-to-all connectivity provided by the MAGIC scheme is a powerful tool for implementing multi-qubit quantum logic operations. It is present whether or not it is desired. The challenge is to use this feature in a desired quantum circuit efficiently. A linear string of trapped ions, confined in a linear Paul trap, can be seen as a quantum memory or quantum processor. Each ion may serve as a memory or processor qubit, depending on the hyperfine level chosen. This flexibility has been shown in the Ph.D. thesis of Christian Piltz [37] and Theeraphot Sriarunothai [9]. A set of bits storing information is called a register in the classical information science context. Since each qubit may be used as memory, a linear ion string is called a quantum register.

A quantum circuit may operate on a register to implement the desired operation. Within such a circuit, single-qubit and multi-qubit gates need to be performed. Individual addressing of the qubits must be possible to carry out single qubit gates. Implementing multi-qubit gates having the always-on coupling comes with the challenge of the inherent coupling of the system as shown in eq. (2.3.3) possibly not matching the interaction required to implement the desired gate.

To implement desired conditional gates on computing qubits in a register, it is necessary to control the coupling of the qubits. For that purpose, different techniques can be applied:

(A) Controlling atomic states to selectively couple [38],

(B) Controlling the trapping potential [63],

(C) Controlling the magnetic field gradient dynamically [64],

(D) Controlling the coupling dynamically [32].

(A) Different atomic levels can be chosen and individually addressed to selectively couple the qubits within a register, selecting whether or not a Zeeman shift is present. The atomic state $|^2S_{1/2}, F = 1, m_F = 1\rangle = |1\rangle$ undergoes a linear Zeeman shift and therefore couples with other qubits present, whereas the atomic state $|^2S_{1/2}, F = 1, m_F = 0\rangle = |1'\rangle$ does not undergo a Zeeman shift and therefore qubits in this memory state do not couple with other qubits. Depending on the chosen atomic state a qubit participates in the coupling or not. Changing the qubit's state from $|1\rangle$ to $|1'\rangle$ or vice versa requires the application of three π-pulses on the qubit, using different RF transitions. This is called recode operation [65]. It must be pointed out that this technique removes the target's qubits coupling to all other ions in a register. Recoding all qubits in a register but two allows an arbitrary coupling to be generated by pairwise step-by-step coupling. Each pairwise coupling is represented by an entry in the coupling matrix and therefore, it would require $(N^2 - N)/2$ steps to synthesize an arbitrary coupling, where N is the number of qubits in the register.

(B) For example, controlling the axial confining potential in a segmented linear ion trap allows us to tailor the interaction strength [63]. Due to the distance of the electrodes, very high voltages might be required to achieve the desired coupling. Therefore, the possible implementable couplings are limited predominantly to local interactions between neighboring ions. In parallel to this work, this method is investigated by Florian Köppen. Details for this approach will be found in his Ph.D. thesis.

(C) Dynamically controlling the gradient present in the setup requires a coil to generate a tunable magnetic field gradient. Due to the distance between the ion and the coil compared to register size, the generated magnetic field gradient can be seen as global. Therefore only global control can be achieved.

(D) The dynamical approach to controlling the qubits' coupling relies on a periodic inversion of the qubit's state. It is carried out by applying local π pulses to the qubits. Using this procedure, the qubits stay in a magnetic sensitive level all the time, so the coupling between all qubits in the register is present. The interaction between two qubits can be interpreted in the single qubit reference frame as a detuning based on the state of the other qubit. Its magnitude is given by the absolute value of the coupling and its direction is given by the σ_z eigenvalue of the other qubit.

The techniques mentioned will most likely be used in a future quantum processor to achieve

an optimized control of the coupling of the qubits. The trap here features a permanent magnetic field gradient and a constant effective trapping potential, ruling out the dynamical control of the magnetic field gradient and the axial trapping potential.

This chapter describes a trapping hardware-independent approach that shapes the coupling topology J_{ij} as introduced in eq. (2.3.1), using timed Dynamical Decoupling (DD) sequences. First, the principle of dephasing and the usage of pulsed dynamical decoupling will be discussed. To introduce these concepts, I will orient myself on the Ph.D. thesis of Christan Piltz, who worked on the same experiment before [8]. This principle will be expanded later to allow tuning the effective coupling while protecting the qubits from dephasing. It will explain how a dynamical decoupling sequence can be adapted to match a specific noise spectrum in the lab and how an arbitrary global $\sigma_z\sigma_z$ interaction on the whole register can be implemented. Later, an extended principle is introduced that allows partitioning a quantum register in multiple subregisters, while the coupling can be tuned within these subregisters.

In the following chapters, this technique is then used to implement a Toffoli gate (chapter 5) or a Perceptron gate (chapter 6).

4.1 Pulsed dynamical decoupling sequences

Let us consider a qubit's quantum state. For one qubit, the state can be described as a Bloch vector, as shown in fig. 2.3.1. The quantum information itself is encoded into this Bloch vector's position on the Bloch sphere's surface, where the two angles θ and ϕ contain the information. The angle θ determines the excitation probability of the qubit in the computational basis $\{|0\rangle, |1\rangle\}$. This excitation probability is accessible in the experimental setup, when a projective measurement is performed, as introduced in section 2.5.5. The information encoded in θ is long-lived and is referred to as coherence time T_1 in literature. The coherence time T_2^* describes the decay of the information encoded in ϕ. Extending the coherence time T_2^* is crucial to allow for deeper quantum circuits and therefore this chapter describes how to extend the coherence time using pulsed dynamical decoupling.

Ultimately, for each experiment described in this thesis, the quantum state is projected in the z- basis $\{|0\rangle, |1\rangle\}$. If a qubits state shall be quantified in another basis, this basis has

to be rotated to the z-basis before readout. The definitions of frequency and phase depend on the exact reference frame chosen. For the following, a specific choice of the reference frame is helpful.

The reference frame of choice is the one that rotates with the assumed resonance frequency of the qubit's transition $|^2S_{1/2}, F = 1, m_F = 1\rangle \leftrightarrow |^2S_{1/2}, F = 0\rangle$ around the z-axis. This frequency is typically the frequency of the RF driving field. In this frame, the RF field applied can be seen as a static magnetic field pointing in a specific direction in the xy-plane of the Bloch sphere, defined by its phase ϕ. Phases occurring in this chapter are usually the phases in this reference frame. After preparation in the ground state $|0\rangle$, the first pulse applied to the qubit defines this frame. The description of RF pulses can be found in section 2.3.

To introduce the concept of decoherence, let us consider a single qubit in a superposition state, consisting of its ground state $|0\rangle$ and excited state $|1\rangle$. Let the quantum state be

$$|\psi\rangle = c_0|0\rangle + c_1|1\rangle, \tag{4.1.1}$$

where the coefficients c_0,c_1 are complex and obey $1 = \sqrt{|c_0|^2 + |c_1|^2}$. Here, $P = |c_1|^2$ is the probability of finding the qubit in state $|1\rangle$.

Once the qubit is excited, its excitation will decay in a time corresponding to a coherence time T_1. For $^{171}\mathrm{Yb}^+$ it is recently reported to exceed 3.3 h [66], using a dynamical decoupling scheme. This long time T_1 can be considered infinite for practical applications.

In addition to the z-axis, quantum information is stored in the xy-plane in the Bloch picture. It can be described as the phase ϕ of a qubits state. The decay of quantum information in xy-plane is associated with the coherence time T_2^*. In the following, it is assumed that the reference frame is co-rotating with the unperturbed ions resonance frequency, such that without a perturbation, the Bloch vector stays at rest. Changes in the ion's resonance lead to a frequency mismatch of the chosen rotating frame and the ion's spin. Let us assume, a time-dependent mismatch of the frequency of the rotating frame co-rotating with the RF field and the qubits resonance $\delta(t)$ exists. The Hamiltonian describing the system is

$$H_{ph} = \frac{\hbar}{2}\delta(t)\sigma_z. \tag{4.1.2}$$

This Hamiltonian induces the unitary evolution from time t_0 to time t_1

$$U_{ph}(t,t_0) = e^{-i\frac{1}{\hbar}\int_{t_0}^{t} H_{ph}(t')\mathrm{d}t'}. \tag{4.1.3}$$

If this unitary is applied to a state, the state will acquire a phase

$$U_{ph}(t,t_0)|\psi_0\rangle = |\psi\rangle = c_0 e^{i\phi(t,t_0)}|0\rangle + c_1 e^{-i\phi(t,t_0)}|1\rangle, \tag{4.1.4}$$

where $|\psi_0\rangle$ is given by equation (4.1.1) and

$$\phi(t,t_0) = \frac{1}{2}\int_{t_0}^{t} \delta(t')\mathrm{d}t'. \tag{4.1.5}$$

Given an unknown random frequency mismatch $\delta(t)$, the quantum state acquires an unknown phase over time. To compensate for this phase, a spin echo pulse can be introduced. If, during the unitary evolution from time t_0 to t_2, a π-pulse is inserted at time t_1, then the evolution can be written as follows:

$$\begin{aligned} U'_{ph}(t_2,t_0) &= U_{ph}(t_2,t_1) i\sigma_x U_{ph}(t_1,t_0) && (4.1.6)\\ &= e^{-i\frac{1}{\hbar}\int_{t_1}^{t_2} H_{ph}(t')\mathrm{d}t'} i\sigma_x e^{-i\frac{1}{\hbar}\int_{t_0}^{t_1} H_{ph}(t')\mathrm{d}t'} \\ &= e^{-i\frac{1}{2}\int_{t_1}^{t_2} \delta(t')\sigma_z\mathrm{d}t'} i\sigma_x e^{-i\frac{1}{2}\int_{t_0}^{t_1} \delta(t')\sigma_z\mathrm{d}t'} \\ &= e^{-i\phi(t_2,t_1)\sigma_z} i\sigma_x e^{-i\phi(t_1,t_0)\sigma_z} \\ &= e^{-i[\phi(t_2,t_1)-\phi(t_1,t_0)]\sigma_z}(-i\sigma_x). && (4.1.7) \end{aligned}$$

Now the properties of the Pauli matrices can be used:

$$\sigma_x\sigma_z = -\sigma_z\sigma_x, \qquad \sigma_y\sigma_z = -\sigma_z\sigma_y, \tag{4.1.8}$$

$$e^{i\frac{\theta}{2}\vec{n}\vec{\sigma}} = \mathbb{1}\cos\left(\frac{\theta}{2}\right) + i\left(n_x\sigma_x + n_y\sigma_y + n_z\sigma_z\right)\sin\left(\frac{\theta}{2}\right). \tag{4.1.9}$$

Here $|\vec{n}| = 1$ is the rotation axis in the Bloch picture and $\mathbb{1}$ is the identity operator [37]. Therefore, the phase is

$$\phi(t_2,t_0) = \phi(t_2,t_1) - \phi(t_1,t_0). \tag{4.1.10}$$

This result holds true, not only for π-pulses around the x axis σ_x , but for σ_y pulses as

well and therefore for each arbitrary π-pulse. A π-pulse with a phase α is defined as:

$$\pi_\alpha = \cos(\alpha)\sigma_x + \sin(\alpha)\sigma_y. \tag{4.1.11}$$

With this follows:

$$U_{ph}(t_2, t_1)\pi_\alpha U_{ph}(t_1, t_0) = e^{-i[\phi(t_2,t_1)-\phi(t_1,t_0)]\sigma_z}\pi_\alpha. \tag{4.1.12}$$

Assuming $\delta(t)$ is constant in time, the acquired phase vanishes, and the phase information is protected. The reappearance of coherence is referred to as a spin echo, while the pulse producing it is referred to as a spin echo pulse.

4.2 J-Tuning

4.2.1 Dynamical decoupling

As introduced in section 4.1, a single spin echo pulse is sufficient to compensate for a fixed frequency offset. If the frequency offset is a function of time, it is beneficial to introduce additional pulses, to reduce the free evolution time between them. Those pulses are called Dynamical Decoupling (DD) pulses. They are routinely used to protect quantum states and consist of a set of π-pulses. Figure 4.2.1 illustrates the timeline of a DD-sequence with π-pulses π_{α_n} at times t_{2n}. If the π-pulses of a DD-sequence are assumed to be instantaneous, the unitary evolution of a system can be seen as a product of unitaries, generated by stepwise constant Hamiltonians and instantaneous π-pulses π_{α_n}. The total time evolution is given by a product of several instances of eq. (4.1.12)

$$\begin{aligned} U &= \prod_{n=1}^{N} U(t_{2n+1}, t_{2n})\pi_{\alpha_n} U(t_{2n}, t_{2n-1}) \\ &= \prod_{n=1}^{N} \left[e^{-i[\phi(t_{2n+1},t_{2n})-\phi(t_{2n},t_{2n-1})]\sigma_z}\pi_{\alpha_n} \right], \end{aligned} \tag{4.2.1}$$

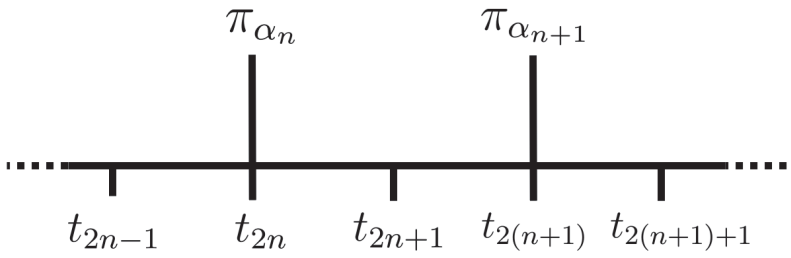

Figure 4.2.1: Illustration of the timeline of a Dynamical Decoupling sequence (DD-sequence), consisting of π-pulses with phase α_n at times t_{2n} as described in eq. (4.1.11). The vertical lines indicate the time when a π-pulse flips the qubits state. For the evolution of the quantum system, it is assumed that the π-pulses are instantaneous.

where we have used eq. (4.1.8). If a dynamical decoupling sequence fulfills the condition

$$\mathbb{1} = \prod_{n=1}^{N} \pi_{\alpha_n}, \tag{4.2.2}$$

the total phase acquired is

$$\Phi = \sum_{n=1}^{N} \phi(t_{2n+1}, t_{2n}) - \sum_{n=1}^{N} \phi(t_{2n}, t_{2n-1}). \tag{4.2.3}$$

Since the phases $\phi(t_{n+1}, t_n)$ are given by the integrated detuning in the time interval $[t_n, t_{n+1}]$, the acquired total phase Φ depends on $\delta(t)$. For a fixed detuning and a periodic DD-sequence, the acquired phase is $\Phi = 0$, if $\delta(t) = \text{const}$. The quantum state is therefore protected against constant detuning.

On the other hand, if the $\delta(t)$ has frequency components with $\nu = 2\pi/(t_{n+1} - t_n)$, it is resonant with the DD-sequence and the effect of the detuning is amplified. This susceptibility to specific noise components can be exploited to construct a quantum sensing device or it can spoil quantum computing. How to construct a magnetometer using this technique is shown by Ingo Baumgart [54]. At the same time, its effect during quantum computation is investigated in the Ph.D. Thesis of Theeraphot Sriarunothai [9].

4.2.2 Qubit-qubit interaction in the presence of a dynamical decoupling sequence

This subsection describes how a DD-sequence on multiple qubits can be used to couple qubits in a register selectively while the susceptibility of the quantum states to external noise is reduced. Let us consider a system of two qubits i and j. Each of those qubits can be described by a Hamiltonian of dimension $2 \cdot 2$, if its motional excitation and other atomic levels are neglected. Similar to the case of a single qubit, the unitary operator generating the time evolution of a n qubit system can be the exponential of the Hamiltonian, describing the system if it is time-independent.

A freely evolving system of a pair of interacting qubits generates the unitary evolution:

$$U_{J_{ij}}(\tau) = e^{-\frac{i}{2} J_{ij} \sigma_z^{(i)} \otimes \sigma_z^{(j)} \tau}, \tag{4.2.4}$$

where J_{ij} is the coupling constant between qubit i and qubit j. A π-pulse applied to the i-th qubit can be written as $\pi_\alpha^{(i)}$. To match the dimension of the Hilbert space, on which the operator acts, it is appropriatly tensored with the unity operation. As an example, π-pulses acting on a system of two qubits are

$$\begin{aligned} \pi_\alpha^{(i)} &= \pi_\alpha \otimes \mathbb{1}, \\ \pi_\alpha^{(j)} &= \mathbb{1} \otimes \pi_\alpha. \end{aligned} \tag{4.2.5}$$

Here $^{(i)}$ denotes the first qubit in a set of two while $^{(j)}$ is the second qubit on which the pulse is applied. If now a π-pulse is applied to qubit i, using eq. (4.1.8), the sign of the coupling is changed such that:

$$\begin{aligned} \pi_\alpha^{(i)} U_{J_{ij}}(\tau) &= (\pi_\alpha \otimes \mathbb{1}) e^{-\frac{i}{2} J_{ij} \sigma_z^{(i)} \otimes \sigma_z^{(j)} \tau} \\ &= e^{\frac{i}{2} J_{ij} \sigma_z^{(i)} \otimes \sigma_z^{(j)} \tau} (\pi_\alpha \otimes \mathbb{1}) \\ &= U_{-J_{ij}}(\tau)(\pi_\alpha \otimes \mathbb{1}) \\ &= U_{-J_{ij}}(\tau) \pi_\alpha^{(i)}. \end{aligned} \tag{4.2.6}$$

This can be interpreted as a reversal of the direction of evolution:

$$U_{J_{ij}}(-\tau) = U_{-J_{ij}}(\tau) = U^{\dagger}_{J_{ij}}(\tau). \tag{4.2.7}$$

If a π-pulse is applied to the second qubit, the previous argument can be applied again:

$$\pi^{(j)}_{\alpha} U_{J_{ij}}(\tau) = U_{-J_{ij}}(\tau)\pi^{(j)}_{\alpha}. \tag{4.2.8}$$

Accordingly, applying two π- pulses alters the coupling J_{ij} twice and therefore the coupling is preserved such that:

$$\begin{aligned}(\pi^{(i)}_{\alpha} \otimes \pi^{(j)}_{\beta}) U_{J_{ij}}(\tau) &= (\pi^{(i)}_{\alpha} \otimes \pi^{(j)}_{\beta}) e^{-\frac{i}{2} J_{ij} \sigma^{(i)}_z \otimes \sigma^{(j)}_z} \\ &= e^{-\frac{i}{2} J_{ij} \sigma^{(i)}_z \otimes \sigma^{(j)}_z} (\pi^{(i)}_{\alpha} \otimes \pi^{(j)}_{\beta}) \\ &= U_{J_{ij}}(\tau)(\pi^{(i)}_{\alpha} \otimes \pi^{(j)}_{\beta}).\end{aligned} \tag{4.2.9}$$

This is used when a DD-sequence is applied to a system of two qubits. A synchronous DD-sequence therefore protects the addressed qubits from noise, while their interaction is conserved. Thus, this principle allows the implementation of conditional qubit dynamics at a time scale longer than the system's unprotected coherence time T_2^*.

An interesting result is that the phases of the π-pulse in the DD sequence are arbitrary. Especially during conditional evolution, applying the DD-pulses with the same phase to all qubits is not necessary. Later on in this thesis, this is used to implement the Toffoli (chapter 5) and the Perceptron gate (chapter 6).

4.2.3 Multi-qubit coupling and dynamical decoupling

The Hamiltonian describing the interaction of the qubit eq. (2.3.1) contains the sum of tensor products $\sigma_z \otimes \sigma_z$ acting on different qubits. The unitary evolution operator is:

$$U_J(\tau) = e^{-\frac{i}{2} \sum_{i<j} J_{ij} \sigma^{(i)}_z \otimes \sigma^{(j)}_z \tau}. \tag{4.2.10}$$

Next the Baker-Campbell-Haussdorf identity

$$e^{A+B} = e^A e^B e^{-[A,B]/2} \tag{4.2.11}$$

is used. Since the σ_z and $\mathbb{1}$ matrices commute, the unitary evolution of the interaction of the full system can be written as:

$$U_J(\tau) = e^{-\frac{i}{2}\sum_{i<j} J_{ij}\sigma_z^{(i)}\otimes\sigma_z^{(j)}\tau} = \prod_{i<j} e^{-\frac{i}{2}J_{ij}\sigma_z^{(i)}\otimes\sigma_z^{(j)}\tau} = \prod_{i<j} U_{J_{ij}}(\tau). \tag{4.2.12}$$

Analogous to the previous argument, a π-pulse applied to qubit k changes the sign of J_{kj} and J_{ik} . For simplicity, the time argument of the unitary evolution and the tensor products with the $\mathbb{1}$ operator are dropped here. A π-pulse applied to qubit k in a register of qubits can be written as:

$$\pi_\alpha^{(k)} \prod_{i<j} U_{J_{ij}} = \prod_{\substack{i<j \\ j,i\neq k}} \left[U_{J_{ij}}\right] \prod_{\substack{i<j \\ i=k}} \left[U_{-J_{ij}}\right] \prod_{\substack{i<j \\ j=k}} \left[U_{-J_{ij}}\right] \pi_\alpha^{(k)}. \tag{4.2.13}$$

Here it is used that all unitary operators $U_{J_{ij}}$ are mapped to $U_{-J_{ij}}$ when a π pulse is applied to either qubit i or j. From this, several useful procedures can be derived. Using that $U_{-J_{ij}} = U_{J_{ij}}^\dagger$ and the unitary evolution of equal duration, the coupling between the k-th qubit and the rest is effectively canceled out:

$$\begin{aligned}\prod_{i<j}\left[U_{J_{ij}}\right]\pi_\alpha^{(k)}\prod_{i<j}\left[U_{J_{ij}}\right] &= \prod_{\substack{i<j \\ j,i\neq k}}\left[U_{J_{ij}}\right]\prod_{\substack{i<j \\ i=k}}\left[U_{J_{ij}}\right]\prod_{\substack{i<j \\ j=k}}\left[U_{J_{ij}}\right]\prod_{\substack{i<j \\ j,i\neq k}}\left[U_{J_{ij}}\right]\prod_{\substack{i<j \\ i=k}}\left[U_{J_{ij}}^\dagger\right]\prod_{\substack{i<j \\ j=k}}\left[U_{J_{ij}}^\dagger\right]\pi_\alpha^{(k)} \\ &= \prod_{\substack{i<j \\ j,i\neq k}}\left[U_{J_{ij}}\right]\prod_{\substack{i<j \\ j,i\neq k}}\left[U_{J_{ij}}\right]\pi_\alpha^{(k)}.\end{aligned} \tag{4.2.14}$$

The remaining qubits interact, while the addressed qubit is removed from the interaction. It has been used that all occurring unitaries except π_α on different qubits $k \neq n$ only contain σ_z and $\mathbb{1}$ operators and therefore commute.

If now two π-pulses are applied simultaneously on different qubits, the unitary evolution transforms as:

$$\begin{aligned}\pi_\alpha^{(k)}\pi_\beta^{(n)}\prod_{i<j}\left[U_{J_{ij}}\right] &= \pi_\beta^{(n)}\prod_{\substack{i<j \\ j,i\neq k}}\left[U_{J_{ij}}\right]\prod_{\substack{i<j \\ i=k}}\left[U_{J_{ij}}^\dagger\right]\prod_{\substack{i<j \\ j=k}}\left[U_{J_{ij}}^\dagger\right]\pi_\alpha^{(k)} \\ &= \prod_{\substack{i<j \\ j,i\neq k,n}}\left[U_{J_{ij}}\right]\prod_{\substack{i<j \\ i=k \\ j\neq n}}\left[U_{J_{ij}}^\dagger\right]\prod_{\substack{i<j \\ j=k \\ j\neq n}}\left[U_{J_{ij}}^\dagger\right]\prod_{\substack{i<j \\ i=n \\ j\neq k}}\left[U_{J_{ij}}^\dagger\right]\prod_{\substack{i<j \\ j=n \\ j\neq k}}\left[U_{J_{ij}}^\dagger\right]U_{J_{kn}}\pi_\alpha^{(k)}\pi_\beta^{(n)}.\end{aligned} \tag{4.2.15}$$

Accordingly it follows for two π-pulses applied to qubits $n \neq k$ that:

$$\prod_{i<j} \left[U_{J_{ij}}\right] \pi_\alpha^{(k)} \pi_\beta^{(n)} \prod_{i<j} \left[U_{J_{ij}}\right] = \underbrace{\prod_{\substack{i<j \\ j,i\neq k,n}} \left[U_{J_{ij}}\right] \prod_{\substack{i<j \\ j,i\neq k,n}} \left[U_{J_{ij}}\right]}_{(a)} \underbrace{U_{J_{kn}}}_{(b)} \pi_\alpha^{(k)} \pi_\beta^{(n)}. \tag{4.2.16}$$

This is a significant result. It shows that using two simultaneous π-pulses on two different qubits allows these two qubits to couple (b), while the interaction between these two qubits with the others is removed. The important part is that all the other qubits still interact (a). This example is the most straightforward way to create two separate interacting subsets of qubits in a register that do not interact. This enables a single register to operate two different conditional unitaries at the same time. An example could be the parallel execution of two CNOT operations on a register containing four qubits. The required CZZ operation is shown in fig. 4.2.9.

4.2.4 Asynchronous dynamical decoupling

Until now, only synchronous π-pulses are considered. For simplicity, let's assume a system of two qubits coupled with J_{ij}. The total evolution time T consists of three times τ_a, τ_b and τ_c such that $T = \tau_a + \tau_b + \tau_c$. The time τ_a is the arrival time of the π-pulse on qubit i, τ_b is the time between the π-pulse on qubit i and qubit j and time τ_c is the time after the π-pulse on qubit j arrives until T. The arrival times of π-pulses are illustrated in fig. 4.2.2.

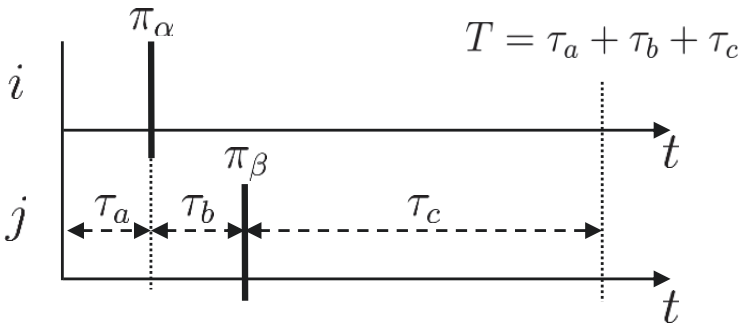

(a)

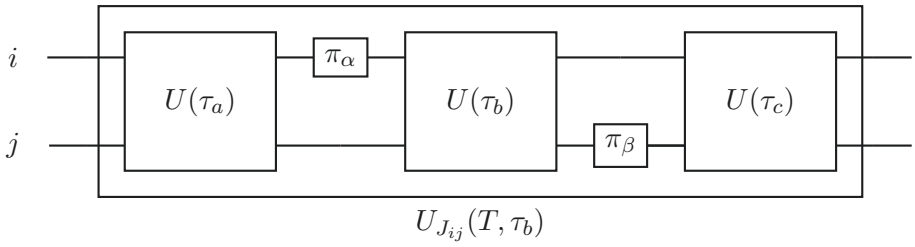

(b)

Figure 4.2.2: Illustration of pulse timings of π_α, π_β-pulses to implement a desired effective J-coupling during the total evolution. The coupling is positive during time τ_a and τ_c, while it is negative during time τ_b. In this case the effective coupling is $J^{eff} = J(T - 2\tau_b)/T$. (a) Time line of pulses. (b) Circuit diagram showing the implementation of J^{eff}. During $U(\tau_a)$ and $U(\tau_c)$ the coupling is positive, while during $U(\tau_b)$ the coupling is negative.

The unitary evolution then is:

$$\begin{aligned} U_{J_{ij}}(\tau_c)\pi_\beta^{(i)}U_{J_{ij}}(\tau_b)\pi_\alpha^{(j)}U_{J_{ij}}(\tau_a) &= U_{J_{ij}}(\tau_c)U_{J_{ij}}(-\tau_b)\pi_\alpha^{(i)}\pi_\beta^{(j)}U_{J_{ij}}(\tau_a) \\ &= U_{J_{ij}}(\tau_c)U_{J_{ij}}(-\tau_b)U_{J_{ij}}(\tau_a)\pi_\alpha^{(i)}\pi_\beta^{(j)} \\ &= U_{J_{ij}}(\tau_a - \tau_b + \tau_c)\pi_\alpha^{(i)}\pi_\beta^{(j)} \\ &= U_{J_{ij}}(T - 2\tau_b)\pi_\alpha^{(i)}\pi_\beta^{(j)}. \end{aligned} \tag{4.2.17}$$

This is a remarkable result. The delay of the pulses with respect to each other can be arbitrarily chosen in a range $0 < \tau_b < T$ and the effective evolution time $T^{eff} = T - 2\tau_b$ can be selected from $-T < T^{eff} < T$. The total evolution time is fixed and therefore one can also think of an effective J coupling, which can be implemented as $-J_{ij} < J_{ij}^{eff} < J_{ij}$.

It follows that:

$$J_{ij}^{eff} = J_{ij}\left(\frac{T-2\tau_b}{T}\right). \tag{4.2.18}$$

During the execution of a quantum gate, usually a DD-sequence is used to protect the qubit's coherence. The simplest DD-sequence is a sequence of π-pulses with a fixed pulse interval. Assuming a periodic DD-sequence with n pulses, total evolution time T and pulse interval T/n, the previous argument can be used to construct the evolution during the full DD-sequence as:

$$\begin{aligned} U_{DD}(T) &= \prod_{k=1}^{n}\left[U_{J_{ij}}(\frac{T}{n}-2\tau_b)\pi_{\alpha_k}^{(i)}\pi_{\beta_k}^{(j)}\right] \\ &= \prod_{k=1}^{n}\left[U_{J_{ij}}(\frac{T}{n}-2\tau_b)\right]\underbrace{\prod_{k=1}^{n}\left[\pi_{\alpha_k}^{(i)}\right]}_{\mathbb{1}}\underbrace{\prod_{k=1}^{n}\left[\pi_{\beta_k}^{(j)}\right]}_{\mathbb{1}} \\ &= U_{J_{ij}}(T-2\tau_b n). \end{aligned} \tag{4.2.19}$$

It has been used that DD-sequences are designed so that the set of pulses is applied to form a unit operation. An example of such sequences is the $\mathrm{CPMG_{XY}}$ [67] sequence or the Universal Robust (UR) [68] pulse sequences, which are specifically designed to compensate for pulse errors. The result is independent of the phases of the applied π-pulses. Therefore it is possible to use a DD-sequence by proper choice of $\tau_{b_{ij}}$, to implement a conditional gate with an effective coupling. This result holds for each pair of qubits i and j in a larger register, where $\tau_{b_{ij}}$ is the time shift between the DD-pulses applied.

To demonstrate that the coupling strength can be chosen continuously in a range $-J < J^{eff} < J$, the couplings in a three ion crystal have been measured as a function of the delay time between dynamical decoupling sequences. To measure the coupling a Ramsey type experiment has been performed. The target qubit 2 has been prepared in an equal superposition state by applying a $\pi/2$-pulse followed by a free evolution time while the control qubits 1 and 3 couple to the target and in the end a $\pi/2$-pulse is applied. The experiment is repeated for different phases ϕ of the second $\pi/2$-pulse, and the excitation probability of the target qubit has been estimated. A sinusoidal has been fitted to the measured excitation probabilities and the phase is extracted. To determine the conditional

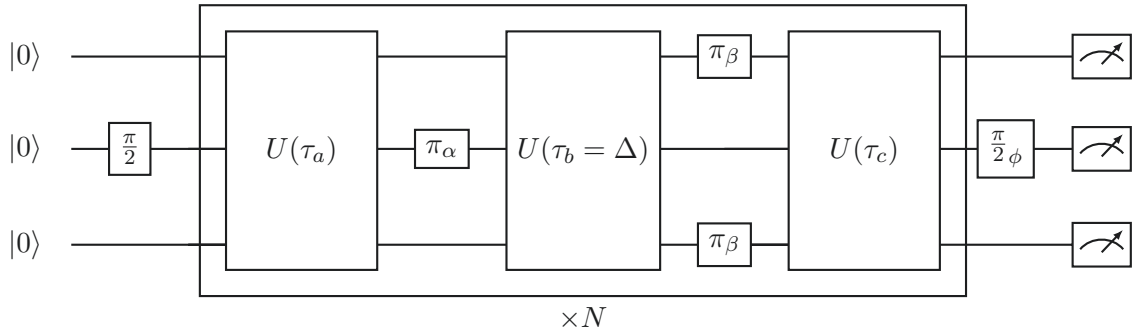

(a)

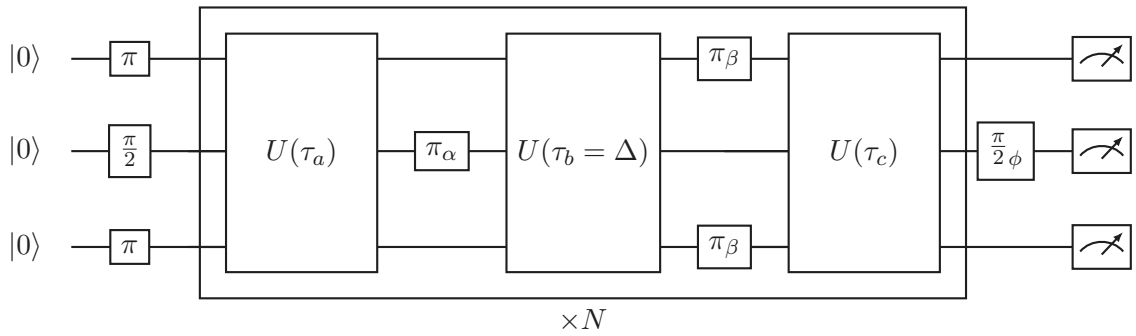

(b)

Figure 4.2.3: Ramsey type circuit to measure the tuned coupling strength of qubit 1 and 3 to qubit 2. Starting with all qubits initialized in state $|0\rangle$, qubit 2 is put into an superposition state. (a) During evolution the target qubit acquires a phase based on the control qubits state and the delay time Δ between the DD-pulses of qubit 1 and 3 with respect to qubit 2. The state of qubit 2 in the end is analyzed using a Ramsey readout pulse with a varying phase $\phi = [0..2\pi]$. The resulting excitation probability of qubit 2 as a function of ϕ is fitted with a sinusoidal and the phase from the fit is extracted. (b) Same as (a) but the control qubits are initialized in state $|1\rangle$. The difference of the measured qubits phase for case (a) and (b) are used to calculate the sum of the coupling between qubits 1 and 2 and 2 and 3.

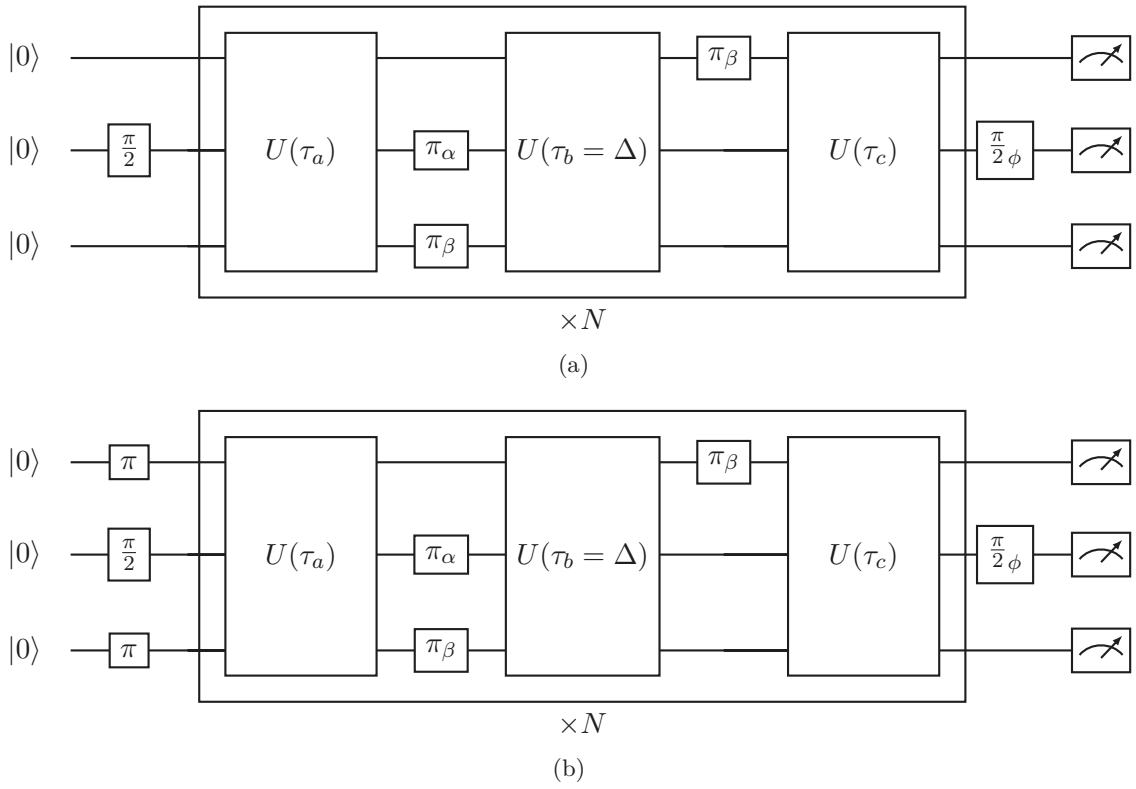

Figure 4.2.4: Ramsey type circuit to demonstrate individual tuning of the coupling strength between qubit 1 and 2. Starting with all qubits initialized in state $|0\rangle$, qubit 2 is put into an superposition state. (a) During evolution the target qubit acquires a phase based on the control qubits state and the delay time Δ between the DD-pulses of qubit 2 and 1. The state of qubit 2 in the end is analyzed using a Ramsey readout pulse with a varying phase $\phi = [0..2\pi]$. The resulting excitation probability of qubit two as a function of ϕ is fitted with a sinusoidal and the phase from the fit is extracted. (b) Same as (a) but the control qubits are initialized in state $|1\rangle$. The difference of the measured qubits phase for case (a) and (b) are used to calculate the sum of the coupling between qubits 1 and 2 and 2 and 3.

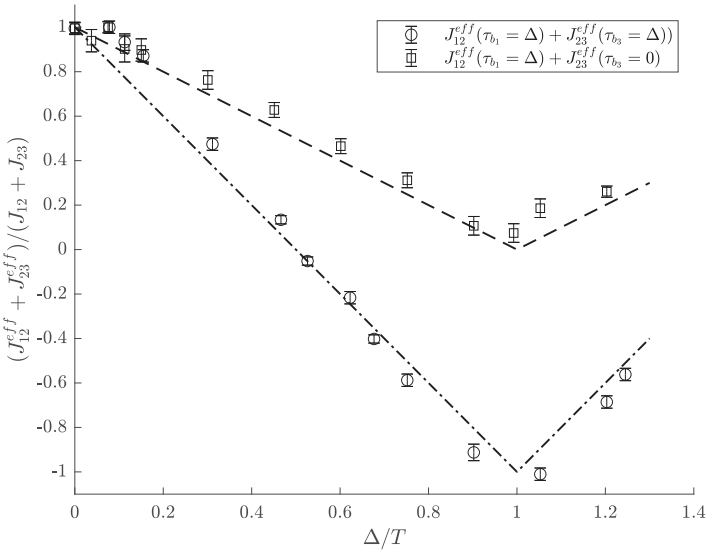

Figure 4.2.5: Here the capability of J-tuning to tune the couplings continuously is demonstrated by measurement of the total J coupling $J^{tot} = J_{12} + J_{23}$ in a three-ion crystal as a function of the delay time Δ in units of the DD-sequence period T see eq. (4.2.18). The delay between the DD-pulses of ion 1 and ion 2 is varied for the data indicated by squares, while the decoupling sequences between ion 2 and 3 are synchronous. The circuit describing this measurement is shown in fig. 4.2.4. The measurement data indicated by circles correspond to a scan of the simultaneous delay of ion 1 to 2 and ion 1 to 3. The corresponding measurement circuit is shown in fig. 4.2.3. The measured delay times exceed a full period of the DD-sequence indicated by the turning point. Following eq. (4.2.18), the dashed line is the theoretical assumption.

acquired phase shift $\delta\phi = (\phi_{|1\rangle} - \phi_{|0\rangle})$ due to the coupling after the total evolution time T_{tot}, the experiment is repeated with the control qubits being in state $|0\rangle$ and $|1\rangle$ respectively . The coupling then is $J = \delta\phi/2T_{tot}$. Figure 4.2.5 shows the measured couplings as a function of the delay time τ_b. To demonstrate the simultaneous tuning of couplings between qubit 1 and 2 and 2 and 3, the total coupling $J_{tot}^{eff} = J_{12}^{eff} + J_{23}^{eff}$ has been measured. For identical J-tuning between qubit's 1 and 2, and 2 and 3, the DD-sequences of qubit 1 and 3 have been delayed by the same time $\tau_b = \Delta$. For different J-tuning between qubits 1 and 2 and 2 and 3 only the DD-sequence of qubit one is delayed, such that the coupling of qubit 2 and 3 is kept constant wile the coupling between qubits 1 and 2 is tuned. Figure 4.2.4 and fig. 4.2.3 visualize the Ramsey-type experiment performed to measure the conditional phase shift of qubit 2.

Selecting the absolute arrival time of the DD-pulse on ion i to be $t = 0$, in a register of size N, $N-1$ times $\tau_{b_{ij}}$ can be chosen to tailor the coupling of qubit i to the qubits j. This allows for a column (row) wise tuning of J. The coupling matrix has N columns (rows) with zeros as diagonal elements. Another tool in the quantum toolbox is the selective re-coding of individual qubits in magnetic insensitive states. It removes the qubit's interaction with all other qubits. Expressed in terms of a J-coupling matrix, if qubit i is in an insensitive magnetic state, the coupling $J_{ij} = 0$. This gives rise to a procedure to stepwise tune the coupling.

The conditional phases can define a general controlled ZZ rotation Φ_{ij}, which shall be acquired by each qubit. The unitary is:

$$U_{phase} = e^{i\frac{1}{2}\sum_{i<j}\Phi_{ij}\sigma_z^{(i)}\sigma_z^{(j)}}. \tag{4.2.20}$$

Using the above-mentioned technique, one can construct a set of tuned effective J-couplings to generate the desired conditional phase rotations.

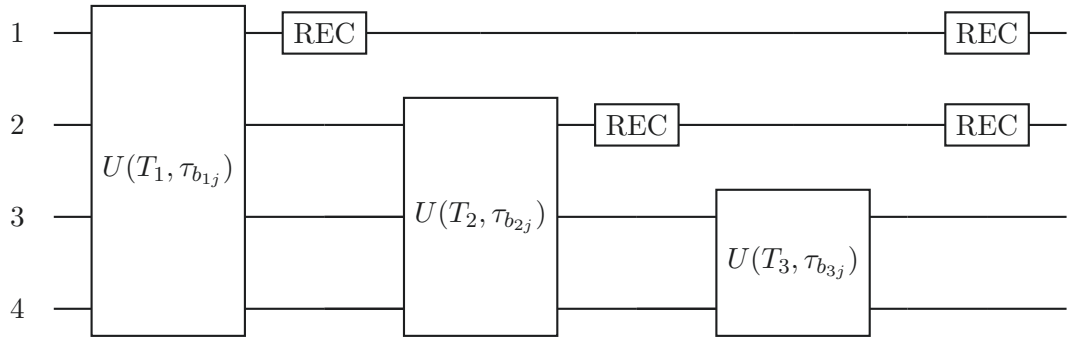

Figure 4.2.6: Example of an implementation of an arbitrary $CZZ(\Phi_{ij})$ gate on four qubits. During each unitary $U(T_i, \tau_{b_{ij}})$ with total evolution time T_i and delays $\tau_{b_{ij}}$ a DD-sequence is applied to implement the J-tuning. After each step, one qubit is removed from the interaction via recoding (REC). Finally, all qubits are recoded to the interacting qubit state. This allows to synthesize an arbitrary coupling between all qubits in a register of size $N = 4$ in $N - 1 = 3$ steps.

For example, in a register of size 4, The arbitrary coupling can be implemented as:

$$\Phi_{ij} = \underbrace{\begin{pmatrix} 0 & J_{12}^{eff} & J_{13}^{eff} & J_{14}^{eff} \\ & 0 & J_{23}^{appl} & J_{24}^{appl} \\ & & 0 & J_{34}^{appl} \\ & & & 0 \end{pmatrix}}_{J_1} T_1 + \underbrace{\begin{pmatrix} 0 & 0 & 0 & 0 \\ & 0 & J_{23}^{eff} & J_{24}^{eff} \\ & & 0 & J_{34}^{appl} \\ & & & 0 \end{pmatrix}}_{J_2} T_2 + \underbrace{\begin{pmatrix} 0 & 0 & 0 & 0 \\ & 0 & 0 & 0 \\ & & 0 & J_{34}^{eff} \\ & & & 0 \end{pmatrix}}_{J_3} T_3. \tag{4.2.21}$$

The implementation is shown in a circuit diagram in fig. 4.2.6. After the first step, in which the coupling of qubits 2, 3 and 4 to qubit 1 is generated, the first qubit is removed from the interaction, and the coupling of qubits 3 and 4 to qubit 2 is tuned. After this step, qubit 2 is also removed from the interaction by re-coding, and the final last step implements the conditional rotation of qubits 3 and 4. Therefore, this procedure allows tuning a given J-coupling matrix with $(N^2 - N)/2$ entries in $N - 1$ steps in any target CZZ gate. The direct approach to implement a CZZ gate would be its decomposition in one step per entry in the coupling matrix where, in each step, only the desired two qubits are interacting while all other qubits are re-coded in the magnetic insensitive state and therefore removed from the interaction. J-tuning improves the number of steps compared to the direct implementation by a factor of $N - 1$.

An example of a relevant coupling matrix is the one having an equal coupling between any pair of qubits. Figure 4.2.6 shows the according circuit diagram to implement a three-step J-tuning, while fig. 4.2.10(a) shows the J-coupling matrix measured following the procedure shown in fig. 4.2.7. Figure 4.2.10(c) Shows the first J-tuning step, fig. 4.2.11(a) shows the second and fig. 4.2.11(c) shows the third J-tuning step. In total, the tuned J-coupling matrix is shown in fig. 4.2.12 and achieves an equal effective coupling between all four qubits of the register with $J_{ij}^{eff} = 2\pi \cdot 30\,\mathrm{Hz}$.

Since arbitrary couplings within a register are a powerful tool to reduce the circuit depth of a quantum algorithm, J-tuning allows to reduce the overall run time. The example coupling shown here is arbitrarily chosen to be an equal coupling between all four qubits. It demonstrates the elaborate coupling mechanism of a MAGIC trapped-ion quantum computer.

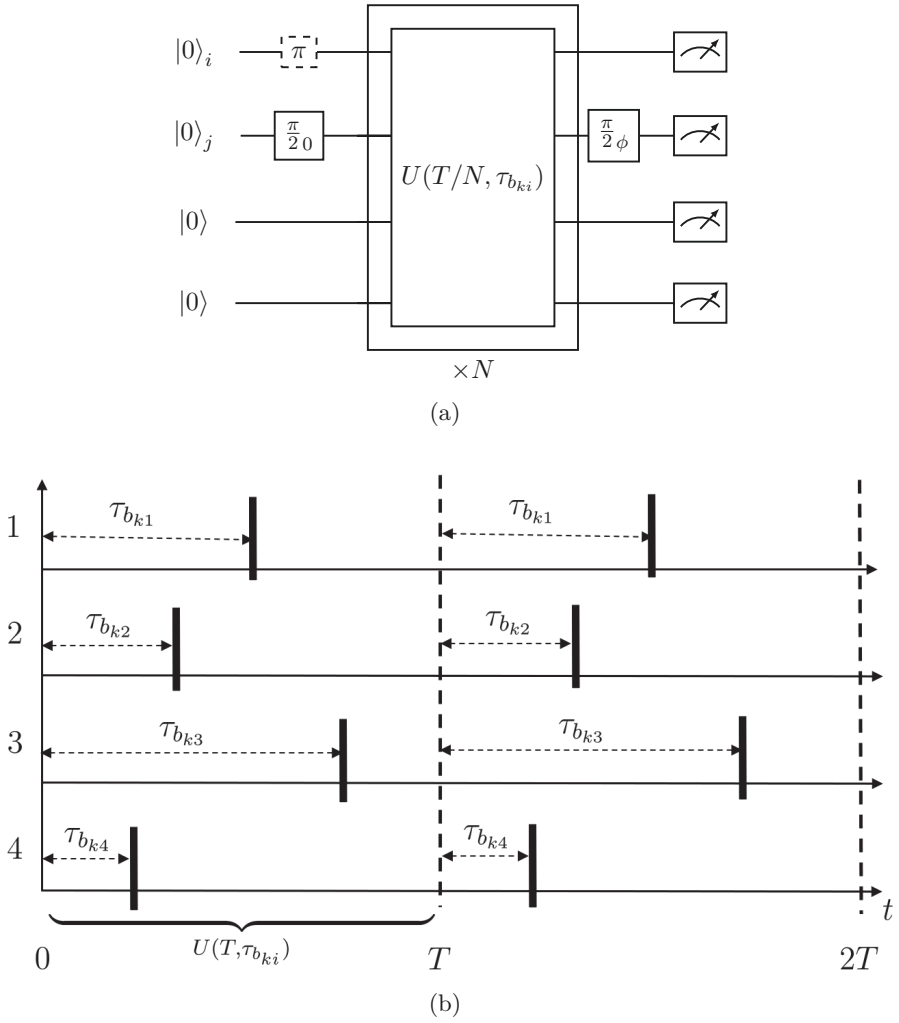

Figure 4.2.7: (a) Circuit diagram showing the measurement of tuned J-coupling matrices, where the target qubit j is prepared in an equal superposition state while the control qubit is prepared in state $|0\rangle_i$ or $|1\rangle_i$. After that, a unitary to tune the J-coupling is applied N times. During each repetition of $U(T/N, \tau_{b_{ki}})$ DD-pulses are applied at times defined by $\tau_{b_{ki}}$ as shown in (b). A readout pulse is applied to the target qubit j with varying phase ϕ. The excitation probability $P(\phi)$ of qubit j is analyzed, and a sinusoid is fitted. From the fit parameter, the phase φ is extracted. φ is a function of the prepared state of the control qubit i and therefore the coupling can be calculated as $J_{ij} = (\varphi(|1\rangle_i) - \varphi(|0\rangle_i))/(2T)$. Results of this measurement are shown from fig. 4.2.8 till fig. 4.2.11.

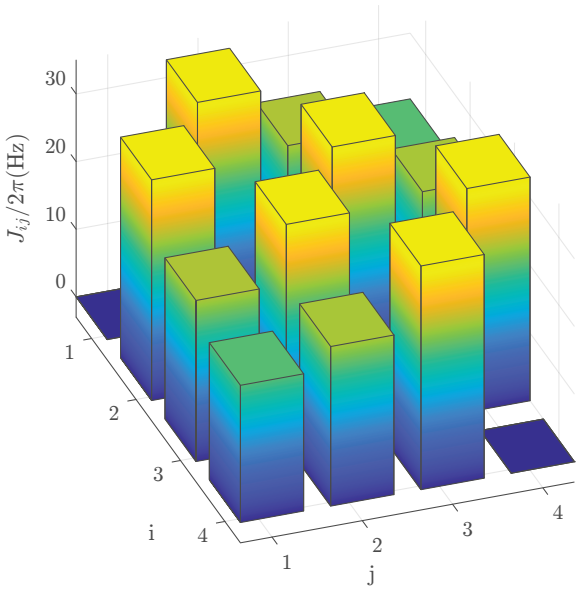

(a)

	$J_{ij}/2\pi$(Hz)
J_{12}	32.6(8)
J_{13}	23.8(6)
J_{14}	20.3(8)
J_{23}	32.6(8)
J_{24}	23.6(11)
J_{34}	33.1(8)

(b)

Figure 4.2.8: J-coupling matrix with simultaneous dynamical decoupling sequences on all four qubits. Total evolution time $T = 6.3\,\text{ms}$. Trap frequency $\omega = 2\pi \cdot 128.24\,\text{kHz}$, $\Omega_i = 2\pi{\cdot}28.27\,\text{kHz}$, DD-sequence UR10 5 blocks, 50 pulses in total. An Arbitrary Waveform Generator (AWG) is used to synthesize four driving fields simultaneously. To measure J_{ij} qubit i (j) was prepared in a superposition state while all other qubits in the register were in state $|0\rangle$. After the unitary evolution, a Ramsey readout pulse is applied to qubit i (j), and a fit determines the phase of the Ramsey fringe to the excitation probability. The experiment is repeated with qubit j (i) prepared in state $|1\rangle$. J_{ij} then is calculated as $J_{ij} = (\varphi(|1\rangle_i) - \varphi(|0\rangle_i)/(2T)$. The measurement sequence is shown in fig. 4.2.7. Although the next-neighbor coupling in a register is dominant, there is coupling between all qubits in the register.

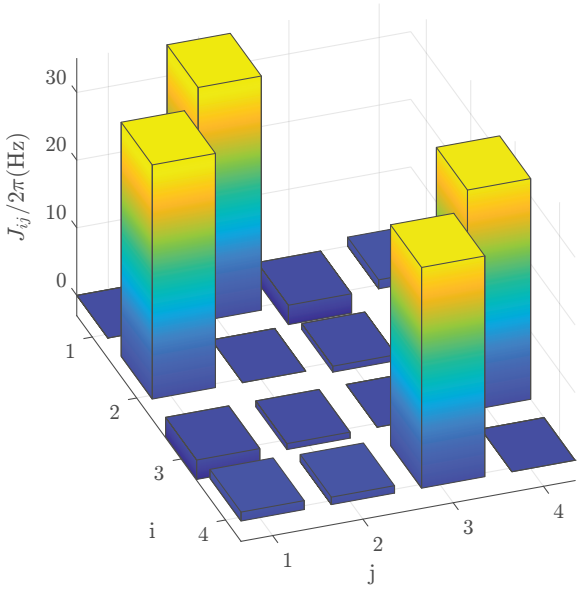

(a)

	$J_{ij}/2\pi$(Hz)
J_{12}	34.6(14)
J_{13}	−2.8(10)
J_{14}	1.3(8)
J_{23}	−0.8(9)
J_{24}	1.1(9)
J_{34}	32.6(10)

(b)

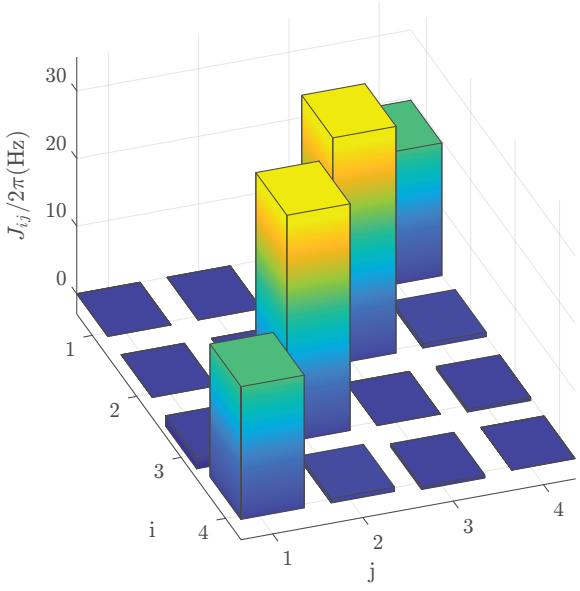

(c)

	$J_{ij}/2\pi$(Hz)
J_{12}	0.0(6)
J_{13}	−1.5(10)
J_{14}	19.6(6)
J_{23}	33.5(9)
J_{24}	0.6(10)
J_{34}	−0.4(9)

(d)

Figure 4.2.9: Exemplary J-coupling matrices showing the separation of a register of four qubits $\{1,2,3,4\}$ into two sub registers (a, b) $\{1,2\},\{3,4\}$ and sub registers (c, d) $\{1,4\},\{2,3\}$ using J-tuning with (a, b) $\tau_b = [0,0,T/(2N),T/(2N)]$ and (c, d) $\tau_b = [0,T/(2N),0,T/(2N)]$ trap frequency $\omega = 2\pi \cdot 128.24(1)\,\text{kHz}$, Evolution time $T = 6.3\,\text{ms}$, DD-sequence UR10 5 blocks, Rabi frequency $\Omega = 2\pi \cdot 28.27\,\text{kHz}$, the measurement sequence is shown in fig. 4.2.7. Splitting a register into subregisters allows two conditional phase gates to be executed in parallel, enabling quantum computation to be parallelized.

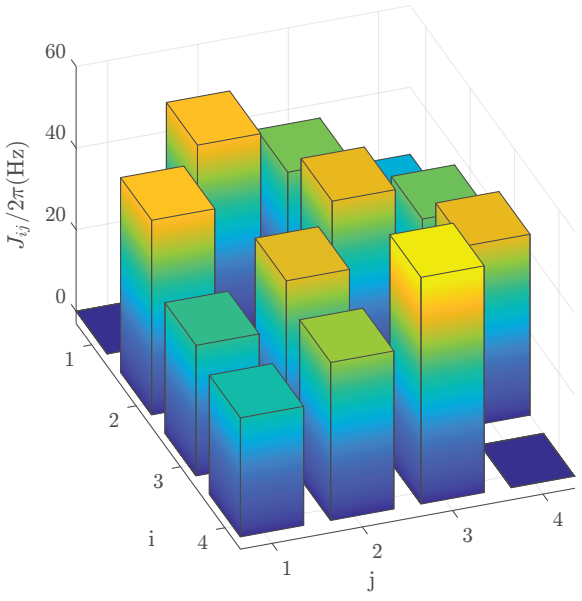

(a)

	$J_{ij}/2\pi$(Hz)
J_{12}	47(2)
J_{13}	36(2)
J_{14}	34(2)
J_{23}	44(2)
J_{24}	35(2)
J_{34}	44(2)
J_{21}	48(2)
J_{31}	33(2)
J_{41}	29(2)
J_{32}	44(2)
J_{42}	39(2)
J_{43}	55(3)

(b)

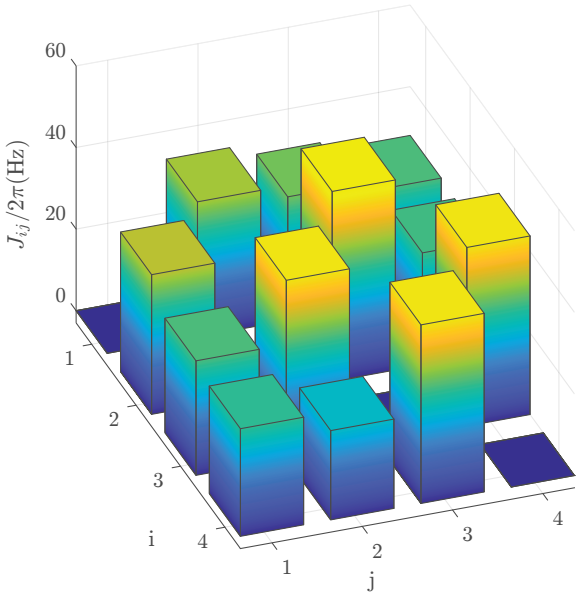

(c)

	$J_{ij}/2\pi$(Hz)
J_{12}	33(2)
J_{13}	30(2)
J_{14}	28(2)
J_{23}	46(2)
J_{24}	27(2)
J_{34}	44(2)
J_{21}	34(2)
J_{31}	28(2)
J_{41}	26(2)
J_{32}	44(2)
J_{42}	21(2)
J_{43}	44(3)

(d)

Figure 4.2.10: (a, b) Untuned J-coupling in a four-qubit register with simultaneous DD-sequence on all four qubits. (c, d) Tuned J-coupling matrix with delays $\tau_{b_{1j}} = [0\,\mu s, 19.3\,\mu s, 12.85\,\mu s, 0\,\mu s]$ implementing the first step in fig. 4.2.6 with all qubits and the first column (row) of J is tuned to match $2\pi \cdot 30\,\text{Hz}$. This implements an equal coupling between qubit 1 and the rest of the register. The trap frequency is $\omega = 2\pi \cdot 115.0(1)\,\text{kHz}$, evolution time $T = 2.475\,\text{ms}$, DD-sequence UR10 5 blocks, Rabi frequency $\Omega = 2\pi \cdot 18.0\,\text{kHz}$, the measurement sequence is shown in fig. 4.2.7. In one step, the coupling to one qubit can be chosen, while the other qubits acquire some conditional phases, which have to be compensated in the next steps.

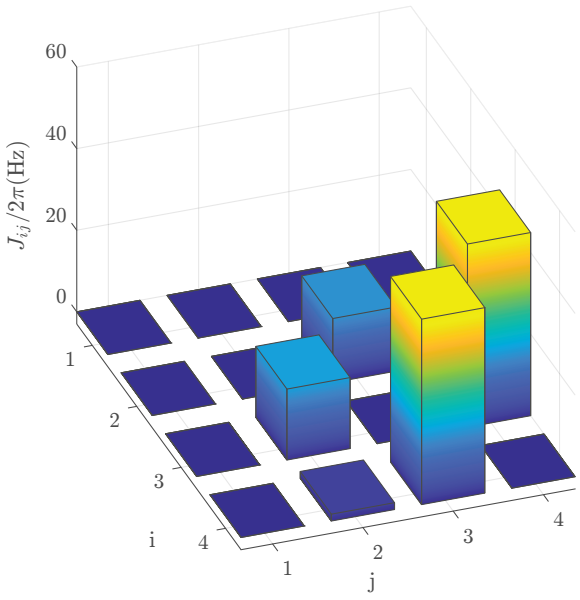

(a)

	$J_{ij}/2\pi$(Hz)
J_{23}	16(2)
J_{24}	1(2)
J_{34}	45(2)
J_{32}	17(3)
J_{42}	2(2)
J_{43}	45(2)

(b)

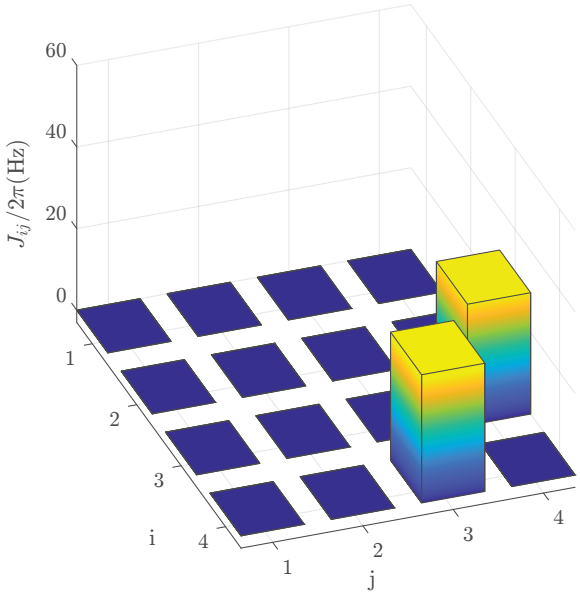

(c)

	$J_{ij}/2\pi$(Hz)
J_{34}	30(2)
J_{43}	31(2)

(d)

Figure 4.2.11: (a, b) Tuned J-coupling in a four-qubit register with DD-sequence on three qubits with delays $\tau_{b_{2j}} = [0\,\mu s, 0\,\mu s, 24.6\,\mu s, 35.2\,\mu s]$, implementing the second step in fig. 4.2.6 for J-tuning where qubit 2, 3 and 4 are interacting. (c, d) Tuned J-coupling matrix with $\tau_{b_{3j}} = [0\,\mu s, 0\,\mu s, 0\,\mu s, 18.0\,\mu s]$ implementing the third step in fig. 4.2.6 with qubits 3 and 4 interacting, trap frequency $\omega = 2\pi \cdot 115.0(1)\,kHz$, evolution time $T = 2.475\,ms$, DD-sequence UR10 5 blocks, Rabi frequency $\Omega = 2\pi \cdot 18.0\,kHz$, the measurement sequence is shown in fig. 4.2.7.

$$J^{eff} = \underbrace{\begin{pmatrix} 0 & J_{12}^{eff} & J_{13}^{eff} & J_{14}^{eff} \\ & 0 & J_{23}^{appl} & J_{24}^{appl} \\ & & 0 & J_{34}^{appl} \\ & & & 0 \end{pmatrix}}_{J_1} + \underbrace{\begin{pmatrix} 0 & 0 & 0 & 0 \\ & 0 & -J_{23}^{eff} & J_{24}^{eff} \\ & & 0 & -J_{34}^{appl} \\ & & & 0 \end{pmatrix}}_{J_2} + \underbrace{\begin{pmatrix} 0 & 0 & 0 & 0 \\ & 0 & 0 & 0 \\ & & 0 & J_{34}^{eff} \\ & & & 0 \end{pmatrix}}_{J_3}$$

(a)

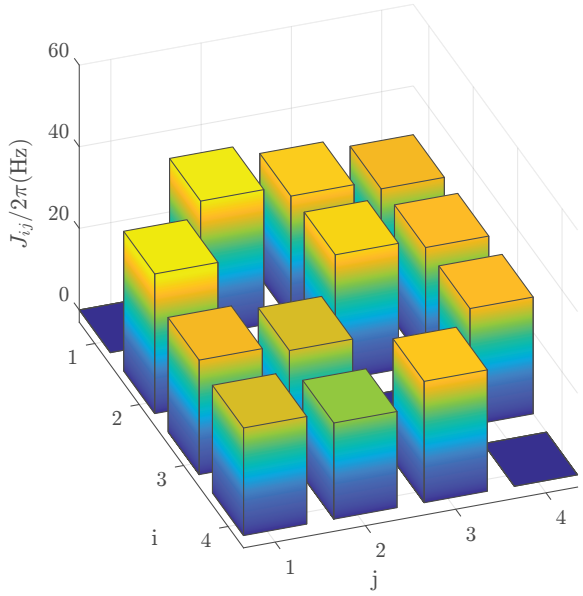

(b)

	$J_{ij}/2\pi$(Hz)
J_{12}	33(2)
J_{13}	30(2)
J_{14}	28(2)
J_{23}	31(3)
J_{24}	29(3)
J_{34}	29(4)
J_{21}	34(2)
J_{31}	28(2)
J_{41}	26(2)
J_{32}	26(3)
J_{42}	24(3)
J_{43}	30(4)

(c)

Figure 4.2.12: (b, c) The total J-coupling matrix tuned to $J = 2\pi \cdot 30\,\text{Hz}$ as the sum of the three-step J-tuning shown in fig. 4.2.10, and fig. 4.2.11 following the scheme in fig. 4.2.6. The resulting J-coupling matrix is not directly measured but calculated from J-tuning steps 1, 2 and 3 assuming a π-pulse on qubit 3 before and after step 2 J_2 as shown in (a). J_2 contributes with the negative sign of entries J_{23}, J_{34}. The same evolution time $T = 2.475\,\text{ms}$ has been chosen for all steps, with the same DD-sequence. In total, an arbitrary coupling matrix consisting of $(N^2 - N)/2 = 6$ couplings could be synthesized in these $N - 1 = 3$ steps, showing a quadratic improvement over selective pairwise coupling.

4.3 Computing dynamical decoupling delay times $\tau_{b_{ij}}$

In the previous subsection it was shown that J-tuning can be used to synthesize an equal coupling between all qubits in a register. Therefore, an asynchronous DD-sequence was applied in three time steps. The delay of the DD-sequences is given by the time $\tau_{b_{ij}}$, where i is the index of the step and j is the index of the qubit.

If a given controlled phase gate with phases Φ_{ij} shall be implemented, the times per step T_k and the delays $\tau_{b_{ij}}$ need to be computed. The following algorithm computes the required times T_k and the delays $\tau_{b_{ij}}$. For each column i of the coupling matrix:

1. Calculate $t_{ij} = \Phi_{ij}/J_{ij}$.
2. Calculate $T_i = \max_j(|t_{ij}|)$ to find the longest time necessary for the desired phase rotation in column i.
3. Calculate $\tau_{b_{ij}} = (T_i - t_{ij})/(2n)$, where n is the number of DD-pulses applied.
4. Calculate the applied phase rotation as

$$\Phi_{ij}^{appl} = -2J_{ij}\left(\frac{1}{2} - 2|\mathrm{mod}_1[\tau_{b_{ij}} n/(2T_i)] - \frac{1}{2}|\right) T_i. \tag{4.3.1}$$

5. Update the conditional phases still to be applied as $\Phi_{ij} = \mathrm{mod}_{2\pi}\left(\Phi_{ij} - \Phi_{ij}^{appl}\right)$, and then repeat steps 1-4 for each column of Φ_{ij}.

The result is a triangular matrix of times $\tau_{b_{ij}}$ containing the required delays to implement the desired controlled z-rotations in $N-1$ steps and the evolution times necessary in each step T_k. Each column (i) of $\tau_{b_{ij}}$ contains the delays to implement in step i.

This procedure is not optimized to the total evolution time but is kept relatively simple.

A DD-sequence acts as a frequency filter [8, 9] and might therefore be susceptible to a specific noise component in the experiment, which might be amplified. It has been shown in the current experiment setup that, for that reason, a sudden drop of the qubit's coherence can occur. It can be circumvented by choosing a different pulse interval and shifting the resonance of the DD-sequence away from the noise components present in the setup. This can be done by selecting a longer evolution time for the gate to implement. If this is not

compensated for, additional conditional phases will occur, limiting the gate's fidelity. Using shifted pulse sequences, the effective coupling during the gate time can be chosen such that no additional unwanted phases are acquired. Therefore, it is experimentally beneficial to tune the coupling. For each step to generate the desired conditional zz-rotation, the run time is chosen such that the applied DD-sequences are not resonant with known noise components. The prior result can be used as a starting point for optimizing the calculated sequence to avoid problematic noise components.

Here a short algorithm shall be described to optimize the sequence accordingly. Assuming a time T_{opt} is known that avoids resonances with noise, the sequence can be modified as follows: For each column i of the coupling matrix:

1. Calculate $t_{ij} = \Phi_{ij}/J_{ij}$.
2. Calculate $T_i' = \max_j(|t_{ij}|)$ to find the longest time necessary for the desired phase rotation in row j.
3. Calculate the optimal number of pulses $n_i^{opt} = T_i'/T_{opt} - \mathrm{mod}_2(T_i'/T_{opt}) + 2$ ensuring an even total number of DD-pulses rounded up.
4. Calculate the optimal total evolution time as $T_i = n_i^{opt} T^{opt}$.
5. Calculate $\tau_{b_{ij}} = (T_i - t_{ij})/(2n_i^{opt})$.
6. Calculate the applied phase rotation as

$$\Phi_{ij}^{appl} = -2J_{ij}\left(\frac{1}{2} - 2|\mathrm{mod}_1[\tau_{b_{ij}} n_i^{opt}/(2T_i)] - \frac{1}{2}|\right) T_i. \tag{4.3.2}$$

7. Update the conditional phases still to be applied as $\Phi_{ij} = \mathrm{mod}_{2\pi}(\Phi_{ij} - \Phi_{ij}^{appl})$ and repeat steps 1-6 for each column of Φ_{ij}.

The result is a triangular matrix $\tau_{b_{ij}}$ containing the required delays to implement the desired controlled zz-rotations in $N-1$ steps, as well as the necessary evolution times in each step T_i and the number of DD-pulses per step n_i^{opt}. This algorithm is designed to deliver a sequence containing an even number of DD-pulses with a specific inter-pulse time T_{opt} making it possible to apply a UR-sequence.

4.4 Parallel computing in an ion chain

A trapped-ion quantum computer based on MAGIC featuring an always-on all-to-all coupling is a powerful platform to implement global CZZ gates on the entire register. Up to here, the powerful tool of J-tuning has been introduced and demonstrated, allowing the implementation of arbitrary CZZ gates on a quantum register. Even though any CZZ gate can be synthesized in principle, the number of steps required is of the order of register size N. For large registers, it might require an unfavorable circuit depth.

If not compiled directly into global unitary gates, several quantum algorithms can be sped up by parallel execution of quantum gates in a register. For example a Quantum Fourier Transform [69–71] or Shors integer factorizing algorithm [72]. Running a quantum circuit in parallel requires disentangling groups of entangling ZZ gates from each other during execution.

Up to here, DD-sequences on a set of qubits have been considered to feature the same period of spin flips. If one now drops the requirement of the same periodicity, using DD-sequences, subsets of the quantum register can be decoupled from each other, while within these subsets, the coupling is preserved. Assuming one subset of qubits is exposed to a DD-sequence with period T and another subset of qubits is exposed to a DD-sequence with period T', it can be shown that for specific choices of T' the subsets can be decoupled from each other while within a subset, J-tuning can be used. Figure 4.4.1 illustrates the pulse timings and the occurring coupling between the qubits.

Assuming a time interval $2T$, a time interval $T' = T/N$, where N is a natural number, one can see that the phase acquired in the first time interval $0 < t < T$ is canceled out by the phase acquired in the second time interval $T < t < 2T$. Here τ is the time shift between the π-pulse on qubit i and the first π-pulse on qubit j. The conditional phases as shown in fig. 4.4.1 are:

$$\phi_1 = 2J\tau = J[\tau + \sum_{k=1}^{N-1}(-1)^k T' + (T' - \tau)] \qquad 0 < t < T, \tag{4.4.1}$$

$$\phi_2 = -2J\tau = J[-\tau - \sum_{k=1}^{N-1}(-1)^k \tau - (T' - \tau)] \qquad T < t < 2T$$

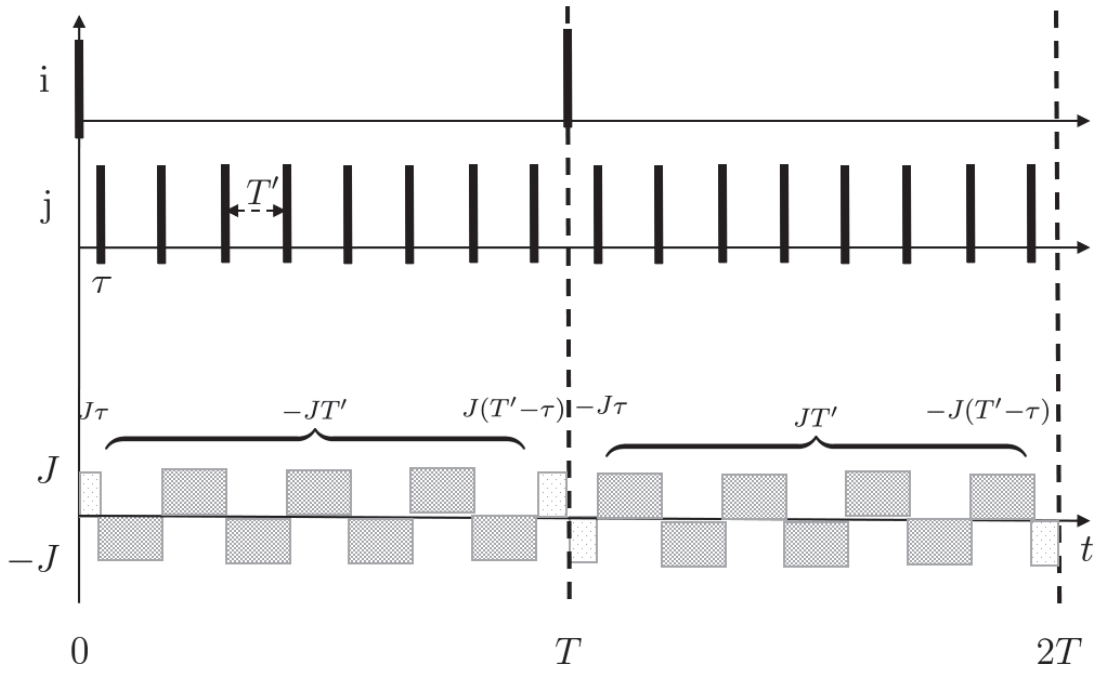

Figure 4.4.1: Top: Schematic DD-sequence on qubit i with periodicity T. The time frame is chosen arbitrarily to be synchronized with the first DD-pulse on qubit i. The π-pulses creating the DD-sequences are indicated by vertical black bars. Middle: DD-sequence applied to qubit j with periodicity T'. For illustration purposes, $T' = T/8$ has been chosen, even though only $T' = T/N$ is required where N is an even number. Additionally, a shift of the DD-sequence on qubit j is chosen to be τ to the DD-sequence on qubit i. Bottom: Resulting coupling J between qubit i and j. As shown in Eq. (4.4.2), the effective coupling cancels out independent of the choice of τ as long as $T' = T/N$ with N even holds.

If N is even the acquired phases add up to zero $\phi_1 + \phi_2 = 0$. This is illustrated in fig. 4.4.1.

If N would be odd, the phases

$$\phi_1' = J[T' + 2\tau] = J[\tau + \sum_{k=1}^{N-1}(-1)^k T' - (T' - \tau)] \qquad 0 < t < T, \tag{4.4.2}$$
$$\phi_2' = J[T' + 2\tau] = J[\tau - \sum_{k=1}^{N-1}(-1)^k T' - (T' - \tau)] \qquad T < t < 2T$$

will not cancel out since $\phi_1' + \phi_2' = J(4\tau + 2T')$.

If the two DD-periods T,T' are fulfilling $T' = T/N$, with N even, the acquired phases vanish independently of a delay τ.

Applying the DD-sequences with different periods to a set of qubits instead of single qubits will allow this subset of qubits to interact with each other. Using this, one can create two disjoint sub registers in a register of qubits. Since the sub registers are decoupled from each other independent of τ, J-tuning can be applied within the sub registers, keeping them decoupled from each other.

Further on, it follows that a register can be split into more than two sub registers if, for each sub register, the condition is fulfilled that each sub registers DD-period fulfilling $T^{(3)} = T^{(2)}/N = T^{(1)}/M$ with M, N even and M is an even multiple of N. Choosing $T^{(n)} = T/2^{n-1}$ directly fulfills this set of conditions for an arbitrary number of sub registers n.

In summary, it is possible to generate sub registers in a quantum register while J-tuning can be applied in each sub register.

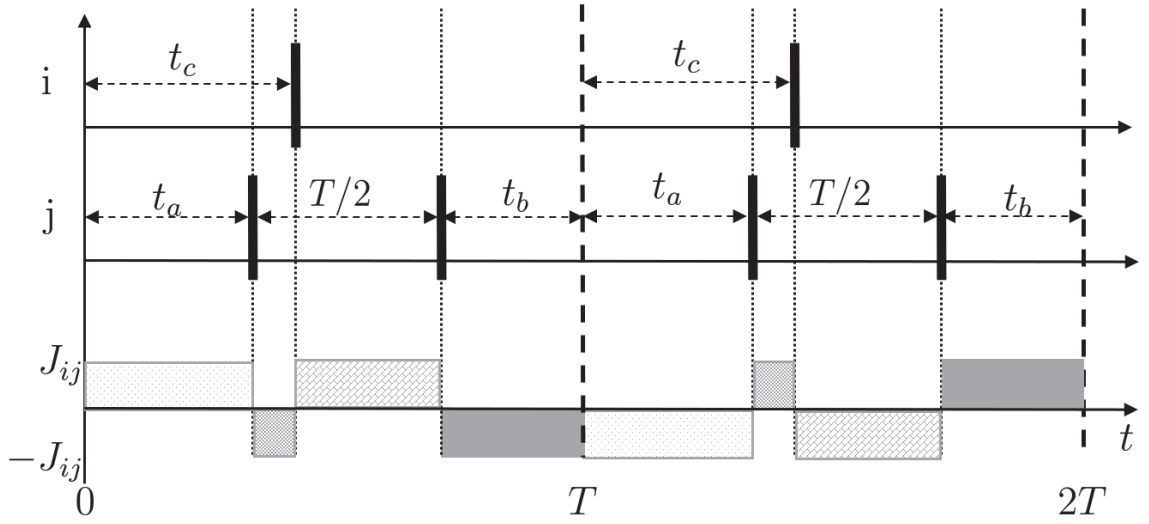

Figure 4.4.2: Schematic of the decoupling of two qubits, independent of the relative time delay between the dynamical decoupling sequences, using two different periodicities for the DD- sequence. The π-pulses that generate the DD-sequences are indicated by vertical black bars. The top graph corresponds to the qubit i protected by a DD-sequence with period T and delay t_c. The middle graph corresponds to the qubit j protected by a DD-sequence with period $T/2$ and delay t_a. $t_a + t_b = T/2$ generates a DD-sequence with fixed periodicity. The lower graph shows the coupling direction between ion i and ion j. To guide the eye of the reader, different areas corresponding to conditional phase shifts are shown in different shades of gray to indicate which couplings cancel out. The areas shaded in the same color cancel independently of the values of t_a, t_b, and t_c, allowing the qubits to be decoupled. This allows to create sub registers of qubits in a larger register and thus provides to implement parallel quantum computing. It should be noted that with this finding, J-tuning in sub registers is possible if they are generated by DD-sequences of different periodicity.

4.5 Summary

In this chapter, a method was introduced, that allows shaping a given coupling matrix such that an arbitrary global CZZ gate can be implemented. The dynamical decoupling technique can be tailored to match the noise spectrum in the device, while simultaneously tuning a given J-coupling matrix.

Analog tuning of the coupling strength has been experimentally demonstrated in a register

containing three qubits as the function of the respective delays of DD-sequences. Tuning a coupling matrix of a register containing four qubits has been demonstrated experimentally to realize an equal coupling strength between each qubit or to enable the parallel execution of two CNOT gates.

Furthermore, a method is introduced to compile a required CZZ gate into a set of DD-pulses. Even though the method is not optimized for the shortest runtimes possible, it outlines a simple way to implement a CZZ gate.

The idea has been proposed that changing the periodicity of the used DD-sequences allows a register to be partitioned in disjoint sub registers while J-tuning within the registers is still possible.

Since these results are obtained exclusively using a dynamical approach implemented in single qubit rotations, by no means is it restricted to a trapped-ion quantum computer. This technique also can be applied to systems that feature a fixed natural qubit-qubit interaction, such as, but not exclusively, to color centers in crystals where the interaction strength is given by the geometric properties of the substrate and the position of the defect centers.

In parallel to this work, based on the same techniques as used in this chapter, a different ansatz to compile an arbitrary multi-qubit gate has been formulated in collaboration with Prof. Martin Kliesch and his group. The work is published in [73] and focuses on the time-optimal decomposition of circuits. This work and the methods described in this chapter rely on the inversion of a qubit's coupling when a π-pulse is applied. Here, a J-tuning sequence is used that uses the asynchronous timing of dynamical decoupling sequences to tune the qubi-qubit interaction. The periodicity of the dynamical decoupling sequence can be optimized with respect to the noise spectrum. In contrast to the work presented here, an arbitrary coupling matrix is achieved by synchronous π-pulses applied to a given subset of qubits in the register followed by a free evolution. The timings for the free evolution result from a novel optimization of overall run time. A dynamical decoupling scheme with a fixed periodicity is not intended to be used. My contribution to the publication [73] mainly is the intense discussion and parts of the ideas presented in this thesis.

5

Implementation of a half-adder

The emergence of quantum computation has led to a commercial interest in different quantum computing platforms. A new branch of industry is currently being created. As the industry grows, so does its energy consumption. Currently, quantum computing devices in the Noisy Intermediate Scale Quantum Computing (NISQ) regime operate on small sets of qubits with limited interconnectivity between them. Once the first systems prove their scalability, they will be replicated and used for many applications. Typical quantum computing applications are, by now, of interest for professional use cases. This can be compared to the current situation in which computation-intensive tasks are mainly carried out in data centers. These include training neural networks, hosting the global Internet infrastructure, and storing all kinds of data. These applications are currently centralized in data centers. Future quantum computers are also likely to be located in such data or quantum computing centers.

The current infrastructure of classical data centers utilizes 1% of the world's total energy budget for electric energy [74]. This figure may be augmented by the potential contributions of quantum computers. To provide a sense of scale, this 1% represents the electric energy demands of the Federal Republic of Germany, assuming a homogenous global population. Consequently, a methodology for estimating the energy consumption of a quantum computer is of interest.

A comparable fundamental operation is studied here to provide a meaningful measure of the required power of a quantum computer in comparison to the classical computing infrastructure. One of the fundamental operations in a classical processor is the addition of two numbers. A full-adder, comprising two half-adders and an OR operation, is commonly used for the bitwise addition of a number. The half-adder circuit is implemented using the MAGIC scheme while utilizing direct multi-qubit operations, providing a practical

demonstration.

Since the unitary evolution by construction describes the time evolution of a quantum system, this time evolution can be inverted by the inverse unitary operator. It can be argued that since the time evolution can be inverted, no energy is dissipated. This leads to the idea that, under idealized assumptions, a quantum computer might need no energy to perform the computation.

This chapter thus examines the implementation of a half-adder circuit comprising a Toffoli and a CNOT gate. Concurrently, the energy consumption of the apparatus is quantified, and an assessment of the requisite power to operate the gate is provided. The work presented in this chapter was conducted in collaboration with Sagar Silva Pratapsi [75].

5.1 Half-adder

The four fundamental mathematical operations of addition, subtraction, multiplication, and division are implemented in digital circuits through the use of a full-adder as a building block. For instance, the addition of two N-digit binary numbers can be accomplished through the use of either one full-adder, repeated N times, or N full-adders in parallel. Regardless of the straightforward implementation, the essential building block is the full-adder. A full-adder takes three inputs, adds them modulo two, and indicates with the carry output if the sum exceeds one. The full-adder is composed of two half-adders and one OR gate, making the half-adder the fundamental building block for all arithmetic operations in digital circuits.

In a quantum computer, the half-adder can be implemented in a variety of ways. Figure 5.1.1 shows the implementation on three qubits using a Toffoli and a CNOT gate. This implementation requires interaction between all three qubits.

In contrast to this implementation, fig. 5.1.2 shows the decomposition of the half-adder circuit into local rotations and next neighbor CNOT operations. In contrast to the simple implementation, shown in fig. 5.1.1, the number of conditional operations is considerably

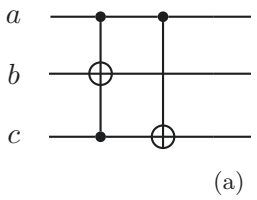

(a)

in	$\|abc\rangle$	$\|abc\rangle$	out
0	$\|000\rangle$	$\|000\rangle$	0
1	$\|001\rangle$	$\|001\rangle$	1
2	$\|010\rangle$	$\|010\rangle$	2
3	$\|011\rangle$	$\|011\rangle$	3
4	$\|100\rangle$	$\|101\rangle$	5
5	$\|101\rangle$	$\|110\rangle$	6
6	$\|110\rangle$	$\|111\rangle$	7
7	$\|111\rangle$	$\|100\rangle$	4

(b)

Figure 5.1.1: (a) Half-adder circuit proposed in [76] consisting of a Toffoli gate and a CNOT gate implemented on three qubits. Two of the qubits are assigned as input (a, b) and two are assigned as output (b, c). The CNOT operation on qubit c calculates the addition of the qubits a and c modulo 2. The Toffoli gate acting on qubit b controlled by qubits a and c checks if the sum exceeds 1 and sets the qubit b accordingly. (b) Logical truth table for all computational basis states of the half-adder. The Toffoli gate's truth table is shown in fig. 5.1.3.

higher.

S. Bose proposed an implementation of a Toffoli gate that is necessary for the simplistic realization of the half-adder circuit in [76]. The CNOT operation is a basic operation first demonstrated on this experimental setup in [10].

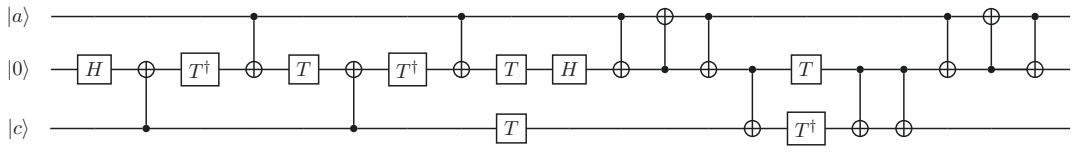

Figure 5.1.2: Decomposition of a half-adder circuit based on the decomposition of a Toffoli gate by [77], where the circuit is extended by SWAP gates assuming only next-neighbor coupling. This corresponds to the decomposition for example in a semiconductor system. Since these limitations do not apply to the system used in this thesis, the circuit can be reduced to the circuit presented in fig. 5.1.1. Here the T gate is a local z-rotation by $\pi/8$.

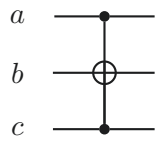

(a)

in	$\|abc\rangle$	$\|abc\rangle$	out
0	$\|000\rangle$	$\|000\rangle$	0
1	$\|001\rangle$	$\|001\rangle$	1
2	$\|010\rangle$	$\|010\rangle$	2
3	$\|011\rangle$	$\|011\rangle$	3
4	$\|100\rangle$	$\|100\rangle$	4
5	$\|101\rangle$	$\|111\rangle$	5
6	$\|110\rangle$	$\|110\rangle$	6
7	$\|111\rangle$	$\|101\rangle$	7

(b)

Figure 5.1.3: (a) Circuit diagram of a Toffoli gate where qubit b is the target and qubits $\{a, c\}$ are the controls. (b) Logical truth table for the Toffoli gate with inputs abc.

5.2 Toffoli implementation

The inherent all-to-all couplings generated by the magnetic field gradient allow to implement global multi qubit gates in a register. As shown in chapter 4, the typical untuned J-coupling in a register in a harmonic trapping potential features symmetries. In a three-qubit system, the couplings are symmetric in a sense that $J_{12} = J_{23}$. This is a useful prerequisite to implement the Toffoli gate, as suggested by S. Bose [76]. This implementation is classical in a sense, since for the gate mechanism the coupling between the two control qubits is neglected. The Toffoli gate is described by the Hamiltonian

$$H_{\mathrm{T}} = \frac{\hbar J}{2}\left(\sigma_z^{(1)}\sigma_z^{(2)} + \sigma_z^{(2)}\sigma_z^{(3)}\right) + \frac{\hbar\delta}{2}\sigma_z^{(2)} + \frac{\hbar\Omega}{2}\sigma_x^{(2)}, \tag{5.2.1}$$

where δ is a detuning of the driving field Ω with respect to the qubit transition. In addition to the J-coupling, a driving field around the x-axis is required. This part of the gate can therefore be seen as being generated by a microwave pulse. The parameters to implement the gate are $\delta = 2J_{12} = 2J_{23}$, and a driving field strength of $\Omega = 1.1J$. The gate mechanism can be visualized using the Bloch sphere of the target qubit. H_T is constant in time such that it describes a rotation of the state vector around some axis in the Bloch sphere. The axis of rotation depends on the control qubits state, allowing for the controlled NOT operation. Assuming a specific state of the control qubits and omitting factors of $\hbar/2$ one can separate three different possible input states of the control qubits. The states of the control qubits are given by $|00\rangle_c$, $|01\rangle_c$, $|10\rangle_c$ and $|11\rangle_c$. Here the subscript c denotes the

control qubits state. Depending on the state, each control qubit can be identified with a state-selective detuning of the target qubit such that three different evolutions of the target qubit can occur:

$$|00\rangle_c \Rightarrow H_T \propto (-J_{12} - J_{23} + \delta)\,\sigma_z + \Omega\sigma_x = -4J\sigma_z + \Omega\sigma_x, \tag{5.2.2}$$

$$|01\rangle_c \Rightarrow H_T \propto (-J_{12} + J_{23} + \delta)\,\sigma_z + \Omega\sigma_x = -2J\sigma_z + \Omega\sigma_x, \tag{5.2.3}$$

$$|11\rangle_c \Rightarrow H_T \propto (J_{12} + J_{23} + \delta)\,\sigma_z + \Omega\sigma_x = \Omega\sigma_x. \tag{5.2.4}$$

The generalized Rabi frequencies for the rotations are $\Omega'_{|00\rangle} = \sqrt{4^2J^2 + \Omega^2}$, $\Omega'_{|01\rangle} = \sqrt{2^2J^2 + \Omega^2}$ and $\Omega'_{|11\rangle} = \Omega$, for a choice of $\delta = 2J$ and $\Omega'_{|11\rangle} = \Omega$. The idea of the gate is such that during the gate time, in case the control qubits are in state $|00\rangle$, $|01\rangle$ or $|10\rangle$, the Bloch vectors trajectory needs to be closed, e.g. the rotation angle around the tilted axis need to be multiples of 2π. Whereas for the case $|11\rangle_c$, a rotation angle of π around the σ_x axis needs to be completed. There are multiple possible approximate solutions to that problem. For example, $\Omega'_{|00\rangle} \approx 4\Omega$ and $\Omega'_{|01\rangle} \approx 2\Omega$. Choosing $\Omega = 1.1J$ approximately fulfills these conditions. The total gate time therefore is given by

$$T = \frac{\pi}{1.1J}. \tag{5.2.5}$$

The evolution time allows for two possible outcomes: either a π_x-rotation on the target is performed or the state of the target qubit is not changed. Starting the target qubits evolution in state $|0\rangle$, therefore results in the trajectory of the qubits state as shown in fig. 5.2.1. Closing the target qubits trajectories during the gate time can also be fulfilled by choices of $\Omega \leq J/2$, while the gate time is extended accordingly. In order to facilitate the experimental realization of this process, it is advantageous to select a gate time that is as brief as possible. The shortest feasible gate time is on the order of $T \approx 15\,\text{ms}$, which exceeds the free coherence time T_2^* by two orders of magnitude, or approximately 200 µs. As the Toffoli gate is a slowly driven π-pulse, it is possible to study the fidelity of the target qubit as a function of pulse errors if it is to be flipped. Figure 5.2.2 depicts the calculated fidelity of the target qubit, $F_1 = |\langle 1|U|0\rangle|^2$, and the fidelity of the target qubit, $F_0 = |\langle 0|U|0\rangle|^2$, as a function of the detuning, δ_e, in units of the Rabi frequency of the Toffoli gate, $\Omega_T = 1.1 \cdot 2J$. The x-axis of this diagram represents the detuning, the y-axis depicts the systematic overshoot and undershoot $\theta = \Omega T$, which is equivalent to an error

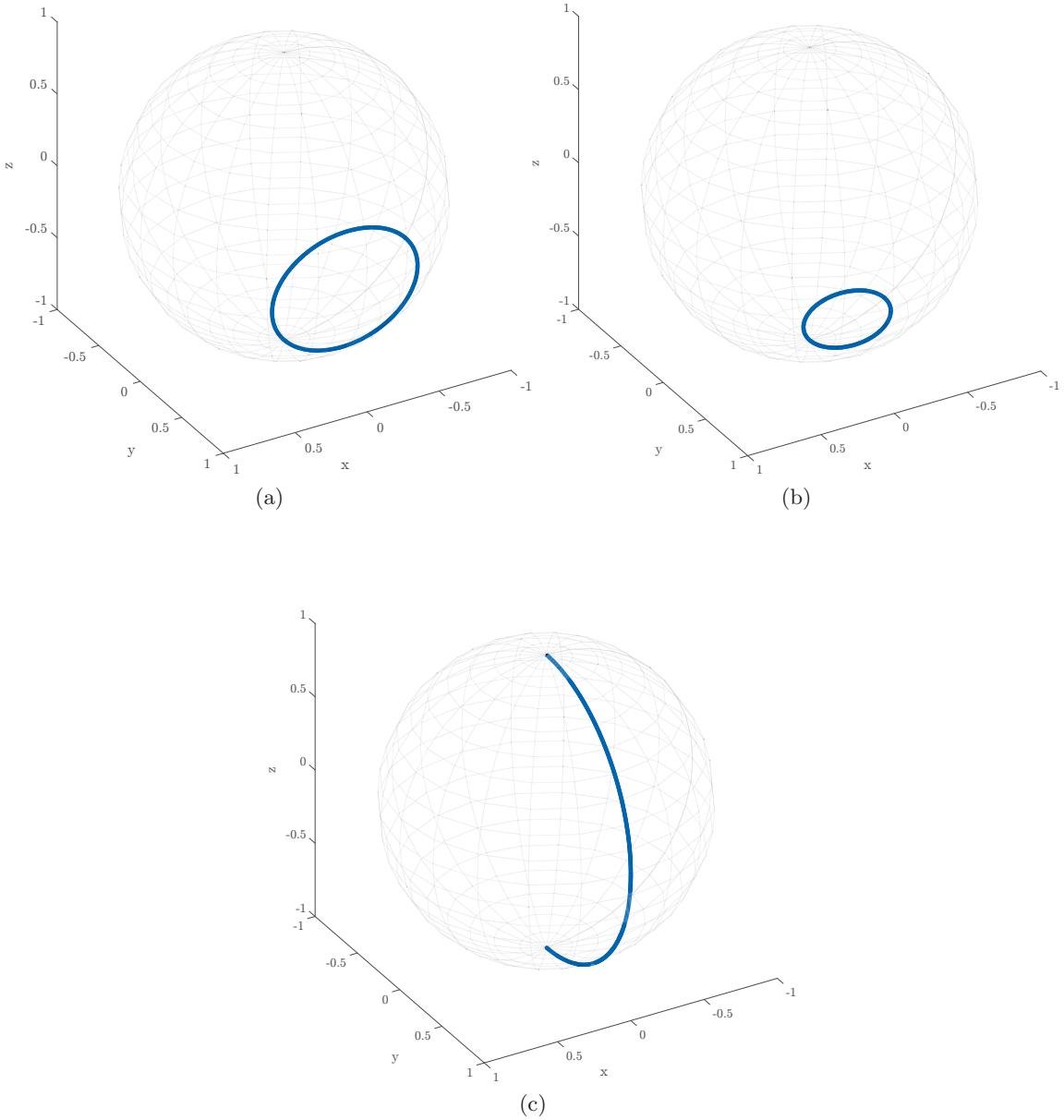

Figure 5.2.1: (a) Trajectory of the Bloch vector of the target qubit of the Toffoli gate for the control qubit's in state $|01\rangle_c$ or $|10\rangle_c$. The qubit's trajectory starts and ends in state $|0\rangle$. The trajectory is completed once during the gate time. (b) Trajectory of the Bloch vector of the target qubit for the control qubits in state $|00\rangle_c$. The qubit's trajectory starts and ends in state $|0\rangle$. The trajectory is completed twice during the gate time. (c) Trajectory of the Bloch vector of the target qubit when the control qubits are in state $|11\rangle_c$. The qubit's trajectory starts in $|0\rangle$ and ends in $|1\rangle$.

in the driving field's amplitude or duration. The effective detuning $\delta_e = [0, -2J, -4J] + \delta$ contains the coupling as well as the detuning of the atomic resonance δ. The color code indicates the expected fidelity for a given parameter set.

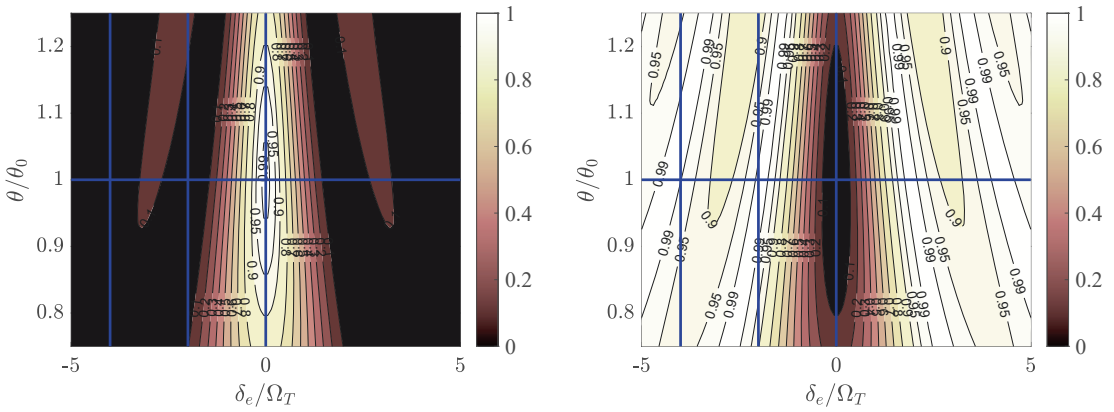

(a) (b)

Figure 5.2.2: Illustration of the probabilities of finding the target qubit of the Toffoli gate in the desired state. (a) The fidelity of the state $|1\rangle$, $F_1 = |\langle 1|U|0\rangle|^2$ and (b) the fidelity of the state $|0\rangle$, $F_0 = |\langle 0|U|0\rangle|^2$ as a function of the effective detuning δ_e and the systematic over- and undershoot θ/θ_0. The unitary U is the Toffoli unitary. Here $\theta = \Omega T$ is the pulse area, where θ_0 is the ideal pulse area, while θ includes errors in pulse time or Rabi frequency. The effective detuning δ_e is a result of the coupling between the control qubits and the target and the error in the addressing frequency δ. Depending on the state of the control qubits, the effective detuning due to the gate construction can be expressed as $\delta_e = [0, -2J, -4J] + \delta$. This is emphasized by the vertical bars. If $\delta_e = 2J$ or $4J$, the qubit state is $|0\rangle$ and F_1 vanishes. Since the Rabi frequency is about $\Omega \approx 2\pi \cdot 36\,\mathrm{Hz}$, an addressing error would cause significant errors even for small absolute detunings. Therefore, implementing the gate as theoretically proposed is challenging.

In the implementation of the gate, the detuning is a variable that can be adjusted to highlight the detuning that generates the Toffoli gate.

It can be observed that detuning errors have a significant impact on the implementation of the Toffoli gate. This is due to the fact that the coupling constants for three qubits are on the order of $J_{12} = J_{23} \approx 2\pi \cdot 36\,\mathrm{Hz}$, whereas the drift rate of the addressing frequency is on the order of $\partial_t \nu \approx 2\pi \cdot 8.1\,\mathrm{Hz/s}$. Furthermore, a systematic offset in Ω influences the expected fidelity of the gates. To mitigate the effect of such detuning

and suppress dephasing, a dynamical decoupling sequence must be employed. Without a dynamical decoupling sequence, the addressing frequency drift and its uncertainty during the experiment would prohibit a successful implementation.

5.2.1 Dynamical decoupling and driving fields.

As demonstrated in chapter 4, a pulsed dynamical decoupling (DD) scheme can be used to prolong coherence times of qubits and tune their interaction strength. In contrast to chapter 4, here the considered gate is generated by a continous driving field Ω. Prior to this investigation, it was unclear how a DD-sequence could be employed with such a driving field. For the sake of simplicity, a single-qubit Hamiltonian is considered:

$$H = \Omega \left(\alpha\sigma_x + \beta\sigma_y + \gamma\sigma_z\right). \tag{5.2.6}$$

The unitary time evolution then is

$$U(t_1, t_0) = \exp\left(-\frac{i}{\hbar}\int_{t_0}^{t_1} Ht\right) \tag{5.2.7}$$

$$= \mathbb{1}\cos(\theta) - i(\alpha\sigma_x + \beta\sigma_y + \gamma\sigma_z)\sin(\theta), \tag{5.2.8}$$

where the angle of rotation driven is $\theta = \int_{t_0}^{t_1} \Omega \mathrm{d}t$.

Assuming a pulse applied to a system undergoing that unitary evolution,

$$\sigma_x U(t_1, t_0) = \sigma_x \left(\mathbb{1}\cos(\theta) - i(\alpha\sigma_x + \beta\sigma_y + \gamma\sigma_z)\sin(\theta)\right) \tag{5.2.9}$$

$$= \left(\mathbb{1}\cos(\theta) - i(\alpha\sigma_x - \beta\sigma_y - \gamma\sigma_z)\sin(\theta)\right)\sigma_x. \tag{5.2.10}$$

The anti-commutation relation of the Pauli operators, given by the equation $\{\sigma_i, \sigma_j\} = 2\delta_{ij}\mathbb{1}$, implies that terms with σ_y and σ_z acquire a minus sign when a σ_x operator is shifted across them. Consequently, the same is true for σ_x and σ_z terms when a σ_y operator is shifted across them. This implies that the Hamiltonian, which has been modified with adjusted signs for the Pauli matrices, produces the same dynamics. Consequently, when the σ_x operator is represented by a π-pulse, the σ_y terms in the Hamiltonian acquire a minus sign.

Assuming a unitary evolution of the state using the Hamiltonian (5.2.6), then from the previous result we can infer that

$$U(H, t_2, t_1)\sigma_x U(H, t_1, t_0) = U(H, t_2, t_1)U(H^{\prime(x)}, t_1, t_0)\sigma_x \tag{5.2.11}$$

with

$$H'^{(x)} = \alpha\sigma_x - \beta\sigma_y - \gamma\sigma_z. \tag{5.2.12}$$

Accordingly with σ_y it follows that

$$U(H, t_2, t_1)\sigma_y U(H, t_1, t_0) = U(H, t_2, t_1)U(H'^{(y)}, t_1, t_0)\sigma_y, \tag{5.2.13}$$

and the modified Hamiltonian is:

$$H'^{(y)} = -\alpha\sigma_x + \beta\sigma_y - \gamma\sigma_z. \tag{5.2.14}$$

From equations (5.2.12) and (5.2.14), a method for modifying Hamiltonians to preserve the quantum dynamics is derived, when a σ_x π-pulse or a σ_y π- pulse can be derived. In both cases, the possible detunings must flip according to the σ_z terms in $H'^{(x,y)}$. This effect is exploited when the coupling is preserved, while the qubit is protected against noise. In the case of a two-ion system with a synchronous DD-sequence, the sign's flip is induced by the inversion of the second qubit's state. This effect is used in chapter 4 to modify the effective coupling strength.

Let us assume the Hamiltonian that creates the desired quantum dynamics of an additional driving field $\Omega\sigma_x$. In the toy Hamiltonian, we have that $\alpha\sigma_x = \Omega\sigma_x$. If we now apply an π_x-pulse, we find that the driving field remains unchanged. However, if we apply a π_y-pulse, we find that $\Omega\sigma_x \rightarrow -\Omega\sigma_x$, which can be achieved by inverting the direction of the driving field by adding a phase of π. If a general pulse, represented by the expression $\pi_\phi = \cos(\phi)\sigma_x + \sin(\phi)\sigma_y$, is considered, the application of the aforementioned recipe results in a contradiction. For the sake of clarity, the times $t_{1,2}$ are dropped:

$$\begin{aligned} U(H)\pi_\phi U(H) &= U(H)\cos(\phi)\sigma_x U(H) + U(H)\sin(\phi)\sigma_y U(H) && (5.2.15)\\ &= U(H)U(H'^{(x)})\cos(\phi)\sigma_x + U(H)U(H'^{(y)})\sin(\phi)\sigma_y && (5.2.16)\\ &\neq U(H)U(H'^{(c)})\pi_\phi. && (5.2.17) \end{aligned}$$

No modified Hamiltonian can simultaneously change the sign of σ_x terms and not change the sign of σ_x terms. The same argument holds for σ_y terms. Nevertheless, it is possible to preserve the quantum dynamics of a system evolving with a Hamiltonian that includes a driving field while protecting it from dephasing.

The simplest DD-sequence is a single π-pulse. Concatenating these pulses has the disadvantage that pulse errors add up in a longer sequence, making it less robust to different errors. Composite DD-sequences can compensate for different types of errors. Since this receipt restricts us to $\sigma_{x,y}$ dynamic decoupling pulses, the eminent DD-sequence is the $\mathrm{CPMG_{XY}}$-sequence.

However, the restriction to such types of DD-sequences is only necessary if there is a driving field in the Hamiltonian. Other dynamical decoupling sequences can address ions that are not exposed to such fields. As the name implies, the coupling that introduces a state-dependent energy shift or detuning depends on the state in the z-basis of the control qubit. This means that the phase of qubit a is irrelevant for qubit b. This is due to the non-existent mixed terms, e.g. $\sigma_x^i \sigma_y^j$ in the effective Hamiltonian (2.3.7). Thus, it is possible to use different types of DD-sequences on different qubits while maintaining the coupling. The Hamiltonian of the Toffoli gate reads

$$H_{\mathrm{T}} = \frac{\hbar J}{2}\left(\sigma_z^{(1)}\sigma_z^{(2)} + \sigma_z^{(2)}\sigma_z^{(3)}\right) + \frac{\hbar\delta}{2}\sigma_z^{(2)} + \frac{\hbar\Omega}{2}\left(\cos(\phi)\sigma_x^{(2)} + \sin(\phi)\sigma_y^{(2)}\right), \tag{5.2.18}$$

where ϕ is the phase of the driving field. The generated unitary is $U(H(\delta,\phi)) = U(\delta,\phi)$.

The pulse sequence to implement the gate therefore can be written as:

$$U_G = \left[U^{1/2}(\delta,0)\pi_x U(-\delta,0)\pi_y U(\delta,\pi)\pi_x U(-\delta,\pi)\pi_y U^{1/2}(\delta,0)\right]^{N/4}. \tag{5.2.19}$$

Here N is a multiple of 4 and denotes the number of CPMG_{XY}-pulses used to realize the gate.

The implementation of this development now allows to protect the dynamics of a quantum system by means of a dynamical decoupling sequence, even if a driving field is present.

In terms of a circuit diagram, this can be represented as shown in fig. 5.2.3.

The fidelity of the Toffoli gate implemented as described above can be simulated as shown in fig. 5.2.4. This figure shows the fidelity $|\langle 0|U|0\rangle|^2$ and $|\langle 1|U|0\rangle|^2$ as a function of the detuning δ. In contrast to the simulation without applied DD-sequence shown in Figure 5.2.2, the simulated detuning range is extended by a factor of 20, while the fidelity plateaus are significantly extended. Figure 5.2.4 (a) shows the fidelity $|\langle 1|U|0\rangle|^2$ when the

control qubits are in state $|11\rangle_c$, (b) shows the fidelity $|\langle 0|U|0\rangle|^2$ when the control qubits are in state $|10\rangle$ or $|01\rangle$, and (c) shows $|\langle 0|U|0\rangle|^2$ when the control qubits are in state $|00\rangle_c$. For this simulation, a Rabi frequency of $\Omega = 2\pi \cdot 35\,\mathrm{kHz}$ has been assumed for the π-pulses implementing the 200 length dynamic decoupling sequence, while the Rabi frequency of the driving field for the Toffoli gate is $\Omega_T = 1.1 \cdot 2\pi \cdot 30\,\mathrm{Hz}$. The three different simulations differ in the assumed conditional detuning $\delta_c = \pm J_{12} \pm J_{23} + 2J = [0, 2J, 4J]$, which changed its sign after each applied π-pulse.

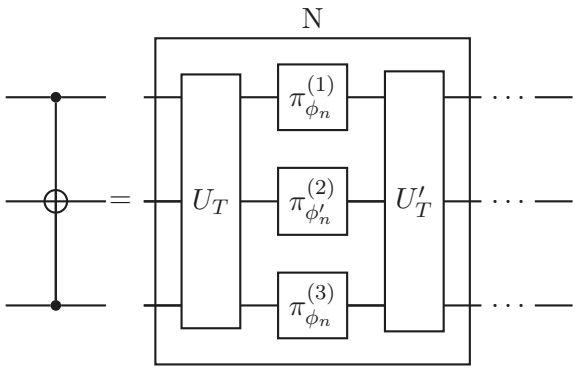

Figure 5.2.3: Decomposition of the Toffoli gate in unitary evolutions $U_T(\delta, \phi)$ that generate the gate and single-qubit rotations that implement dynamical decoupling. These blocks are repeated 200 times with updated phases of the DD-pulses as well as updated U_{TOF}. $\pi^{(k)}_{\phi_n}$ denotes a π-pulse on qubit k with phase ϕ_n. The phases of the DD-pulses are chosen to implement a universal robust DD-sequence on qubit 1 and 3 while a ϕ'_n is chosen to implement a $\mathrm{CPMG_{XY}}$-sequence on qubit 2.

Implementing the Toffoli gate requires precise control of three driving fields in amplitude over three orders of magnitude. Generating a weak driving field and measuring Rabi oscillations is challenging. In the weak field regime, the driving field no longer protects the qubit from decoherence. The required gate time of the Toffoli is $T_T = \pi/\Omega_T$, which realizes a π-pulse. Therefore, the measurement of a Rabi oscillation frequency requires the sampling of the pulse time on a time scale above 15 ms. Similar to the gate implementation, a dynamic decoupling sequence must be used. Since there is no detuning, it is sufficient to change the phase of the driving fields each time a π_y-pulse is applied during the DD-sequence. A $\mathrm{CPMG_{XY}}$-sequence is used to be consistent with the gate implementation. The applied sequence is the same as shown in eq. (5.2.19), where the evolution time between

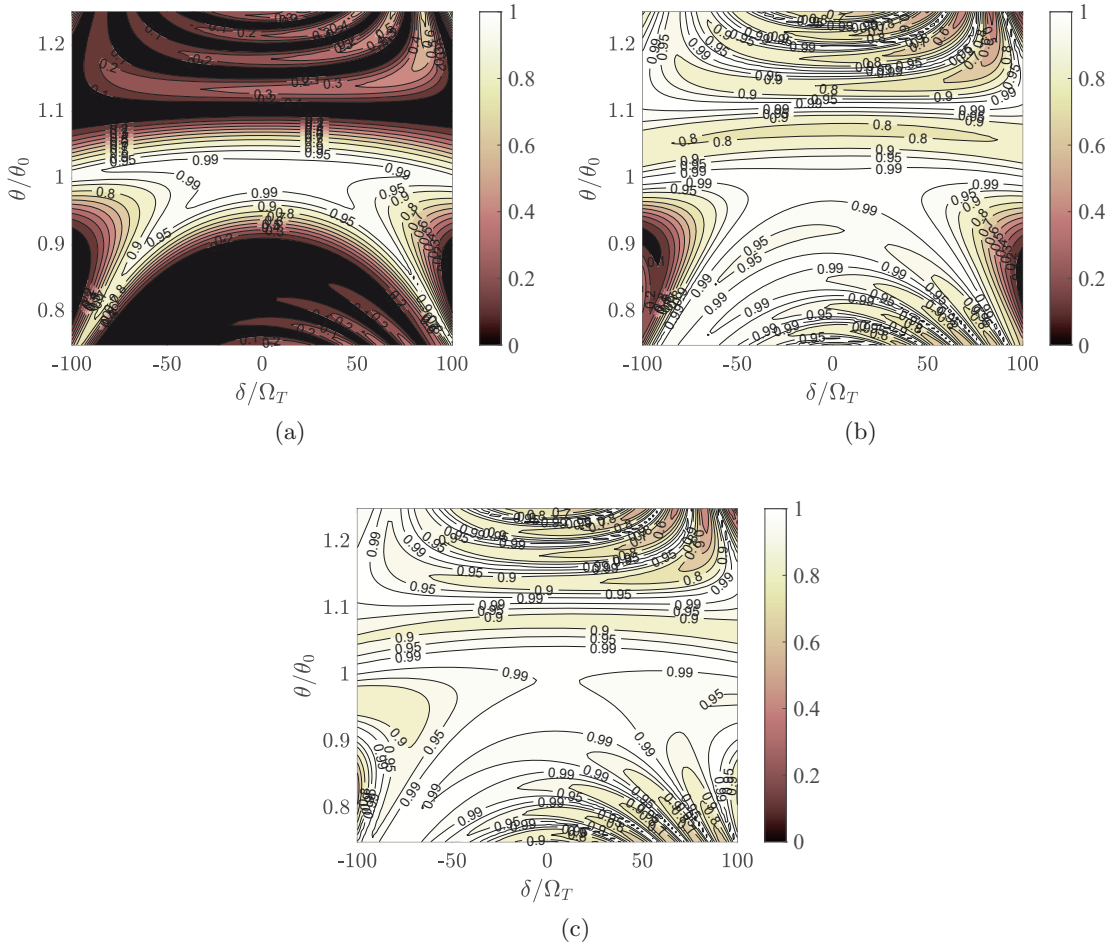

Figure 5.2.4: Illustration of the probabilities of finding the target qubit of the Toffoli gate in the desired state. During the Toffoli gates evolution, the control qubits create a detuning δ_c. The fidelity of the state $|1\rangle$, $F_1 = |\langle 1|U|0\rangle|^2$ is shown in (a) and the fidelity of the state $|0\rangle$, $F_0 = |\langle 0|U|0\rangle|^2$ is shown in (b, c). (a) The control qubits state is $|11\rangle_c$, generating $\delta_c = 0$. (b) The control qubits state is $|01\rangle_c$ or $|01\rangle_c$, generating $\delta_c = 2J$. (c) The control qubits state is $|00\rangle_c$, generating $\delta_c = 4J$. The simulation consists of the Toffoli driving field interleaved with 200 CPMG_{XY}-pulses. θ/θ_0 is the relative pulse area error of the Toffoli driving field, while δ/Ω_T is the detuning of the Toffoli's driving field with respect to the atomic resonance ν. For all three different cases of the control qubits, the high fidelity region is significantly increased, allowing the implementation of the gate.

the applied DD-pulses is sampled. In contrast to the gate, only qubit 2 is addressed with microwave fields, so that detunings due to the other present qubits cancel out. Figure 5.2.5 shows an example of a Rabi oscillation observed on qubit 2 in a three-qubit system with a total pulse duration of up to 25 ms. The amplitude of the RF generator signal is $A = 2{\cdot}10^{-3}$ with a measured Rabi frequency of $\Omega = 2\pi{\cdot}55(10)\,\mathrm{Hz}$. Although the excitation of the qubit does not reach 1, this demonstrates the ability to drive the target qubit of a Toffoli gate with Rabi frequencies relevant to the implementation of the gate mechanism as a frequency-selective pulse. Besides the required amplitude of the frequency generator to drive Ω_T, the

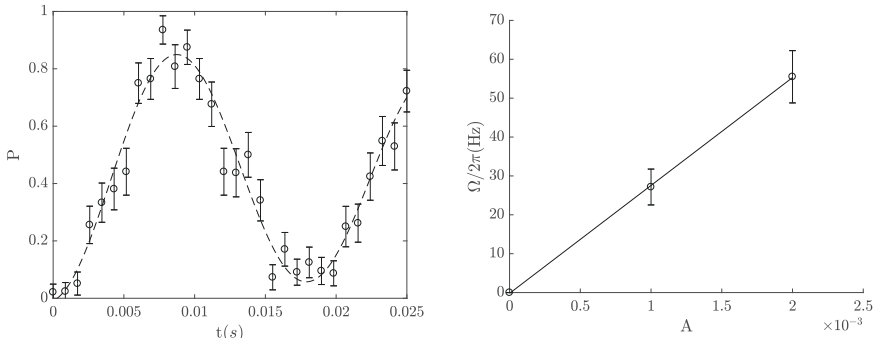

(a) (b)

Figure 5.2.5: (a) Rabi oscillations at signal generator amplitude $A = 0.002$. The driving field is nested in a 250 pulse $\mathrm{CPMG_{XY}}$-sequence driven with $\Omega_{\mathrm{DD}} = 2\pi \cdot 27.54\,\mathrm{kHz}$ at $A_{\mathrm{DD}} = 0.9129$. The nesting sequence used is shown in eq. (5.2.19). The fitted Rabi frequency is used in (b). The evolution time used here is up to 25 ms, exceeding the gate time of the Toffoli gate of 15 ms and the coherence time $T_2 \approx 200\,\mu\mathrm{s}$. (b) Linear fit to measured Rabi oscillation frequency with respect to the signal generators amplitude. The Rabi frequency as a function of the set amplitude is found to be $\Omega(A) = 2\pi \cdot 27.8(2)\,\mathrm{kHz} \cdot A$. This allows to extrapolate the required amplitude A to values relevant for the Toffoli gate implementation.

.

coupling must be known. As shown in chapter 4, a Ramsey-type experiment can be used to estimate the coupling constant. The coupling constant can then be calculated from the observed conditional phase shift. Figure 5.2.6 shows the Ramsey-type measurement of the coupling constant J_{12} in a three-qubit register. The experiment includes a Universal Robust (UR) dynamic decoupling sequence with a block length of 10 pulses (UR10). For each sampled evolution time, the periodicity of the dynamical decoupling sequence has been kept constant to avoid sampling different frequency components of the noise spectrum, as

shown in [9]. UR10 blocks are concatenated with a conditional evolution time of $T_{10} = 1\,\text{ms}$ each. The coupling was found to be $J_{12} = 2\pi \cdot 36.5(1.1)\,\text{Hz}$.

To implement the Toffoli gate, all parameters are known. Nevertheless, it is necessary to fine-tune the gate parameters. The parameters accessible in the experiment are the logical input state $|ijk\rangle$, the gate time T_T, the amplitude A, and the detuning δ. A working set of parameters was found by measuring the excitation probability of the target qubit. An iterative search for the best working parameters was performed. The best parameters found were $A = 0.003571$, $T_T = 14.86\,\text{ms}$, $\delta = -2\pi \cdot 78\,\text{Hz}$ and a DD-sequence on control qubits consisting of 20 UR10 blocks and on target qubit 200 CPMG_{XY}-pulses.

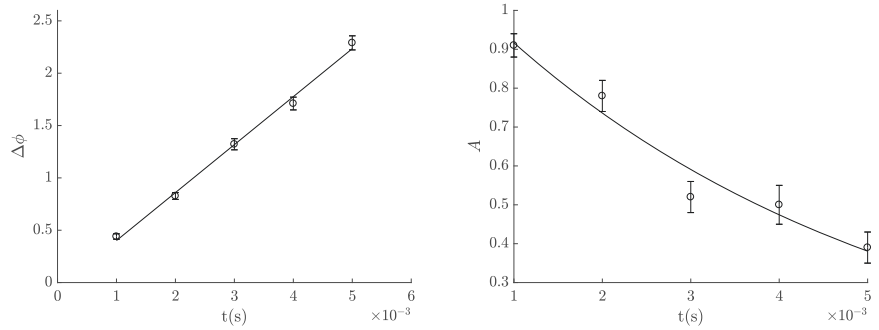

Figure 5.2.6: (a) Relative acquired phase $\Delta\phi$ of qubit 2 in a three-qubit system as a function of the evolution time. The phases are measured by a Ramsey type experiment. Linear fit of coupling constant results in $J_{12} = 2\pi \cdot 36.5(1.1)\,\text{Hz}$, here t is the total evolution time. The applied DD-sequence was one UR10 block per ms, such that the free evolution time between DD-pulses was kept constant at $\tau = 0.1\,\text{ms}$. Two experiments have been interleaved with control qubit state $|1\rangle$ and $|0\rangle$ and $\Delta\phi$ is the phase difference of the fitted Ramsey fringe. The axial trap frequency is $\nu_T = 2\pi \cdot 128.4(1)\,\text{kHz}$. (b) Ramsey amplitude decay of the experiment shown in (a) to detemine the coherence time of a qubit in a three-qubit register. The fitted Ramsey fringe amplitudes A are shown. The fitted decay time is $T_2 = 4.5(5)\,\text{ms}$.

5.3 CNOT

Besides the Toffoli gate, a half-adder consists of a CNOT gate between the control qubits of the Toffoli gate. For symmetry reasons, the target of the Toffoli gate has been chosen to be

the center qubit in a register of size three. Therefore, it is necessary to implement a CNOT operation on qubit 3 controlled by qubit 1. Due to the inherent all-to-all coupling, as shown in chapter 4, a CNOT gate can be implemented among any arbitrary pair of qubits in a register. The typical implementation of the CNOT gate consists of a $\pi/2$-pulse on the target qubit, a waiting time of a duration $T_C = \pi/2J$, and a second $\pi/2$-pulse applied on the target. A CNOT operation based on MAGIC has been demonstrated by [10]. The unitary operation to implement the gate is:

$$U_C = \left(\frac{\pi}{2}\right)_0^{(t)} U_{zz}(T_c) \left(\frac{\pi}{2}\right)_{3\pi/2}^{(t)}. \tag{5.3.1}$$

Here the superscript (t) denotes the target qubit, the subscript ϕ denotes the phase, and T_c is the free evolution time. Similar to the implementation of the Toffoli gate, a DD-sequence is required to extend the coherence time. Implementing a CNOT gate on a subset of qubits in a register requires removing the interaction with other present qubits. This can be done dynamically by addressing only the participating qubits with a DD-sequence, or by recoding all other qubits to a magnetically insensitive state [37]. The application of the recode operation or J-tuning is necessary if the phase of the qubits not participating in the gate is of interest. Since the implementation of the half-adder presented here is classical due to the neglected coupling between the control qubits of the Toffoli gate, it is sufficient to use only a DD-sequence on the qubits participating in the CNOT gate. The implemented pulse sequence is shown in fig. 5.3.2. The DD-sequence used is a UR-sequence, since there are no restrictions on the phase of the DD-pulses. For the CNOT implemented here $T_c = 8.75\,\text{ms}$. In the experiments shown here 120 DD-pulses of a UR12-sequence repeated ten times were used. The results of the CNOT implementation are shown in fig. 5.4.2.

5.4 Quantum channel tomography

Quantum channel tomography can be used to quantify the implemented gate. Each possible state in the computational basis must be prepared and propagated through the gate, and its result in the same computational basis must be measured. The procedure is as follows:

1. Prepare state $|abc\rangle$.

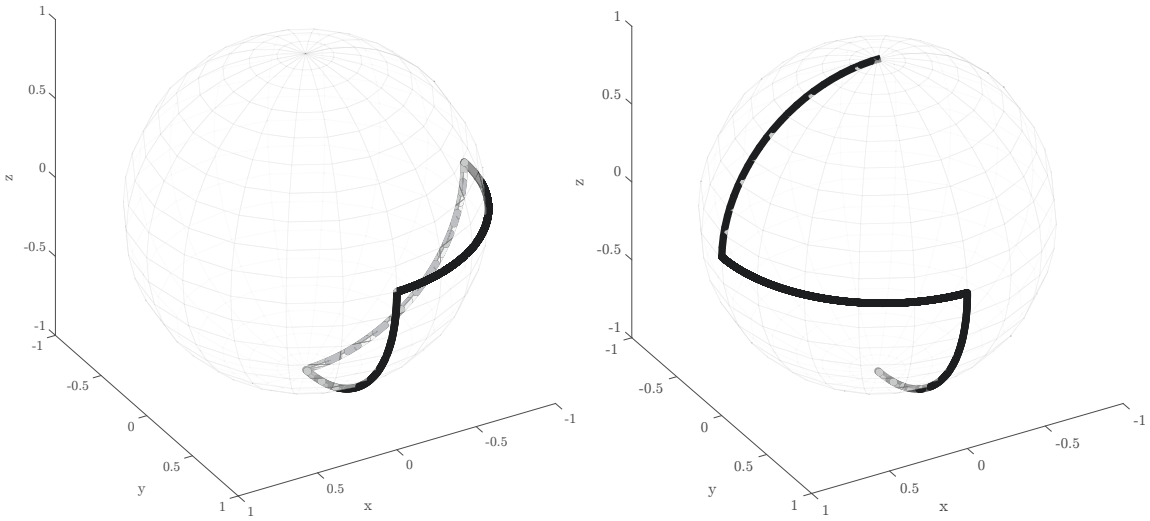

Figure 5.3.1: (a) Bloch vector trajectory of the target qubit of a CNOT when the control qubit is in state $|0\rangle_C$ assuming the target qubit starting in state $|0\rangle_T$. After the first $\frac{\pi}{2}_0$-pulse is applied, the conditional evolution implements a rotation of $\phi = +\pi/2$ around the z-axis and the second $\frac{\pi}{2}_{3\pi/2}$-pulse transfers the population back to $|0\rangle$. (b) Bloch vector trajectory if the control qubit is in state $|1\rangle$ assuming the target qubit starting in state $|0\rangle_T$ after the first $\frac{\pi}{2}_0$-pulse is applied, the conditional evolution implements a rotation of $\phi = -\pi/2$ around the z-axis and the second $\frac{\pi}{2}_{3\pi/2}$-pulse transfers the population to $|1\rangle$. Therefore, the state of the target qubits is inverted conditioned by the state of the control qubit.

2. Apply gate.

3. Read the quantum state projected onto the computational basis and note the result, also in this case from $|000\rangle$, $|001\rangle$ to state $|111\rangle$.

4. Repeat steps 1-3 to collect statistics.

5. Select another state prepared in step 1 and repeat until all possible 2^3 basis states have been measured.

6. Calculate the frequency of readouts as $f_{nk} = N_{nk}/N$, where N_{nk} is the number of readout values n that occur in the total N measurements performed for a given input state k $|abc\rangle$.

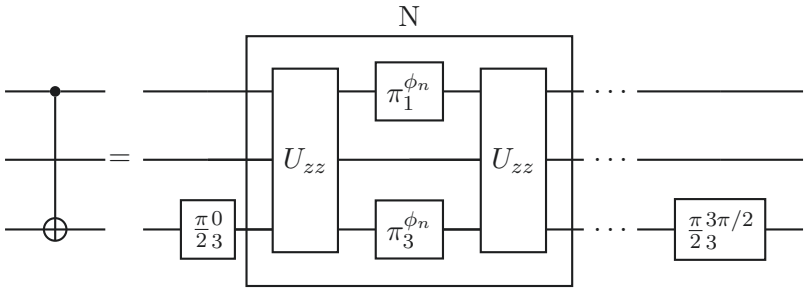

Figure 5.3.2: Decomposition of the CNOT gate between ions 1 and 3. Here ion 3 is the target. The unitary evolution U_{zz} implements the zz-coupling, whereas the single-qubit π-pulses implement the dynamical decoupling sequence. This sequence is repeated 120 times. $\pi_k^{\phi_n}$ denotes a π-pulse on qubit k with phase ϕ_n. The phases of the DD-pulses are chosen to implement a universal, robust DD-sequence on the control and target qubit.

7. Use the measured frequencies f_n for each possible input state to perform a maximum likelihood analysis according to [78, 79] to reconstruct the quantum gate.

8. Use the reconstructed quantum gate to evaluate the classical fidelity F as

$$F = \sum_{kl} \frac{1}{n} M_{kl} G_{kl}, \tag{5.4.1}$$

   where M_{kl} is the reconstructed gate and G_{kl} is the gate to be implemented, and n is the dimension. Here $n = 2^3 = 8$.

The numerical data analysis was performed using an analysis script developed by Sagar Silva Pratapsi.

The tomography of the Toffoli gate, the half-adder gate and the CNOT gate was performed as an interleaved experiment.

Interleaved experiments allow a direct comparison of the results of two experiments. Because the experimental setup is subject to slow drifts, such as drifts in addressing frequency, Rabi frequency, noise spectrum drifts, or laser frequency. It can be difficult to compare two experiments run in sequence. The experiment control framework provides automatic recalibration of the addressing frequencies, automatic scanning of the 369 nm laser resonance and a feedback loop to actively stabilize the cooling fluorescence during the experiment. The procedures used are described in chapter 2. Typical experiment durations are on the

order of 10 min, so consecutive experiments will experience different experimental drifts, making direct comparison difficult. Therefore, experiments can be run interleaved. Typically, an experiment tests a set of parameters, and the measurement result is a probability distribution. To approximate these distributions, experiments are repeated. Typical experiments are repeated on the order of 100 times. During each repetition, the experiment is performed for each sample point. If two experiments, A and B, are interleaved, one repetition of experiments A and B is measured before the next repetition is measured for experiments A and B. Depending on the experiment settings, a single cycle corresponding to one sample point with one repetition takes about 100 ms time. Therefore, the experiments can be changed on the time scale of 100 ms in such a way that the time for free drifts compared between two consecutive experiments is reduced by at least two orders of magnitude, making the interleaved experiments more comparable with each other. The half-adder tomography was always interleaved with either the CNOT or the Toffoli tomography in order to collect more measurement data for the half-adder and to make it comparable to the tomography of its components. The result can be found in fig. 5.4.1. For the CNOT operation, the results can be found in fig. 5.4.2 and for the half-adder in fig. 5.4.3.

5.5 Creating a GHZ state

The Toffoli implementation shown here has been tested using computational basis states as product states. A typical prototype state is the GHZ state. A two-qubit GHZ state is generated by supplying an equal superposition state to control a CNOT operation. The output GHZ state on two qubits is then present at the control inputs of the Toffoli such that it generates the three-qubit GHZ state. Omitting the phases, since the Toffoli is implemented as a classical gate, the following stepwise evolution can be implemented:

$$|000\rangle \overset{\frac{\pi}{2}(1)}{\rightarrow} |000\rangle + |100\rangle \overset{CNOT^{(1,3)}}{\rightarrow} |000\rangle + |101\rangle \overset{Toffoli}{\rightarrow} |000\rangle + |111\rangle. \tag{5.5.1}$$

Since all prerequisites introduced in this chapter are known, the circuit can be implemented as shown in fig. 5.5.1. Finally, the quantum state can be projected and the frequency of the

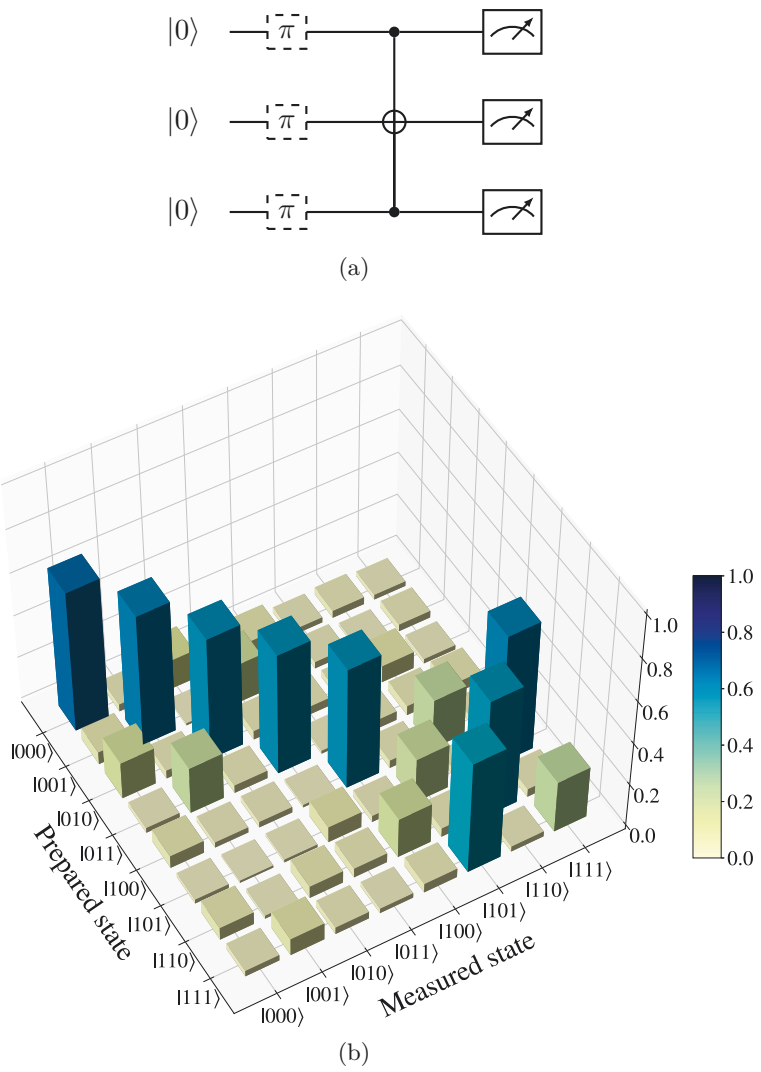

Figure 5.4.1: (a) Quantum process tomography of the Toffoli gate. For the experiment, all different input states were prepared, the Toffoli gate was performed, and the qubit states were read out.For each prepared basis state, the most likely output distribution was evaluated. The parameters for the experiment were $A = 0.003571$, $T_T = 14.86\,\text{ms}$, $\delta = -2\pi \cdot 78\,\text{Hz}$, DD-sequence on control qubits 20 UR10 blocks and on target qubit 200 CPMG_{XY}-pulses with $\Omega = 2\pi \cdot 28.23\,\text{kHz}$. The system was cooled with a two step three mode sideband cooling of $T_{C1} = 50\,\text{ms}$ and $T_{C2} = 10\,\text{ms}$. The trapping frequency was $\nu = 2\pi \cdot 128.4(1)\,\text{kHz}$ with a gradient of $\partial_z B = 19.09(1)\,\text{T/m}$ resulting in the coupling $J_{12} = J_{23} = 2\pi \cdot 36.5(1.1)\,\text{Hz}$. This experiment was interleaved with the half-adder experiment. (b) Maximum likelihood estimation of the Toffoli gate, with a 99% confidence interval of $F_{0.99} = [0.15, 0.70]$, with the most likely classical fidelity $F_C = 0.58$.

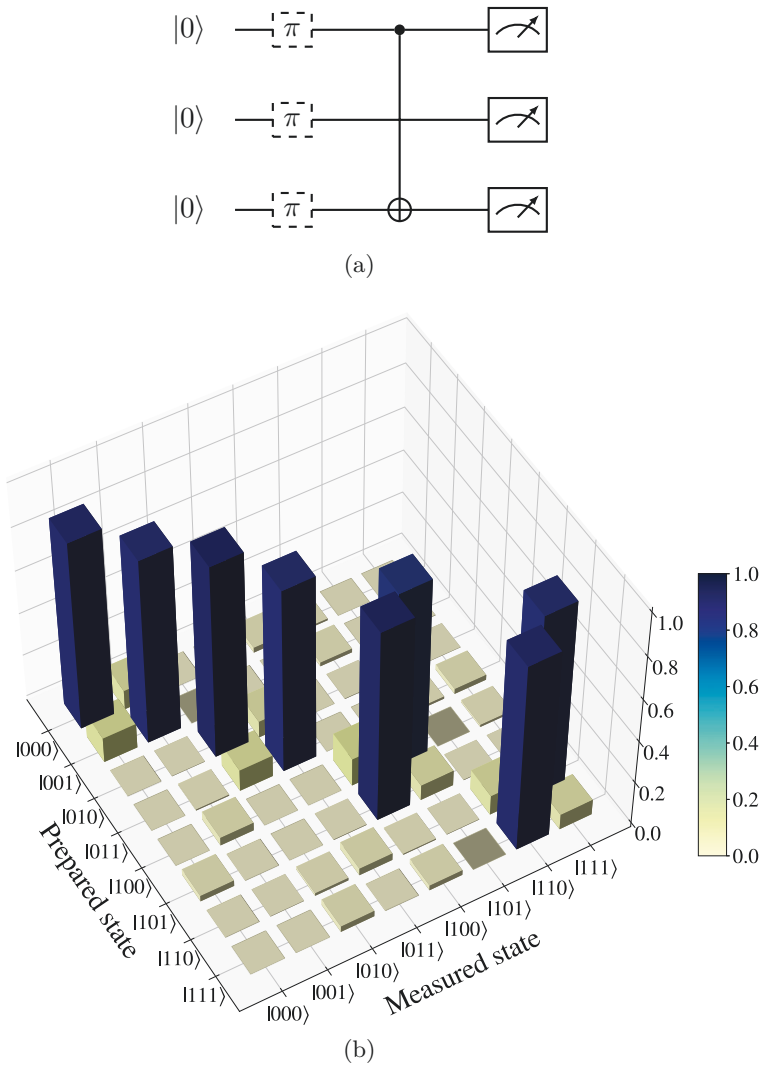

Figure 5.4.2: (a) Quantum process tomography of the CNOT gate between control qubit 1 and target qubit 3. For the experiment all different input sates have been prepared, the CNOT gate was performed and the qubits state have been read out. For each prepared basis state the most likely output distribution has been evaluated. The system was cooled with a two step three mode sideband cooling of $T_{C1} = 50\,\mathrm{ms}$ and $T_{C2} = 10\,\mathrm{ms}$. The trapping frequency $\nu = 2\pi \cdot 128.4(1)\,\mathrm{kHz}$ with a gradient of $\partial_z B = 19.09(1)\,\mathrm{T/m}$ resulting in the gate time $T_c = 8.75\,\mathrm{ms}$ The DD-sequence was 10 UR12 blocks with $\Omega = 2\pi \cdot 28.23\,\mathrm{kHz}$. The experiment was interleaved with the experiment for the half-adder. (b) Maximum likelihood estimation of the CNOT gate, with a 99% confidence interval of $F_{0.99} = [0.61, 0.95]$ with the most likely classical fidelity $F_C = 0.87$.

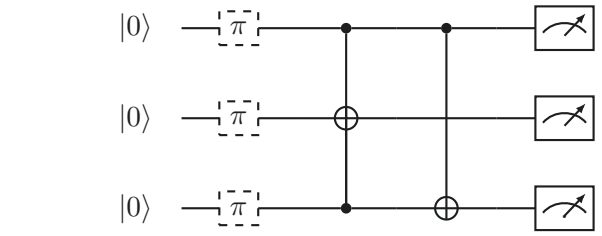

(a)

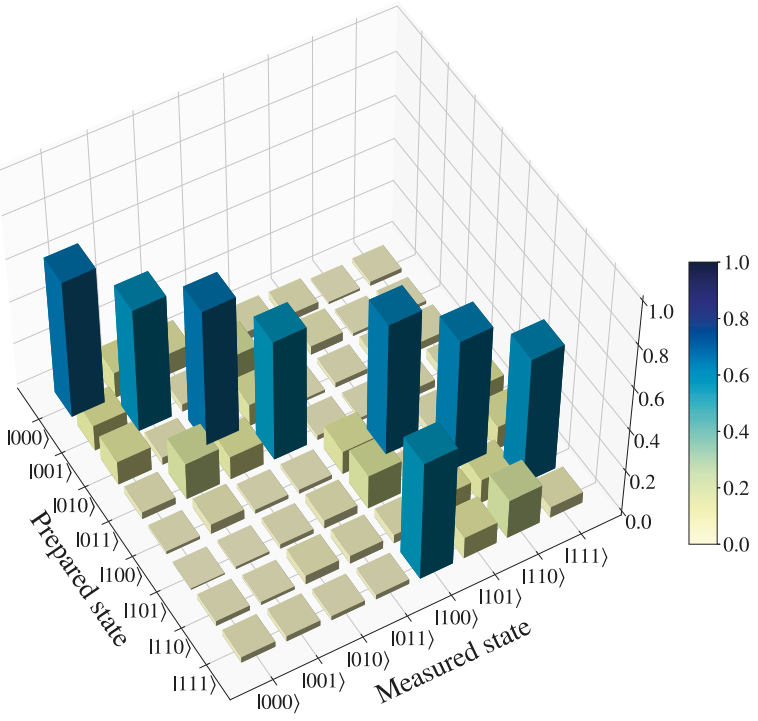

(b)

Figure 5.4.3: (a) Quantum process tomography of the half-adder. For the experiment, all different input states were prepared, the Toffoli gate was performed, followed by the CNOT gate, and the qubit state was read out. For each prepared basis state, the most likely output distribution was evaluated. The parameters for the experiment where for the Toffoli gate, $A = 0.003571$, $T_T = 14.86\,\text{ms}$, $\delta = -2\pi \cdot 78\,\text{Hz}$, DD-sequence on control qubits 20 UR10 blocks and on target qubit 200 CPMG_{XY}-pulses with $\Omega = 2\pi \cdot 28.23\,\text{kHz}$ have been performed. CNOT was performed with gate time $T_{CNOT} = 8.75\,\text{ms}$ 10 UR12 blocks on qubit 1 and 3. The system was cooled with two step three mode sideband cooling of $T_{C1} = 50\,\text{ms}$ and $T_{C2} = 10\,\text{ms}$. The trapping frequency was $\nu = 2\pi \cdot 128.4(1)\,\text{kHz}$ with a gradient of $\partial_z B = 19.09(1)\,\text{T/m}$ resulting in the coupling $J_{12} = J_{23} = 2\pi \cdot 36.5(1.1)\,\text{Hz}$. The experiment was interleaved with the CNOT gate and Toffoli gate experiments. (b) Maximum likelihood estimation of the CNOT gate, with a 99% confidence interval of $F_{0.99} = [0.37, 0.67]$ with the most likely classical fidelity $F_C = 0.61$.

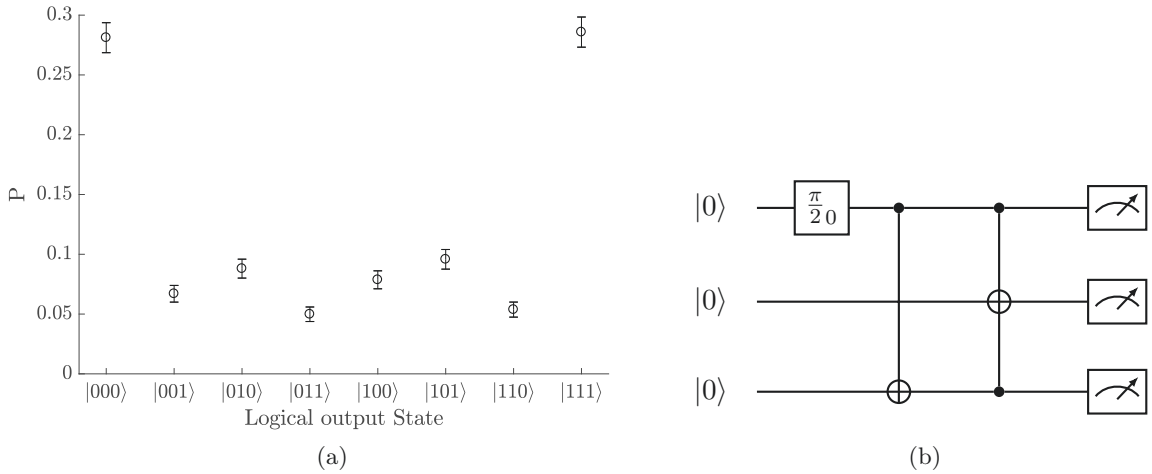

Figure 5.5.1: (a) The CNOT gate was performed with the control qubit in a superposition state, followed by the Toffoli gate and readout. The parameters for the experiment were for the Toffoli gate, $A = 0.003571$, $T_T = 14.86\,\text{ms}$, $\delta = -2\pi \cdot 78\,\text{Hz}$, DD-sequence on control qubits 20 UR10 blocks and on target qubit 200 CPMG_{XY}-pulses with $\Omega = 2\pi \cdot 28.23\,\text{kHz}$. CNOT was performed with a gate time of $T_c = 8.75\,\text{ms}$ using 10 UR10 blocks on qubit 1 and 3. The system was cooled with a two step three mode sideband cooling of $T_{C1} = 50\,\text{ms}$ and $T_{C2} = 10\,\text{ms}$. The trapping frequency is $\nu = 2\pi \cdot 128.4(1)\,\text{kHz}$ with a gradient of $\partial_z B = 19.09(1)\,\text{T/m}$ resulting in the coupling $J_{12} = J_{23} = 2\pi \cdot 36.5(1.1)\,\text{Hz}$. The desired output state is $|\psi\rangle = 1/\sqrt{2}|000\rangle + e^{i\phi}/\sqrt{2}|111\rangle$ where ϕ is an arbitrary unknown phase since the Toffoli is a classical gate. Therefore, the quantum state is evaluated only in the z-basis. (b) Generation of a GHZ state using a CNOT and a Toffoli gate.(b) Quantum circuit for generating a three-qubit GHZ state using a CNOT and a Toffoli gate.

occurring identified product state can be calculated. It can be seen that predominantly the states $|000\rangle$ and $|111\rangle$ occur in the readout, indicating a three-qubit GHZ state, measured in the z-basis. Due to the classical nature of the Toffoli gate, the phases of the quantum state are omitted here.

5.6 Energy consumption

Up to this point in this chapter, the implementation of the half-adder circuit has been discussed. It has been shown that the implementation shown here is suitable to reproduce a classical half-adder, which is a fundamental building block of classical arithmetic units. Every classical computation consumes energy. In contrast to classical computation, the unitary evolution of a quantum state can by definition be completely inverted, since $U^\dagger U = \mathbb{1}$. From a thermodynamic point of view, this means that no energy is lost in the system. Theoretically, if one could realize an ideal quantum control of the system, arbitrary computations could be performed without energy cost.

In reality, a lot of power is needed to generate the EM fields for quantum control. The trapping potential to store the qubits, the laser field of cooling to prepare and read out the qubits, the microwave field to carry out the coherent control, or the generation of magnetic fields to control the quantization axis require power. Currently, the DC magnetic field is generated by sets of Helmholtz coils. These Helmholtz coils could be replaced by a suitable permanent magnet arrangement, thus eliminating the power requirement for generating the DC magnetic fields. On the other hand, the trapping potential must be generated and maintained during a computation, which adds a fixed power consumption during the computation. Depending on the realization of the trapping apparatus, a driving power in the order of $P_{Tr} \approx 10\,\mathrm{mW}$ might be achievable with current traps [80]. Compared to future planar ion traps, the trap setup used in this work is macroscopic and must be operated at a trapping power of $P_{Tr} \approx 10\,\mathrm{W}$. This is by far the largest contribution to energy consumption. A near-ideal resonator could significantly reduce the power requirement in the future. By definition, the laser light used for cooling, preparation, and readout drives a dissipative process. In the case of cooling, heat must be transported away. In the case of preparation, the excitation of the qubit must be dissipated. For readout, the qubit is intentionally excited to a state that quickly decays while emitting a photon that is eventually detected. All of these laser processes are dissipative by design. Therefore, energy must be dissipated. However, in principle there is no interaction between the qubits and the laser light during the computation until the quantum state is projected. Therefore, the energy spent on cooling the system before preparation and readout can be considered a one-time energy cost, since it does not contribute to the energy consumption during

the actual computation. The energy consumed is therefore independent of the length of the computation and can be considered insignificant in the limit of an arbitrarily long computation. The delivered laser power can be measured using a power meter that probes the laser beams before they enter the vacuum receiver. Integrated over time, the required energy delivered by the laser beams can be estimated. The results are shown in table 5.6.2.

In addition to the one time energy expenses for the laser light, as shown in chapter 2, a microwave field is required in the Doppler cooling and sideband cooling step. In case of Doppler cooling it is required to close the cooling cycle while during sideband cooling it is required to drive the motional sideband transition. To estimate the microwave power required, the power delivered to the vacuum recipient has been measured using a Rhode und Schwarz spectrum analyzer to be $P_{MW} = 0.58\,\mathrm{W/ion}$ corresponding to a Rabi frequency $\Omega \approx 2\pi \cdot 33\,\mathrm{kHz}$. This exceeds the power required in the laser fields for the 369 nm laser beam and the 935 nm laser beam for re pumping by three orders of magnitude. The full term scheme of $^{171}\mathrm{Yb}^{+}$ can be found in the appendix in fig. D.1. The total energy required by the laser field and the microwave field adds up to $E_1 \geq 100\,\mathrm{mJ}$ per cycle of the experiment. The results are summarized in table 5.6.2

In contrast to the one-time cost of cooling preparation and readout, the microwave signal is required to perform a computation. By design, the interaction between the qubits is free of energy cost, since it is generated by a permanent magnet setup that produces the magnetic field gradient for the MAGIC scheme. For the half-adder circuit presented here, the dominant contribution of energy consumption is the π-pulses to implement the DD-sequences. In the case of the half-adder, three parallel microwave fields are required. The duration of a π-pulse is $t_\pi \approx 15\,\mu\mathrm{s}$, resulting in an energy dissipation per π-pulse of $E_\pi \approx 8.8\,\mu\mathrm{J}$. The measured power P_{MW} is transferred to the receiver via the SMA feedthrough. As shown in [7], inside the vacuum receiver, an additional coaxial cable connects the feedthrough to the circular waveguide, which is excited by a pin antenna. The waveguide then conducts the generated microwave field to the trap consisting of steel blade electrodes. A.Khromova in [7] states an output power loss of about 8 dB for the waveguide. Based on the dimensions of the waveguide calculated by S. Patrapasi in [75], the theoretically required microwave energy is $E_{\pi t} = 1.8\,\mu\mathrm{J}$. This theoretical estimation, together with the output power loss of 8 dB, the estimated energy required for a π-pulse on the σ_+-transition with a Rabi frequency $\Omega = 2\pi \cdot 33\,\mathrm{kHz}$ is $E_E \approx 11\,\mu\mathrm{J}$. This corresponds

to the measured power required and can be used to estimate the energy required for other pulses.

The energy required for a pulse given a fixed angle of rotation scales as:

$$E \propto P_{MW} \frac{1}{\Omega} \propto \frac{\Omega^2}{\Omega} = \Omega. \tag{5.6.1}$$

Reducing the Rabi frequency of the pulse, therefore, reduces the energy required for the single qubit rotation. Since the $\Omega_T \approx \Omega_\pi \cdot 10^{-3}$ the required energy to implement the Toffoli gate would be on the nJ scale. If all sources of incoherence are eliminated, which for the present setup makes DD-sequences obsolete, the CNOT gate would require at least one π-pulse to decouple the Toffoli target qubit from the qubits involved in the CNOT, and two $\pi/2$-pulses to implement the CNOT operation itself. This would make the CNOT gate three orders of magnitude more expensive in terms of energy required compared to the Toffoli gate. The ultimate goal of building a quantum computer that, when used as a

Gate		**MW Pulse**	**Dyn. decoupling**		**Total**
			# π-pulses	Cost	
NOT	Estimated	1.8 µJ	—	—	1.8 µJ
	Measured	8.8 µJ		—	8.8 µJ
CNOT	Estimated	1.8 µJ	$2 \cdot 120$	0.44 mJ	0.44 mJ
	Measured	8.8 µJ		2.1 mJ	2.1 mJ
Toffoli	Estimated	2.0 nJ	$3 \cdot 200$	1.1 mJ	1.1 mJ
	Measured	9.2 nJ		5.3 mJ	5.3 mJ
Half-Adder	Estimated	1.8 µJ	840	1.5 mJ	1.5 mJ
	Measured	8.8 µJ		7.4 mJ	7.4 mJ

Table 5.6.1: Estimated and measured power consumption of the experimentally realized gates. "MW Pulse" refers to the microwave energy required to implement the Hamiltonian. "Total" includes the cost of dynamical decoupling π-pulses.

classical computer, is still more energy efficient than a classical computer seems unrealistic. In such a classical application, each qubit could be replaced by a transistor. Controlling a quantum register, even in a very simple way, requires at least accurate timing. For example, the time at which a qubit state needs to be manipulated, e.g. a π-pulse needs to be applied,

	Laser 369 nm	Laser 935 nm	MW/ion	Duration	Energy
Doppler cooling	48.0 µW	1.35 mW	0.58 W	8.0 ms	14 mJ
Sideband cooling	0.16 µW	1.35 mW	0.58 W	60 ms	100 mJ
Ground state prep.	35.0 µW	1.35 mW	—	0.20 ms	0.28 µJ
Readout	48.0 µW	1.35 mW	—	3.0 ms	4.2 µJ
				Total	120 mJ

Table 5.6.2: Power and energy costs of one-time operations that contribute to the baseline energy expenditure.

needs to be stored in a classical numerical value, using already some classical bits to store this timing information. Even if the qubit control is idealized in a way that it does not need any electronics and therefore does not consume any energy, the sequence definition for the qubit manipulation still needs more electronics, since the circuit execution can be substituted. As long as the control of a qubit requires at least one transistor, the energy cost of a classical quantum computer will exceed the energy cost of a classical computer.

Nevertheless, the finding that the scaling of the energy cost of pulses is $E_P \propto \Omega \propto \frac{1}{T_P}$, where T_P is the duration of the pulse, allows us to estimate this part of the energy cost of quantum computation in the future, since this result is not restricted to classical computation, but is also valid for quantum computation.

5.7 Outlook

In this chapter, the classical half-adder has been investigated theoretically and experimentally. As mentioned above, a classical implementation of the Toffoli gate is not advantageous in terms of energy efficiency if the gate is used only as a classical gate. However, an advantage of the gate arises when it is modified to be a quantum Toffoli gate. The basic idea is sketched in this section. The extension of the gate mechanism to more control qubits is then briefly discussed.

5.7.1 A proposal for a quantum Toffoli gate

The Toffoli gate presented here is classical in the sense that the interaction between the control qubits is neglected. The unwanted coupling must be removed if a quantum version of the Toffoli gate is to be constructed. One possibility is to apply a correction to the gate after its completion, inverting one of the Toffoli control qubits, followed by a zz-interaction of the duration of the Toffoli gate. As shown in chapter 4, the effect of the evolution over the entire evolution time would cancel the coupling between qubits one and three. To protect qubit two from decoherence, either recoding is required, or J-tuning must selectively decouple qubit two from qubits one and three.

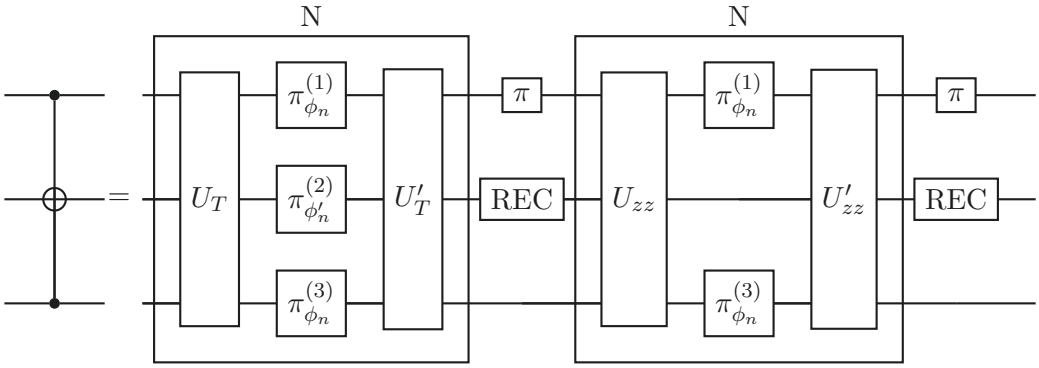

Figure 5.7.1: A possible extension to the classical Toffoli gate shown in this chapter is to incorporate the zz-coupling of qubits 1 and 3 and remove this effect by an effective refocusing step after the Toffoli gate. For this scheme, the evolution time would be effectively doubled.

5.7.2 J-Tuning and driving field

As described in chapter 4, the effective coupling between arbitrary qubits in a register can be achieved by an appropriately timed DD-sequence. In contrast to the Toffoli gate implementation and the perceptron gate implementation shown in chapter 6, for the derivation of J-tuning only a Hamiltonian consisting of $\sigma_z^{(i)}\sigma_z^{(j)}$ terms is considered. Without a driving field, the solution obtained is exact. For the gate implementation, which requires a driving field, the use of J-tuning is not exact, but it approximates the ideal J-tuned case. To quantify the approximation to the ideal J-tuned unitary, an approximation fidelity F_A can be defined as

$$F_A = 1 - \frac{1}{4}\sum_{ij} |U_{ij}^{(A)} - U_{ij}|, \tag{5.7.1}$$

which goes to 1 if the approximation $U^{(A)}$ approaches the exact U. With the rotation introduced in eq. (2.3.9), $R(\theta, \phi, \delta, \Omega)$, the approximated unitary is

$$U^{(A)} = \left[R(\frac{\theta\tau_b}{N_{avg}T}, \phi, J+\delta, \Omega) R((1-\frac{\tau_b}{T})\frac{\theta}{N_{avg}}, \phi, -J+\delta, \Omega) \right]^{N_{avg}}, \tag{5.7.2}$$

$$U = R(\theta, \phi, J(1-2\frac{\tau_b}{T})+\delta, \Omega). \tag{5.7.3}$$

Where θ is the angle of rotation assuming a resonant Rabi frequency Ω. ϕ is the phase, J is the coupling flipped at times τ_b, and N_{avg} is the number of spin flips of the control qubit during the evolution of the gate. The fidelity of the approximate unitary with J-tuning in the presence of a control field can be calculated. For the calculation $\theta = \pi$, $\Omega = 2\pi \cdot 30\,\mathrm{Hz}$, $J = 2\pi \cdot 30\,\mathrm{Hz}$, and $\delta = [0, 2J]$ were used. The resulting F_A as a function of N_{avg} and the relative J-tuning time τ_b/T is shown in fig. 5.7.2. For both cases of detuning $\delta = [0, 2J]$, it can be seen that the approximation accuracy $F_A \geq 0.99$ for $N_{avg} = 50$ and, respectively, $N_{avg} = 10$. J-Tuning in the case of an active control field is not an exact solution, but it is a good approximation.

5.7.3 Expanding the Toffoli gate to more control qubits

The basic idea of the Toffoli gate is that a narrow-band pulse selectively drives a rotation of π, if due to the effective field generated by the control qubits, the qubit resonance frequency

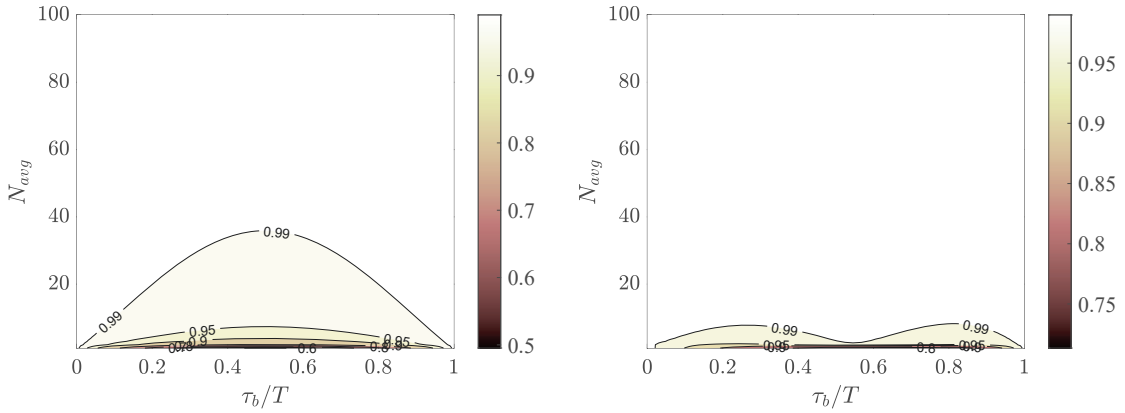

Figure 5.7.2: (a) Approximation fidelity F_A of a rotation $U = R(\theta, \phi, J(1-2\frac{\tau_b}{T})+\delta, \Omega)$ as a function of N_{avg} spin flips introduced to realize a J-tuning with relative delay τ_b/T where $\theta = \pi$, $\Omega = 2\pi \cdot 30\,\mathrm{Hz}$, $J = 2\pi \cdot 30\,\mathrm{Hz}$, and $\delta = 0$. Here eq. (5.7.1) is used to calculate the approximation fidelity using the unitary in eq. (5.7.3). (b) Approximation fidelity F_A with the same parameters as in (a) but with a fixed detuning $\delta = 2J$. For an increasing number of average steps N_{avg}, the approximation fidelity exceeds $F_A \geq 0.99$, making it feasible to be implemented in gates requiring a driving field Ω.

is shifted by a certain detuning. The duration of this narrowband tophat-pulse is chosen so that, if it is not resonant, the effective axis of rotation is tilted and a full $n \cdot 2\pi$ rotation is performed.

Assuming a register of qubits of size $N+1$ and an equal coupling of all qubits to the target, in principle, by a proper choice of the detuning δ, a gate can be constructed so that for a given number of $|1\rangle$ compared to $|0\rangle$ states occurring among the control qubits, the state of the target qubit flips.

A detuning $\delta = nJ$ would be compensated by having n more control qubits in the $|1\rangle$ state than in the $|0\rangle$ state. The Toffoli gate is a special case, where δ is chosen such that a flip of the target qubit occurs if and only if the control qubits are in state $|11\rangle_c$. Choosing $\Omega \approx J/2$ would allow closing all trajectories where the residual detuning does not vanish, while at the same time having $\delta \approx nJ$ allows trajectories for all possible control qubit states besides the one chosen to flip the target qubit. Thus, J-tuning allows the direct implementation of a quantum Toffoli gate with more than two control qubits.

5.8 Summary

In this chapter, the implementation of the Toffoli gate, as proposed by S. Bose in [76], has been modified by interleaving a dynamical decoupling sequence with the gate Hamiltonian. The implementation in the experiment has been demonstrated using the Toffoli gate to create an GHZ state in the computational basis. The Toffoli gate and a long-range CNOT operation were used to implement a half-adder circuit on three qubits. A stepwise evaluation of the performance of the classical gate has been demonstrated. Possible ways to improve the fidelity of the Toffoli gate were identified, such as using different RF sources for the RF to generate low Ω driving fields. A possible way to create a full quantum gate from this classical gate was formulated by adding a hypothetical disentangling step for the two control qubits. Additionally, extensions to Toffoli gates with three or more control qubits have been sketched. The given coupling topology requires the use of J-tuning in the extended gate implementation. Numerical calculations show that J-tuning can be used to implement gates requiring a driving field. Furthermore, the energy requirements in the current experimental setup have been measured and the energy requirements of the half-adder have been estimated.

The results obtained in this chapter are published as [75].

6

Perceptron gate

Neural networks implemented on classical computers have proven to revolutionize computer science. They can identify faces, read a handwritten document, or understand the spoken word. This classification power allows one to autonomously understand and translate a text, or to control a machine using multiple sensor inputs. This chapter reports on the implementation of a small quantum mechanical neural network (NN). The implementation reported here is based on the ideas of E. Torrontegui and J. J. García-Ripoll [81].

A single neuron is an essential element in biological systems that allows an organism to respond adaptively to its environment. A neuron is a cell that can produce or receive electrochemical signals. The excitation of a neuron is a direct response to its environment. If the external stimulus is large enough, the neuron can be activated. This external stimulus may come from other nearby neurons. This activation of the neuron can in turn stimulate other neurons through connections between them, forming a network. An important property of a biological neural network is its ability to learn. Learning is realized by strengthening the connections between neurons. This defines the circumstances under which a neuron can be activated. Because of this flexibility, a given number of neurons can solve different tasks based on the learned strength of their connections.

A classical mathematical neural network mimics this behavior [82]. Here, a neuron, or for the scope of this work, a perceptron, can be viewed as a function whose arguments are the states of other neurons. If the neurons can be ordered, it can be represented as a layered graph in which nodes correspond to neurons and edges represent the weighted input for each neuron. A simple example is given in fig. 6.0.1.

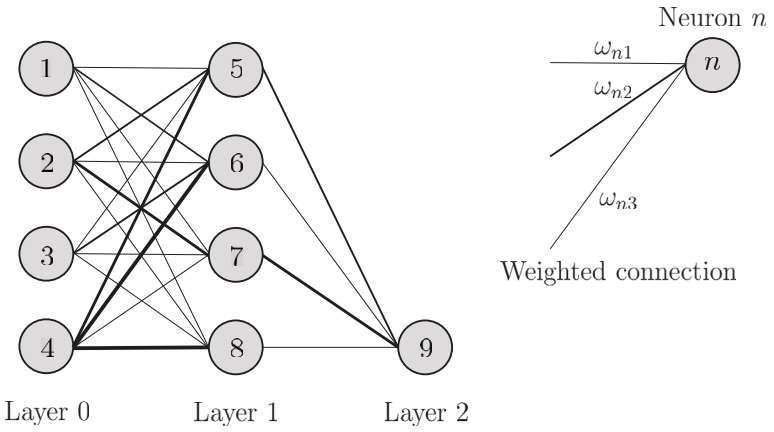

Figure 6.0.1: (left) Example of a three-layer neural network with nine neurons and weights indicated by different lines connecting each layer. (right) A perceptron controlled by weights ω_{nj} described the control field of the perceptron gate shown in eq. (6.1.1).

6.1 Perceptron

The state of a neuron is given by an activation function $s_n = f(x_n)$, where the input of the neuron is

$$x_n = \sum_{k<n} \omega_{kn} s_k - \theta_n. \tag{6.1.1}$$

Here, ω_{kn} is the weight of the input of neuron k to the neuron n, and θ_n is the neuron's bias. Suppose the function $f(x)$ is a continuous sigmoid function. In that case, it is proven that a three-layer neural network may serve as a universal approximation of an arbitrary continuous function of the input state [83].

In analogy, E. Torrontegui and J. J. García-Ripoll have shown that the quantum version of the universal approximator theorem holds [81]. This theorem states that any bounded continuous function $Q(\sigma_1, ..., \sigma_n) \in [-1, 1]$ of the quantum observables $\{\sigma_i\}_{i=1}^N$ can be reconstructed up to an error ϵ onto the state of a qubit using N input qubits and $M_\epsilon + 1$ applications of the quantum perceptron gate.

In a MAGIC trapped-ion quantum computer, the inherent all-to-all coupling J_{kn} can be associated with the weights appearing in the network ω_{kn}. The state of the input neuron s_k can be seen as the eigenstate of the control with respect to $\sigma_z^{(k)}$. Therfore the weight

can be associated with the coupling and the state of the input neuron can be associated with the $\sigma_z^{(k)}$ operator as

$$\omega_{kn} \to J_{kn} \text{ and } s_k \to \sigma_z^{(k)}.$$

In addition to the weighted inputs, the classical model of a perceptron requires a bias. The bias strength θ needs to be on the order of magnitude of the interaction strength and therefore might be generated by an additional neuron. In the system given in the experiment, the standard procedure of simulating a bias θ with other neurons can be used.

A Hamiltonian has been found to implement the desired sigmoid excitation of a perceptron [81]. The Hamiltonian reads

$$H(t) = \frac{\hbar}{2}\left(-\Omega(t)\sigma_x^{(j)} - x\sigma_z^{(j)}\right). \tag{6.1.2}$$

Here, the activation is

$$x_j = \sum_{i<j} J_{ij}\sigma_z^{(i)}\sigma_z^{(j)} - \theta_j, \tag{6.1.3}$$

where θ_j is the bias of the perceptron j. In our implementation, it will be generated by an additional qubit k as

$$\theta_j = J_{kj}\sigma_z^{(j)}. \tag{6.1.4}$$

The full Hamiltonian is

$$H = \Omega(t)\sigma_x^{(j)} + \sum_{i<j} J_{ij}\sigma_z^{(i)}\sigma_z^{(j)}, \tag{6.1.5}$$

where $\theta\sigma_z$ is absorbed in the sum.

The required sum of a weighted input for a perceptron [84] is shown in equation (6.1.1). As shown in chapter 4, tuning of the average qubits interaction strength is possible by applying J-tuning or by shaping of the trapping potential.

The ground state of the system is given in [81] as

$$|\psi\rangle = \sqrt{1 - g(x/\Omega)}|0\rangle + \sqrt{g(x/\Omega)}|1\rangle \tag{6.1.6}$$

for a driving field $\Omega \ll J$ with

$$g(x/\Omega) = \frac{1}{2}\left(1 + \frac{x/\Omega}{\sqrt{1 + (x/\Omega)^2}}\right), \tag{6.1.7}$$

whereas for a driving field $\Omega\sigma^x$ alone ($\Omega \gg J$) the ground state is

$$|+\rangle = \frac{1}{\sqrt{2}} \left(|0\rangle + |1\rangle \right). \tag{6.1.8}$$

The adiabatic theorem states that when a system is in its ground state and this ground state evolves slowly enough, the system will stay in its ground state [85]. This means that starting with the ground state $|+\rangle$, application of a large driving field $\Omega\sigma^x$ and turning it off slowly enough, the system will end up in the ground state given by (6.1.6).

The Hamiltonian (6.1.5) is similar to the Hamiltonian shown in Eq. (5.2.1). As shown in chapter 5, interleaving a driving field that generates a gate with a dynamical decoupling sequence is possible. Furthermore, as shown in section 5.7.2, J-tuning can also be applied with a driving field present. Therefore, all prerequisites to implement a perceptron gate are set.

To generate the sigmoid excitation of the perceptron, during the evolution with the Hamiltonian (6.1.2), the driving field $\Omega(t)$ has to be shaped in time. The only requirement to the driving fields amplitude is that it changes from $\Omega \gg J$ to $\Omega \ll J$ slowly enough that the state can follow. The exact shape can be chosen freely. It has been shown that a FAst QUasi ADiabatic (FAQUAD) [86, 87] state transfer can be achieved time efficiently. To minimize the required evolution time while ensuring an adiabatic state transfer, the driving field amplitude as calculated by E. Torrontegui is

$$\Omega(s) = \Omega_i(A_0) \sqrt{\frac{4A_f^4 \frac{1+\sqrt{5}}{2} s + (A_f^2 + (1-s) 4 \frac{1+\sqrt{5}}{2} A_f^2)}{(1-s)A_f^2 + s + 4\frac{1+\sqrt{5}}{2} A_f^2}}, \tag{6.1.9}$$

where $s = t/T_P$ is a dimensionless time with T_P being the gate time of the perceptron. Ω_i is the initial large driving field generated by a dimensionless microwave amplitude A_0, while A_f is a dimensionless microwave amplitude corresponding to Ω_f, where Ω_f is the final Rabi frequency at the end of the gate. For the adiabatic approximation to hold, the final driving fields amplitude needs to be small $\Omega_f \ll J$ to allow the eigenstate to be $|0\rangle$ or $|1\rangle$ in the z-basis. Different from the Toffoli gate's implementation, the evolution time of the gate is not fixed, since no condition like a full rotation around some axis needs to be met. Nevertheless, $\Omega_f \ll J$ is a challenging condition due to the limited dynamic range of the frequency generator available. The initial amplitude of the driving field needs to be as

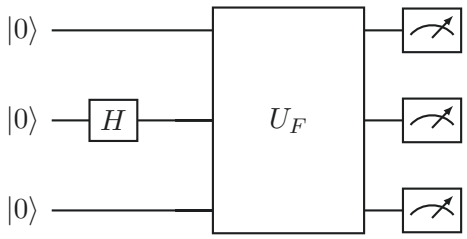

Figure 6.1.1: Circuit diagram of the perceptron gate, where the first Hadamard gate creates a superposition that is the eigenstate of the driving field that is applied during the unitary evolution of the FAst QUasi ADiabatic passage (FAQUAD) U_F.

big as possible, e.g. the frequency generator's output amplitude needs to start at $A = 1$ and needs to be ramped down to $A \approx 10^{-4}$. The signal has to be generated by a single frequency generator to ensure coherence of the microwave signal. A detailed description of the approximation of the FAQUAD ramp using a VFG150 frequency generator can be found in the appendix section C. The driving field is then interleaved with a $\mathrm{CPMG_{XY}}$-sequence consisting of 200 pulses and is modified according to chapter 5 to implement the gate.

The sequence for the perceptron gate is to prepare the perceptron or target of the gate in a state $|+\rangle$, which is an eigenstate to the applied driving field $\Omega\sigma^x$. Starting with $\Omega_i = \Omega(t = 0)$, a driving field is switched on instantaneously and is adiabatically ramped down to transfer the system to the σ^z eigenstate. This circuit is shown in fig. 6.1.1. The perceptron is controlled by its potential shown in eq. (6.1.3). The activation or excitation probability as a function of the control must be shown to demonstrate a working gate implementation. As shown in chapter 5, a small driving field generates a measurable Rabi oscillation. Nevertheless, the requirement for the gate is the adiabatic state transfer by ramping down the driving field to the regime $\Omega \ll J$. To observe an entire period of Rabi oscillations, the evolution time would be on the scale of seconds. Given the bare state coherence time on the order of $T_2 \approx 200\,\mu\mathrm{s}$ or the extended coherence time of the system using a DD-sequence on the order of some ms, a Rabi measurement on the second scale is challenging due to decoherence.

Since Rabi oscillations much slower than the coupling is challenging to be observed, the required amplitudes A of the frequency generator, in a low amplitude regime, are extrap-

olated to implement the perceptron gate.

The activation potential, which is generated by the control qubits, can be tailored using J-tuning to be:

$$\frac{x}{\Omega_f} = \frac{s_1 J_{12}^{eff} + s_3 J_{23}^{eff}}{\Omega_f}. \tag{6.1.10}$$

Here, J^{eff} is the effective coupling, Ω_f is the final amplitude of the FAQUAD ramp, and $s_k = \pm 1$ is the control qubits logical state. For the state $|0\rangle_k$ we have $s_k = -1$ and for $|1\rangle_k$ we have $s_k = +1$ accordingly. The J-tuned effective coupling or the input state can be varied to choose a specific input potential for the perceptron.

Figure 6.1.2 shows the scanned input potential with and without a bias θ. Due to the limitations of the frequency generator, the scanned parameter range has been split into multiple measurements. At first, the control qubits are set to $|00\rangle_c$ while the delay of the target qubit to both control qubits has been scanned in a range of $\tau_{b_2} = [0\,\mu s, 68\,\mu s]$ while the gates evolution time is $T = 15\,\text{ms}$ with 150 CPMG_{XY}-pulses for dynamical decoupling. Therefore following eq. (4.2.18) the effective coupling constant J_{12}^{eff} (J_{23}^{eff}) is scanned in a range $[J_{12}, 0]$ ($[J_{23}, 0]$). The final driving field Rabi frequency is $\Omega_f = 2\pi \cdot 8.1\,\text{Hz}$ while the coupling constant was $J_{12} = 2\pi \cdot 37.5(1.5)\,\text{Hz}$. This effectively realizes a scan of the input potential in a range from $x/\Omega_f = [-9.2, 0]$. For positive input potentials, the control qubits have been prepared in $|11\rangle_c$ implementing a scan of $x/\Omega_f = [0, 9.2]$.

The same experiment has been repeated to demonstrate the possibility of bias in the perceptron. However, instead of the target qubit's delay, the delay of one control qubit has been scanned. In this case, one control qubit biases the perceptron with $\theta/\Omega_f = J_{12}/\Omega_f = \pm 4.6$ while the effective range is limited to half the scanning range of two control qubits. Therefore, the measured perceptron's excitation for the scanning range of $x/\Omega_f = [-4.6, 4.6]$ with the bias beeing $\theta/\Omega_f = \pm 4.6$, shows a rising edge at the end of the scanning range.

Choosing the input state of the bias qubit allows one to choose the bias direction.

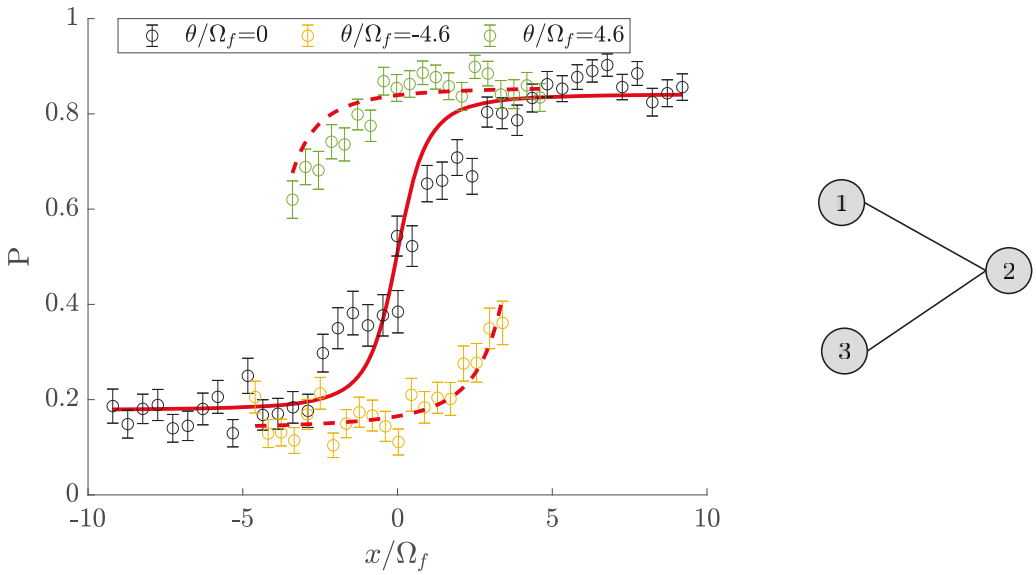

(a) (b)

Figure 6.1.2: (a) Perceptron activation with target qubit 2 in a three-qubit register controlled by qubit 1 and 3 as depicted in (b). Maximal coupling between qubit 1 and 2, and 2 and 3 respectively: $J_{12} = 2\pi \cdot 37.5(1.5)\,\mathrm{Hz}$, $J_{23} = 2\pi \cdot 37.5(1.5)\,\mathrm{Hz}$. Maximal amplitude step for the approximation of the FAQUAD ramp using a DDS synthesizer (VFG) $\delta A = 5 \cdot 10^{-4}$. Final amplitude of the VFG $A_F = 3 \cdot 10^{-3}$ realizing $\Omega_f = 2\pi \cdot 8.1\,\mathrm{Hz}$, start amplitude of the VFG at the beginning of the FAQUAD ramp $A_0 = 1$. Minimal VFG switching time $\delta t = 100\,\mathrm{ns}$, Rabi frequency of the applied dynamical decoupling sequence $\Omega_{DD} = 2\pi \cdot 27.95\,\mathrm{kHz}$, gate time without DD-pulses $T = 15\,\mathrm{ms}$, dynamical decoupling pulses on the control qubits 15 UR10 blocks, 150 pulses total. DD-sequence applied to the target qubit 150 $\mathrm{CPMG_{XY}}$-pulses. Scan of the activation potential x is implemented by a scan of the effective coupling constant J_{12}^{eff} and J_{23}^{eff} respectively by a delay of the DD-sequences of the control qubits following eq. (4.2.18).

The bias can be chosen freely using J-tuning. Figure 6.1.3 shows a scan of the perceptron activation, where the bias qubit generates a bias of $\theta = \pm J/2$. The scanned activation range therefore is $\theta/\Omega_f = [-0.5J/\Omega_f, -0.5J/\Omega_f]$ using the control qubit. This demonstrates the applicability of J-tuning to control the bias of a perceptron.

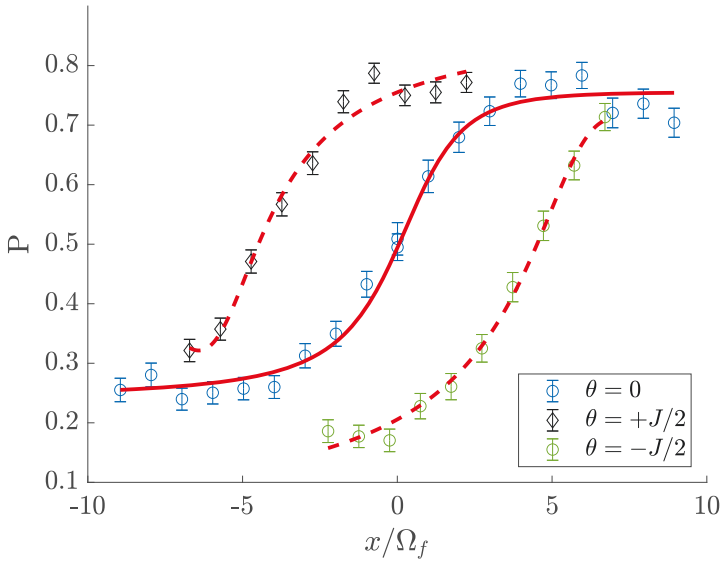

Figure 6.1.3: (a) Perceptron activation with target qubit 2 in a three-qubit register controlled by qubit 1. Qubit 2 is chosen as bias qubit. The bias here is $\theta = \pm J_{23}/2$ to show the flipping point of the target. For $\theta = 0$, qubits 1 and 3 are used as control qubits, doubling the scanning range for x/Ω_f effectively. Maximal coupling between the control qubit 1 and the target qubit 2 $J_{12} = 2\pi \cdot 37.5(1.5)\,\mathrm{Hz}$. Amplitude step size of the DDS synthesizer (VFG) $\delta A = 5 \cdot 10^{-5}$. Final amplitude of the VFG at the end of the FAQUAD ramp $A_F = 3 \cdot 10^{-3}$. Initial amplitude of the VFG for the FAQUAD ramp $A_0 = 1$. VFG switching time $\delta t = 50\,\mathrm{ns}$. Rabi frequency of the DD-sequences applied $\Omega_{DD} = 2\pi \cdot 28.2\,\mathrm{kHz}$. Gate time without DD-pulses $T = 15\,\mathrm{ms}$. DD-sequence on the control qubits 20 UR10 blocks, 200 pulses in total. On the target qubit 200 $\mathrm{CPMG_{XY}}$-pulses are applied. Scan of the activation potential x is implemented by a scan of the effective coupling constant J_{12}^{eff} and J_{23}^{eff} respectively by a delay of the DD-sequences of the control qubits following eq. (4.2.18).

Until now, the perceptron qubit was chosen to be the center qubit in a three-qubit register. Since a J-tuned control field controls the perceptron, this choice is arbitrary. In contrast to the Toffoli gate shown in chapter 5, the perceptron does not require a symmetric coupling. Using J-tuning, the perceptron can be chosen freely in a register. This is demonstrated in fig. 6.1.4, where qubit 1 is chosen to be the target qubit of the perceptron gate. The different coupling constants $J_{12} = 2\pi \cdot 37.5(1.5)\,\mathrm{Hz}$ and $J_{13} = 2\pi \cdot 30(1)\,\mathrm{Hz}$ of the control qubits to the target are taken into account using eq. (4.2.18) and eq. (6.1.10).

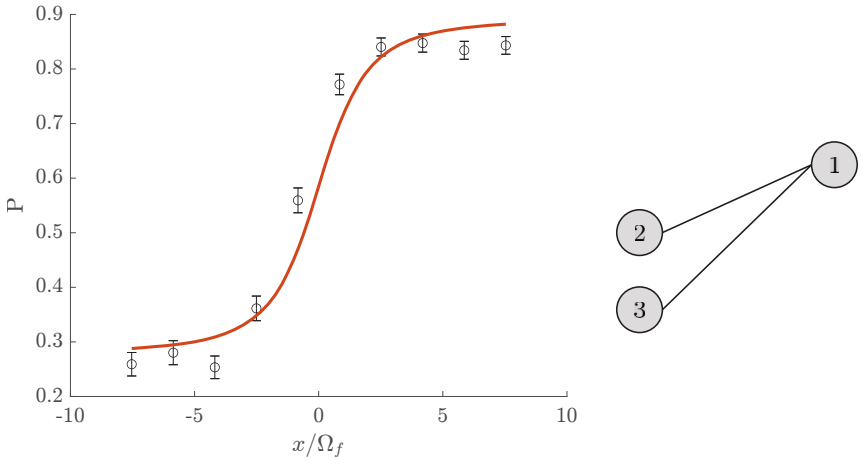

(a)

(b)

Figure 6.1.4: (a) Perceptron activation with target qubit 1 in a three qubit register controlled by qubit 2 and 3 as depicted in (b). Maximal coupling between qubit 1 and 2, and 1 and 3 respectively $J_{12} = 2\pi \cdot 37.5(1.5)\,\mathrm{Hz}, J_{13} = 2\pi \cdot 30(1)\,\mathrm{Hz}$. Parallel scan of the couplings $J_{13}^{eff}, J_{12}^{eff}$ using a delay between the control qubits and the target qubit's DD-sequence in a range of $\tau_{b1} = \tau_{b2} = [0\,\mu\mathrm{s}, 92.7\,\mu\mathrm{s}]$. Maximal amplitude step to aproximate the FAQUAD ramp $\delta A = 5 \cdot 10^{-5}$. Final amplitude of the VFG at the end of the gate $A_F = 3 \cdot 10^{-3}$, initial VFG amplitude at the beginning of the FAQUAD ramp $A_0 = 1$. Initial control qubits state $|11\rangle_c$. VFG switching time $\delta t = 50\,\mathrm{ns}$. Rabi frequency of the DD sequences applied $\Omega_{DD} = 2\pi \cdot 28.2\,\mathrm{kHz}$. Gate time without DD-pulses $T = 15\,\mathrm{ms}$. DD-sequence on the control qubits 20 UR10 blocks, 200 pulses in total. On the target qubit 200 $\mathrm{CPMG_{XY}}$-pulses are applied. Scan of the activation potential x is implemented by a scan of the effective coupling constant J_{12}^{eff} and J_{13}^{eff} respectively by a delay of the DD-sequences of the control qubits following eq. (4.2.18).

6.2 Neural network

Neural Networks (NN) can be seen as a graph, where each vertex represents a neuron, whereas each edge depicts an interconnect between the neurons as shown in fig. 6.0.1. The more complex the task to be solved is, the more neurons are necessary for a network. As

universal approximator, a neural network also can approximate basic logic gates. As a simple example the XOR gate can be implemented. It requires at least two layers in a neural network and therefore may serve as a proof of principle gate to be implemented.

To implement an XNOR gate, two perceptron gates must be executed consecutively. The overall evolution time $T = 30\,\mathrm{ms}$ is challenging due to the limited coherence time. Nevertheless, a two-layer neural network approximating an XNOR operation on the two control qubits could be implemented. For this implementation, the weights for both applications of the perceptron have been chosen based on estimations by E. Torrotegui and are optimized for actual implementation in the lab. This has been necessary, since the implementation of the perceptron has imperfections. The resulting weights selected to implement the XNOR gate are shown in fig. 6.2.1.

The two-layer neural network output shown in fig. 6.2.2 differs from the ideal outcome. The success probability is

$$P_s = \frac{1}{2}\left(P_{|00\rangle} + P_{|11\rangle} - P_{|01\rangle} - P_{|10\rangle}\right) = 0.327(13), \tag{6.2.1}$$

where $P_{|ij\rangle}$ is the probabiliy to find the target qubit in state $|1\rangle$ given the control qubits state $|ij\rangle$. This success probability must be compared with the expected coherence decay during the evolution of the NN. A Ramsey type experiment using the same evolution time and number of DD-pulses as the NN, but without the FAQUAD ramp, shows a Ramsey fringe amplitude of $A = 0.25(3)$. The Ramsey fringe contrast and the success probability of the XNOR gate differ by $P_s - A = 0.08(3)$ and are therefore comparable, although both are subject to fluctuations. Since no adiabatic gate is performed during the Ramsey fringe amplitude measurement, the errors in the Ramsey experiment are due to decoherence processes as well to imperfections in the applied dynamical decoupling sequence. Therefore, no significant deviation is found within the fluctuations of the coherence time and the fluctuations of the success probability of the XNOR gate implemented by a two-layer neural network. It should be noted that both experiments are challenging because the bare state coherence time is $T_2 \approx 200\,\mu\mathrm{s}$, which is 150 times shorter than the evolution time of the neural network.

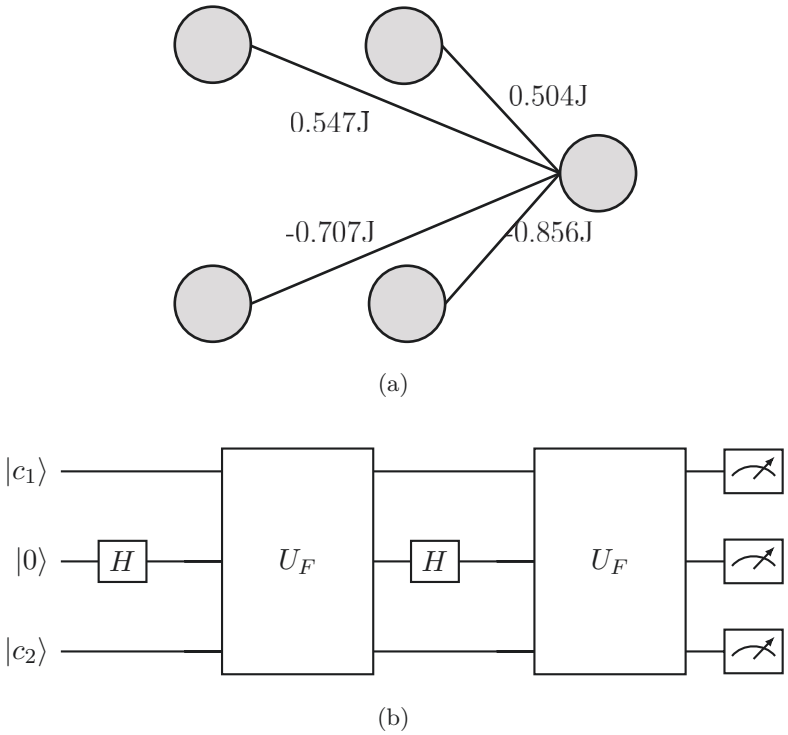

Figure 6.2.1: (a) Two layer neural network implementing a XNOR operation of input qubits 1 and 3 while the target qubit is qubit 2. (b) Circuit diagram of the neural network implemented to identify the states with the same input. The weights indicated in graph (a) are implemented using J-tuning and are updated during the second application of the perceptron gate.

6.3 Outlook

To implement the perceptron gate described in this chapter, a qubit has been used to provide a bias field $\theta = J^{eff}\sigma_z$. Therefore, the bias is limited by the coupling of the qubits. Another option would be to implement a detuning of the FAQUAD ramp to implement an arbitrary bias. As shown in chapter 2, the error of the qubits addressing frequency exceeds the coupling of the qubits, rendering a direct implementation of a detuned field on the scale of Hz difficult. Nevertheless, as shown in chapter 5, using a dynamical decoupling sequence allows tolerating bigger addressing frequency errors. At the same time, a selective detuning on the Hz level is possible. This way to bias the perceptron would eliminate the qubit overhead in a neural network.

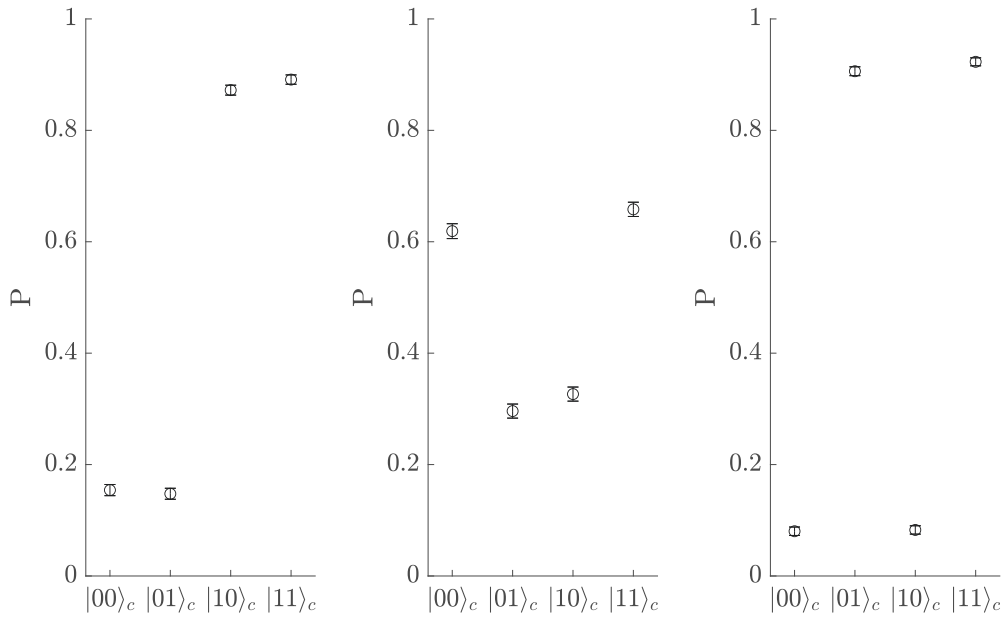

Figure 6.2.2: (a ,b, c) Measured excitation probabilities after the implementation of an XOR gate where qubit 1 (a) is the input qubit and qubit 3 (c) is the second input. The excitation probabilities here are shown as a function of the control qubits input states $|jk\rangle_c$. The gate parameters were: Evolution time per perceptron $T_P = 15\,\text{ms}$ DD-sequence on the target qubit 200 CPMG_{XY}-pulses, 20 UR10 blocks on the control qubits with $\Omega = 2\pi \cdot 28.2\,\text{kHz}$. FAQUAD ramp parameter $A_0 = 1$, $A_F = 2.14{\cdot}10^{-4}$ FAQUAD amplitude step $\delta A = 5{\cdot}10^{-5}$, minimal FAQUAD step duration $\delta t = 150\,\text{ns}$ delays of the control qubits DD-sequence for perceptron 1 $\tau_{b_1}^{(1)} = 17\,\mu\text{s}$, $\tau_{b_2}^{(1)} = 86\,\mu\text{s}$ for perceptron 2 $\tau_{b_1}^{(2)} = 18.6\,\mu\text{s}$, $\tau_{b_2}^{(2)} = 69.6\,\mu\text{s}$.

Further more, in this chapter, the RF signals to control the qubits were synthesized using three VFG150 frequency generators. The frequency generator used in the experiments described in chapter 4 would eliminate the need to approximate the FAQUAD ramp with a stepwise constant driving field. However the AWG used in chapter 4 was installed only after the experiments in this chapter were conducted. Using the AWG as a source of microwave control signals would also allow to extend the number of ions controlled simultaneously while eliminating the memory limitations of the VFG150 frequency generators.

The perceptron gate can be directly generalized to an arbitrary number of control qubits, given that they are directly coupled to the target qubit and are therefore located in the

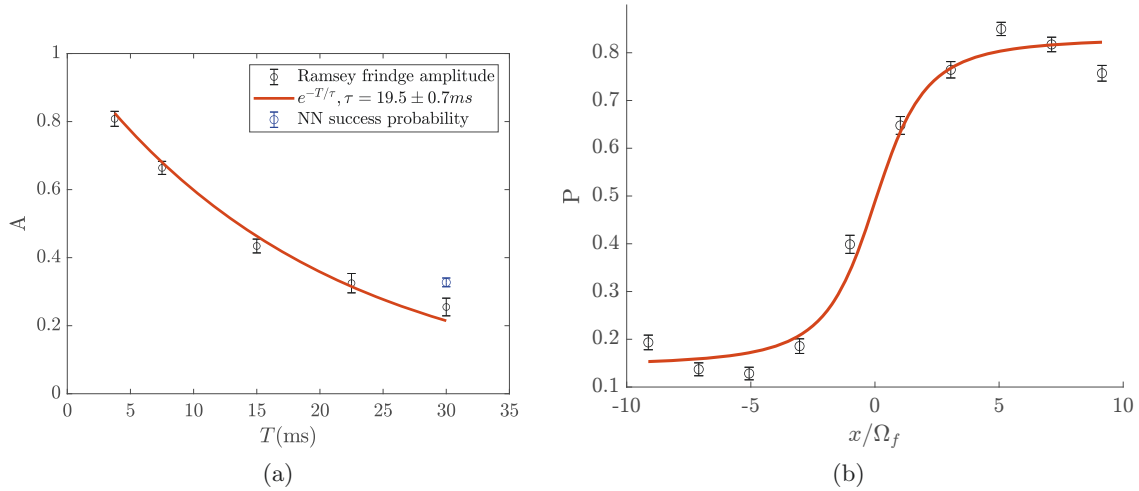

(a) (b)

Figure 6.2.3: (a) Decay of Ramsey fringe amplitude as a function of evolution time. The last measurement point at $T = 30\,\text{ms}$ was measured interleaved with the NN shown in fig. 6.2.2. The used DD-sequence was 400 CPMG_{XY}-pulses, to be comparable with the execution of two layers of perceptrons. Measurement points for other evolution times where conducted on the same day without interleaving and adjusting the number of DD-pulses to keep the same DD-period. (b) Perceptron measurement interleaved with the measurement of the NN shown in fig. 6.2.2. Initial state $|00\rangle_c$ $T = 15\,\text{ms}$ 200 CPMG_{XY}-pulses on target and 20 UR10 blocks on the control qubits with $\Omega = 2\pi \cdot 28.2\,\text{kHz}$. FAQUAD ramp parameter $A_0 = 1$, $A_F = 2.14 \cdot 10^{-4}$ FAQUAD amplitude step $\delta A = 5 \cdot 10^{-5}$, minimal FAQUAD step duration $\delta t = 150\,\text{ns}$. The delay of the control qubits was scanned in a range $\tau_b = [0\,\mu\text{s}, 82.8\,\mu\text{s}]$. The NN success probability is found to exceed the Ramsey fringe contrast at the gate time.

same register. In such a scenario, J-tuning allows tuning the coupling of all control qubits to the target at once, so that a perceptron controlled by multiple qubits in a register can be executed in one step. As for the Toffoli gate implementation shown in chapter 5, the gate Hamiltonian (6.1.2) ignores the coupling between the control qubits.

6.4 Summary

In this chapter the implementation of the perceptron gate suggested by E. Torrontegui, and J. J. García-Ripoll [81] has been described. For this, several techniques introduced in this thesis have been used. The gate, as proposed, relies on an adiabatic state transfer

that is realized by a Fast Quasi ADiabatic (FAQUAD) passage. The FAQUAD passage is realized by a stepwise approximation of a driving field's trajectory. Since the activation of a perceptron gate depends on the weighted input potential of control neurons, J-tuning was used to select the desired coupling reflecting the weights of the control neurons. Since the gate time required for the gate's implementation is on the order of several ms, a dynamical decoupling scheme is introduced during the gate's evolution following chapter 5.

This technique allowed us to measure the perceptron excitation as a function of its effective activation potential. To realize a bias of the perceptron, one of the two control qubits can be used to generate a bias for the perceptron. The shift of the perceptron's activation as a function of the bias field has been demonstrated.

A two-layer neural network has been implemented to approximate a XNOR gate to demonstrate a small use case for a neural network. The success probability of this two-layer neural network is reduced but comparable to a Ramsey fringe amplitude measured after the same evolution time using the same DD-sequence. This indicates that the perceptron gate implementation is subject to the same sources of noise as the MAGIC phase gates, and that improvements in overall fidelity would also benefit the perceptron gate.

The results obtained are partially published as [88].

7

Summary and outlook

In this thesis, novel methods for trapped-ion quantum computing are explored. A MAGIC-based trapped-ion quantum computer with a permanent magnetic field gradient and a harmonic trapping potential generates an all-to-all two-body coupling between qubits in a quantum register. The all-to-all interaction in a quantum register is a tool to parallelize quantum computing and to directly implement multi-qubit gates. In chapter 4 a method that uses only a pulsed dynamical decoupling sequence to tune the coupling between qubits is presented. Up to a register size of four qubits, it is shown how J-tuning can be used to implement a desired coupling topology. The chosen example realizes an equal coupling between all four qubits. Using J-tuning, a coupling matrix can be synthesized column by column. Therefore, J-tuning provides a quadratic improvement over pairwise sequential interaction between pairs of qubits. A second example is the parallel execution of conditional gates in a quantum register. The partitioning of a register into non-interacting sub registers can be achieved by choosing a different repetition rate of dynamic decoupling pulses on a sub register of qubits. Using this method, J-tuning can be applied within sub registers of qubits, enabling parallel quantum computation. The choice of qubits to form a sub register is arbitrary, allowing parallel execution of quantum algorithms on sub registers. A simple algorithm to compute the required pulse timings is demonstrated.

Furthermore, section 5.2 shows how the driving fields required to implement a gate can be interleaved with a dynamic decoupling sequence. This was used to demonstrate a three-qubit Toffoli gate with a fidelity of $F = 0.58$ and a 99% confidence interval of $F_{0.99} = [0.15, 0.70]$. The Toffoli gate is then used in a half-adder circuit consisting of a Toffoli gate and a CNOT gate, which reduces the circuit depth compared to the decomposition in next neighbor conditional gates. The fidelity of the half-adder circuit is $F = 0.61$ with a 99% confidence interval of $F_{0.99} = [0.37, 0.67]$. Half-adders are a fundamental

building block of arithmetic operations in classical computers. The classical computing infrastructure contributes significantly to the world's energy consumption. The emerging quantum computing industry will contribute to this demand, making it worthwhile to study the energetics of quantum computing. As a prototypical system, the half-adder implementation shown in this thesis is used to estimate its energy consumption. The primary energy demands in the current setup are the trap drive and the microwave signals used for local rotations applied to the participating qubits.

The combination of J-tuning and driving fields is studied numerically in section 5.7.2 and it is shown that a Hamiltonian consisting of a driving field and an effective J-coupling can be approximated. The combination of J-tuning with a driving field is then used to implement a perceptron gate on three qubits. Here, the perceptron gate is realized by an adiabatic state transfer, while J-tuning is used to select a desired interaction strength between the two control qubits and the target. In section 6.2, a two-layer neural network is implemented to realize a XNOR operation.

In order to scale up the current quantum computer to a useful device, it is necessary to increase the number of qubits and their interaction strength. J-tuning becomes a tool to implement multi-qubit gates in larger quantum systems. For example, it allows the direct implementation of gates that operate on more and more qubits. Both the perceptron gate and the Toffoli gate can be generalized to more than three qubits, demonstrating the inherent scalability of a MAGIC-driven trapped-ion quantum computer. Nevertheless, there are still challenges to be overcome in future devices.

A critical step in overcoming these challenges is the automated operation of the system. Within this thesis, the automated operation of the lab has been implemented up to the limitations given by the available hardware. An automatic loading procedure has been installed, following the procedure outlined in section 2.8.1, based on live analysis of camera images. In section 2.8.2 the automated laser scanning procedure is outlined, while section 2.8.3 describes the active stabilization of the Doppler cooling fluorescence, which allows to compensate the relative drift of the laser reference cavity of the 369 nm laser by observing the optical fluorescence during the experiments. This allows drift rates up to $2\pi \cdot 240\,\mathrm{kHz/s}$ to be compensated. These routines, together with the automatic recalibration of addressing frequencies developed in previous work, allow the user to focus on the implementation of quantum gates and algorithms.

The sympathetic multi-tone sideband cooling significantly reduced the experiment time per cycle. Prior to this work, sideband cooling of an ion crystal required $\approx 120\,\mathrm{ms}$ per cooled vibrational mode. Applying the parallel cooling scheme to three vibrational modes as described in section 2.7 requires $\approx 60\,\mathrm{ms}$, achieving a sixfold speedup of the sideband cooling step. Effectively, the repetition rate could be increased up to five times due to the comparatively short times of Doppler cooling, preparation, coherent operation and readout, which require less than 20 ms. Optimization of the parameters of this cooling scheme is efficiently implemented by a minimal experiment to observe the excitation of up to three motional modes simultaneously as a function of the cooling laser intensity.

Automated recalibration of the addressing frequency of the qubits allows, besides precise addressing, the observation of the magnetic field at the ion's position. The magnetic field gradient was found to be $\partial_z B = 19.09(1)\,\mathrm{T/m}$. Assuming a constant magnetic field gradient generated by the installed permanent magnets, the position of the ions can be determined. Chapter 3 describes the observation of a single ion and the measurement of DC forces with a sensitivity of $2.2 \cdot 10^{-23}\,\mathrm{N}/\sqrt{\mathrm{Hz}}$. By evaluating the frequency calibration data obtained during the measurements presented in chapter 4, the ion's position and corresponding long-term thermal stability of the axial trapping potential were measured. The relative stability of the ion coupling over one day $\sigma J/J = 2.6 \cdot 10^{-4}$ was determined as described in section 3.3.

The main challenge in the further development of the MAGIC trapped-ion quantum computer is the susceptibility of the qubits to magnetic fields. Magnetic field perturbations can be either external magnetic field perturbations or indirect electric field perturbations that change the position of the qubits in the magnetic field gradient, so that the electric field perturbations indirectly create a magnetic field perturbation that limits the coherence of the qubits. In future quantum processors, external magnetic fields can be shielded. Controlling the electric field noise seems to be the most promising strategy to reduce qubit dephasing and consequently improve the fidelity of multi-qubit gates. After the measurements in this work were completed, two qubit-gates were investigated on the same experimental setup and it was shown that two-qubit fidelities in the 99% range are already possible with the existing setup [89]. Therefore, it seems reasonable that further improvements in dynamical decoupling strategies will allow for high-fidelity multi-qubit gates.

8

Appendix

A Hardware

Experimental control

DSP	Jäger GmbH ADwin-Pro - Pro-CPU-T9 - Ethernet computer link - 2x DIO 32 - AIN8/12 - AOUT8/16
Experiment sequence	National Instruments LabVIEW 2015
DAC	PLUG-IN Electronics USB-3112
Frame grabber card	BitFlow Neon-CLB CameraLink

Paul trap

Function Generator	RigolDG1022Z
Power amplifier	RFPA 1500-20
RF Helical resonator	Prague University Ivo Polak's design
Permanent magnets	Magnetic Component Engineering (UK) Ltd SmCo tubes S2869 [7]

VFG synchronization

Atomic clock	Stanford Research Systems FS725
4-way Power splitter	Mini-Circuits ZCSC-3-R3+
Schmitt trigger	In-house [90]
Data flip-flop	In-house [91]
TTL Fan-out	In-house [90]

RF control chain

AWG	Agilent M8190A
RF sequence	In-house VFG-150 Versatile Frequency Generator
RF power amplifier	Globes 10W PA Elisra (+35dB)
RF power amplifier	Microwave Amplifiers Ltd AM43-12.4-12.8-43-43 (+45dB)
RF pre-amplifier	Mini-Circuits ZFL-500LN+
RF pre-amplifier	Mini-Circuits ZX60-183A+
RF pre-amplifier	Mini-Circuits ZX60-14012L+
Power supply (for AM43)	TOELLNER TOE 8851-16
RF low-loss cable	Elspec Phase Master 300 PM300-SMA11-SMA11-1500
Dual loop PLL oscillator	MITEQ DLCRO-010-12568-3-15P
MW switch	Narda SPST S213D
3-way Power cominer/splitter	Mini-Circuits ZFRSC-183-S+
3-way Power cominer/splitter	Mini-Circuits ZFRSC-2-1W+
4-way Power cominer/splitter	Mini-Circuits ZCSC-3-R3+
High-pass filter	Mini-Circuits SHP-50+
MW mixer (SSB)	Maki SSB-0618MXW-2
MW attenuator (-10dB)	Elisra MW21110
MW attenuator (-6dB)	Mini-Circuits BW-S6W2+
MW attenuator (-3dB)	Mini-Circuits BW-S3W2+
MW isolator	AtlanTecRF ACI-20240-SF-SF (5W)
MW isolator	TKI Ferrit IC 12,5 (1W)
MW isolator	TKI Ferrit IC 12,5-10W (10W)
MW isolator	(Unknown) MW 11218
MW isolator	MSC Microwave Ltd MCSM 0616 P-0190-08 (25W)
MW isolator	Raditek RADI-10-15-S3-1WR-60W Fwd-g18 (60W)
MW isolator	UIY UIYCI1220A10T13SF (60W)
MW termination	api technologies corp. 50W SMA termination TS180M-50W

Vacuum Components

Ion Getter Pump	StarCell VacIon Varian 919-0110 20l/s
Vacuum Controller	Varian MiniVac Controller 2008 Model 929-0290

Helmholtz Coils

3-channel power supply	Low residual ripple power supply Toellner TOE 8733-2

Optical Resonator

CF Windows (369 laser)	Kurt J. Lesker Company UV Quartz DN16CF VPZL-133Q
Lemo cable	Lemo cable Lemo Gmbh FGG.1B.306.CLAD52
Lemo connector (6 pins)	Air-tight connector Lemo Gmbh HGG.1B.306.CLLSV
Lemo connector	Air-tight connector Lemo Gmbh HGP.00.250.CTLSV
Pressure measurement	In-house μTrap MPX4100A [92]

AOM Components

Acousto-optic modulator	AOM (new) 90 MHz ISOMET AOM 1206C-833
Acousto-optic modulator	AOM 960 MHz Brimrose TEF-1050-50-369
AOM driver (SUB-D9 port)	Brimrose VFF-1050-50SPS-B1/B2-C1
Acousto-optic modulator	AOM 115 MHz Crystal Technology 31110-125
Voltage-controlled oscillator	VCO (for old AOM 65 MHz) Mini-Circuits ZX95-100-S+
Voltage-controlled oscillator	VCO Mini-Circuits ZX95-200-S+
Five-Axis Kinetic mount	Newport Five-Axis Aligner 9081-M
Stable mounting	Radiant Dyes RD-PDT-B

Lasers

Laser diode (369 nm)	Nichia NDU1113E 20 mW
Laser diode (399 nm)	Unknown
Laser diode (638 nm)	Thorlabs Mitsubishi ML520G54-01 110 mW
Laser diode (935 nm)	eagleyard photonics EYP-RWE-0980-08020-1500-SOT02-0000 (serial AG-02607) 1 mW
Fiber collimator	Schäfter+Kirchhoff 60FC-4-A11-01
Electro-optic modulator (EOM)	Photline NIR-MPX800 for 935 laser

Ion Detection

EMCCD Camera	Andor iXon Ultra 890 DU-897U-CS0-EXF X-8188
EMCCD software	Andor Solis 64bit 4.28.30001.0
Photo-multiplier tube	Hamamatsu R5600P

B AWG Sequencer

- Direct Digital Synthesizer (DDS)
  A direct digital synthesizer generates a continuous monochromatic RF signal using amplitude, frequency, phase, and duration parameters. It calculates a digital amplitude at time t and transfers it to the DAC at sampling rate f_s. The digital amplitudes encode a sinusoidal signal of a given amplitude, frequency, and phase at a given time. To generate a top-hat π- or $\pi/2$-pulse, a time is required for which the signal is generated. Using a DDS is therefore a reasonable choice if only a few qubits need to be addressed. If multiple qubits need to be addressed simultaneously, it is necessary to operate one DDS per qubit and add their output signals before the upmixing and amplification stages of the microwave chain to generate a multi-tone RF field. The DDS used for experiments with up to three qubits is the VFG150.

- Arbitrary Waveform Generator (AWG)

  An Arbitrary Waveform Generator (AWG) is a device for generating arbitrary waveforms. Synthesis can be done by precomputing an RF waveform as a set of voltage amplitudes a_n. Given a fixed sampling rate of a DAC, the signal amplitude at time t_n is given by $a_n = A(t_n)$, so that each waveform is stored in the memory of the AWG prior to signal generation. A typical sampling rate used in this work is 1 GS/s (giga samples per second). It is required to synthesize frequencies in the IF range of $30 - 80$ MHz. Creating a longer RF signal for the AWG means more samples to calculate and store in memory. The key advantage of an AWG over a DDS would be its ability to encode an arbitrary number of RF tones in amplitudes $A(t_n)$ simultaneously. An AWG is therefore able to address many qubits simultaneously. In contrast, one DDS per qubit is required to generate a polyphonic RF signal. As the number of qubits increases, an AWG becomes advantageous over a DDS, with the drawback

of the massive data rate required to generate the RF signal.

An Agilent M8190A AWG was used for the experiments requiring four RF tones in parallel, as used in chapter 4. The bottleneck when using an AWG is the limited memory of the instrument and the time required to precalculate and upload the waveforms to the instrument.

The simple method of writing a sequence into the memory of the AWG for each run of the experiment is time consuming and memory inefficient. At a sampling rate of 1 GS/s (giga samples per second), an amplitude resolution of 14 bits, and an experiment run time on the order of 5 ms per run of the experiment, 70 MBit of data is required. A typical experiment presented here to determine the J-coupling as described in chapter 4 consists of 21 points to sample 21 different phases for a Ramsey readout pulse, 100 repetitions to achieve the required statistical significance, and two different control qubit states, totaling up to 294 GBit of AWG data. To save memory and computation time, the sequencing capabilities of the AWG can be used. The memory in the device is divided into segments. A segment is a chunk of waveform data that can be selectively transferred to the DAC. Due to electronic limitations, a segment must contain a minimum number of samples to allow the hardware to load the data from memory in real time. The minimum segment length is 12336 samples. During playback, the segments played can be selected in a sequence table. Sequencing allows to reuse parts of the AWG memory.

A typical experiment consists of varying parts of the waveform from measurement step to measurement step. For each measurement of the J-coupling, a Ramsey-type experiment with 21 different readout phases was performed to extract a phase of the qubit from a fit of the oscillating excitation probability. For each step, the pulse sequence is identical except for the readout pulse, which varies with each step. Therefore, the fixed part of the waveform can be played for each cycle of the experiment, followed by a $\pi/2$-readout-pulse, which is different for each measurement point. A DD-sequence consists of π-pulses and times with no signal. Although the signal before the readout pulse can be repeated, it is advantageous for storage that the times between the DD-pulses are not only filled with zero amplitudes. The sequencing option of the AWG allows to generate a sequence table, which defines the order in which the segments are to be played. It is advantageous to predefine a segment that contains only amplitudes of value 0 and has the duration of a

minimal segment. During the execution of a quantum circuit on a MAGIC trapped-ion quantum computer, there are several waiting times that allow the qubits to interact. The segment containing only 0 amplitudes can be repeated in such waiting times as defined by the sequence table. Since it contains no signal, it can be played at any time without affecting the coherence of the RF control signals, thus saving memory. To allow the AWG to jump from one part of its memory to another, e.g. from one segment to another, it must have a minimum linear playtime. The minimum segment length is therefore 12336 entries. Figure B.1 illustrates a Ramsey type experiment to measure the coupling between two qubits in the J-tuned case. Uploading a segment to the device has some overhead to initialize a connection. Therefore, it is advantageous to upload as few segments as possible. To minimize this overhead, adjacent segments can be combined into a block. As mentioned above, there is a minimum duration of a segment, but they can be longer. A block is a set of adjacent segments of minimal length that are combined to form a segment of longer length. This is the case, for example, when a pulse is longer than a single minimum segment, or when it crosses the boundary between two minimum segments. These minimum segments can then be considered as a block and can be loaded into a longer segment in the device at once. The procedure for calculating the signal for an experiment follows these steps:

1. Loop over each step of the experiment, one step corresponds to one measurement point to be sampled.
    - Loop over each qubit addressed during the experiment.
        - Define the start time of the waveform in machine units.
        - Calculate waveforms using mathematical expressions.
        - Define the stop time of the waveform in machine units.
        - Flag if the waveform changes during the experiment.
2. Find the maximal duration of the experiment.
3. Generate minimal segments according to the maximal duration of the experiment.
    - Loop over all steps.
        - Initialize all segments as empty.

- Loop over all waveforms in this step. There is a waveform for each qubit in each pulse in each step.
  - Find the start minimal segment.
  - Find the stop minimal segment.
  - Flag all segments which contain a signal.
  - Flag segments variable if their waveform is flagged as variable.
  - Find the start sample in the minimal start segment.
  - Find the stop sample in the minimal stop segment.
  - If the minimal start and stop segment are identical, add the signal to this segment. Flag the segment as variable, if the waveform is variable otherwise:
    - Add waveform samples to the start segment, from start sample in the segment till the end sample in the segment and flag as variable if the waveform is variable.
    - Add waveform samples to the stop segment, from start sample in the segment till stop sample if the waveform is variable flag the segment accordingly.
  - If the waveform extends over at least three segments, loop over intermediate segments
    - Add the waveform to intermediate segments.
    - Flag intermediate segment as variable, if the waveform is variable.

4. Generate Blocks.

- Loop over each step.
  - Find adjacent minimal segments that contain a signal.
  - Generate a block containing minimal segments. This block might now be

longer than a single minimal segment.

- Flag the block as variable, if it contains at least one variable segment.

5. Upload blocks to segments in the device.
   - Upload constant blocks to segments.
   - Upload variable blocks to segments.
6. Calculate the sequence table.

This procedure for minimizing memory requirements for an experiment is graphically illustrated in fig. B.1. The resulting segment table is shown in table B.1. The resulting sequence table is shown in table B.2.

The sequencing option allows to play a segment in a loop. It is used during pauses that exceed the minimum segment length. The pause segment will be repeated accordingly. In addition, the first segment contains no signal and is used to wait for an external trigger. This external trigger is provided by the real-time experiment control system after the qubits have been prepared in $|0\rangle$. From this point on, the AWG only performs coherent qubit control. After the waveform playback from the AWG is finished, the real-time control system continues with the readout of the qubits' states.

Although the AWG can loop over segments, it is unlikely to repeat a segment containing a waveform without phase jumps. Each waveform can contain multiple signals of any frequency. The architecture of the AWG requires a fixed sample rate, a minimum number of samples per segment, and a minimum granularity of segment length. Since the experiment requires a distinct phase of the waveforms, repeating waveforms would require that the playtime and the signal period match. Since the required frequencies are arbitrary, it is unlikely to repeat a signal segment.

This method reduces the amount of memory required for an experiment. However, this method is limited. For example, if a waveform parameter is changed for each step during the experiment. For example, if the amplitude of a driving field is changed in each step. In such a case, the entire waveform must be uploaded to the instrument for each step. Thus, the efficiency of the method depends on the experiment.

So far, the method has only been optimized for memory consumption of the frequency generator, but not for computation time or memory consumption on the host computer. The first step in optimizing the computation time is to divide the procedure into three parts. In the first part, no actual waveforms are calculated, but the start and stop times are calculated and assigned to segments. The second part is memory optimization, while the third part calculates and transfers the waveforms. In contrast to the implemented method, in which the waveforms are stored in memory and copied from one variable to another, these multiple storage and copying processes can be optimized. This optimization will be critical in the future, as the expected longer coherence times and increased number of qubits will increase the length and complexity of waveforms.

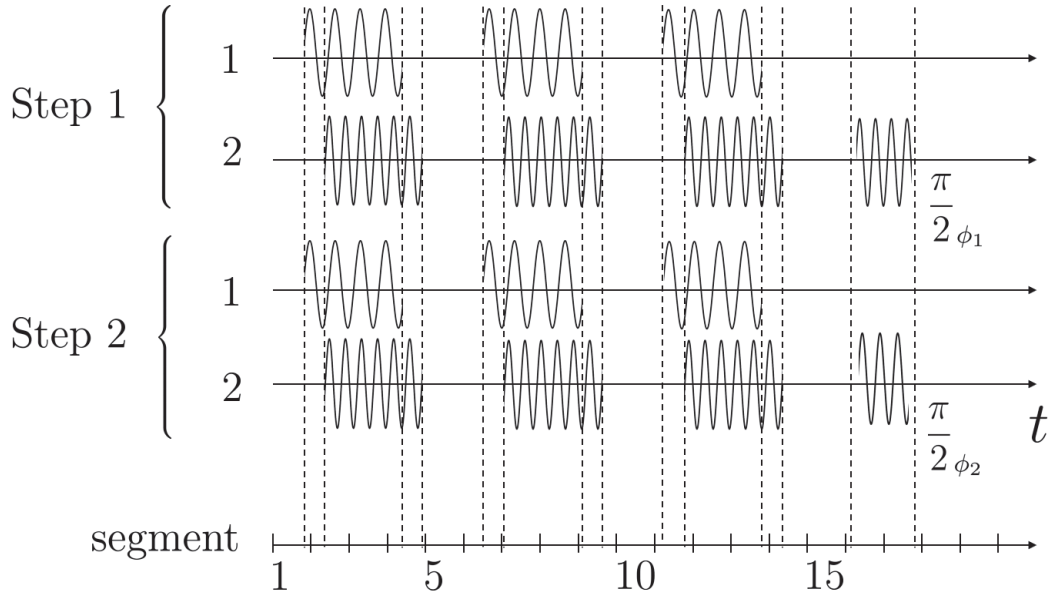

Figure B.1: An instructive example of a typical multitone signal synthesized for J-tuning measurements. In this example, two DD-sequences are applied to qubit 1 and 2 for a fixed evolution time in two steps, and a $\pi/2$-readout-pulse is applied to qubit 2 at the end. All waveforms addressing different qubits but assigned to the same step are summed, allowing a single DAC to produce a waveform that simultaneously addresses multiple qubits. Here, each signal shown in row 1 corresponds to a π-pulse on qubit 1. The vertical dashed lines indicate the start and stop times of the pulses. The bottom line shows the segment number at which a signal starts or stops, assuming the same minimum segment duration. This pulse sequence can be efficiently stored in AWG memory because the parameter changed from step 1 to 2 is the phase ϕ of the Ramsey pulse. Although a DD-sequence is used in steps 1 and 2, it is sufficient to store only one in the generator memory. In addition, several segments do not contain a waveform, so during playback there may be instances of the same segment containing only amplitudes of value 0. The assigned segments and the resulting sequence table are shown in table B.1 and table B.2.

min segment	1	2	3	4	5	6	7	8	9	10	11	12	13	14	15	16	17	18
contains signal?	1	1	1	1	0	1	1	1	1	0	1	1	1	1	0	1	1	0
variable?	0	0	0	0	0	0	0	0	0	0	0	0	0	0	0	1	1	0
combined block			1		#			2		#			3		#		4	#
block variable?			0		#			0		#			0		#		1	#

Table B.1: Exemplary table showing the steps necessary to minimize the usage of AWG memory, following the example given in fig. B.1. The first row indicates the number of the minimal segment, and therefore each column corresponds to the time interval of this minimal segment. The second row indicates whether a signal is present in the minimal segment. The third row indicates which minimal segments contain waveforms that change for each step. The fourth row enumerates the combined block that can be written to the AWGs memory. A combined block contains numerous minimal segments to reduce the number of signals to upload, saving upload time. The last row indicates, whether or not a block contains a waveform that changes during the experiment.

Sequence table	Segment	loops	Contains
Step 1	1	inf	Wait for trig
	3	1	Block 1
	2	1	Pause
	4	1	Block 2
	2	1	Pause
	5	1	Block 3
	2	1	Pause
	6	1	Block 4 Step 1
Step 2	1	inf	Wait for trig
	3	1	Block 1
	2	1	Pause
	4	1	Block 2
	2	1	Pause
	5	1	Block 3
	2	1	Pause
	7	1	Block 4 Step 2

Table B.2: The sequence table of the example is shown in fig. B.1. This sequence table implements memory efficient playback of the stored waveform. At the first external trigger, provided by the real-time experiment control system, the sequence is played until the following wait for trigger segment is reached. The next trigger starts the playback of the waveform for the second cycle. Since the sequence table ends, the AWG goes to row one of the sequence table and waits for the next trigger. The third trigger starts the waveform for step 1 again.

C FAQUAD ramp using a VFG150

The frequency generator VFG150, is a direct digital synthesizer capable of generating only top-hat-shaped output amplitudes of a given frequency. The adiabatic ramp needs to be approximated by such. Even though the device can store 1000 sets of parameters to generate the waveform, it is necessary to update the memory of the frequency generator at the run time. The FAQUAD ramp is discretized in defined amplitude steps $\delta A = 5 \cdot 10^{-4}$ to limit the memory requirements and streaming bandwidth. At the beginning of the FAQUAD ramp, its slope is significant, making it beneficial to calculate the amplitude in time steps $\delta t = 50\,\text{ns}$. Overall to save memory and bandwidth, The FAQUAD ramp is recalculated in time steps of $\delta t = 50\,\text{ns}..150\,\text{ns}$ and afterward, the calculated amplitudes are rounded towards a multiple of δA. Only when the amplitude changes a new set of parameters for the frequency generator is generated and transferred.

Limiting the sample time reduces the data rate at the steep slope while limiting the amplitude resolution reduces the data rate required for the part of the FAQUAD ramp featuring a low slope. The FAQUAD ramp and its approximation are shown in fig. C.1.

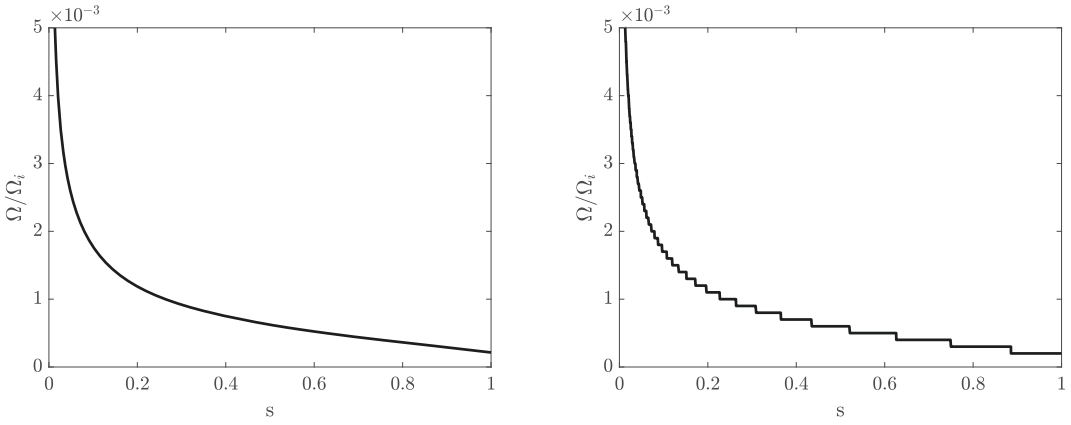

Figure C.1: (a) FAQUAD ramp calculated with $\delta t = 150\,\text{ns}$, a gate time of $T = 15\,\text{ms}$, and $\Omega_f = 2.14 \cdot 10^{-4}\Omega_i$. Here the dimensionless gate time is $s = t/T$. (b) Approximation of the FAQUAD ramp shown in (a) using a minimal $\delta A = 1 \cdot 10^{-4}$ to limit the data rate required to update the frequency generators memory.

D The ion

My successor T. Sriarunothai wrote a very exhaustive collection of properties of the $^{171}Yb^{+}$ ion [9]. Even though only some of them are relevant for this thesis, it would be incomplete without this information. T. Sriarunothai allowed me to use his work in my appendix; Therefore, this section is a faithful replica of his collection of properties.

The detailed information about the energy structure of $^{171}Yb^{+}$ ions is summarized in tables D.1, D.2, and D.3. It is visualized in D.1.

Table D.1: Yb II energy levels and their lifetime. The energy levels are the calculated values provided by the atomic database from NIST. The experimental observation of the hyperfine splittings was performed using $^{171}Yb^{+}$ ions. N/A means the experimental data is not available.

Term	Energy (cm^{-1}) [93]	Hyperfine splitting $\Delta/2\pi$ (GHz)	Lifetime	Ref.
$^2S_{1/2}$	0	$12.642\,812\,118\,466 \pm 0.000\,000\,000\,002$	-	[26, 27]
$^2P_{1/2}$	27 061.82	2.1049 ± 0.0013	(8.12 ± 0.02) ns	[35, 36]
$^2P_{3/2}$	30 392.23	1.7508 ± 0.0010	(6.15 ± 0.09) ns	[94, 95]
$^2D_{3/2}$	22 960.80	0.86 ± 0.02	(52.7 ± 2.4) ms	[96, 97]
$^2D_{5/2}$	24 332.69	0.191 ± 0.002	(7.2 ± 0.3) ms	[98, 99]
$^2F_{7/2}$	21 418.75	3.620 ± 0.002	$5.4^{+9.3}_{-3.6}$yr	[100–102]
$^3D[3/2]_{1/2}$	33 653.86	2.2095 ± 0.0011	(37.7 ± 0.5) ns	[97, 103]
$^3D[1/2]_{1/2}$	33 378.89	N/A	N/A	
$^1D[3/2]_{3/2}$	34 575.37	N/A	(28.6 ± 0.4) ns	[103]
$^1D[5/2]_{5/2}$	37 077.59	0.321 ± 0.018	< 172 ms	[95, 98]

Table D.2: Yb II transitions. The upper shows our main transitions with the corresponding laser wavelength in vacuum. The lower shows the other known transitions with their references. The energy differences are provided by the atomic database from NIST. [9]

Transition	Linewidth	ΔE (cm^{-1}) [93]	Wavelength (nm)	Ref.
$^2S_{1/2} \leftrightarrow ^2P_{1/2}$	19.6 MHz	27 061.82	369.5	[103, 104]
$^2D_{3/2} \leftrightarrow ^3D[3/2]_{1/2}$	4.2 MHz	10 693.06	935.2	[103, 104]
$^2F_{7/2} \leftrightarrow ^1D[5/2]_{5/2}$	> 0.9 Hz	15 658.84	638.6	[98, 101, 104]
$^2S_{1/2} \leftrightarrow ^1D[3/2]_{3/2}$	5.4 MHz	34 575.37	289.139	[93, 103, 104]
$^2S_{1/2} \leftrightarrow ^3D[3/2]_{1/2}$	4.2 MHz	33 653.86	297.056	[104, 105]
$^2S_{1/2} \leftrightarrow ^2P_{3/2}$	25.8 MHz	30 392.23	328.937	[104]
$^2S_{1/2} \leftrightarrow ^2D_{5/2}$	22.9 Hz	24 332.69	410.97	[98, 99]
$^2S_{1/2} \leftrightarrow ^2D_{3/2}$	3.02 Hz	22 960.80	435	[101, 106]
$^2S_{1/2} \leftrightarrow ^2F_{7/2}$	0.9 nHz	21 418.75	467	[100, 101]
$^2D_{3/2} \leftrightarrow ^3D[1/2]_{1/2}$	N/A	16 418.09	609.1	[107]
$^2F_{7/2} \leftrightarrow ^1D[3/2]_{3/2}$	5.4 MHz	13 156.62	760.072	[103, 108, 109]
$^2F_{7/2} \leftrightarrow ^2D_{5/2}$	22.9 Hz	2913.94	$3.43 \cdot 10^3$	[98, 110]

Table D.3: Yb II branching ratio. [9]

Initial state	Final state	Ratio	Ref.
$^2P_{1/2}$	$^2S_{1/2}$	$0.994\,99 \pm 0.000\,15$	[97]
	$^2D_{3/2}$	$0.005\,01 \pm 0.000\,15$	
$^2D_{5/2}$	$^2F_{7/2}$	0.83 ± 0.03	[98]
	$^2S_{1/2}$	0.17 ± 0.03	
$^2P_{3/2}$	$^2S_{1/2}$	0.9875 ± 0.0006	[95]
	$^2D_{3/2}$	0.0017 ± 0.0001	
	$^2D_{5/2}$	0.0108 ± 0.0005	
$^3D[3/2]_{1/2}$	$^2S_{1/2}$	0.982*	[111]
	$^2D_{3/2}$	0.018*	

*Calculated values

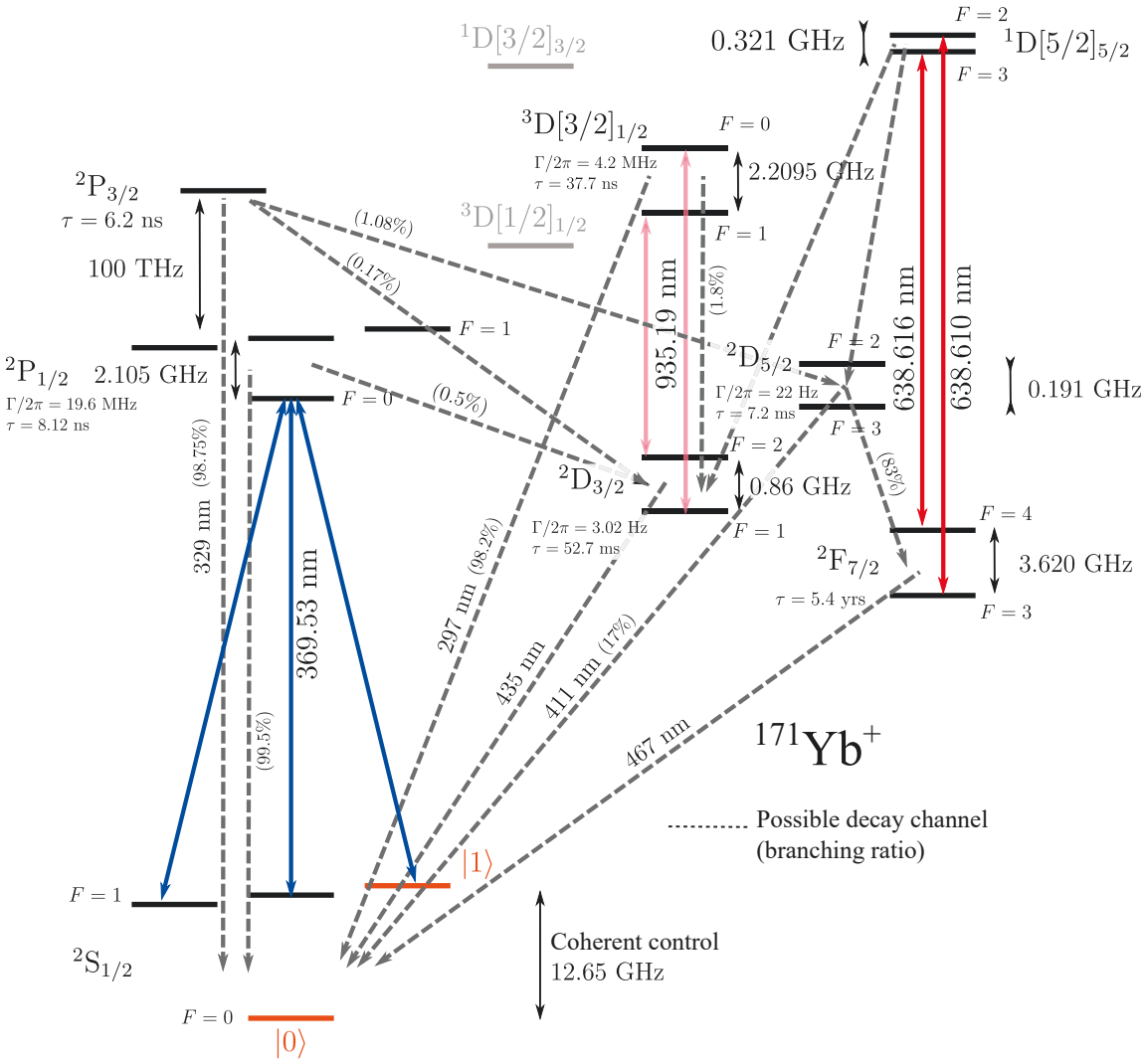

Figure D.1: Energy level structure of $^{171}Yb^+$. The schematic, not to scale, shows optical transitions for Doppler cooling and repumping, indicated by color arrows. Dashed lines show significant decay channels. Numbers in round parentheses show the branching ratio for each possible channel. The main qubit states are highlighted in orange. Our optical repumping scheme depopulates the states $|^2D_{3/2}\rangle$ and $|^2F_{7/2}\rangle$, using the 935 nm and the 638 nm laser. [9]

E Acknowledgments

"If I have seen further, it is by standing on the shoulders of giants." [1]

None of the work presented in this thesis would have been possible without the support of my predecessors. Starting with Prof. Dr. Christof Wunderlich, who started the work on quantum computers in Siegen and all the students, graduate students and postdocs, who worked on the experimental setup, I was allowed to use during my time as a graduate student.

I would especially like to thank Prof. Dr. Christof Wunderlich for his supervision and the opportunity to work freely on this project and follow my ideas.

During my time in the lab, I was accompanied by Patrick Barthel, who is a great pleasure to work with. Without his support, I would not have been able to accomplish what is presented in this thesis.

I would also like to thank my theoretical collaborators, namely Sagar Pratapsi, Erik Torrontegui and J. J. Garcia-Ripoll, for their unique insights and great discussions.

[1] Turnbull, H. W. ed., 1959. The Correspondence of Isaac Newton: 1661-1675, Volume 1, London, UK: Published for the Royal Society at the University Press. p. 416

Bibliography

[1] A. G. Bromley, "Charles babbage's analytical engine, 1838," *Annals of the History of Computing*, vol. 4, no. 3, pp. 196–217, 1982.

[2] I. Ross, "The invention of the transistor," *Proceedings of the IEEE*, vol. 86, no. 1, pp. 7–28, 1998.

[3] J. Kilby, "Invention of the integrated circuit," *IEEE Transactions on Electron Devices*, vol. 23, no. 7, pp. 648–654, 1976.

[4] T. Berners-Lee, R. Cailliau, A. Luotonen, H. F. Nielsen, and A. Secret, "The world-wide web," *Communications of the ACM*, vol. 37, no. 8, pp. 76–82, 1994.

[5] W. S. McCulloch and W. Pitts, "A logical calculus of the ideas immanent in nervous activity," *Bull. Math. Biophys.*, vol. 5, pp. 115–133, dec 1943.

[6] R. P. Feynman, "Simulating physics with computers," *International Journal of Theoretical Physics*, vol. 21, pp. 467–488, jun 1982.

[7] A. Khromova, *Quantum Gates with Trapped Ions using Magnetic Gradient Induced Coupling.* PhD thesis, Universität Siegen, 2012.

[8] C. M. Piltz, *Maßgeschneiderte Spin-Spin-Kopplung und Quanten-Fouriertransformation mit gespeicherten Yb^+ -Ionen in einem Magnetfeldgradienten.* PhD thesis, Universität Siegen, 2016.

[9] T. Sriarunothai, *Multi-Qubit Gates and Quantum-Enhanced Deliberation for Machine Learning using a Trapped-Ion Quantum Processor.* PhD thesis, Universität Siegen, 2018.

[10] A. Khromova, C. Piltz, B. Scharfenberger, T. F. Gloger, M. Johanning, A. F. Varón, and C. Wunderlich, "Designer spin pseudomolecule implemented with trapped ions in a magnetic gradient," *Phys. Rev. Lett.*, vol. 108, p. 220502, Jun 2012.

[11] W. Paul and H. Steinwedel, "Notizen: Ein neues massenspektrometer ohne magnetfeld," *Zeitschrift für Naturforschung A*, vol. 8, jan 1953.

[12] S. Bock, "Konstruktion und Simulation einer linearen Paulfalle mit hohem axialen Magnetfeldgradienten," Master's thesis, Universität Siegen, 2020.

[13] A. Steane, "The ion trap quantum information processor," *Applied Physics B: Lasers and Optics*, vol. 64, pp. 623–643, jun 1997.

[14] D. F. V. James, "Quantum dynamics of cold trapped ions with application to quantum computation," *Applied Physics B*, vol. 66, pp. 181–190, Feb 1998.

[15] F. Mintert and C. Wunderlich, "Ion-trap quantum logic using long-wavelength radiation," *Phys. Rev. Lett.*, vol. 87, pp. 257904–1–257904–4, dec 2001.

[16] T. P. Harty, D. T. C. Allcock, C. J. Ballance, L. Guidoni, H. A. Janacek, N. M. Linke, D. N. Stacey, and D. M. Lucas, "High-fidelity preparation, gates, memory, and readout of a trapped-ion quantum bit," *Phys. Rev. Lett.*, vol. 113, p. 220501, Nov 2014.

[17] D. P. Divincenzo, "Topics in quantum computers," in *Mesoscopic Electron Transport*, pp. 657–677, Springer Netherlands, 1997.

[18] D. P. DiVincenzo, "The physical implementation of quantum computation," *Fortschritte der Physik*, vol. 48, pp. 771–783, sep 2000.

[19] C. Wunderlich, T. Hannemann, T. Körber, H. Häffner, C. Roos, W. Hänsel, R. Blatt, and F. Schmidt-Kaler, "Robust state preparation of a single trapped ion by adiabatic passage," *Journal of Modern Optics*, vol. 54, no. 11, pp. 1541–1549, 2007.

[20] R. Noek, G. Vrijsen, D. Gaultney, E. Mount, T. Kim, P. Maunz, and J. Kim, "High speed, high fidelity detection of an atomic hyperfine qubit," *Opt. Lett.*, vol. 38, pp. 4735–4738, Nov 2013.

[21] S. Wölk, C. Piltz, T. Sriarunothai, and C. Wunderlich, "State selective detection of hyperfine qubits," *Journal of Physics B: Atomic, Molecular and Optical Physics*, vol. 48, p. 075101, mar 2015.

[22] C. Monroe, D. M. Meekhof, B. E. King, W. M. Itano, and D. J. Wineland, "Demonstration of a fundamental quantum logic gate," *Phys. Rev. Lett.*, vol. 75, pp. 4714–4717, Dec 1995.

[23] N. Akerman, N. Navon, S. Kotler, Y. Glickman, and R. Ozeri, "Universal gate-set for trapped-ion qubits using a narrow linewidth diode laser," *New J. Phys.*, vol. 17, no. 11, p. 113060, 2015.

[24] N. Timoney, I. Baumgart, M. Johanning, A. F. Varon, M. B. Plenio, A. Retzker, and C. Wunderlich, "Quantum gates and memory using microwave-dressed states," *Nature*, vol. 476, pp. 185–188, 08 2011.

[25] R. Blatt and D. Wineland, "Entangled states of trapped atomic ions," *Nature*, vol. 453, pp. 1008–1015, 2008.

[26] M. J. Sellars, P. T. H. Fisk, M. A. Lawn, and G. Coles, "Further investigation of

a prototype microwave frequency standard based on trapped $^{171}Yb^{+}$ ions," in *Proceedings of the 1995 IEEE International Frequency Control Symposium (49th Annual Symposium)*, Ieee, 1995.

[27] P. T. H. Fisk, M. J. Sellars, M. A. Lawn, and G. Coles, "Accurate measurement of the 12.6 GHz "clock" transition in trapped $^{171}yb^{+}$ ions," *IEEE Transactions on Ultrasonics, Ferroelectrics and Frequency Control*, vol. 44, pp. 344–354, mar 1997.

[28] P. H. Huber, "Adaptive frequency measurement of for radio frequency driven trapped ion qubits," Master's thesis, Universität Siegen, 2017.

[29] Mayer-Kuckuk, *Atomphysik*. Stuttgart Leipzig: B.G. Teubner, 1997.

[30] C. H. Balzer, *Zur Dynamik eines beobachteten einzelnen Quantensystems*. PhD thesis, Universität Hamburg, 2003.

[31] M. Johanning, A. Braun, N. Timoney, V. Elman, W. Neuhauser, and C. Wunderlich, "Individual addressing of trapped ions and coupling of motional and spin states using rf radiation," *Phys. Rev. Lett.*, vol. 102, p. 073004, Feb 2009.

[32] C. Piltz, B. Scharfenberger, A. Khromova, A. F. Varón, and C. Wunderlich, "Protecting conditional quantum gates by robust dynamical decoupling," *Phys. Rev. Lett.*, vol. 110, p. 200501, May 2013.

[33] C. Wunderlich, *Conditional Spin Resonance with Trapped Ions*, pp. 261–273. Berlin, Heidelberg: Springer Berlin Heidelberg, 2002.

[34] M. Johanning, A. Braun, D. Eiteneuer, C. Paape, C. Balzer, W. Neuhauser, and C. Wunderlich, "Resonance-enhanced isotope-selective photoionization of Yb I for ion trap loading," *Appl. Phys. B*, vol. 103, pp. 327–338, May 2011.

[35] A.-M. Mårtensson-Pendrill, D. S. Gough, and P. Hannaford, "Isotope shifts and hyperfine structure in the 369.4-nm 6s-$6p_{1/2}$ resonance line of singly ionized ytterbium," *Phys. Rev. A*, vol. 49, pp. 3351–3365, May 1994.

[36] S. Olmschenk, D. Hayes, D. N. Matsukevich, P. Maunz, D. L. Moehring, K. C. Younge, and C. Monroe, "Measurement of the lifetime of the $6p\ ^2P^o_{1/2}$ level of yb^{+}," *Phys. Rev. A*, vol. 80, p. 022502, Aug 2009.

[37] C. Piltz, *Maßgeschneiderte Spin-Spin-Kopplung und Quanten-Fouriertransformation mit gespeicherten Yb^{+} -Ionen in einem Magnetfeldgradienten*. PhD thesis, Universität Siegen, 2016.

[38] C. Piltz, T. Sriarunothai, S. S. Ivanov, S. Wölk, and C. Wunderlich, "Versatile microwave-driven trapped ion spin system for quantum information processing," *Sci-*

ence Advances, vol. 2, p. e1600093, jul 2016.

[39] P. Kaufmann, T. F. Gloger, D. Kaufmann, M. Johanning, and C. Wunderlich, "High-Fidelity preservation of quantum information during trapped ion transport," *ArXiv e-prints*, Apr. 2017.

[40] M. Lefebvre, R. Keeler, R. Sobie, and J. White, "Propagation of errors for matrix inversion," *Nuclear Instruments and Methods in Physics Research Section A: Accelerators, Spectrometers, Detectors and Associated Equipment*, vol. 451, no. 2, pp. 520–528, 2000.

[41] W. Vogel and R. L. de Matos Filho, "Nonlinear jaynes-cummings dynamics of a trapped ion," *Phys. Rev. A*, vol. 52, pp. 4214–4217, Nov 1995.

[42] T. Sriarunothai, G. S. Giri, S. Wölk, and C. Wunderlich, "Radio frequency sideband cooling and sympathetic cooling of trapped ions in a static magnetic field gradient," *Journal of Modern Optics*, vol. 65, no. 5-6, pp. 560–567, 2018.

[43] D. Eiteneuer, "Bau und Charakterisierung einer Ytterbium-Quelle für mikrostrukturierte Ionenfallen," Master's thesis, Universität Siegen, 2007.

[44] D. W. Pohl, W. Denk, and M. Lanz, "Optical stethoscopy: Image recording with resolution $\lambda/20$," *Appl. Phys. Lett.*, vol. 44, no. 7, pp. 651–653, 1984.

[45] J. K. Trautman, J. J. Macklin, L. E. Brus, and E. Betzig, "Near-field spectroscopy of single molecules at room temperature," *Nature*, vol. 369, pp. 40–42, may 1994.

[46] F. Keilmann, D. van der Weide, T. Eickelkamp, R. Merz, and D. Stöckle, "Extreme sub-wavelength resolution with a scanning radio-frequency transmission microscope," *Opt. Commun.*, vol. 129, no. 1, pp. 15–18, 1996.

[47] A. Kramer, F. Keilmann, B. Knoll, and R. Guckenberger, "The coaxial tip as a nano-antenna for scanning near-field microwave transmission microscopy," *Micron*, vol. 27, no. 6, pp. 413–417, 1996.

[48] H. Zhang, K. Arai, C. Belthangady, J.-C. Jaskula, and R. L. Walsworth, "Selective addressing of solid-state spins at the nanoscale via magnetic resonance frequency encoding," *npj Quantum Information*, vol. 3, p. 31, aug 2017.

[49] S. Bodenstedt, I. Jakobi, J. Michl, I. Gerhardt, P. Neumann, and J. Wrachtrup, "Nanoscale spin manipulation with pulsed magnetic gradient fields from a hard disc drive writer," *Nano Letters*, vol. 18, no. 9, pp. 5389–5395. Publisher: American Chemical Society.

[50] I. Jakobi, P. Neumann, Y. Wang, D. B. R. Dasari, F. E. Hallak, M. A. Bashir,

M. Markham, A. Edmonds, D. Twitchen, and J. Wrachtrup, "Measuring broadband magnetic fields on the nanoscale using a hybrid quantum register," *Nat. Nanotechnol.*, vol. 12, pp. 67–72, sep 2016.

[51] J. A. Sidles, "Noninductive detection of single proton magnetic resonance," *Applied Physics Letters*, vol. 58, no. 24, pp. 2854–2856, 1991.

[52] D. Rugar, C. S. Yannoni, and J. A. Sidles, "Mechanical detection of magnetic resonance," *Nature*, vol. 360, pp. 563–566, Dec 1992.

[53] S. Kotler, N. Akerman, Y. Glickman, A. Keselman, and R. Ozeri, "Single-ion quantum lock-in amplifier," *Nature*, vol. 473, no. 61, 2011.

[54] I. Baumgart, J.-M. Cai, A. Retzker, M. B. Plenio, and C. Wunderlich, "Ultrasensitive magnetometer using a single atom," *Phys. Rev. Lett.*, vol. 116, p. 240801, Jun 2016.

[55] T. Ruster, H. Kaufmann, M. A. Luda, V. Kaushal, C. T. Schmiegelow, F. Schmidt-Kaler, and U. G. Poschinger, "Entanglement-based dc magnetometry with separated ions," *Phys. Rev. X*, vol. 7, p. 031050, Sep 2017.

[56] S. Knünz, M. Herrmann, V. Batteiger, G. Saathoff, T. W. Hänsch, K. Vahala, and T. Udem, "Injection locking of a trapped-ion phonon laser," *Phys. Rev. Lett.*, vol. 105, p. 013004, Jul 2010.

[57] M. J. Biercuk, H. Uys, J. W. Britton, A. P. VanDevender, and J. J. Bollinger, "Ultrasensitive detection of force and displacement using trapped ions," *Nature Nanotechnology*, vol. 5, pp. 646–650, 08 2010.

[58] R. Maiwald, A. Golla, M. Fischer, M. Bader, S. Heugel, B. Chalopin, M. Sondermann, and G. Leuchs, "Collecting more than half the fluorescence photons from a single ion," *Phys. Rev. A*, vol. 86, p. 043431, Oct 2012.

[59] T. F. Gloger, P. Kaufmann, D. Kaufmann, M. T. Baig, T. Collath, M. Johanning, and C. Wunderlich, "Ion-trajectory analysis for micromotion minimization and the measurement of small forces," *Phys. Rev. A*, vol. 92, p. 043421, Oct 2015.

[60] V. Blums, M. Piotrowski, M. I. Hussain, B. G. Norton, S. C. Connell, S. Gensemer, M. Lobino, and E. W. Streed, "A single-atom 3d sub-attonewton force sensor," *Science Advances*, vol. 4, no. 3, 2018.

[61] K. Sugiyama and J. Yoda, "Disappearance of Yb^+ in excited states from rf trap by background gases," *Japanese Journal of Applied Physics*, vol. 34, pp. L584–l586, may 1995.

[62] A. M. Hankin, E. R. Clements, Y. Huang, S. M. Brewer, J.-S. Chen, C. W. Chou,

D. B. Hume, and D. R. Leibrandt, "Systematic uncertainty due to background-gas collisions in trapped-ion optical clocks," *Phys. Rev. A*, vol. 100, p. 033419, Sep 2019.

[63] M. Johanning, "Isospaced linear ion strings," *Applied Physics B*, vol. 122, no. 71, 2016.

[64] P. J. Kunert, D. Georgen, L. Bogunia, M. T. Baig, M. A. Baggash, M. Johanning, and C. Wunderlich, "A planar ion trap chip with integrated structures for an adjustable magnetic field gradient," *Applied Physics B*, vol. 114, pp. 27–36, Jan 2014.

[65] C. Piltz, T. Sriarunothai, A. Varón, and C. Wunderlich, "A trapped-ion-based quantum byte with 10e-5 next-neighbour cross-talk," *Nat. Commun.*, vol. 5, p. 4679, Aug 2014.

[66] P. Wang, C.-Y. Luan, M. Qiao, M. Um, J. Zhang, Y. Wang, X. Yuan, M. Gu, J. Zhang, and K. Kim, "Single ion qubit with estimated coherence time exceeding one hour," *Nature Communications*, vol. 12, p. 233, Jan 2021.

[67] S. Meiboom and D. Gill, "Modified spin echo method for measuring nuclear relaxation times," *Review of Scientific Instruments*, vol. 29, no. 8, pp. 688–691, 1958.

[68] G. T. Genov, D. Schraft, N. V. Vitanov, and T. Halfmann, "Arbitrarily accurate pulse sequences for robust dynamical decoupling," *Phys. Rev. Lett.*, vol. 118, p. 133202, 3 2017.

[69] R. Cleve and J. Watrous, "Fast parallel circuits for the quantum fourier transform," *Proceedings 41st Annual Symposium on Foundations of Computer Science*, pp. 526–536, 2000.

[70] D. Maslov, "Linear depth stabilizer and quantum fourier transformation circuits with no auxiliary qubits in finite-neighbor quantum architectures," *Phys. Rev. A*, vol. 76, p. 052310, Nov 2007.

[71] D. Maslov, G. Dueck, D. Miller, and C. Negrevergne, "Quantum circuit simplification and level compaction," *Computer-Aided Design of Integrated Circuits and Systems, IEEE Transactions on*, vol. 27, pp. 436–444, 04 2008.

[72] A. G. Fowler, S. J. Devitt, and L. C. Hollenberg, "Implementation of shor's algorithm on a linear nearest neighbour qubit array," *arXiv preprint quant-ph/0402196*, 2004.

[73] P. Baßler, M. Zipper, C. Cedzich, M. Heinrich, P. H. Huber, M. Johanning, and M. Kliesch, "Synthesis of and compilation with time-optimal multi-qubit gates," *Quantum*, vol. 7, p. 984, Apr. 2023.

[74] E. Masanet, A. Shehabi, N. Lei, S. Smith, and J. Koomey, "Recalibrating global data

center energy-use estimates," *Science*, vol. 367, no. 6481, pp. 984–986, 2020.

[75] S. Silva Pratapsi, P. H. Huber, P. Barthel, S. Bose, C. Wunderlich, and Y. Omar, "Classical half-adder using trapped-ion quantum bits: Toward energy-efficient computation," *Applied Physics Letters*, vol. 123, p. 154003, 10 2023.

[76] L. Eloie, L. Banchi, and S. Bose, "Quantum arithmetics via computation with minimized external control: The half-adder," *Phys. Rev. A*, vol. 97, p. 062321, Jun 2018.

[77] V. V. Shende and I. L. Markov, "On the cnot-cost of toffoli gates," *Quantum Info. Comput.*, vol. 9, pp. 461–486, 05 2009.

[78] M. Ježek, J. Fiurášek, and Z. c. v. Hradil, "Quantum inference of states and processes," *Phys. Rev. A*, vol. 68, p. 012305, Jul 2003.

[79] E. O. Kiktenko, D. O. Norkin, and A. K. Fedorov, "Confidence polytopes for quantum process tomography," *New Journal of Physics*, vol. 23, p. 123022, dec 2021.

[80] I. Boldin, B. Okhrimenko, E. Esteki, and C. Wunderlich, "Under preparation,"

[81] E. Torrontegui and J. Garcia-Ripoll, "Universal quantum perceptron as efficient unitary approximators," *EPL (Europhysics Letters)*, vol. 125, 01 2018.

[82] W. S. McCulloch and W. Pitts, "A logical calculus of the ideas immanent in nervous activity," *The bulletin of mathematical biophysics*, Dec 1943.

[83] K. Hornik, M. Stinchcombe, and H. White, "Multilayer feedforward networks are universal approximators," *Neural Networks*, vol. 2, no. 5, pp. 359–366, 1989.

[84] J. J. Hopfield, "Neurons with graded response have collective computational properties like those of two-state neurons.," *Proceedings of the national academy of sciences*, vol. 81, no. 10, pp. 3088–3092, 1984.

[85] M. Born and V. Fock, "Beweis des adiabatensatzes," *Zeitschrift für Physik*, vol. 51, pp. 165–180, Mar 1928.

[86] S. Martínez-Garaot, A. Ruschhaupt, J. Gillet, T. Busch, and J. G. Muga, "Fast quasiadiabatic dynamics," *Phys. Rev. A*, vol. 92, p. 43406, oct 2015.

[87] D. Guéry-Odelin, A. Ruschhaupt, A. Kiely, E. Torrontegui, S. Martínez-Garaot, and J. G. Muga, "Shortcuts to adiabaticity: Concepts, methods, and applications," *Rev. Mod. Phys.*, vol. 91, p. 045001, oct 2019.

[88] P. H. Huber, J. Haber, P. Barthel, J. J. García-Ripoll, E. Torrontegui, and C. Wunderlich, "Realization of a quantum perceptron gate with trapped ions," *arXiv 2111.08977*, 2021.

[89] P. Barthel, P. H. Huber, J. Casanova, I. Arrazola, D. Niroomand, T. Sriarunothai, M. B. Plenio, and C. Wunderlich, "Robust two-qubit gates using pulsed dynamical decoupling," *New Journal of Physics*, vol. 25, p. 063023, jun 2023.

[90] P. Barthel, "Microwave-Dressed States for Quantum Gates with 171Yb+ Ions," Master's thesis, Universität Siegen, 2016.

[91] T. Gloger, "Mikrowellenquelle mit phasen kohärenter Frequenzumschaltung zur Quantenzustands manipulation," Master's thesis, Universität Siegen, 2011.

[92] P. Kaufmann, "Präzise Wellenlängenmessung und Computer-Steuerung für Experimente mit gespeicherten Yb-Ionen," Master's thesis, Universität Siegen, 2012.

[93] A. Kramida, Yu. Ralchenko, J. Reader, and and NIST ASD Team. NIST Atomic Spectra Database (ver. 5.5.6), [Online]. Available: `https://physics.nist.gov/asd` [2018, September 5]. National Institute of Standards and Technology, Gaithersburg, MD., 2018.

[94] E. H. Pinnington, G. Rieger, and J. A. Kernahan, "Beam-laser measurements of the lifetimes of the 6p levels in yb ii," *Phys. Rev. A*, vol. 56, pp. 2421–2423, Sep 1997.

[95] T. Feldker, H. Fürst, N. V. Ewald, J. Joger, and R. Gerritsma, "Spectroscopy of the $^2s_{1/2} \rightarrow^2 p_{3/2}$ transition in yb ii: Isotope shifts, hyperfine splitting, and branching ratios," *Phys. Rev. A*, vol. 97, p. 032511, Mar 2018.

[96] N. Yu and L. Maleki, "Lifetime measurements of the $4f^{14}5d$ metastable states in single ytterbium ions," *Phys. Rev. A*, vol. 61, p. 022507, Jan 2000.

[97] S. Olmschenk, K. C. Younge, D. L. Moehring, D. N. Matsukevich, P. Maunz, and C. Monroe, "Manipulation and detection of a trapped Yb^+ hyperfine qubit," *Phys. Rev. A*, vol. 76, nov 2007.

[98] P. Taylor, M. Roberts, S. V. Gateva-Kostova, R. B. M. Clarke, G. P. Barwood, W. R. C. Rowley, and P. Gill, "Investigation of the $^2S_{1/2}-^2D_{5/2}$ clock transition in a single ytterbium ion," *Phys. Rev. A*, vol. 56, pp. 2699–2704, Oct 1997.

[99] M. Roberts, P. Taylor, S. V. Gateva-Kostova, R. B. M. Clarke, W. R. C. Rowley, and P. Gill, "Measurement of the $^2S_{1/2}-^2D_{5/2}$ clock transition in a single $^{171}yb^+$ ion," *Phys. Rev. A*, vol. 60, pp. 2867–2872, Oct 1999.

[100] M. Roberts, P. Taylor, G. P. Barwood, W. R. C. Rowley, and P. Gill, "Observation of the $^2S_{1/2}-^2F_{7/2}$ electric octupole transition in a single $^{171}yb^+$ ion," *Phys. Rev. A*, vol. 62, p. 020501(r), Jul 2000.

[101] M. Roberts, P. Taylor, G. P. Barwood, P. Gill, H. A. Klein, and W. R. C. Rowley,

"Observation of an electric octupole transition in a single ion," *Phys. Rev. Lett.*, vol. 78, pp. 1876–1879, Mar 1997.

[102] P. Taylor, M. Roberts, G. M. Macfarlane, G. P. Barwood, W. R. C. Rowley, and P. Gill, "Measurement of the infrared $^2F_{7/2}-^2D_{5/2}$ transition in a single $^{171}yb^+$ ion," *Phys. Rev. A*, vol. 60, pp. 2829–2833, Oct 1999.

[103] R. W. Berends, E. H. Pinnington, B. Guo, and Q. Ji, "Beam-laser lifetime measurements for four resonance levels of yb II," *Journal of Physics B: Atomic, Molecular and Optical Physics*, vol. 26, pp. L701–l704, oct 1993.

[104] W. F. Meggers, C. H. Corliss, and B. F. Scribner, *Tables of Spectral-Line Intensities Part I–Arranged by Elements*. National Bureau of Standards Monograph 145, Government Printing Office, Washington, DC, 2nd ed., 1975.

[105] H. M. Meyer, M. Steiner, L. Ratschbacher, C. Zipkes, and M. Köhl, "Laser spectroscopy and cooling of yb^+ ions on a deep-uv transition," *Phys. Rev. A*, vol. 85, p. 012502, Jan 2012.

[106] D. Engelke and C. Tamm, "Dark times in the resonance fluorescence of trapped ^{171}yb ions caused by spontaneous quantum jumps to the ^{2}d3/2($f = 2$) state," *Europhysics Letters (EPL)*, vol. 33, pp. 347–352, feb 1996.

[107] P. T. H. Fisk, M. A. Lawn, and C. Coles, "Laser cooling of $^{171}Yb^+$ ions in a linear paul trap," *Applied Physics B*, vol. 57, pp. 287–291, Oct 1993.

[108] K. Sugiyama, "Laser cooling of single174yb$^+$ions stored in a RF trap," *Japanese Journal of Applied Physics*, vol. 38, pp. 2141–2147, apr 1999.

[109] N. Huntemann, M. Okhapkin, B. Lipphardt, S. Weyers, C. Tamm, and E. Peik, "High-accuracy optical clock based on the octupole transition in $^{171}Yb^+$," *Phys. Rev. Lett.*, vol. 108, p. 090801, Feb 2012.

[110] A. Bell, P. Gill, H. Klein, A. Levick, and W. Rowley, "Precision measurement of the $^2f_{1/2}-^2d_{5/2}$ 3.43 μm intervel in trapped $^{172}yb^+$," *Journal of Modern Optics*, vol. 39, pp. 381–387, feb 1992.

[111] B. C. Fawcett and M. Wilson, "Computed oscillator strengths, landé g values, and lifetimes in yb II," *Atomic Data and Nuclear Data Tables*, vol. 47, pp. 241–317, mar 1991.